An Inclusive Analysis of the Leptonic Decay Modes of the Z^0 boson

Rashid Shahid Zuberi

Balliol College, Oxford

A thesis submitted for the degree of Doctor of Philosophy
at the University of Oxford

Michaelmas Term, 1994

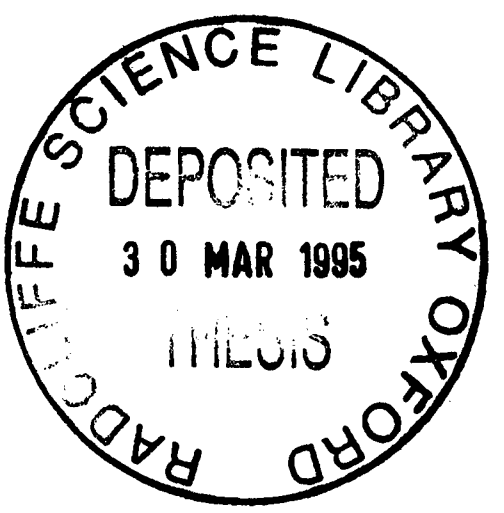

An Inclusive Analysis of the Leptonic Decay Modes of the Z^0 boson

Rashid Shahid Zuberi
Balliol College, Oxford

Submitted for the degree of Doctor of Philosophy
at the University of Oxford
Michaelmas Term, 1994

ABSTRACT

This thesis describes an analysis of the process $e^+e^- \rightarrow l^+l^-$ (where $l = e, \mu, \tau$) at centre-of-mass energies between 88 GeV and 94 GeV, using the data collected by the DELPHI detector between the years 1991 and 1993. The leptonic decays of the Z^0 boson are selected without attempting to separate the three lepton types, thus making it an inclusive lepton analysis.

The theory behind lepton pair production is introduced and the extraction of various electroweak parameters from the experimental observables is discussed. The LEP collider and the DELPHI detector are described, with special emphasis being given to the sub-detectors used in the analysis. The criteria used to select a high purity leptonic sample are described along with calculations of various backgrounds and efficiencies. The sample of selected leptonic events is then used to measure the cross-sections and forward-backward asymmetries.

Finally, a fit to these cross-sections and asymmetries, together with the hadronic ($e^+e^- \rightarrow q\bar{q}$) cross-sections, is carried out. Various Z^0 parameters are obtained: the mass and total width $M_Z = 91.1876 \pm 0.0052\,\mathrm{GeV/c^2}$, $\Gamma_Z = 2.4971 \pm 0.0061$ GeV, the ratio of the hadronic to leptonic partial widths $R_l = 20.73 \pm 0.09$, and the pole leptonic asymmetry $(A^0_{FB})^l = 0.0195 \pm 0.0042$. Using these results and the value of the strong coupling constant (α_s), determined by the DELPHI collaboration, the number of light neutrino species is determined to be $N_\nu = 3.045 \pm 0.035$. The leptonic partial width is found to be: $\Gamma_l = 83.82 \pm 0.29$ MeV. Using the measured leptonic forward-backward asymmetries, the squared vector and axial-vector couplings of the Z^0 to charged leptons are found to be $(\hat{g_v}^l)^2 = (1.65 \pm 0.36) \times 10^{-3}$ and $(\hat{g_a}^l)^2 = 0.2505 \pm 0.0009$. These values can be used to determine the effective rho parameter and the effective weak mixing angle: $\hat{\rho} = 1.0020 \pm 0.0036$, and $\sin^2\theta^{\mathrm{eff}}_{\mathrm{lept}} = 0.2297 \pm 0.0024$.

A full Standard Model fit to the data gives the values of the strong coupling constant, α_s, and the mass of the top quark, m_{top}, as being:

$$\begin{aligned} \alpha_{\mathrm{s}} &= 0.123 \pm 0.010, \\ m_{\mathrm{top}} &= 178\ ^{+22}_{-25}(\mathrm{expt})\ ^{+18}_{-16}(\mathrm{Higgs})\ \mathrm{GeV/c^2}, \end{aligned}$$

where $60 < m_{\mathrm{Higgs}}\ (\mathrm{GeV/c^2}) < 1000$ with a central value of 300 $\mathrm{GeV/c^2}$. All the results obtained agree with the results from the lepton-identified analyses (analyses in which leptonic events are selected on the basis of their individual flavour) and with the predictions of the Standard Model.

ACKNOWLEDGEMENTS

Bismillah-hir-rahman-hir-rahim.

I knew this would happen. There would finally come a day when it was all over and I would not know what to say. Let me try to show my appreciation to the hundreds of people involved directly or indirectly with this thesis. Please bear with me.

First and foremost, I would like to thank my supervisor Peter Renton for his consistently good advise and encouragement, Simon Hodgson who was instrumental in my decision to do the analysis reported in this thesis and for his patience in replying to my thousand and one questions and Gerald Myatt for providing me with invaluable help and motivation all the way to the end. I sincerely thank you all.

I am grateful to the Nuclear Physics Laboratory for financial support on various occasions.

Special mention has to go for Stevie 'poo' Bosworth who has been a wonderful friend and office mate, be it in Oxford or in Geneva. I advise him to see a doctor who can tell him how to improve his swift movements on a squash court. Simon 'its triviaaal' Blyth has to be thanked for having put up with my, as he so aptly put it, "spurious emissions" in the last few weeks. I wish him all the best in his Oriental endeavours. The two 'peeegs' Paul 'llpd' Dauncey and Gary 'not bad for a woman from Ipswich' Barker have to be thanked simply for being themselves ! Thanks also go to, Christine 'aunty' Beeston for all her help with the muon analysis, Guy 'mogul' Wilkinson for all the useful discussions, Martin 'not mister' Bates for showing me how to appreciate the University Parks, Tim 'I am a vegetarian but a baby would be fine' Adye for all his help, Paulage 'great' Collins for simply being a nice person, and to John 'boy wonder' Holt for being be able to cook really 'awesome' curries. I thank you all for allowing me to be part of such a highly intellectual group of people !

My time at CERN was one of the most enjoyable parts of the whole experience. I made some very good friends all of whom deserve a mention. I would like to thank, Davide 'I am on a diet' Vite who is an extremely nice person and always has 'very nice' things to say about me, Bruna 'oy oy' Bertucci and Giovanni Ambrosi for all their hospitality, Antonella 'ma no' Del Rosso for all the dinners she organized, Francesco 'o sole mio' Marchetti-Stasi and Anna 'catalan' Pascual for helping me through some difficult times, and Erhan 'what are you talking about' Pesen who is a good friend. Special thanks go to Maria-Grazia 'grazie' Setzu for all the 'outings to the lago' and for being such a sympathetic listener.

On the academic side at CERN, I want to thank Teddy Todorov, Pete Ratoff, Paolo Checchia, Oreste Nicrosini, and Sasha Olshevsky for countless fruitful discussions.

I would like to thank Louis Lyons for all his help with 'errors', and Bill Williams who can argue on anything from Particle Physics to religion to politics. I would like to specially thank Bill for all the help he has given to me over the last 3 years.

I had some great times in London, thanks to, Aun 'int' and Sajjad 'sayandad' Habib, Alia 'Ali's cousin' Ali, Kanval 'behans' Mehta, Masood 'bil' Khan, Shariq and Samira Abdullah, and Ali 'joo' Jameel. The last person has to be mentioned especially for putting up with me on many occasions. Special thanks to Ali Haider who was certainly a friend in need and has always stood by me.

Coming on to a very important person in my life, I want to say that without the constant support and love from Nilofar this thesis would not have been possible. As we say 2 months and counting !

I would like to thank all my family, my brother (Abid) his wife (Shazia B.), my sister (Raheela) and her husband (Mansoor) and the kiddies, Saad, Nadia and Ali for their continuous support. Heads and shoulders above the rest, I want to thank Amma and Abba, without whom I would not be where I am today.

Dedicated To My Parents

Contents

Chapter 1

The Standard Model of Particle Physics

Chapter Abstract

The Standard Model of Particle Physics is briefly described in this chapter. Before summarizing the Standard Model, the principle of gauge theories and the invariance of the Lagrangians under a local transformation are discussed. Calculations of the cross-section and the forward-backward asymmetry for the the electron-positron annihilations into charged lepton pairs, $e^+e^- \rightarrow Z^0 \rightarrow l^+l^-$ (l= e, μ, τ) are shown, along with higher order corrections. A brief introduction is also given to the t-channel Bhabha scattering process which is relevant to the analysis detailed in this thesis.

1.1 Introduction

The fundamental particles in nature consist of:

- Spin $\frac{1}{2}$ **fermions**. These consist of **quarks** with fractional electric charges ($-\frac{1}{3}e$ and $\frac{2}{3}e$) and **leptons** with integral charges.
- Spin 1 **bosons**. These are the propagators of the forces of nature and consist of γ, $W^{\pm}$, Z^0 and g (see table 1.1).

These particles together form all structures from atoms to galaxies, under the influence of four forces : the electromagnetic force, the strong and weak forces, and gravity (see table 1.2). There exist, three generations of particles, table 1.3, each containing two leptons and two quarks, with the top quark[1] still undiscovered. The understanding that exists today of the Standard Model is that, it is the theory which encompasses all these leptons and quarks and the interactions between them.

[1]The CDF collaboration have recently published a paper [1] in which they report observing a top quark signal consistent with a mass of $m_{\text{top}} = 174 \pm 10\ ^{+13}_{-12}$ GeV.

Force	Mediating boson	
Electro-weak force	γ	photon
	W	W
	Z	Z
Strong force	**g**	gluon
Mass mechanism	**H**	Higgs

Table 1.1: The bosons which are the carriers of the fundamental forces along with the Higgs boson which may underlie the mechanism through which all particles acquire mass.

- **Gravity**, within the context of particle physics, is by far the least important force due to the mass and scales involved and its effects are many orders of magnitude smaller then the other forces. It is postulated that the carrier of the gravity force is the **graviton** which is so far undiscovered.

- The **electromagnetic** force is mediated by the massless photon and is responsible for the bound states of atoms and molecules. Both the electromagnetic force and gravity have an infinite range.

- The **strong** force is a short-range force and accounts for the interaction between quarks. Quarks are manifest in two kinds of bound states (no free quarks have been observed), the **mesons**, $q\overline{q}$ state, and the **baryons**, qqq state, both states known as **hadrons**. The $\overline{q}$ stands for the anti-quark. The existence of anti-fermions is implicit in our description. The strong force is mediated by eight massless vector particles called **gluons**.

- The **weak** force is a short-range force felt by all fermions and has as its mediators the two massive charged bosons W^+ and W^- and the massive neutral boson Z^0.

The nature of these forces is investigated through the use of high energy particle accelerators.[2] The use of high energies being imperative, firstly, because of the masses of the matter constituents and secondly, because of the small scales of distances involved.

[2]Not exclusively particle accelerators as there are some non-accelerator experiments that investigate these matters.

Comparison of Forces					
Type of Interaction	Relative Strength	Range	Typical Lifetime (sec)	Typical Cross-section (mb)	Particles that 'feel' force
Gravitational	10^{-45}	∞	-	-	All
Weak	10^{-7}	Short	10^{-12}	10^{-11}	All
Electromagnetic	10^{-2}	∞	10^{-20} - 10^{-16}	10^{-3}	Charged
Strong	10	Short	10^{-23}	10	Hadrons

Table 1.2: A summary of the properties of the four fundamental forces arranged in order of increasing strength.

Quarks		Leptons	
d	down	e^-	electron
u	up	ν_e	electron neutrino
s	strange	μ^-	muon
c	charm	ν_μ	muon neutrino
b	bottom	τ^-	tau
t	top	ν_τ	tau neutrino

Table 1.3: The six type of leptons and quarks which make up all matter according to the Standard Model.

The leptons, quarks and the bosons acquire a mass through a mechanism, called the **Higgs Mechanism** [2], according to which all particles interact via a spin-0 boson, called the **Higgs** boson. As it stands this mechanism has not been verified experimentally, as this boson still eludes the particle physicists.

The Standard Model is well documented in various places, see for example [3], and only a brief description is given here. To understand this **gauge** theory it is necessary to begin with the gauge principle.

1.2 The Principle of Gauge Theories

To understand the principle of gauge theories one has to understand the principles of **global** and **local** invariances. A global invariance is one in which the same transformation is carried out at all space-time points, and in contrast a local invariance is one in which different transformations are carried out at all space-time points. In general, a theory which is globally invariant will not be invariant under locally varying transformations. But through the introduction of new force fields that interact with the original particles in the theory in a specific way, and which also transform in a particular way under local transformations, local invariance can be restored.

For a field ψ, invariance under a constant change in phase, a global invariance, has the form

$$\psi \rightarrow \psi' = e^{i\alpha}\psi, \tag{1.1}$$

where α is a constant and the same for all space-time points. Equation 1.1 expresses the fact that once a phase convention (choice of α) has been made at one space-time point, the same convention must be adopted at all other points. For a local phase invariance the transformation becomes:

$$\psi(\mathrm{x},t) \rightarrow \psi'(\mathrm{x},t) = exp\left[-i\alpha(\mathrm{x},t)\right]\psi(\mathrm{x},t). \tag{1.2}$$

In the case of a Dirac Lagrangian, describing a free particle of mass m,

$$\mathcal{L}_D = \overline{\psi}(i\gamma^\mu\delta_\mu - m)\psi, \tag{1.3}$$

demanding an invariance under a local phase transformation, equation 1.2, leads to the re-definition of

$$\delta^\mu \rightarrow D^\mu = \delta^\mu + ieA^\mu, \tag{1.4}$$

where A^μ is a 4-vector potential which should transform as

$$A^\mu \rightarrow A'^\mu = A^\mu + \delta^\mu \alpha, \tag{1.5}$$

where equation 1.4 is referred to as the 'minimal coupling'. Thus it can be seen that demanding a local phase invariance of the Dirac lagrangian, equation 1.3, has lead to the addition of an interaction term

$$\mathcal{L}_D \rightarrow \mathcal{L}_D + \mathcal{L}_{\text{int}}, \tag{1.6}$$

where the interaction term is

$$\mathcal{L}_{\text{int}} = -e\overline{\psi}\gamma^\mu \psi A_\mu, \tag{1.7}$$

where e represents the strength with which the quanta of excitation of the field A_μ interact with particles of the matter field ψ. Equation 1.2 can be rewritten as

$$\psi(\mathrm{x}, t) = U\psi(\mathrm{x}, t), \tag{1.8}$$

where U is a unitary operator that is a representation of gauge group U(1). As $\alpha(\mathrm{x}, t)$ is a continuous variable it has an infinite number of elements all of which commute making U(1) an **abelian** group.

The quantum of excitation of the A_μ field is a vector particle (photon in QED) which must be massless, as the addition of a term such as

$$\mathcal{L}_{\text{mass}} = \frac{1}{2} m^2 A_\mu A^\mu, \tag{1.9}$$

to the Dirac lagrangian in equation 1.6

$$\mathcal{L}_D \rightarrow \mathcal{L}_D + \mathcal{L}_{\text{int}} + \mathcal{L}_{\text{mass}}, \tag{1.10}$$

would destroy the gauge invariance.

Thus gauge theories represent a *local* symmetry, in which the physical equations are invariant under transformations applied independently at each space-time point. One such well known gauge theory is the **Standard Model** of particle physics.

1.3 The Standard Model

The Standard Model of particle physics is the most successful achievement of modern day particle physics, because it has been able to explain many[3] observed experimental particle physics results. It is a gauge theory which describes the unification of the electromagnetic and weak forces into one single electroweak force and is based on the gauge theories postulated by Glashow, Salam, and Weinberg and hence referred to as the **GSW** model. More recently, the Standard Model has been extended to encompass **QCD** the gauge theory which describes the interactions between quarks.

As QCD is not directly relevant to the subject matter of this thesis, that is the process $e^+e^- \rightarrow l^+l^-$, it will not be further discussed. The Standard Model from now on will refer to the Standard Model of Electroweak interactions.

The GSW model is gauge invariant under the symmetry group $SU(2)_L \times U(1)_Y$ of weak isospin and hypercharge.

Gauge group SU(2)$_L$: This represents a unitary group, **non-abelian** as its generators do not commute, of 2×2 matrices with the special condition that their determinant is one. In the GSW model, demanding a local phase invariance on $\mathrm{SU}(2)_L$ under rotations in a weak isospin space, entails the introduction of three gauge fields, with three corresponding massless vector bosons $W^i_\mu (i = 1, 2, 3)$. These bosons couple with strength g to all left-handed fermions[4] with a weak isospin of t. Two of the bosons are charged $\pm$ 1 and one is neutral. See equations 1.13, and 1.14.

Gauge Group U(1)$_Y$: Demanding local phase invariance on $U(1)_Y$ under transformations in the weak hypercharge (Y) space, introduces one gauge field with an associated massless vector boson B_μ which is neutral. This boson couples with strength g' to all particles with a weak hypercharge, Y.[5]

The invariance of the GSW gauge group $SU(2)_L \times U(1)_Y$ leads to four massless fields, which can be associated with 'physical' fields through the following relations:

$$A_\mu = -\sin\theta_W W^3_\mu + \cos\theta_W B_\mu \qquad (\gamma), \tag{1.12}$$

[3] Among other things, it has not been able to explain particle masses.

[4] The L of $SU(2)_L$ denoting left-handedness.

[5] Where the weak hypercharge is defined in terms of the electric charge Q, and the third component of weak isospin t_3, as being

$$Y = 2(Q - t_3). \tag{1.11}$$

$$W_\mu^\pm = \frac{1}{\sqrt{2}}(W_\mu^1 \pm iW_\mu^2) \qquad (W^\pm), \tag{1.13}$$

$$Z_\mu = \cos\theta_W W_\mu^3 + \sin\theta_W B_\mu \qquad (Z^0), \tag{1.14}$$

where θ_W is the 'weak mixing angle' formerly known as the 'Weinberg angle'. It can be seen in the above relations, that the field A_μ represents the neutral photon field γ, the $W_\mu^\pm$ fields represent the charged $W^\pm$ boson fields, and the field Z_μ represents the neutral Z^0 boson field. All the above bosons, along with the Higgs boson and the leptons and quarks, are the fundamental constituents of the Standard Model. Their quantum number assignments in terms of the electric charge (q), the weak hypercharge (Y), the weak isospin (t) and its third component (t_3) are shown in table 1.4 and table 1.5.

Fermion	Q	Y	t	t_3
$\begin{pmatrix} \nu_e \\ e \end{pmatrix}_L$	$\begin{matrix} 0 \\ -1 \end{matrix}$	-1	+1/2	$\begin{matrix} +1/2 \\ -1/2 \end{matrix}$
$\begin{pmatrix} \nu_\mu \\ \mu \end{pmatrix}_L$	$\begin{matrix} 0 \\ -1 \end{matrix}$	-1	+1/2	$\begin{matrix} +1/2 \\ -1/2 \end{matrix}$
$\begin{pmatrix} \nu_\tau \\ \tau \end{pmatrix}_L$	$\begin{matrix} 0 \\ -1 \end{matrix}$	-1	+1/2	$\begin{matrix} +1/2 \\ -1/2 \end{matrix}$
$\begin{pmatrix} u \\ d' \end{pmatrix}_L$	$\begin{matrix} +2/3 \\ -1/3 \end{matrix}$	1/3	+1/2	$\begin{matrix} +1/2 \\ -1/2 \end{matrix}$
$\begin{pmatrix} c \\ s' \end{pmatrix}_L$	$\begin{matrix} +2/3 \\ -1/3 \end{matrix}$	1/3	+1/2	$\begin{matrix} +1/2 \\ -1/2 \end{matrix}$
$\begin{pmatrix} t \\ b' \end{pmatrix}_L$	$\begin{matrix} +2/3 \\ -1/3 \end{matrix}$	1/3	+1/2	$\begin{matrix} +1/2 \\ -1/2 \end{matrix}$

Table 1.4: Table showing the quantum number assignments for the standard model leptons and quarks.

Boson	Q	Y	t	t_3
γ	0	0	0	0
$\begin{pmatrix} W^+ \\ Z^0 \\ W^- \end{pmatrix}$	$\begin{matrix} +1 \\ 0 \\ -1 \end{matrix}$	0	+1	$\begin{matrix} +1 \\ 0 \\ -1 \end{matrix}$
H	0	0	0	0

Table 1.5: Table showing the quantum number assignments for the standard model bosons.

Through the use of these new fields it can be seen that the electroweak Lagrangian,

$$\mathcal{L}_{\mathrm{EW}} = \mathcal{L}_{\mathrm{CC}} + \mathcal{L}_{\mathrm{NC}}, \tag{1.15}$$

is made up of

- a charged current part which represents the $W^{\pm}$ bosons coupling to all left-handed fermions and conserving the charge at the vertices;
- a neutral current part representing the γ and Z^0 bosons also coupling to all fermions and conserving the flavour at the vertices.[6]

Thus, the Standard Model of Electroweak interactions is a gauge theory which encompasses all known fermions (leptons and quarks), and describes their interactions via the $W^{\pm}, Z^0$, and γ gauge bosons.

1.3.1 Electroweak Interactions

The electroweak couplings of the bosons $W^{\pm}$, Z^0, and γ are a mixture of pure vector and axial-vector couplings. The 'mediators' of the charged current interactions, the $W^{\pm}$ bosons, are of a pure V-A (vector - axial vector) nature. The neutral current interactions mediated by γ are of a pure vector type, and the ones mediated by the Z^0 are a mixture of V-A and V+A. The vertex factors for these couplings are displayed in figure 1.1.

- The V-A interactions of the $W^{\pm}$ can be parameterized [4] by the charged current

$$\mathcal{J}^{\mathrm{CC}}(V-A) = \overline{\psi}\gamma_{\mu}\frac{(1-\gamma^5)}{2}\psi. \tag{1.16}$$

[6] No Flavour Changing Neutral Currents (FCNC) have been discovered to date.

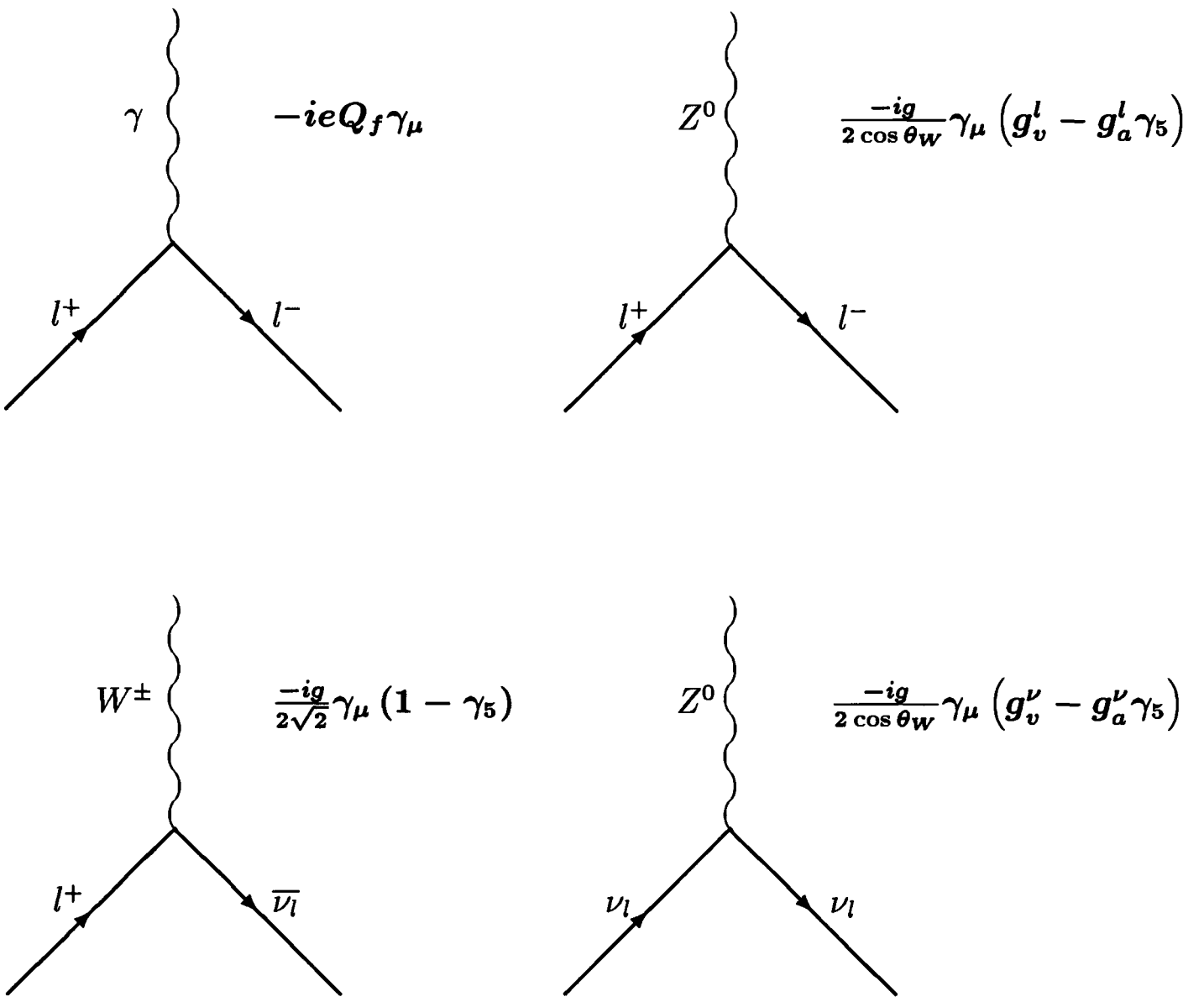

Figure 1.1: The interactions of gauge bosons with leptons.

As these bosons are said to couple to left-handed fermions only, the field ψ can be written as ψ_L

$$\psi_L = \frac{1}{2}(1-\gamma^5)\psi, \tag{1.17}$$

where $\frac{1}{2}(1 \pm \gamma^5)$ are termed 'projection operators' because acting on a field, $\frac{1}{2}(1-\gamma^5)$ projects out only the left-handed components of the wave-function and $\frac{1}{2}(1+\gamma^5)$ the right-handed components only. Thus the choice in equation 1.17 ensures that the $W^\pm$ couple to left-handed particles and so the charged current can be re-written as

$$\mathcal{J}^{CC}(V-A) = \overline{\psi}_L\gamma_\mu\psi_L. \tag{1.18}$$

- The Z^0 has a mixture of V-A and V+A interactions. The argument here is the same as before but the only difference is that the Z^0 also couples to right-handed particles and so the current has a V-A part as above and also a V+A

part.

$$\mathcal{J}^{\mathrm{NC}}(V+A) = \overline{\psi}\gamma_\mu \frac{(1+\gamma^5)}{2}\psi = \overline{\psi}_R \gamma^\mu \psi_R, \tag{1.19}$$

where

$$\psi_R = \frac{1}{2}(1+\gamma^5)\psi. \tag{1.20}$$

- For the neutral couplings with the photon as the mediator, the current which is purely vector, can be written as

$$\mathcal{J}^{\mathrm{NC}}(V) = \overline{\psi}\gamma_\mu\psi. \tag{1.21}$$

The basic QED interaction, mediated by the photon, is

$$-(j^{\mathrm{em}})^\mu A_\mu, \tag{1.22}$$

where $(j^{\mathrm{em}})^\mu$, is the electromagnetic current which couples to the electromagnetic field:

$$(j^{\mathrm{em}})^\mu = Q_f \overline{\psi}\gamma^\mu\psi, \tag{1.23}$$

where Q_f is the electric charge. It is $-e$ in the case of electrons and $+e$ in the case of positrons. Now, just as the electromagnetic current is coupled to the photon, it is assumed that the electroweak current is coupled to the vector bosons. Hence, using the isotriplet of vector fields W^i_μ coupled with a strength g to the weak isospin current $(j^3_t)^\mu$, together with a single vector field B_μ coupled to the weak hypercharge current $(j^Y)^\mu$ with a strength conventionally taken to be $\frac{g^{'}}{2}$, the basic electroweak interaction becomes:

$$-g(j^3_t)^\mu W^3_\mu - \frac{g^{'}}{2}(j^Y)^\mu B_\mu, \tag{1.24}$$

and using the equations 1.12, 1.13, and 1.14 the electroweak neutral current interaction can be written as

$$-\left(g\sin\theta_W (j^3_t)^\mu + g^{'}\cos\theta_W \frac{(j^Y)^\mu}{2}\right) A_\mu - \left(g\cos\theta_W (j^3_t)^\mu - g^{'}\sin\theta_W \frac{(j^Y)^\mu}{2}\right) Z_\mu. \tag{1.25}$$

The first term in this expression is just the electromagnetic interaction, equation 1.22, and hence the following relation can be written

$$g\sin\theta_W = g^{'}\cos\theta_W = e. \tag{1.26}$$

Using equation 1.26 the weak neutral current interaction can be written in the form

$$j_\mu^{\mathrm{NC}} = \frac{e}{\cos\theta_W \sin\theta_W}\overline{\psi}\gamma^\mu \left[t_3\frac{1-\gamma_5}{2} - Q_f \sin^2\theta_W\right]\psi, \tag{1.27}$$

or

$$j_\mu^{\mathrm{NC}} = \frac{e}{2\cos\theta_W \sin\theta_W}\overline{\psi}\gamma^\mu(g_v - g_a\gamma^5)\psi, \tag{1.28}$$

where g_v and g_a are the vector and axial-vector couplings respectively, and using equation 1.27 and equation 1.28 their definitions become

$$g_a = t_3\sqrt{\rho}, \tag{1.29}$$

$$g_v = (t_3 - 2Q_f \sin^2\theta_W)\sqrt{\rho}, \tag{1.30}$$

where t_3 represents the third component of weak isopspin, Q_f the 'physical' charge of the fermion in units of e, and ρ has been introduced as a measure of the relative strengths of the neutral and charged currents. The values of g_a and g_v for different fermions are given in table 1.6.

Fermion	Q_f	g_v	g_a
e^-, μ^-, τ^-	-1	$-\frac{1}{2} + 2\sin^2\theta_w$	$-\frac{1}{2}$
ν_e, ν_μ, ν_τ	0	$\frac{1}{2}$	$\frac{1}{2}$
d, s, b	$-\frac{1}{3}$	$-\frac{1}{2}+\frac{2}{3}\sin^2\theta_W$	$-\frac{1}{2}$
u, c, t	$\frac{2}{3}$	$\frac{1}{2}-\frac{4}{3}\sin^2\theta_W$	$\frac{1}{2}$

Table 1.6: The axial-vector (g_a) and vector (g_v) coupling constants for elementary fermions.

1.3.2 Mass Generation and Renormalizability

In the Standard Model it is assumed that the underlying local gauge symmetry is **spontaneously broken** through a process known as the **Higgs mechanism.** It is required that the $SU(2) \otimes U(1)$ symmetry be broken spontaneously in such a way that that the photon remains massless, that is, there must be a residual $U(1)$ symmetry for the electromagnetic interaction. The remaining three bosons must acquire masses in this process. This can be achieved via the introduction of

four independent scalar fields, the simplest choice[7] being a weak isospin doublet of complex scalar fields (equation 1.31), which transforms as a $t = \frac{1}{2}$ multiplet under $SU(2)_L$.

$$\phi(x) = \begin{pmatrix} \phi^+(x) \\ \phi^0(x) \end{pmatrix}, \tag{1.31}$$

with

$$\phi^+ \equiv \frac{\phi_1(x) + i\phi_2(x)}{\sqrt{2}}, \tag{1.32}$$

$$\phi^0 \equiv \frac{\phi_3(x) + i\phi_4(x)}{\sqrt{2}}. \tag{1.33}$$

The symmetry is said to be a spontaneously broken symmetry, or a **Hidden** symmetry, if the the choice of the ground state vacuum-expectation-value (VEV) of the Higgs field $\phi(x)$ is non-zero. That is

$$< 0|\hat{\phi}(x)|0 >= \phi_0(x) \neq 0, \tag{1.34}$$

where $\phi_0(x)$ transforms as

$$\phi_0(x) \rightarrow \phi_0^{'} = exp[-i\alpha(x)]\phi_0(x), \tag{1.35}$$

for any value of $\alpha(x)$. Thus, invoking this mechanism with a non-zero VEV, gives mass to the $W^{\pm}$ and Z^0 bosons, whilst the photon remains massless and as a consequence the following relationship is obtained[8]:

$$\cos\theta_W = \frac{M_W}{\sqrt{\rho}M_Z}. \tag{1.36}$$

This mechanism, called the **Higgs mechanism**, must not only generate the masses of all the elementary particles but also lead to a **renormalizable** theory. This is a theory in which the observables can be calculated to any order of perturbation theory in terms of a finite number of input parameters. Thus the choice of these input parameters has to be such that the theory remains renormalizable[9].

The Standard Model Lagrangian has in its manifest $SU(2)_L \otimes U(1)_Y$ symmetric form the input parameters [5]:

- Basic parameters : $g, g^{'}, \mu, \lambda$

[7]This choice is valid within the framework of the Minimal Standard Model (MSM).

[8]Where ρ is the Veltman parameter which is 1 at Tree level in the Standard Model, see section 1.4.3.

[9]It has been shown that all gauge theories are renormalizable [6].

- Relation to experiment

$$e = \frac{gg'}{(g^2 + g'^2)^{\frac{1}{2}}} = \sqrt{4\pi\alpha}, \tag{1.37}$$

$$\frac{M_W}{M_Z} = \frac{g}{(g^2 + g'^2)^{\frac{1}{2}}}, \tag{1.38}$$

$$M_W = g\frac{\mu}{\sqrt{\lambda}}, \tag{1.39}$$

$$M_H = \mu\sqrt{2}, \tag{1.40}$$

where g and g' represents the coupling constants, the coefficients μ^2 and λ describe the Higgs potential. Direct measurement of these is not possible, hence an alternative but common choice is

$$\alpha, M_Z, M_W, M_H, m_f. \tag{1.41}$$

The choice in equation 1.41 is defined as the 'on-shell renormalization scheme [7] and the values of these parameters are known except for the Higgs boson, M_H, and top quark, m_{top} masses. M_Z and M_W are defined on-mass shell, that is the pole position of their corresponding propagators and the fine structure constant α is defined at $q^2 = 0$[10]. Once these input parameters are defined then the Standard Model can be **tested**, that is to say the parameters can be related to the experimental observables.

1.4 The Reaction $e^+e^- \longrightarrow l^+l^-$ at Tree Level

All is now in place for the calculations of the cross-section and forward-backward asymmetry. Figure 1.2 shows the production of charged leptons from the annihilations of an electron-positron pair, through the exchange of a Z^0 and a γ. There is a third diagram which is specific to the final-state being an electron pair, this is discussed later.

The matrix element, which is the sum of the individual matrix elements, for the reaction is:

$$M = M_Z + M_\gamma. \tag{1.42}$$

[10]Where q denotes the momentum transfer.

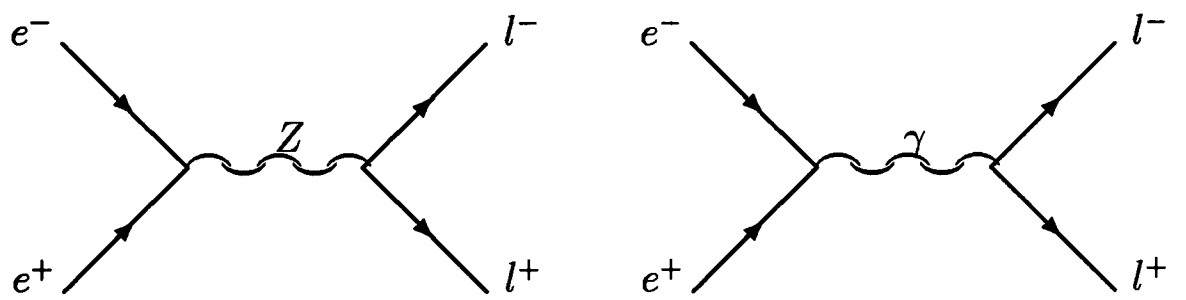

Figure 1.2: Feynman diagram for electron positron annihilation into a l^+l^- via a γ or Z particle

Now defining the electron (positron) spinor(s) as u_a ($\overline{v}_b$) and the lepton (antilepton) as $\overline{u}_c$ (v_d), the individual matrix elements become

$$M_\gamma = ie^2(\overline{v}_b\gamma_\mu u_a)\frac{1}{k^2}(\overline{u}_c\gamma^\nu v_d), \tag{1.43}$$

and

$$M_Z = \frac{ig^2}{\cos^2\theta_W}\left[\overline{v}_b\gamma_\mu\left(\frac{g_v^l - g_a^l\gamma^5}{2}\right)u_a\right]\frac{1}{k^2 - M_Z^2 - iM_Z\Gamma_Z}\left[\overline{u}_c\gamma^\nu\left(\frac{g_v^e - g_a^e\gamma^5}{2}\right)v_d\right], \tag{1.44}$$

where Γ_Z is the width of the Z^0, k is the four momentum transfer and $g_v^{e/l}$ and $g_a^{e/l}$ are the vector and axial-vector couplings to the initial-state electron (positron) or the final-state lepton (antilepton).

Now, the differential cross-section for the interaction of two particles 1 and 2 to a final-state containing n_f particles (fermions or bosons) [8], is

$$d\sigma = \frac{(2\pi)^4\delta^4(p_i - p_f)\,|M_{fi}|^2}{4\left[(p_1\cdot p_2)^2 - m_1^2m_2^2\right]^{\frac{1}{2}}}\prod_{j=1}^{n_f}\frac{d^3p_j}{(2\pi)^3 2E_j}, \tag{1.45}$$

where p_i and p_f are the total initial and final-state four-momenta respectively and m_1 and m_2 are the masses of particles 1 and 2. Thus it can be seen that the differential cross-section is directly proportional to $|M|^2$, where M is the amplitude, which for the process in question becomes

$$|M|^2 = |M_\gamma|^2 + |M_Z|^2 + (M_\gamma^*M_Z + M_\gamma M_Z^*). \tag{1.46}$$

Therefore, there are terms with pure Z^0 exchange, pure γ exchange, and $Z^0 - \gamma$ interference. Using equation 1.45 and summing over the spin states of the spinors, the resulting differential cross-section can be written as:

$$\frac{d\sigma}{d\Omega} = F(s)(1 + \cos^2\theta) + G(s)\cos\theta, \tag{1.47}$$

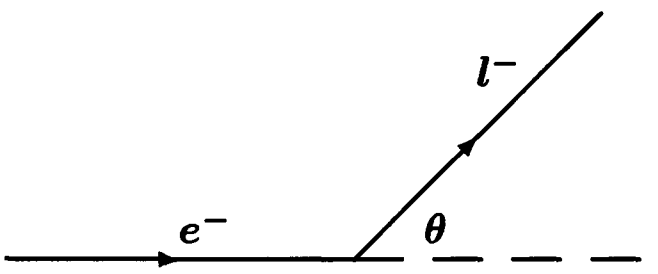

Figure 1.3: The definition of the polar angle, θ.

where

$$F(s) = \frac{\alpha^2}{4s}\left[1 + 2g_v^e g_v^l \mathcal{R}e(\chi) + [(g_v^e)^2 + (g_a^e)^2][(g_v^l)^2 + (g_a^l)^2]\,|\chi|^2\right], \tag{1.48}$$

$$G(s) = \frac{\alpha^2}{4s}(4g_a^e g_a^l \mathcal{R}e(\chi) + 8g_v^e g_v^l g_a^e g_a^l\,|\chi|^2), \tag{1.49}$$

and

$$\chi = \frac{1}{4\sin^2\theta_W \cos^2\theta_W}\frac{s}{(s - M_Z^2 + iM_Z\Gamma_Z)} \tag{1.50}$$

where $\sqrt{s}$ is the centre-of-mass energy, $\mathcal{R}e(\chi)$ denotes the real part of function χ, θ is the polar angle as defined in figure 1.3. Terms with $|\chi|^2$ are due to Z^0 exchange, terms independent of χ are due to γ exchange, and the ones with $\mathcal{R}e(\chi)$ are due to the $Z^0 - \gamma$ interference. These equations are not valid for the top quark as they assume negligible fermion mass compared to the Z^0 but the top quark has a mass known to be greater than the Z^0.[11]

1.4.1 Lowest Order Predictions : Cross-Sections

The total **cross-section** is:

$$\sigma_T = \sigma_F + \sigma_B, \tag{1.51}$$

where $\sigma_{F/B}$ are the forward/backward cross-sections defined as:

$$\sigma_F = 2\pi \int_0^1 \frac{d\sigma}{d\Omega} d\cos\theta, \tag{1.52}$$

and

$$\sigma_B = 2\pi \int_{-1}^0 \frac{d\sigma}{d\Omega} d\cos\theta. \tag{1.53}$$

[11]Note that the b quark mass of $\simeq 5$ GeV is also not negligible compared to that of the Z^0.

Integrating over the whole θ distribution by substituting equation 1.52 and equation 1.53 into equation 1.47 the following is obtained

$$\sigma_T(s) = \frac{16\pi}{3} F(s). \tag{1.54}$$

In the vicinity of $\sqrt{s} = M_Z$ the cross-section is dominated by Z^0 exchange as $\mathcal{R}e(\chi) \to 0$ the interference and the pure electromagnetic terms can be neglected[12] thus

$$\sigma_T(s) = \frac{4\pi\alpha^2}{3s}[(g_v^e)^2+(g_a^e)^2][(g_v^l)^2+(g_a^l)^2] \left(\frac{s^2}{(s-M_Z^2)^2 + M_Z^2\Gamma_Z^2}\right)\left(\frac{1}{16\cos^4\theta_W \sin^4\theta_W}\right). \tag{1.55}$$

At Born level the cross-section can therefore be written as

$$\sigma(s) = \sigma_l^0 \frac{s\Gamma_Z^2}{(s-M_Z^2)^2 + M_Z^2\Gamma_Z^2} + \gamma Z^0 + \gamma, \tag{1.56}$$

where σ_l^0 represents the cross-section for the process $e^+e^- \to l^+l^-$ at $\sqrt{s} = M_Z$, 'γ' and 'γZ^0' the small contributions from the pure photon exchange and the γZ^0 interference, and Γ_Z the decay width[13] of the Z^0. The pole cross-section σ_l^0 can be written in terms of the Z^0 partial decay widths into e^+e^- and l^+l^- states, Γ_e, Γ_l

$$\sigma_l^0 = \frac{12\pi}{M_Z^2}\frac{\Gamma_e\Gamma_l}{\Gamma_Z^2}. \tag{1.58}$$

In the Standard Model the partial widths of the Z^0 are not free parameters but can be written in terms of the vector and axial-vector couplings (equations 1.30 and 1.29) of the Z^0:

$$\Gamma_l = \frac{G_F M_Z^3}{6\pi\sqrt{2}}\left[(g_a^l)^2 + (g_v^l)^2\right], \tag{1.59}$$

with

$$\sin^2\theta_W \cos^2\theta_W = \frac{\pi\alpha}{G_F\sqrt{2}}\frac{1}{\rho M_Z^2}, \tag{1.60}$$

where G_F is the Fermi coupling constant and α is the QED coupling constant. In the Minimal Standard Model (MSM), which is assumed when referring to the Standard

[12] At the Z^0 peak the contribution to the total cross-section from the γ and $Z^0 - \gamma$ terms is of $\mathcal{O}(1\%)$. However, this is fully accounted for in the programs used in the analysis, but is omitted here for simplicity.

[13] The total decay width of the Z^0 is defined as the sum for all the partial widths for leptons and quarks.

$$\Gamma_Z = \sum_{\text{leptons,quarks}} \Gamma(Z \to f\bar{f}). \tag{1.57}$$

Model with only one Higgs doublet, $\rho = 1$ at the tree level. This parameter can differ from unity at tree level if Higgs structures beyond doublets are chosen or in the MSM when higher-order corrections (such as radiative corrections) are taken into account.

The ρ parameter can be determined from a measurement of the cross-section. Assuming lepton universality, the cross-section is related to the leptonic width (see equations 1.56 and 1.58) as:

$$\sigma \approx \Gamma_l^2. \tag{1.61}$$

Now, using equation 1.59

$$\Gamma_l \approx \left[(g_v^l)^2 + (g_a^l)^2\right], \tag{1.62}$$

and the fact that $g_v^2 \ll g_a^2$ (see table 1.6), it can be seen that the leptonic width is related to ρ as:

$$\Gamma_l^2 \approx \rho^2. \tag{1.63}$$

Thus, the cross-section is a measure of the leptonic width which itself is a measure of the ρ parameter.

1.4.2 Lowest Order Predictions : Asymmetries

The **forward-backward** asymmetry in $e^+e^- \rightarrow l^+l^-$ is also an important quantity as it is sensitive to the weak mixing angle which is also a prediction of the MSM. The forward-backward asymmetry is:

$$A_{FB} = \frac{\sigma_F - \sigma_B}{\sigma_F + \sigma_B}, \tag{1.64}$$

where $\sigma_{F/B}$ are the forward/backward cross-sections defined in equations 1.52 and 1.53. Substituting $\sigma_{F/B}$ in equation 1.64 and using the differential cross-section, equation 1.47 gives :

$$A_{FB} = \frac{3}{8}\frac{G(s)}{F(s)}. \tag{1.65}$$

At the Z^0 pole when $s \simeq M_Z^2$ and neglecting any fermion masses and the γ and $\gamma - Z$ contributions, substituting equations 1.48, 1.49, and 1.50 into equation 1.65 gives:

$$A_{FB} = \frac{3 g_v^e g_a^e g_v^l g_a^l}{[(g_e^v)^2 + (g_e^a)^2][(g_l^v)^2 + (g_l^a)^2]} = \frac{3}{4} A_e A_l, \tag{1.66}$$

where

$$A_l = \frac{2 g_v^l g_a^l}{(g_v^l)^2 + (g_a^l)^2}. \tag{1.67}$$

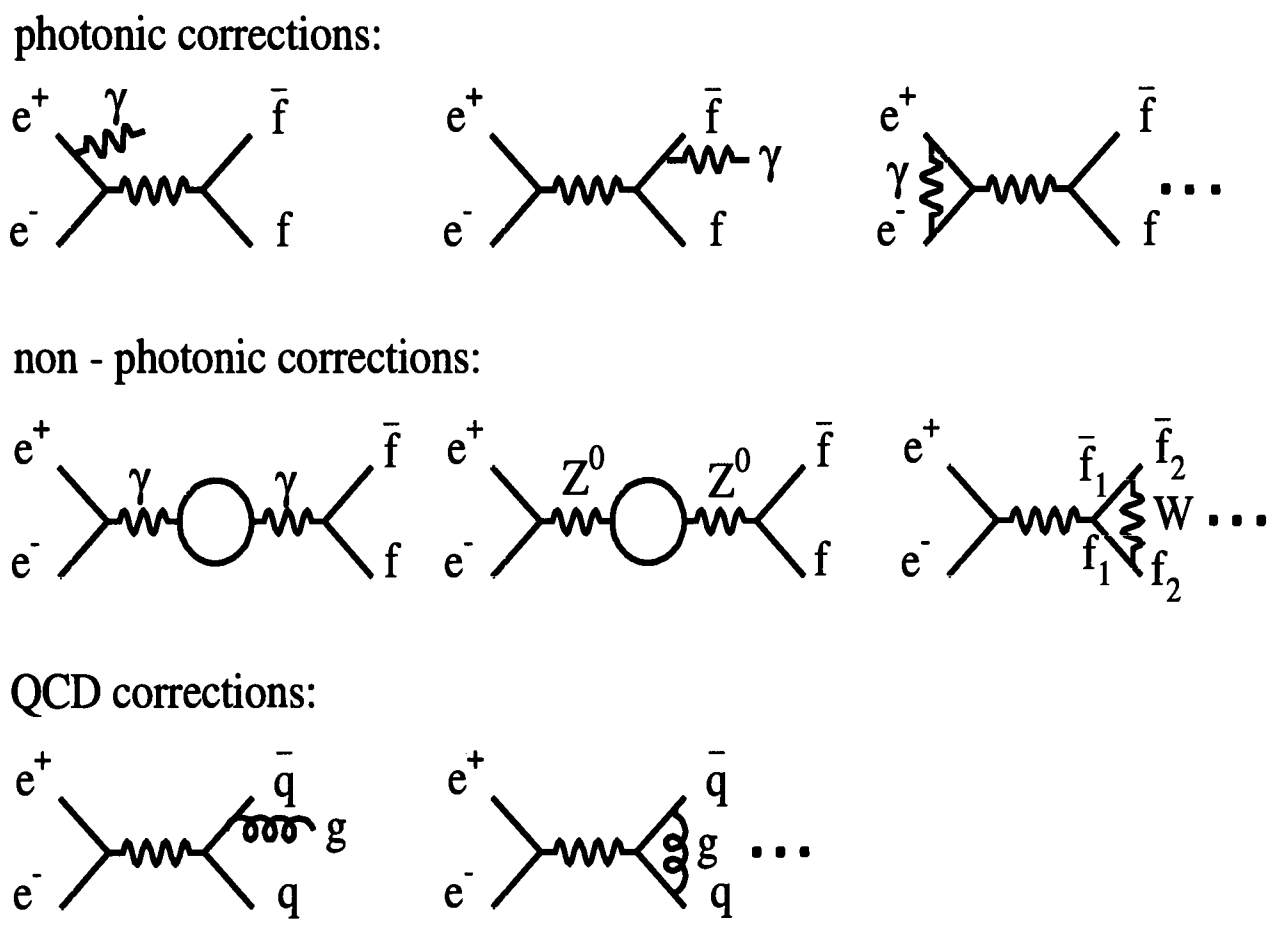

Figure 1.4: The different classes of electroweak radiative corrections which modify the Born level relations.

Thus the peak asymmetry is proportional to $A_e A_l$ and it is determined by g_v/g_a (assuming that $g_v^2 \ll g_a^2$). In general the A_{FB} is a rapidly varying function of $\sqrt{s}$, the centre-of-mass energy, around the Z^0 resonance and switches sign close to the Z^0 pole.

1.4.3 Radiative Corrections

The relationships given above are strictly valid at the Born Level (or Tree level) and have to be re-defined in order to take into account the radiative corrections. For both cross-sections and forward-backward asymmetries these corrections are separated into three classes[14], as shown in figure 1.4, **QED (photonic)** corrections, **Weak (non-photonic)** corrections, and **QCD** corrections.

QED (photonic) corrections : These encompass all diagrams with real or virtual photon loops added to the Born diagram, are the dominant ones ($\mathcal{O}(30\%)$)

[14]See for example [9] or [10].

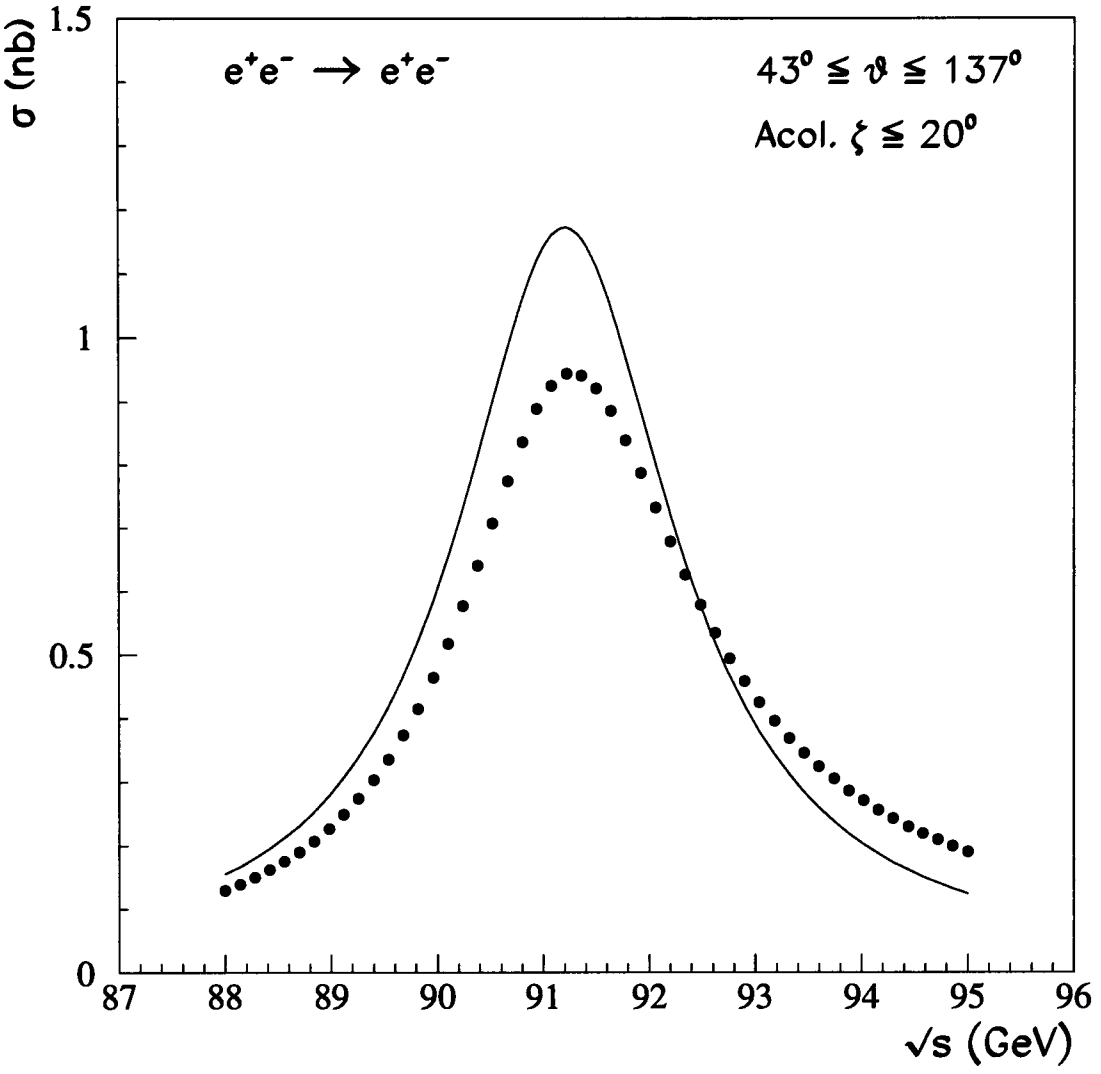

Figure 1.5: The effect of initial-state radiation for the process (s-channel only) $e^+e^- \to e^+e^-$. The solid line represents the Born cross-sections and the circles represent the cross-sections after the $\mathcal{O}(\alpha^2)$ QED corrections, both sets calculated using the ALIBABA program. For a definition of the acollinearity (acol.) please see section 3.5.3.

of the three kinds mentioned above and depend on experimental cuts. They can be divided into:

- **Initial-state corrections.** These provide the dominant contribution and arise when a photon(s) is emitted by one or both of the incoming electron or positron, thus modifying the effective centre-of-mass energy, and causing a substantial effect on the cross-section close to the Z^0 resonance (see figure 1.5).

- **Final-state corrections.** Final-state radiation takes place when the photon(s) is emitted by the final-state, outgoing lepton pair. At $\mathcal{O}(\alpha)$, the correction factor to the total cross-section is $(1 + \delta_{\mathrm{QED}})$ where δ_{QED},

defined in terms of the coupling constant α and fermion charge Q_f, is

$$\delta_{\text{QED}} = \frac{3\alpha}{4\pi} Q_f^2. \tag{1.68}$$

For leptons this turns out to be approximately 0.17 %.

- **Initial-final state corrections.** These include box-diagrams (diagrams containing virtual photons between the initial and final-state e^+e^- pair) and interference in the initial and final-state diagrams. They provide a correction to the cross-section of the order of 0.2 % for leptons.

For the asymmetries the required precision [11] of $\delta A_{FB} = \pm 0.001$ is achieved via the computation of the $\mathcal{O}(\alpha)$ and leading $\mathcal{O}(\alpha^2)$ corrections with the exponentiation of multiple soft photons in the intial state. Corrections due to final-state radiation and initial-final state corrections are negligible if no tight cuts are applied to the photon phase space.

Weak (non-photonic) Corrections : These represent all the rest of the corrections. They can be divided into three sub-classes:

- **Vertex corrections.** These consist of loop corrections to the vertices.
- **Box corrections.** Consist of diagrams with multiple boson interchange between the initial e^+e^- pair and the outgoing fermion pair.
- **Vacuum polarization corrections.** They consist of loop corrections to the boson propagators.

These corrections have all been evaluated to at least one-loop level. A familiar example of the weak corrections is the vacuum-polarization of the photon, which leads to an s-dependent (energy dependent) correction of the electromagnetic coupling constant α[15]:

$$\alpha \rightarrow \alpha(\text{s}) = \frac{\alpha}{1 - \Delta\alpha(\text{s})}, \tag{1.69}$$

where $\alpha(M_Z^2)$ is 1/128.82 and the dominant uncertainty on $\Delta\alpha(\text{s})$ is due to the contributions of the light quarks to the vacuum-polarization of the photon and amounts to $\delta\Delta\alpha(\text{s}) = 0.0009$ [13].

[15]Where $\alpha = 1/137.035989$ (at $q^2 = m_e^2$), see [12].

As in the case of the cross-sections, the weak corrections to the asymmetries are small but theoretically interesting as they depend on the unknown parameters of the MSM: the Higgs boson and top quark masses. They are independent of the experimental cuts applied and the main contributions are due to the Z^0 propagator corrections, including the γ/Z^0 mixing diagrams, which are independent of the final-state fermion flavour. The corrections due to the remaining vertex and box diagrams are small and fermion flavour dependent. At the resonance the Born-level asymmetry, equation 1.66, can be rewritten as:

$$A_{FB}^{f}(M_Z^2) = \frac{3}{4} A_e A_f + \Delta A_{FB}^{f,RC}, \tag{1.70}$$

where the $\Delta A_{FB}^{f,RC}$ is the extra final-state fermion flavour-dependent term.

QCD corrections : Involve corrections to take into account gluon radiation from quarks. They can lead to the modification of the $q\bar{q}$ partial decay width, $\Gamma_{q\bar{q}}$, of the forward-backward asymmetry, $A_{FB}^{q\bar{q}}$, and loop diagrams. They will not be further discussed as they are not directly relevant to this thesis.

1.5 The Improved Born Approximation (IBA)

This is a parameterization of the corrected cross-section written in a form where the Born relations are left almost unmodified. The corrections due to the $\mathcal{O}(\alpha)$ diagrams, except for the initial-state radiation, are absorbed into the coupling constants and widths. The predictions of such parameters depend on the Standard Model and its unknown parameters, which are the Higgs and top masses and the uncertainty in the strong coupling constant α_s.
The corrections taken into account in this formulation are:

- One loop weak corrections such as the self-energies and vertex corrections. These are absorbed in the re-definition of the couplings, $\hat{g_v}$ and $\hat{g_a}$, equations 1.73 and 1.74, which exhibit an energy dependence that is negligible around the Z^0 peak.

- QED corrections on the initial-state up to $\mathcal{O}(\alpha^2)$.

- QED corrections on the final-state up to all orders of α in the Z^0 exchange term only.

In this approach the physical width of the Z^0, equation 1.59, can be written as

$$\Gamma_l = \frac{G_F M_Z^3}{6\pi\sqrt{2}} \left[(\hat{g}_a^l)^2 + (\hat{g}_v^l)^2\right](1 + \delta_{\text{QED}}), \tag{1.71}$$

or

$$\Gamma_l = \frac{\alpha(s) M_Z}{3} \left[(\hat{g}_a^l)^2 + (\hat{g}_v^l)^2\right](1 + \delta_{\text{QED}}), \tag{1.72}$$

where

- δ_{QED} is the QED correction given in equation 1.68.
- $\hat{g_v}$ and $\hat{g_a}$ are the effective vector and axial-vector couplings:

$$g_v \rightarrow \hat{g_v} = t_3\sqrt{\hat{\rho}}, \tag{1.73}$$

$$g_a \rightarrow \hat{g_a} = (t_3 - 2Q_f \sin^2\theta_W^{\text{eff}})\sqrt{\hat{\rho}}, \tag{1.74}$$

- $\alpha(s)$ is the effective value of the QED coupling constant, as shown in equation 1.69.

The introductions of the effective couplings $\hat{g_v}$ and $\hat{g_v}$ also motivates the definition of an effective $\hat{\rho}$ parameter and an effective weak mixing angle, θ_W^{eff}. These are shown in equation 1.75, which represents the modified mass relationship of the bosons (equation 1.36)

$$\cos^2\theta_W^{\text{eff}} = \frac{M_W^2}{\hat{\rho} M_Z^2}, \tag{1.75}$$

where $\hat{\rho}$ can be defined from the ratio of the neutral to charged current amplitudes at low energies

$$\hat{\rho} = \frac{1}{1 - \Delta\hat{\rho}}, \tag{1.76}$$

with the $\Delta\hat{\rho}$ parameter depending on the top mass quadratically ($\propto m_{\text{top}}^2$) and logarithmically on the Higgs mass ($\propto \ln M_{\text{Higgs}}$).

A frequently used definition of the effective weak mixing angle in terms of the effective couplings is:

$$\sin^2\theta_{\text{lept}}^{\text{eff}} = \frac{1}{4}\left(1 - \frac{\hat{g}_v^l}{\hat{g}_a^l}\right). \tag{1.77}$$

The IBA is implemented by convoluting the photon radiation spectrum with the Born level expressions for the cross-sections and forward-asymmetries. The observed cross-sections can be rewritten as:

$$\sigma^{\text{obs}}(s) = \int_0^s \left[\sigma_W(s')F_i(s', s) + \Delta_{\text{int}}\right] ds', \tag{1.78}$$

where σ_W is the Born level cross-section with full $\mathcal{O}(\alpha)$ corrections, F_i is the initial-state pure QED radiative correction, Δ_{int} represents QED box-diagrams and the interference of the initial and final-state radiation, and s' is the square of the invariant mass of the final-state fermions. The dominant initial-state 'radiator' function F_i is

$$F_i(s',s) = \beta_e \left(1 - \frac{s'}{s}\right)^{\beta_e - 1} (1 + \delta_{s+v}) + \delta_h(s'), \tag{1.79}$$

where the first term takes into account all the exponentiated leading contributions of soft and hard photons multiplied by the remaining soft and virtual corrections up to $\mathcal{O}(\alpha^2)$. The second term absorbs the remaining hard photon contributions. The expressions for β_e, δ_{s+v} and δ_h can be found in [14].

For the asymmetries a similar convolution leads to the asymmetry (in the absence of experimental cuts)

$$A_{FB}^f(s) = \frac{\int_{Z_0}^1 dZ\, H_1(Z)\,[\sigma_F(Zs) - \sigma_B(Zs)]}{\int_{Z_0}^1 dZ\, H_2(Z)\,[\sigma_F(Zs) + \sigma_B(Zs)]}, \tag{1.80}$$

where H_1 and H_2 are the radiator functions similar to the one above, $Zs = s'$ and $Z_0 = \frac{m_f^2}{s}$ which is $\simeq 0$ in the case of leptons.[16] To account for the introduction of the effective weak mixing angle in the IBA, equation 1.70 becomes

$$A_{FB}^f(M_Z^2) = \frac{3}{4}\hat{A}_e\hat{A}_f + \Delta A_{FB}^{f,\text{res}}, \tag{1.81}$$

where $\hat{A}_{e/f}$, see equation 1.67, contain the effective vector and axial-vector couplings, and $\Delta A_{FB}^{f,\text{res}}$ represents a flavour-dependent residual term which contains the weak corrections (box diagrams and imaginary part of the propagator). This residual term for leptonic asymmetries is 0.0021 ± 0.0002 [10] for $100 < m_{\text{top}} < 250$ GeV and $50 < m_{\text{Higgs}} < 1000$ GeV and the main contribution comes from the imaginary part of the Z^0 propagator.

Thus, in the Improved Born Approximation, the dominant weak corrections are taken into account through the introduction of a new effective weak mixing angle (θ_W^{eff}) and a new effective $\hat{\rho}$ parameter, and then the IBA relations are convoluted with a photon radiator function to account for the initial-state radiation.

[16] In fact, this is not strictly valid for the τ-lepton.

1.6 The t-channel Scattering

When the final-state leptons are electrons then the initial-state is indistinguishable from the final-state, and there are extra diagrams and physical processes which contribute to the total cross-section for $e^+e^- \rightarrow l^+l^-$. One of these extra diagrams (see figure 1.6) is known as the t-channel. In terms of the contribution to the cross-section (see figure 1.7(a)) the fraction of the cross-section due to the t-channel and s-t interference varies from about 64 % at lowest energies[17] (around 88 GeV), to about 14 % at the peak (around 92 GeV) and only a few percent on the high energy side (around 94 GeV) of the resonance. Similarly for the asymmetries the difference between the s-channel and the full (s+t) channel is very significant for energies below below the Z^0 pole (see figure 1.7(b)). This process is important in the context of this thesis and further discussed in Chapter 5.

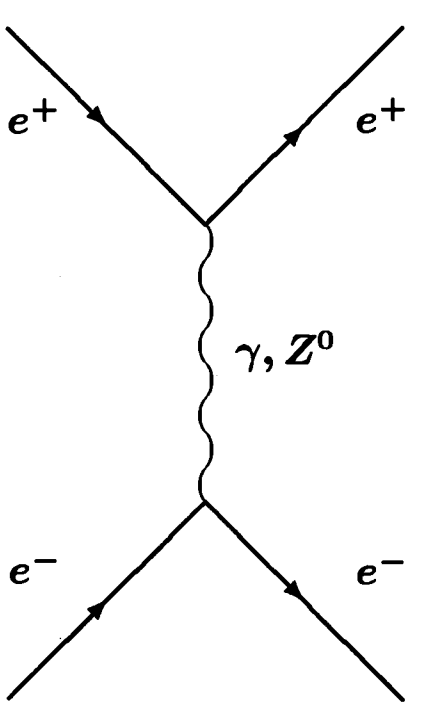

Figure 1.6: The t-channel diagram for Bhabha scattering, which contributes to the process $e^+e^- \rightarrow l^+l^-$.

1.7 ZFITTER

In the previous sections, it has been shown that:

[17]These energies refer to the LEP scan energies.

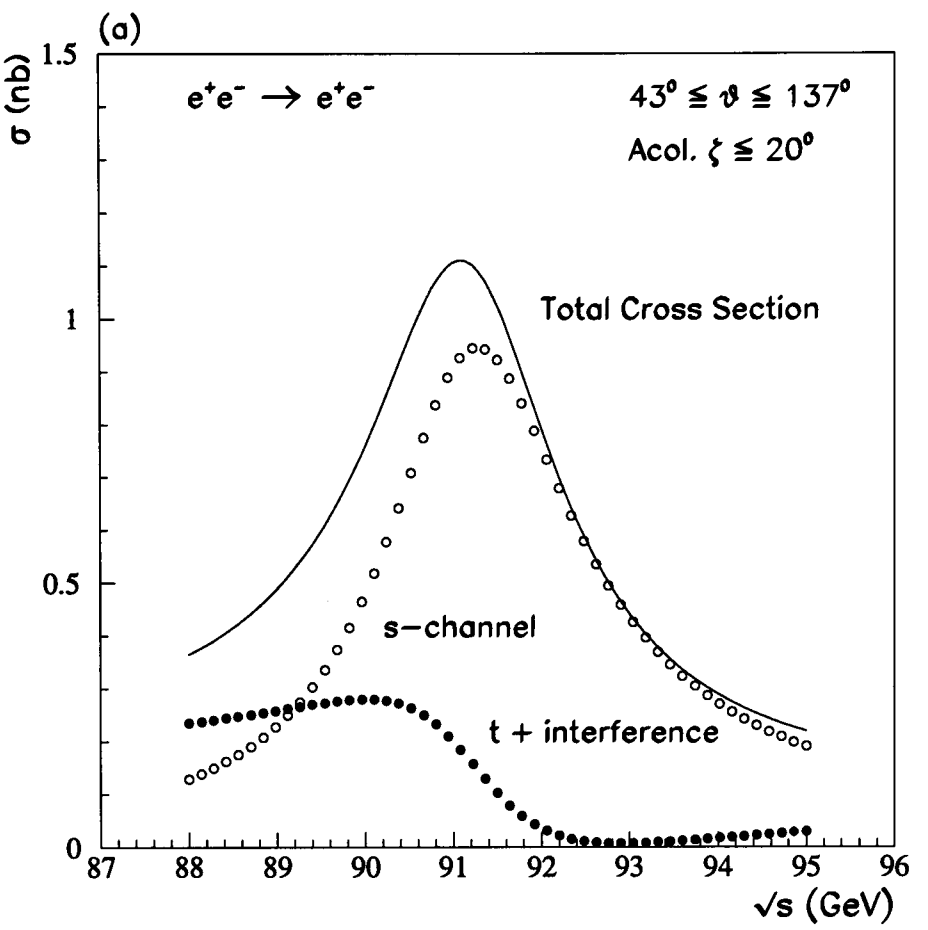

Figure 1.7: (a) shows the various contributions to cross-section for the process $e^+e^- \rightarrow e^+e^-$ and (b) shows the contributions to the forward-backward asymmetries. The cross-sections and asymmetries were calculated using ALIBABA which incorporates $\mathcal{O}(\alpha^2)$ QED and weak corrections. In both figures the solid lines represent the Standard Model full s+t channel predictions.

- a measurement of the cross-section, for the process $e^+e^- \to l^+l^-$, is a measure of the leptonic width, Γ_l. Now, using the IBA expressions and equations 1.56-1.63, the following is obtained:

$$\sigma \approx (\Gamma_l)^2 \approx (\hat{\rho})^2. \tag{1.82}$$

Thus, a measurement of the cross-section, σ, is a measurement of the effective rho, $\hat{\rho}$, parameter.

- the asymmetry is a function of the effective vector and axial-vector couplings (using the IBA expressions and equation 1.67):

$$A_{FB} \approx \frac{\hat{g}_v^l}{\hat{g}_a^l}, \tag{1.83}$$

and using equation 1.77

$$A_{FB} \approx \sin^2 \theta_{\text{lept}}^{\text{eff}}. \tag{1.84}$$

Thus, a measurement of the forward-backward asymmetry, A_{FB}, is a measurement of the effective weak mixing angle, $\sin^2 \theta_{\text{lept}}^{\text{eff}}$.

To extract these parameters, $\hat{\rho}$ and $\sin^2 \theta_{\text{lept}}^{\text{eff}}$, a comparison of the experimentally determined cross-sections and asymmetries is made with the corresponding Standard Model values as calculated using **ZFITTER** [15]. This program employs a semi-analytical approach to the fermion pair production in e^+e^- annihilation and Bhabha scattering. The theoretical formalism used, allows an almost model independent interpretation of the cross-sections and asymmetries, taking into account the most up-to-date knowledge of the initial and final-state QED effects, weak, and QCD corrections.

The following quantities are used to model the experimental cuts employed in an analysis:

- The minimum polar angle, θ, of the final-state anti-fermion.
- The maximum acollinearity angle (for a definition see section 3.5.3), η^{max}, of the $f\overline{f}$ (fermion and anti-fermion) pair.
- The minimum energy, E_f^{min}, of the fermion and anti-fermion.

The experimentally determined cross-sections and asymmetries are fitted with the theoretical formulae using a χ^2 minimization procedure including a full covariance matrix treatment of the errors. For the cross-sections the χ^2 is defined as:

$$\chi^2_{\text{cross}} = \sum_{i=1}^{N} \frac{(\sigma_i^{\text{exp}} - \sigma_i^{\text{the}})^2}{\delta^2(\sigma_i^{\text{exp}})} \tag{1.85}$$

where

- The sum is taken over all the centre-of-mass energies represented by N.
- σ_i^{exp} represents the experimentally determined cross-section at energy point i.
- $\delta(\sigma_i^{\text{exp}})$ is the error (statistical and systematic added in quadrature) on the experimentally determined cross-section at energy point i.
- σ_i^{the} is the Standard Model cross-section (determined by ZFITTER) at energy point i.

Similarly for the asymmetries the χ^2 is defined as:

$$\chi^2_{\text{asym}} = \sum_{i=1}^{N} \frac{(A_{FBi}^{\text{exp}} - A_{FBi}^{\text{the}})^2}{\delta^2(A_{FBi}^{\text{exp}})} \tag{1.86}$$

- The sum is taken over all the centre-of-mass energies represented by N.
- A_{FBi}^{exp} represents the experimentally determined forward-backward asymmetry at energy point i.
- $\delta(A_{FBi}^{\text{exp}})$ is the error (statistical and systematic added in quadrature) on the experimentally determined forward-backward asymmetry at energy point i.
- A_i^{the} is the Standard Model asymmetry (determined by ZFITTER) at energy point i.

In the fit to the experimental data, these two χ^2's are minimized using the MIGRAD algorithm in the CERN function minimization program MINUIT [16].

Leptonic and hadronic lineshape and lepton asymmetry fit

Leptonic asymmetries in conjunction with the leptonic and hadronic cross-sections are used and a 5 parameter fit is carried out. ZFITTER is used to calculate the cross-sections and asymmetries at different centre-of-mass energies as a function of:

$$M_Z, \Gamma_Z, \sigma_h^0, R_l, A_{FB}^0, \tag{1.87}$$

where

- σ_h^0 represents the peak hadronic cross-section, same as equation 1.58 but with $\Gamma_{\mathbf{had}}$ rather than Γ_l.
- R_l represents the ratios of the hadronic to the leptonic widths:

$$R_l = \frac{\Gamma_{\mathbf{had}}}{\Gamma_l}. \tag{1.88}$$

- A_{FB}^0 is the peak leptonic asymmetry (see equation 1.66).

Amongst other quantities, the effective vector and axial-vector couplings, $(g_v^l)^2$ and $(g_a^l)^2$ or $\sin^2\theta_{\mathbf{lept}}^{\mathbf{eff}}$ and $\hat{\rho}$ can be derived from this fit. Note that, the fit parameters of equation 1.87 are chosen in particular as there is minimal correlation between them.

1.8 Chapter Summary

At the beginning an introduction was given to modern particle physics. The principle of gauge theories was then discussed and the Standard Model of Electroweak interactions was described within the context of this principle. Relations for the Born level cross-sections and forward-backward asymmetries, for the process $e^+e^- \rightarrow l^+l^-$, were calculated and extended to account for the electroweak radiative (QED and weak) corrections. It was shown that the peak cross-section was proportional to the leptonic partial width and so to the ρ parameter. It was also shown that the peak forward-backward asymmetry was proportional to the ratio of the vector and axial-vector couplings and so it represented a measure of the weak mixing angle (θ_W). The Improved Born Approximation (IBA) was then introduced. In the IBA the dominant weak corrections are taken into account through the re-definition of

the weak mixing angle ($\theta_W \rightarrow \theta_W^{\rm eff}$) and the ρ parameter ($\rho \rightarrow \hat{\rho}$). The resulting IBA expressions are then convoluted with the photon radiator function which includes the dominant QED corrections. The concept of an extra Feynman diagram to be included in the Bhabha scattering was introduced. Finally, the extraction of the electroweak observables $\hat{\rho}$ and $\sin^2\theta_{\rm lept}^{\rm eff}$, with use of the semi-analytical program ZFITTER, was discussed.

Chapter 2

The DELPHI Experiment at the LEP collider

Chapter Abstract

This chapter contains the description of the DELPHI detector at LEP. After a brief look at LEP, the LEP energy measurement is discussed. The various sub-detectors which make up DELPHI are described. Due to the complexity of the DELPHI apparatus, only a brief summary is given of the components of the detector but with special emphasis on the sub-detectors used directly for the analysis described in this thesis. Finally, the data acquisition system and the trigger system are described.

2.1 LEP, the Large Electron Positron Collider

The Large Electron Positron collider, LEP, is a circular accelerator and storage ring operating at the Z^0 resonance energy of approximately 2×45.6 GeV, the first phase of the operation. The next phase, LEP200, has an intended energy upgrade to around 200 GeV sufficient to produce W bosons, to be achieved around the year 1996.

It is situated 100 m underground between Geneva and the foothills of the Jura mountains (see figure 2.1). The complex is not entirely circular as there are eight straight sections, four of which have experimental halls called 'pits' housing the four experiments : ALEPH, DELPHI, L3 and OPAL [17] and the other four points are intended for the RF accelerating cavities, beam dump and for beam cleaning. The circumference of the ring is 26.658 km[1], so that energy loss due to synchrotron

[1]This is the minimum size at which synchrotron radiation losses maybe replaced when the upgrade to 200 GeV is made.

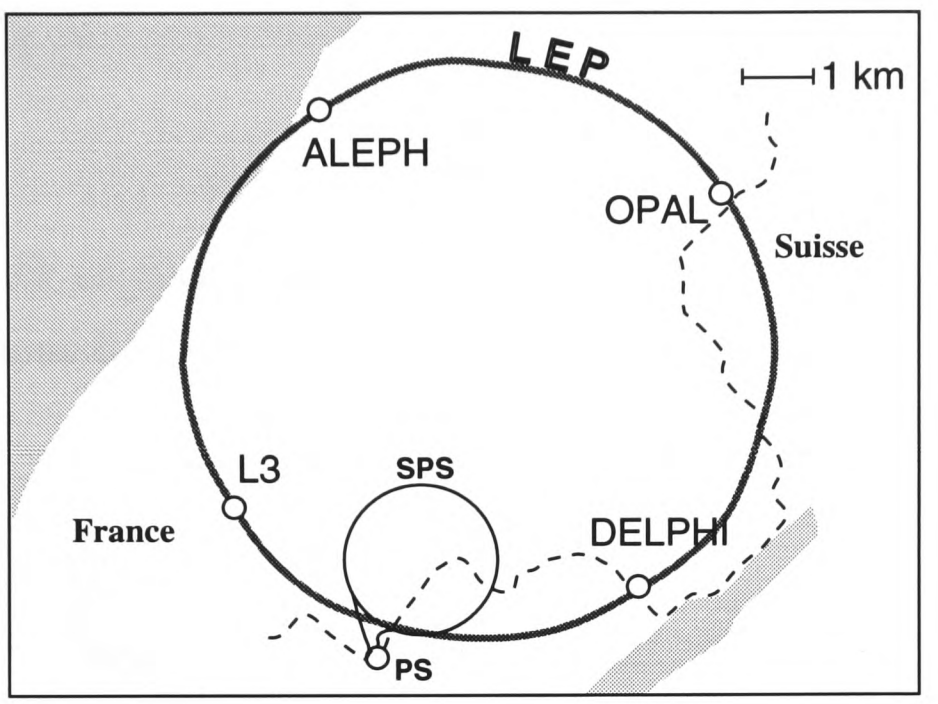

Figure 2.1: The LEP ring.

radiation[2] maybe kept to a minimum. The four experiments are housed in the middle of the straight sections so that beams have finite straight lines to traverse before the interaction point, leading to the reduction the synchrotron radiation density at the experiments.

The design luminosity [3] is of the order of 1.6×10^{31} cm$^{-2}s^{-1}$ and at present LEP provides each crossing point 2 pb^{-1} per week, which at the Z^0 peak corresponds to 60 000 Z^0's decaying hadronically. The number of bunches in each beam was four from the start of LEP operations until mid-1992 when it was increased to eight bunches.

The beam dimensions depend on the equilibrium between the damping of the oscillations and the noise excitation from quantum emission due to the synchrotron radiation. The current beam dimensions at LEP are:

$$\sigma_x \simeq 200\ \mu\text{m}$$

[2]The energy radiated, ΔE, by an electron of energy E, in a radius of curvature ρ, circulating in LEP is:

$$\Delta E = 0.0885 \frac{E^4(\text{GeV})}{\rho(\text{m})} \text{per turn.} \tag{2.1}$$

This loss is of the order of 130 MeV at the Z^0 increasing up to 2.3 GeV at LEP200.

[3]The luminosity is

$$\mathcal{L} = f_{\text{rev}} K \frac{N_+^{\text{bunch}} N_-^{\text{bunch}}}{4\pi\sigma_x\sigma_y}, \tag{2.2}$$

where f_{rev} is the LEP revolution frequency of the order of 11 KHz, K is the number of bunches in each beam and σ_x and σ_y are the beam dimensions. For a process of collision cross-section σ, the yield is $\mathcal{L}\sigma$ events per second.

$$\sigma_y \simeq 10\,\mu\text{m}$$

$$\sigma_z \simeq 20000\,\mu\text{m} \tag{2.3}$$

$$\tag{2.4}$$

To achieve the nominal beam energies at LEP I there exists a whole injector complex [18], figure 2.2 , which comprises:

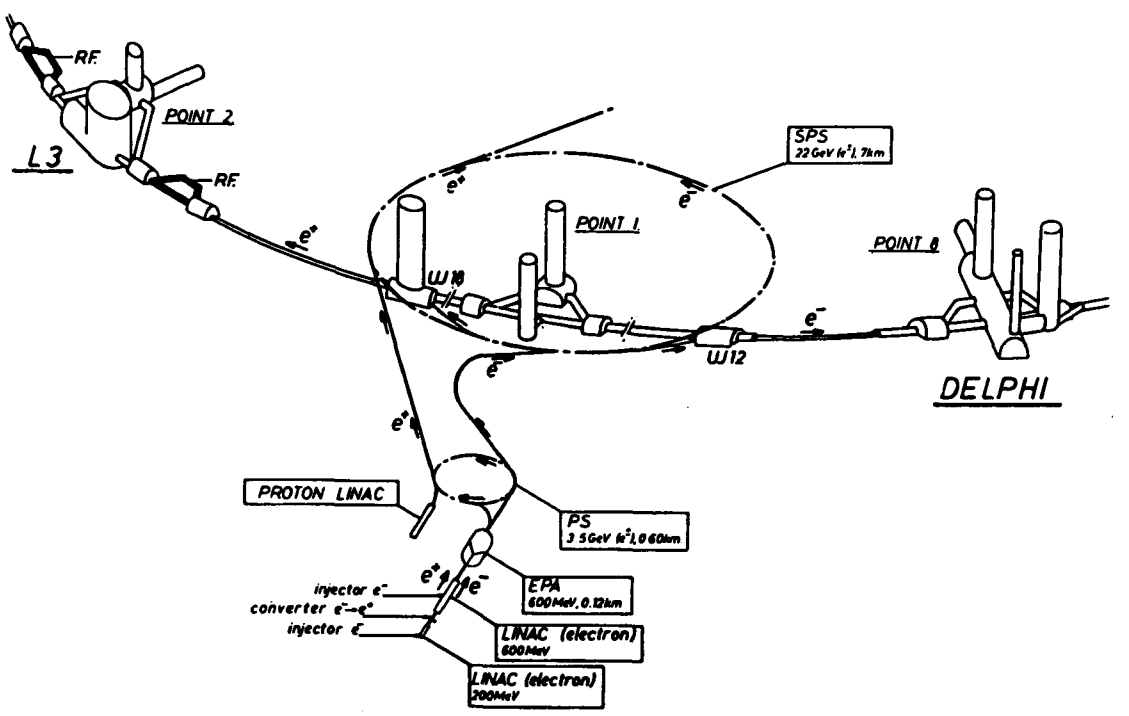

Figure 2.2: The LEP injector complex. Also shown are the positions of the two experiments L3 and DELPHI.

- A 200 MeV LINAC which supplies an intense electron beam on to a tungsten target to produce positrons.
- A second LINAC to accelerate both the electrons and the positrons to 600 MeV.
- The EPA, the Electron Positron Accumulator, which accumulates electrons and positrons at 600 MeV.
- The PS, the Proton Synchrotron, to accelerate the beams to 3.5 GeV.
- The beams are transferred from the PS to the SPS, the Super Proton Synchrotron, where they are accelerated to 20 GeV.

- From the SPS the beams at 20 GeV are transferred into LEP for the accumulation of sufficient luminosity.

- In the final phase of the whole process, the beams are accelerated to 45 GeV and 'squeezed' until the luminosity is optimized.

2.2 The LEP Energy Measurement

For the precision test of the standard model a precision measurement of the mass of the Z^0, M_Z, is imperative. The error on this mass is dominated by the uncertainty in the absolute energy scale and hence the beam energy [19] at LEP has to be measured to a very high degree of accuracy.

Initially, until 1990, the energy was calculated from the physical dimensions of the LEP ring, and a knowledge of the magnetic fields in the bending magnets, and was determined with an error of approximately 20 MeV. The three methods used were:

- **The field display method.** Use was made of flip coil measurements in a reference dipole magnet connected with the dipole magnets in the LEP ring.

- **The flux loop method.** This involved the calibration of the magnetic field by flux loops mounted on the pole faces of all the LEP dipole magnets.

- **Proton calibration method.** In this, measurements were made of the revolution frequency of 20 GeV protons circulating on the same orbit as the positrons.

Starting from 1991, the technique of **resonant depolarization** [20] has been used and a much higher precision achieved. As electrons circulate around the LEP ring they acquire a natural transverse polarization. The spins then precess about the vertical direction with a frequency which is expressed as the spin tune[4]. In LEP the spin tune is approximately 105 and is related to the beam energy according to the following relation:

$$\nu_s = E_{\text{beam}} \frac{1}{m_e c^2} \left(\frac{g_e - 2}{2} \right) \tag{2.5}$$

[4]The number of rotations of the spin for one complete passage around the LEP ring, is known as the spin tune.

where $E_{\mathbf{beam}}$ is the beam energy, m_e is the mass of the electron, and the term in the bracket represents the anomalous magnetic moment.

Circularly polarized laser light is shone on to the beam and the asymmetry in the scattering of the light is a measure of the degree of polarization. Resonant depolarization occurs if an oscillating transverse magnetic field is applied to the beams, the frequency of which is adjusted to equal the fractional part of the spin tune. In 1991, the precision achieved on the centre-of-mass energy, using this method, was 6 MeV. The preliminary value for 1994 is 4 MeV.

2.3 The DELPHI Detector

DELPHI[5], **DE**tector with **L**epton, **P**hoton and **H**adron **I**dentification, figures 2.3 and 2.4 , is one of the four detectors at the LEP collider situated at interaction point 8. It is a general purpose detector with an emphasis on good particle identification, three-dimensional information and very accurate vertex reconstruction. It consists of a cylindrical section known as the barrel and two end-caps which can be removed to access the different sub-detectors.

DELPHI is in the breed of modern day particle detectors [21] in the sense that it consists of:

- Tracking devices to measure the momentum of charged particles in a solenoidal field of 1.2 T.
- An electromagnetic calorimeter for energy measurements of electrons and photons.
- A hadron calorimeter for measuring hadronic energy deposition and Muon detection chambers.

It has to be mentioned that out of the four detectors on the LEP ring DELPHI is the only one which identifies charged hadrons by directly detecting the photons emitted by Cherenkov radiation in the RICH (**R**ing **I**maging **CH**erenkov) detectors.

Before going into a detailed description of the sub-detectors, which make up DELPHI, it is necessary to define the coordinate system used. The x direction is

[5]A list of DELPHI members is given in Appendix A.

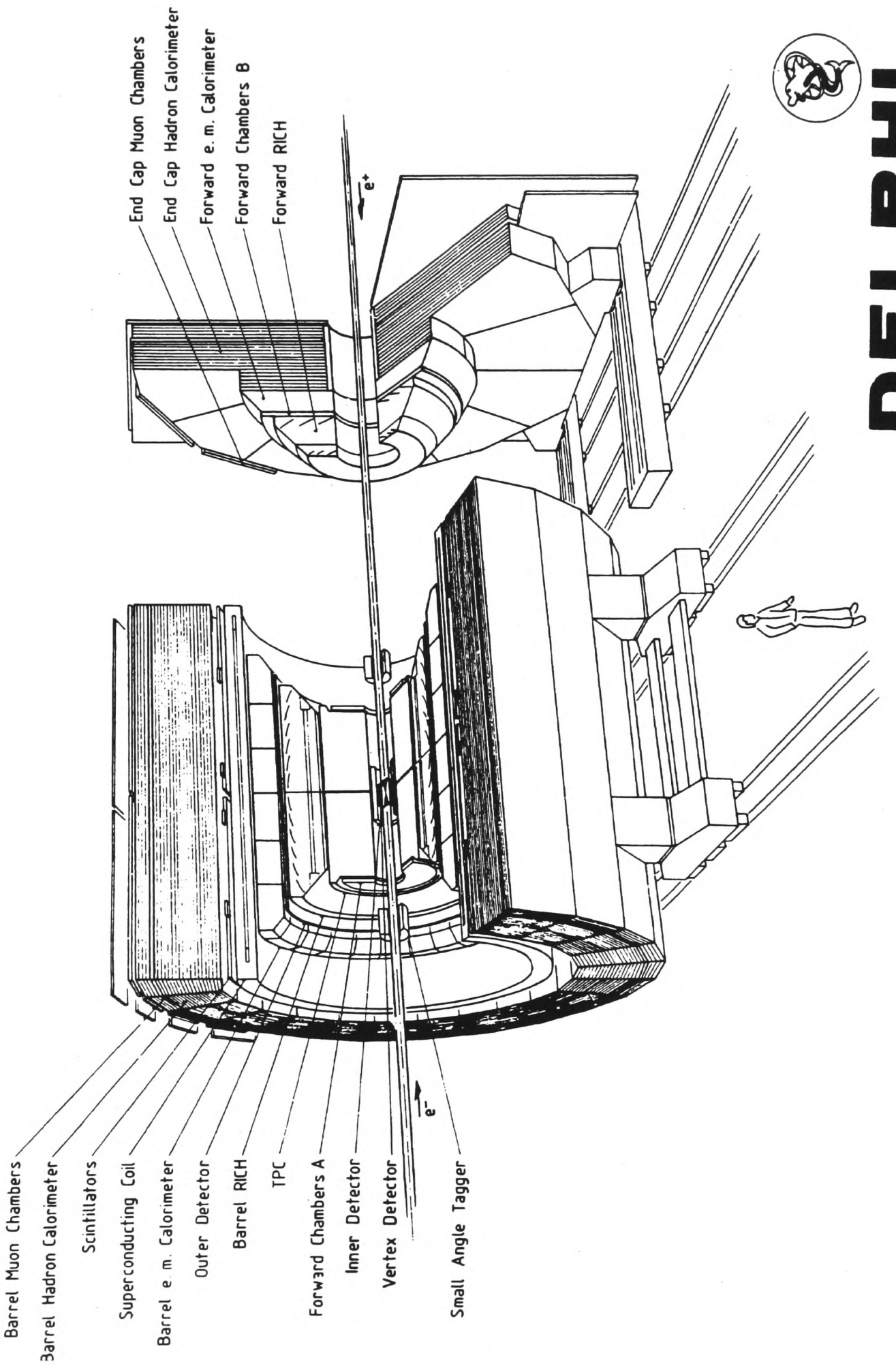

Figure 2.3: The DELPHI detector at LEP.

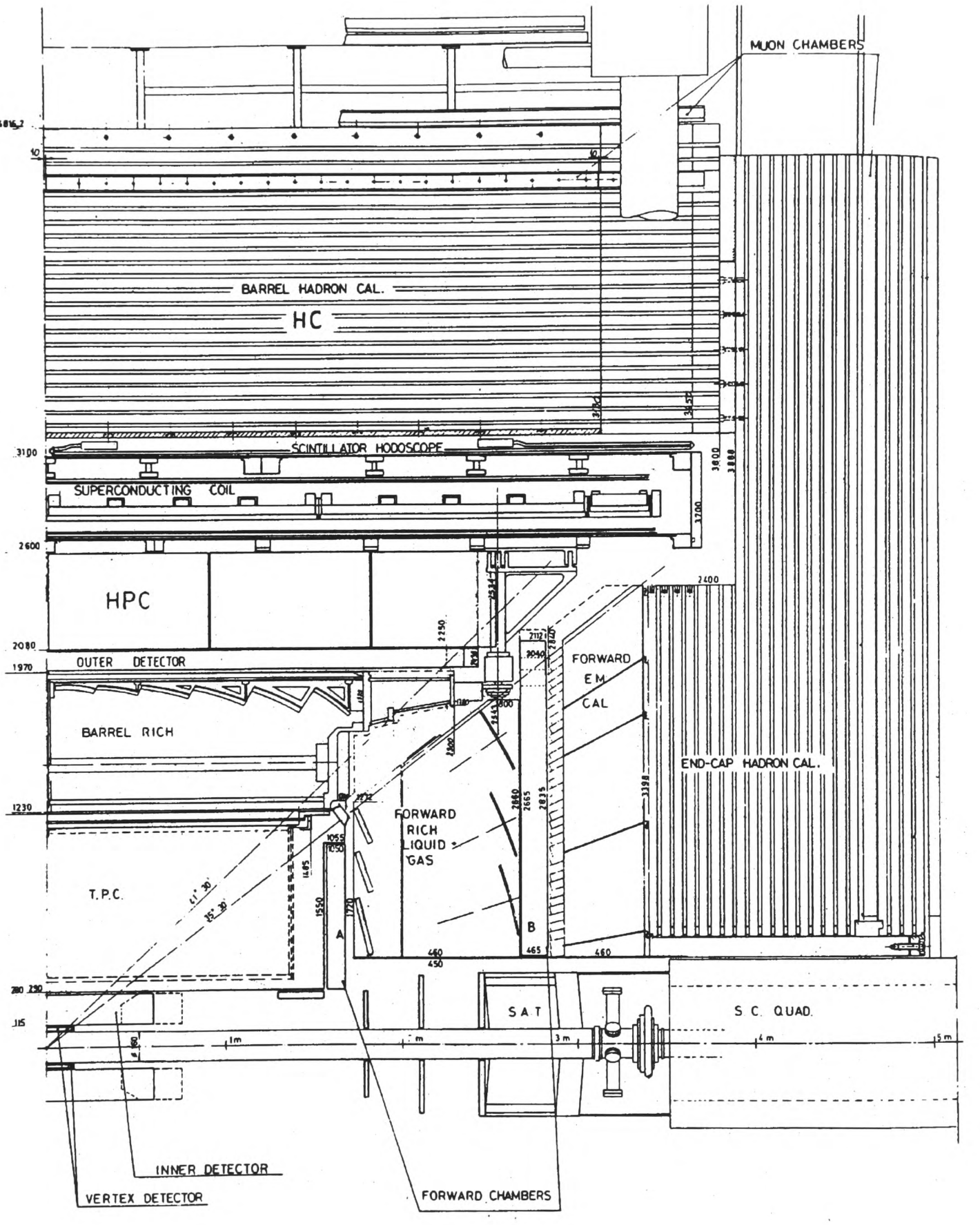

Figure 2.4: A longitudinal view, parallel to the beam pipe, of the DELPHI detector.

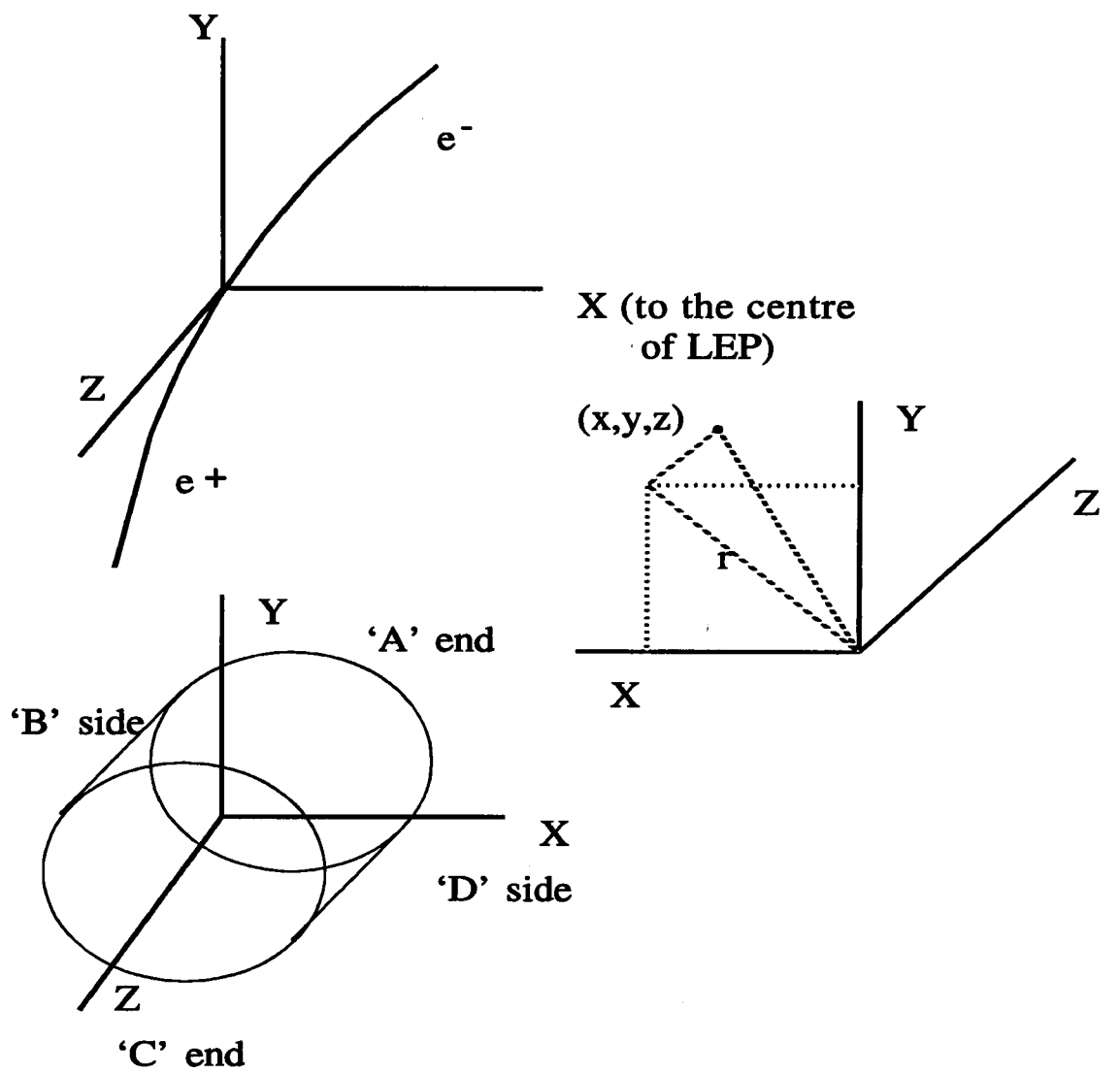

Figure 2.5: The DELPHI coordinate system.

towards the centre of the LEP ring and y is in the vertical direction. The electron beam travels in the positive z direction and the positron beam in the negative z direction. The polar angle θ is the angle from the positive z axis and the azimuthal angle ϕ is measured clockwise in the $x-y$ plane, as seen in the direction of positive z, from the positive x axis. The coordinate r is the cylindrical radius associated with a point, and $r\phi$ refers to a distance measurement made at constant r. This coordinate system is shown in figure 2.5.

DELPHI comprises a solenoid and 16 sub-detectors, which are described only briefly here. For a detailed description, see [22]. Particular emphasis has been given to sub-detectors which are directly relevant to the analysis in this thesis.

The DELPHI superconducting **solenoid** has a length of 7.4 m and an inner diameter of 5.2 m. This magnet, one of the largest of its kind in the world, has a field of 1.2 T. The coil is cooled to 4.5 K and the current required is 5000 A. Correcting

coils placed at the ends of this coil enable the magnetic field to be trimmed to be parallel to the electron direction, the direction of positive z. The use of such a high field (1.2 T) is imperative to the accurate determination of particle momenta.

The ensemble of sub-detectors are divided into tracking detectors, calorimeters, and scintillation counters.

2.3.1 Tracking Detectors

A summary of the principal parameters and the performance of the tracking detectors is given in table 2.1.

Microvertex Detector, (VD) : see section 2.4.2

Inner Detector, (ID) : provides high redundancy for vertex reconstruction and trigger information. It covers a polar angle range of $29^0 \leq \theta \leq 151^0$ and consists of:

- an inner drift chamber giving 24 $r - \phi$ points per track and
- 5 cylindrical MWPC (Multi Wire Proportional Chambers), each layer with 192 sense wires and 192 circular cathode strips with a variable pitch, proportional to r, and averaging 5 mm. The wires provide fast triggering signals and resolve left/right ambiguities from the inner drift chamber section. The strips also give z information for the trigger.

During LEP operations the average single wire resolution was determined to be $\sigma_{r\phi} = 90$ μm in the inner drift chamber layer and $\sigma_z < 1$ mm in the outer layers.

Time Projection Chamber, (TPC) : see section 2.4.1.

Outer Detector, (OD) : has the purpose of providing fast triggering information in both $r\phi$ and z, and to enhance the momentum resolution by a factor of 5 for fast particles reconstructed in conjunction with the TPC. This sub-detector, comprising 24 modules divided into 5 layers, is mounted on the outside of the BRICH (see below). Full azimuthal coverage is achieved by having staggered layers which are overlapped with adjacent modules. Resolution results are: $\sigma_{r\phi} = 110$ μm and $\sigma_z = 4.4$ cm.

Barrel Muon Chambers, (MUB) : were built by the Nuclear Physics Laboratory at Oxford University. They consist of inner, outer, and peripheral modules made up of a total of seven overlapping layers of drift chambers. The inner module, is inserted in a gap in the magnet return yoke, and has 3 layers, two of which are fully read out and the third is to compensate for any dead chambers. Both the outer and peripheral planes have two layers. All the drift chambers operate in proportional mode with a $Ar/CH_4/CO_2$ by volume mixture of 85.5/8.5/6 % . The resolution in $r\phi$, $\sigma_{r\phi}$ is of the order of 1 mm and the resolution in z is about 10 mm.

As mentioned before DELPHI is divided into a barrel and end-cap regions. The sub-detectors mentioned so far exist in the barrel region, the corresponding tracking detectors in the end-cap regions are described below.

Forward Chambers (FCA, FCB) : are the equivalent of the barrel OD in DELPHI's endcaps. They cover the polar angles of $11^0 \leq \theta \leq 33^0$ and consist of layers of drift chambers which provide powerful tracking and triggering information. The FCA chambers are mounted on both ends of the TPC whereas the FCB chambers are placed between the FRICH and the FEMC (see below). For FCA the resolution is approximately 300 μm and for FCB both σ_x and σ_y are approximately 130 μm.

Forward Muon Chambers, (MUF) : These consist of two planes of MWPC , one inside the yoke and the other 30 cm further out, outside the yoke. Both planes contain two layers of chambers operating in limited streamer mode. The resolutions obtained are, $\sigma_{x/y} \simeq 3$ mm.

Small Angle Tagger, (SAT) : See section 2.4.3.

Very Small Angle Tagger, (VSAT) : This is used as a tool for fast monitoring of both luminosity and machine operation, and for the determination of the relative luminosity (see section 2.4.3). The detector in each arm (forward/backward) is composed of two rectangular Tungsten-Silicon (W-Si) calorimeter stacks, 24 radiation lengths deep, 5 cm high, 3 cm wide, and 10 cm long, and mounted on the support of the superconducting beam quadrupoles. Their

polar angle coverage is between 5 and 7 mrad and 45^0 in azimuth. It is also designed to measure the background of single electrons and X-rays. The energy resolution is of the order of 5 % at 45 GeV.

2.3.2 Scintillation Counters

The scintillation counters are made up of the TOF and the HOF.

Time-Of-Flight counter, (TOF) : It is made up of 172 scintillation counters arranged in 24 sectors and mounted in the barrel between the solenoid and the iron return yoke. The polar angle coverage is $41^0 \leq \theta \leq 139^0$. The purpose of this detector is to serve as a fast trigger for beam events and cosmics and maybe used to veto cosmic muons in time with the BCO's (Beam Cross Overs). The time resolution for cosmic muons is $\sigma_t = 1.2$ ns which corresponds to a σ_z of 20 cm.

Forward Hodoscope, (HOF) : These scintillation counters are mounted between the end-cap yoke and the second layer of MUF chambers. They improve the muon detection and trigger system efficiencies for beam events and cosmics. More importantly, they are the only trigger for beam related halo muons[6]. The time resolution measured with halo muons is 5 ns.

2.3.3 Calorimeters

There are two types of calorimeters in DELPHI, electromagnetic and hadronic. A summary of the specifications and performance of the calorimeters is shown in table 2.2.

High density Projection Chamber, (HPC) : uses the time-projection principle to measure the three-dimensional charge distribution induced by electromagnetic showers, achieving high granularity in all coordinates with an acceptable number of readout channels. The detector has 144 modules, 24 in azimuth and 6 in z, mounted inside the solenoid, covering the polar angles $43^0 \leq \theta \leq 137^0$. Each module has 41 planes of lead converters separated

[6]At LEP halo muons accompanying the beams are used to investigate the detector performance and alignment.

	Position/fiducial Acceptance			No. Points along Track	Resolution per point (σ) (mm)
	r (cm)	$\|z\|$ (cm)	θ(deg)		
VD (1990)	9/11	12	$37-143$	2	$r\phi$: 0.007
VD (1991)	6.3/9/11	12	$28-152$	3	
ID:					
jet chamber	$11.8-22.3$	40	$17-163$	24	$r\phi$: 0.11
trigger layer	$23-28$	≤ 50	$30-150$	5	z :< 1
TPC	$35-111$	≤ 134	$20-160$	16	$r\phi$: 0.23
				192	z: 0.9
OD	$198-206$	≤ 232	$43-137$	5	$r\phi$: 0.11
				3	z: 44
MUB	~ 445	≤ 385	$52-128$	$2-6$	$r\phi$: 1.5
					z: 10
FCA	$30-103$	$155-165$	$11-33$	$2\times(x,u,v)$	x,u,v: 0.3
FCB	$53-195$	$267-283$	$11-35$	$2\times(x,u,v)$	x,u,v: 0.25
MUF	$70-460$	463	$9-43$	$(2+2)\times(x,y)$	x,y: 1.0
		500			z: 10

Table 2.1: Specifications and performance of the DELPHI tracking detectors [22].

by gas gaps, which act as time projection chambers. The ionization charge of tracks in electromagnetic showers drift onto a single multi-wire plane at the end of each module. It has a read-out precision of 4 mm along z, 1^0 in azimuth, a nine-fold radial sampling over 18 X_0 (radiation lengths), and an energy resolution of $\left[\frac{\Delta E}{E} = \frac{23}{\sqrt{E}} \oplus 1.1\right]$ %, E being the energy in GeV.

Forward Electromagnetic Calorimeter, (FEMC) : is the equivalent of the barrel HPC in the DELPHI end-caps. It consists of two 5 metre diameter discs, one in each end-cap, covering polar angles $10^0 \leq \theta \leq 36^0$. Each of the discs contains lead-glass blocks 20 X_0's deep and in the shape of truncated pyramids pointing back to the interaction region. The read-out granularity is of the order of 1^0 in ϕ and θ and the shower resolution is $\frac{\Delta E}{E} = [(0.35 + 5/\sqrt{E})^2 + (6/E)^2]^{\frac{1}{2}}$ %, E in GeV.

Hadron Calorimeter, (HCAL) : is a sampling gas detector incorporated in the return yoke of the superconducting magnet. It consists of a barrel part covering the polar range $42.6^0 \leq \theta \leq 137.4^0$ and two end-caps between polar ranges $11.2^0 \leq \theta \leq 48.5^0$ and $131.5^0 \leq \theta \leq 168.8^0$. There are 24 sectors in the barrel,

with 20 layers of limited streamer mode detectors inserted into 2 cm slots between 5 cm iron plates in each sector. The chambers operate stably with relatively low iso-butane content : Ar/CO_2/i-butane in a 1/6/3 ratio. This small i-butane level is important as the HCAL contains a large volume of gas and small leaks are unavoidable. The resolution is about $\frac{\Delta E}{E}$ =120%/$\sqrt{E}$, E in GeV.

	Position/Fiducial Acceptance			Depth
	r(cm)	$\|z\|$ (cm)	θ (degrees)	
HPC	$208-260$	≤ 254	$43-137$	$18X_0$
FEMC	$46-240$	$284-340$	$10-36.5$	$20X_0$
SAT	$10-36$	$233-285$	$2.5-7.7$	$28X_0$
VSAT	$\sim 6-9$	770	$5-7$ mrad	$24X_0$
HCAL (barrel)	$320-479$	< 380	$10-170$	6λ
HCAL (forward)	$65-460$	$340-489$		

Table 2.2: Specifications and performance of calorimeters.

2.3.4 Ring Imaging CHerenkov counters (RICH)

The aim of the novel RICH detectors, the BRICH and FRICH, is to have good hadron identification over most of the momentum range by Cherenkov angle reconstruction from both gas and liquid radiators. The BRICH (Barrel RICH) detector is situated between the TPC and the OD, whereas the FRICH (Forward RICH) is situated between the FCA and FCB.

The drift volume between the liquid radiator (C_6F_{14}) and the gas radiator (C_5F_{12}) contains methane (CH_4), ethane (C_2H_6) and TMAE, a photo-ionising substance.

Due to the complexity of the RICH systems, it has taken some time for them to become operational. For the 1992 LEP running period only the BRICH was partially functional with both the liquid and gas radiators. In 1993, due to a leak the BRICH was operated only with the gas radiator, and the FRICH was used for the first time.

2.4 Analysis Related Sub-detectors

There are three sub-detectors which were used for the analysis reported in this thesis. The Time Projection Chamber (TPC), which is the main tracking detector, the

Small Angle Tagger (SAT), which is the DELPHI 'luminometer' and the microvertex detector, (VD).

2.4.1 The Time Projection Chamber

The TPC [23] is the principal tracking device of DELPHI. It is relatively small in size, radius of 120 cm and a length of 2×150 cm, restricted due to the inclusion of the RICH's in the design of DELPHI. The detector contains Ar/CH_4 (ratio 80 : 20) at 1 atm. pressure resulting in a lower radiation thickness but the reduced dE/dx information is still sufficient to separate electrons from pions below 8 GeV.

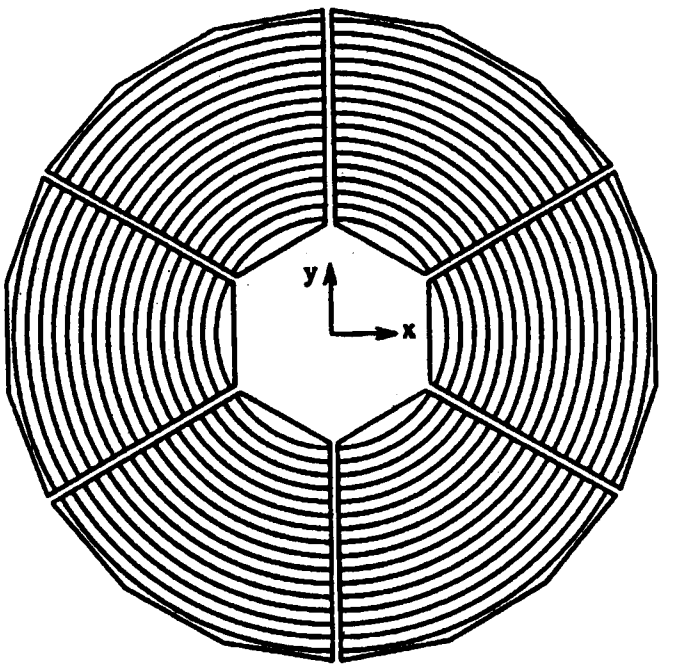

Figure 2.6: A view of the 6 sector plates of a TPC end-cap, with the 16 circular pad rows.

The chamber is split into two halves along the $z = 0$ plane and both halves have a uniform and homogeneous electric field of strength 150 V cm^{-1} pointing inwards from the end planes. As the name itself suggests, the TPC uses the time projection principle in which ionized tracks in the gaseous volume of the TPC are drifted under the influence of a uniform electric field to the sensitive walls of the detector. The electric and magnetic fields are parallel to one another with the intense magnetic field bending the drift electrons in to a helical trajectory around the field lines and hence attenuating any transverse diffusion. The longitudinal diffusion is not affected by the presence of the magnetic field.

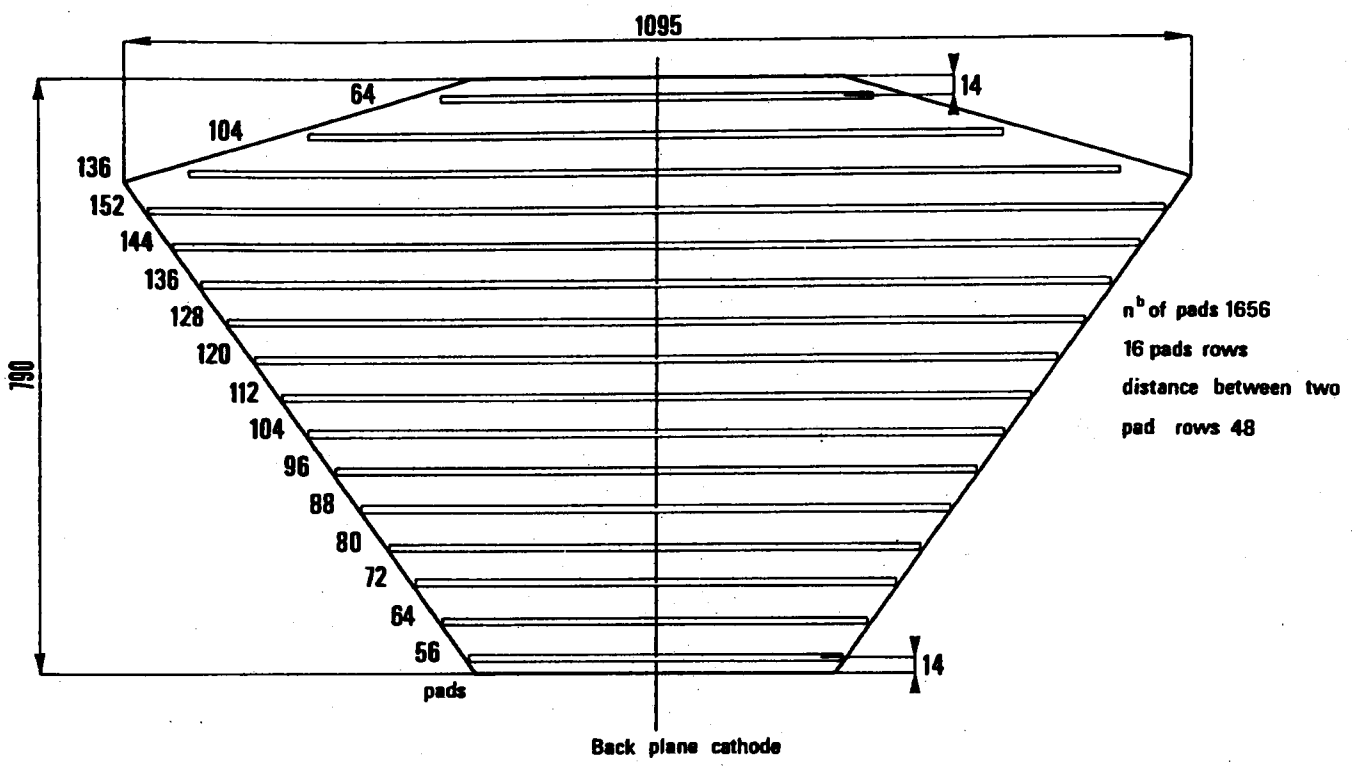

Figure 2.7: A detailed view of one of the 6 sector plates. Dimensions in mm.

When a charged particle traverses the TPC it creates, through ionization, electron-ion pairs at the rate of approximately 70 primary pairs per cm. Under the influence of the electric field these electrons drift at a constant rate (6.7 cm μs^{-1}) parallel to the magnetic field until they reach either of the two end-planes. The final detection of the drift electrons is carried out by anode sense wires operating in the proportional mode. Both ends of the TPC, the end-planes, are equipped with 6 sectors of wire arrays, each consisting of 192 sense wires and 16 pad rows. See figures 2.6 and 2.7. Each sector covers 60^0 in the azimuth with the first sector boundary being at $\phi = 30^0$. The drifting electrons avalanche near the anode sense wires and hence induce a pulse on the cathode back plane (pad rows), which are about 7.5 mm long and 8 mm wide. The centre-of-gravity of the charges is used in the determination of the azimuth, ϕ. The sense wires are aligned perpendicularly to a line running through the centre of each plane and the information on the radial coordinate, r, is determined essentially from the wire number hit. The time-of-arrival of the drifted electrons is used to determine the z coordinate and the energy deposited by the charges is used to estimate the $\mathrm{d}E/\mathrm{d}x$ along the length of tracks.

The positive ions from the avalanches can feed back into the drift region of the TPC and distort the field lines and hence degrade the track reconstruction. To avoid this problem of 'space charge' build-up a gating grid is placed 4 mm in front of the

anode wires. It is made up of wires at 1 mm interval and alternately biassed at ± 100 V.

The current TPC resolutions are:

- $\sigma_{r\phi}$ = 180 to 200 μm (depending on ϕ and z).
- $\sigma_z < 0.9$ mm.
- a two-track separation of 1.5 cm.

2.4.2 The Microvertex Detector

The aim of the microvertex detector [24], VD, is to provide high precision measurements of the position of particles close to the primary collision point, allowing accurate track reconstruction and precise extrapolations to the interaction region. This aids in the reconstruction of any decay chain through the identification of primary and secondary vertices.

Three concentric shells of silicon microstrip detectors at average radii of 6.3, 9, and 11 cm, see figure 2.8, cover the polar angular region of $43^0 \leq \theta \leq 137^0$ and surround the beam pipe. The two shells at the larger radii, called the Inner and the Outer, were completed for the LEP running period of 1990 while the one at the smallest radius, the Closer, was added in 1991. The closer shell is 22 cm long, while the Inner and the Outer are 24 cm long. Each shell has 24 modules with about 10 % overlap in ϕ between the modules and each module consists of 4 silicon detectors, with strips parallel to the beam.

The impact parameter which is defined as the distance of closest approach of a given track to the primary interaction point, should be zero for a charged particle produced at that point, but resolution effects smear this. There are two types of smearing effects:

- Multiple scattering for low momentum tracks.
- Track reconstruction uncertainties due to the intrinsic resolution of the sub-detectors used in the track fit. This limits the precision of the measurement of high momentum tracks. Note, these also include finite errors on the alignment of the detector (VD).

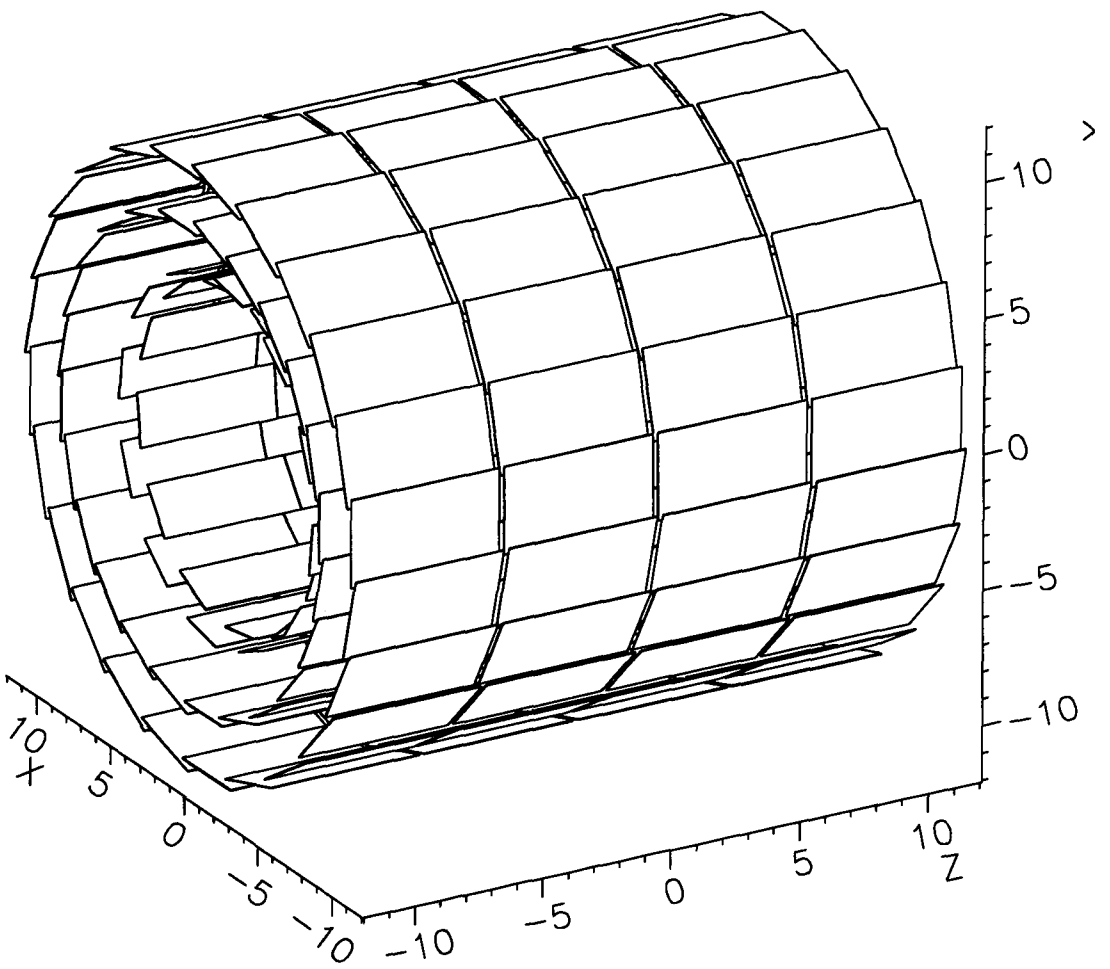

Figure 2.8: The DELPHI three layer microvertex detector (VD). Dimensions in cm.

Taking these two effects into account, the impact parameter resolution is defined by:

$$\sigma_{\mathrm{IP}}^2 = \sigma_{\mathbf{asympt}}^2 + \left(\frac{\sigma_{\mathbf{ms}}}{p_t}\right)^2, \tag{2.6}$$

where the first term on the right represents the high momentum track resolution uncertainties and the second term represents the multiple scattering effects; p_t is the transverse momentum in GeV/c. The impact parameter uncertainty is determined using tracks from hadronic Z^0 decays and is well described in equation 2.7:

$$\sqrt{\left(\frac{69}{p_t}\right)^2 + 24^2 \mu m}. \tag{2.7}$$

For 45 GeV/c tracks from $Z^0 \rightarrow \mu^+\mu^+$ decays, the impact parameter resolution, $\sigma_{r\phi}$, is 21 μm, which corresponds to a precision per point of 8 μm. This includes an error due to the uncertainty in the absolute alignment of the microvertex detector. For minimum ionizing particles (m.i.p) the signal to noise ratio is 15:1.

2.4.3 The Small Angle Tagger

The small angle tagger, SAT, is the principal DELPHI luminometer which is optimized for the detection of small angle Bhabha scattering events. It is mounted close to the beam pipe with both arms containing a calorimeter.

The calorimeter, covering the polar angles from 43 mrad to 135 mrad from the $\pm$ Z axis, consists of alternating layers of lead sheets and plastic scintillating fibres, aligned parallel to the beam. Scintillating fibres were chosen because of their radiation hardness and because they can be easily fitted into a cylindrical geometry. The fibres and the lead layers provide a total thickness of 28 radiation lengths. Behind the calorimeters the fibres are collected in bundles and coupled via conical light-guides to circular photodiodes. A typical energy resolution, from a prototype, is given in equation 2.8

$$\frac{\Delta E}{E} = \left[\left(1.2^2 + \frac{11.4^2}{E}\right)^{\frac{1}{2}} \oplus 2.3\right] \%, \tag{2.8}$$

where the energy E is in GeV.

The fiducial region is accurately defined by a precisely machined mask, lead for 1991 and tungsten from 1992, in front of one of the calorimeters. The position of this mask and the SAT read-out segmentation are shown in figure 2.9. An additional 'ϕ mask' covers $\pm 15^0$ around the vertical junction between the two calorimeter half-barrels.

In 1991, a two-plane silicon tracker with a radial pitch of 1 mm and an azimuthal segmentation of 5^0 was introduced and operated for one third of the beam crossings during the first 65 % of the data taking. Distortions in the calorimeter position reconstruction were measured by the tracker in events in which there were unambiguous 2-hit tracks pointing to the impact point reconstructed by the calorimeter. This tracker was also used in 1992.

The SAT is used to calculate the total integrated luminosity L, which is given by the relation in equation 2.9:

$$L = \frac{N_{\mathrm{ev}} - N_{\mathrm{bk}}}{\sigma_B}, \tag{2.9}$$

where N_{ev} and N_{bk} are the number of selected Bhabha events and the number of background events and σ_B is the visible Bhabha cross-section within the SAT

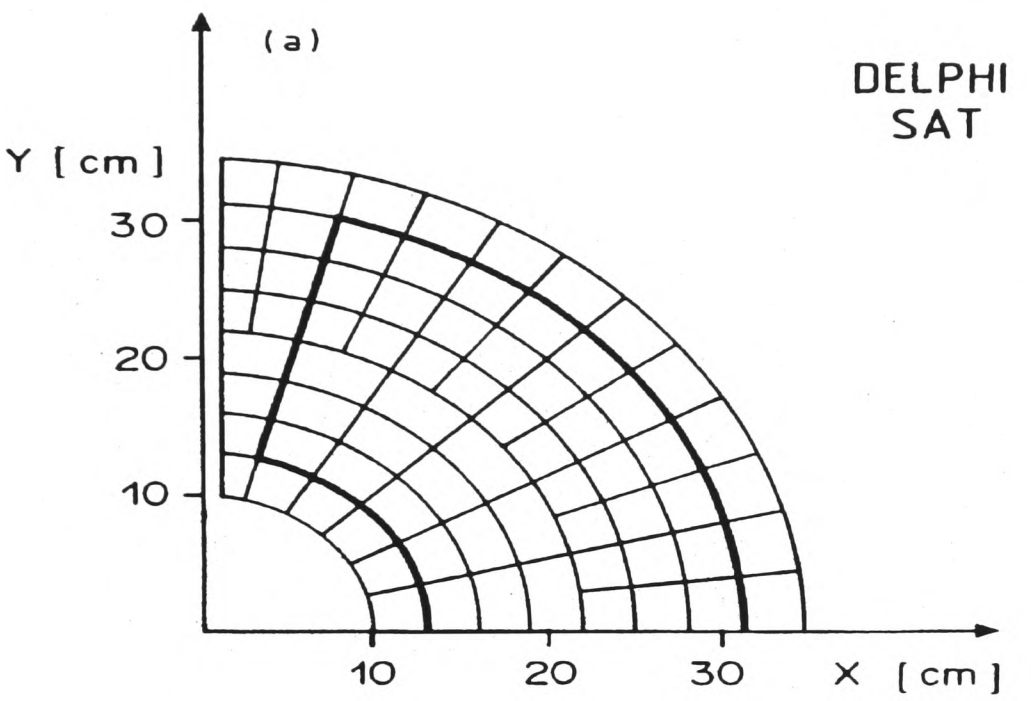

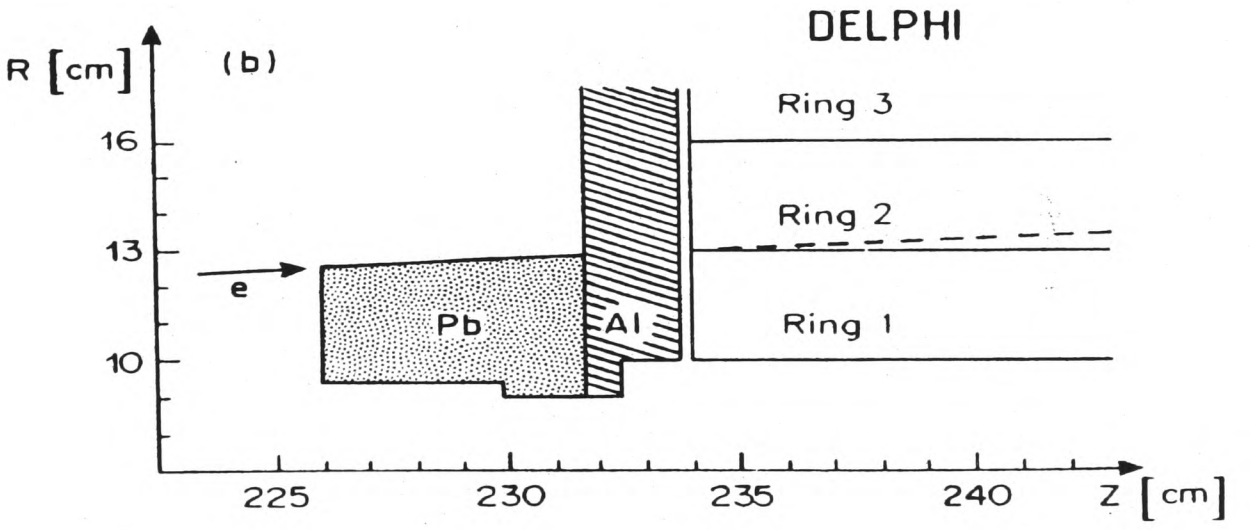

Figure 2.9: The read-out segmentation of the SAT, (a), and the position of the lead mask which tightly defines the acceptance of the tagger, (b).

angular acceptance. Possible background events to small-angle Bhabha scattering include both e^+e^- interactions, accidentally coincident off-momentum particles from beam-gas interactions and backgrounds from two-photon processes (found to be negligible). The visible Bhabha cross-section is calculated using detector simulation of Bhabha events generated by the event generators BABAMC [25] (which takes into account $\mathcal{O}(\alpha)$ corrections) and BHLUMI [26] (which takes into account higher-order corrections).

The VSAT is used to measure the relative luminosity at the off-peak[7] points. The VSAT has a much smaller statistical error on the identification of small-angle Bhabha events (the VSAT modules are closer to the beam-pipe) but a larger systematic error (the VSAT modules are placed after the superconducting quadrupoles). Hence, the luminosity calculated using the VSAT at the Z^0 resonance energy (peak point) is normalized to the luminosity at that point determined using the SAT, which results in a smaller statistical error.

2.5 The Data Acquisition System

To provide a high degree of independence to the individual sub-detectors, the DELPHI Data Acquisition System (DAS) [27] has been divided in to several individual partitions.[8] The principal components of a partition are:

- The Fastbus readout system, which works under the control of a pyramid hierarchy of FASTBUS Intersegment Processors (FIP's), in each of which data is moved from the detector front-end electronics and then formatted and transported to detector partition buffers.
- The monitor and control system for technical aspects (i.e gas, volts, pressure, temperature also called the Slow Control System).
- The handling of data flow in the on-line computers.
- The overall partition control.

[7]For definitions of the on-peak and the off-peak points, see the glossary (Appendix D).

[8]Each sub-detector has its own partition, but note, that there is not necessarily a one to one correspondence between partitions and sub-detectors.

This modular system allows malfunctioning sub-detectors to be taken out from the readout and hence allow normal data taking for the rest of DELPHI. Embedded in this system is the trigger system which controls whether an event is written on to the recording medium and hence minimize the dead-time.

2.6 The Trigger System

The DELPHI trigger system [28] is organised in four levels:

- The first and second level triggers, T1 and T2, are hardware triggers synchronous with respect to the BCO (Beam Cross Over). The trigger decisions are taken at 3 μs for T1 and 39 μs for T2, after the BCO. During the first BCO, following a positive T1, the apparatus has a 'deadtime' of about 1 % for a typical T1 rate of 400 Hz. The typical T2 rate is of the order of a few Hz. The T1 behaves as a pre-trigger and only minimal information such as energy or transverse momentum thresholds, satisfying certain criteria in terms of multiplicities, are considered in this decision. At the T2 level a combination of signals arising from different sub-detectors is used to refine the data.

- The third and fourth level triggers, T3 and T4, are software filters performed asynchronously with respect to the BCO. Thus there is no deadtime as long as the T2 rate does not exceed the rate at which T3 and T4 process events, and there is sufficient storage space for events which are waiting to be processed. The T2 decision is validated by the T3 implying that the same logical structure is used for both. But, more detailed information is used at T3 since the data has already been processed by the sub-detectors and a higher reliability is achieved in the decision. The T4 tags the events and rejects those regarded as empty.

  Even though the T3 was commissioned towards the end of 1991, it was first included for the 1992 data taking. The T4 has been in use since 1993 to reject empty events.

Each detector taking part in the trigger has a subtrigger module which provides information to PYTHIA, the central trigger supervisor module. This information is

in the form of tracks from tracking detectors and energy clusters from the calorimeters.

The components of the trigger are divided into two types: **'single-majority' triggers**, and **'majority-2' triggers.**

Single majority triggers : Any combination of these is sufficient to trigger DELPHI. The prefix 'i' denotes the charge multiplicity, i = 1 for 1 track and i = 2 for $\geq$ 2 tracks. The symbol $*$ refers to a logical .AND. function.

- The B1 trigger, the original DELPHI trigger, was used for the last time in 1991 to increase redundancy.[9] It has the following combination of hits in the ID, OD and TOF sectors. The IDOD ($\geq$ 1 ID sector $*$ $\geq$ 2 OD sectors), the TOMJ ($\geq$ 2 TOF octants[10]), and the SCOD ($\geq$ 1 TOF octant $*$ $\geq$ 1 OD sector).
- The iCT0 and iCT1 : a barrel single track trigger which uses the TPC pad information to trigger on tracks with a transverse momentum with respect to the beam axis, p_t, $\geq$ 1 GeV/c.
- The iIDOD : is again a single barrel track trigger which uses correlations between an OD sector and any one of the corresponding 3 sectors of the ID.
- The OD_MJ2_GEO : two OD sectors triggering which are 'back-to-back' through the interaction point in the $x - y$ plane.
- The TOF_MJ2 : $\geq$ 2 TOF octants hit.

Majority-2 triggers : For these triggers at least two signals are needed prior to the event being read out:

- The MUB_LLC_MJ1 : $\geq$ 2 hits in the any MUB sector, but not allowed with OD and HCAL.
- The TOF_MJ1 : $\geq$ 1 TOF octant firing.
- The ID_MJ1 : $\geq$ 1 ID sector firing, but only allowed with the MUB.

[9] Redundancy refers to events of the same class providing several triggers.

[10] An octant divides the detector into eight equal parts, with a horizontal plane at $y = 0$ and a vertical plane at $x = 0$ and $z = 0$

- The OD_MJ1 : $\geq$ 1 OD sector firing, not allowed with the HCAL or the ID_AND_OD.
- The ID_AND_OD : $\geq$ 1 ID sector $*$ $\geq$ 1 OD sector.
- The HAMU_BL_MJ1 : a low energy deposit in the HCAL consistent with a muon.

To trigger on Bhabha events the SAT and the VSAT are used:

The SAT trigger : requires high energy (30 GeV) or low energy (11 GeV) coplanar deposits in each of the calorimeters.

The VSAT trigger : requires coincidences between opposite modules with energy depositions exceeding 25 GeV.

The different detector combinations in the triggers described are relevant for the current analysis and the list does not include various forward triggers, and a combination of forward and backward triggers.

Almost all sub-detectors participate in the trigger system, but ones with longer drift times (the TPC and MUF) take part only at the second-level. Some of the trigger combinations given above are trigger components loosely grouped into classes which trigger on tracks, muon pair events, electromagnetic energy and hadronic energy depositions, and Bhabha events. The emphasis in the trigger system is on high efficiency and high redundancy.

2.7 Chapter Summary

This chapter started with a general description of the Large Electron Positron Collider (LEP), and various steps performed to achieve the intersection of electron and positron beam energies each with a nominal energy of 45 GeV. The different methods of measuring the beam energy were described, with particular emphasis on the latest and most accurate technique of resonant depolarization. An overview was given of the sub-detectors which make up the DELPHI detector, with a more detailed look at the analysis related sub-detectors, the main tracking detector (TPC), the microvertex detector (VD), and the luminometer (SAT). Finally, a description was given of the data acquisition system (DAS) followed by a description of the DELPHI trigger system, which is part of the central DAS.

Chapter 3

Data Analysis and Event Selection

Chapter Abstract

This chapter describes the event selection criteria used for the determination of cross-sections and forward-backward asymmetries for the process $e^+e^- \rightarrow l^+l^-$. After a description of data processing and reduction to produce data in a Micro-DST format, the run-selection criteria (selection of runs via the use of sub-detector operational efficiencies) are described. The selection cuts include cuts on track multiplicity and momentum, on the event topology, and vertex cuts. The last section further describes the changes in the event selection criteria to select a data sample for the forward-backward asymmetries calculation.

3.1 The DELPHI Data Management

During a typical LEP data-taking period, DELPHI accumulates a large amount of data. For the analysis described in this thesis a reduced data set which contains only relevant event information is used. This is achieved by applying very loose selection criteria to ensure that events of physics interests are not rejected, a process which leads to the final sample containing a considerable number of cosmic ray events and beam-gas interactions. The procedure of data reduction is known as the DELPHI data management and it is a three level process:

Raw Data : Raw data[1] is collected at the DELPHI pit on IBM cassettes in the ZEBRA [29] structure, which allows the efficient handling of large amounts of data. From the pit these cassettes are transported to the CERN main site where they are processed by a group of workstations operating in parallel called DELFARM [30].

[1] RAW data refers to data which originates from the various sub-detectors and trigger data.

TANAGRA Data : The raw data is processed by an offline analysis program called DELANA (**DEL**phi **ANA**lysis) [31] which has a highly modular structure to ensure software development in a safe and manageable way. DELANA produces data in a TANAGRA (**T**rack **ANA**lysis and **GRA**phics package) [32] data structure. The purpose of TANAGRA is to provide a coherent way of handling the basic event information from large detectors. It has a well defined data structure called VETBAS (**VE**rtex and **T**rack **BA**sic **S**tructure) which contains the track and vertex information independent of the particular detector component(s) from which it originated. Several kinds of data exist in the VETBAS structure and they are organised in correspondingly different levels.

- **Detector data (TD) :** The first stage of DELANA event reconstruction involves detector data, TD, that is space points, energy deposits, and the corresponding pulse heights or times in the sub-detectors. This stage includes only data from the individual sub-detectors.
- **Track elements (TE) :** Pattern recognition is made locally by software modules for the various detector components. This is first of all made as a local pattern recognition, with track reconstruction in the individual tracking detectors and clustering of energy deposits in the calorimeters, results in the combination of various elements of the tracks into track elements, TEs. In a second stage the information from the other sub-detectors is used to improve local pattern recognition.
- **Track strings (TS) :** The next step involves the gathering of the TE's to build up strings of track elements called track strings, TSs.
- **Tracks (TK) :** One or more strings can be put together to build up a track by means of a track fitting procedure which resolves the ambiguities and contradictions that are allowed at the level of strings and produce a clean and consistent set of tracks TKs.
- **Bundle of tracks (TB) :** After establishing tracks, a vertex search combines the tracks into vertices. A list of tracks, possibly originating from the same vertex is stored, as a track bundle, TB. Any track is allowed to be included in more than one bundle.

- **Vertices (TV)** : From one or several bundles a global vertex fit results in the determination of a secondary vertex position and track parameters at the vertex. This is only useful for secondary vertices as a full vertex fit for high momentum and highly collinear leptonic events is not accurate.

In the final stage of processing the tracks are extrapolated out to the calorimeters and muon chambers and an attempt is made to associate them with energy clusters and muon chamber hits.

DST data : Further data reduction takes place at the end of DELANA reconstruction when a package called the PXDST package strips down the TANAGRA data to produce **D**ata **S**ummary **T**apes (DSTs) which contain only information relevant to the physics analysis and occupy considerably less storage space than the TANAGRA data. The DSTs contain events which have been 'filtered' or 'tagged' as triggers of interest.

3.2 Tagging and the Micro-DST

3.2.1 Leptonic Tagging

The data that has been written onto the DSTs have gone through either the general DELANA tags [33] or the more specific 'Team' tags [34].

DELANA tags : These classify events as hadronic, leptonic, or ambiguous and involve three triggers[2] : the track trigger (TT) the calorimeter (CT), and the vertex track trigger (VTT). For tracks to filter through the TT they must have an impact parameter, R_{imp}, that is less than 8 cm, and a corresponding distance of closest approach in the Z plane, Z_{imp} less than 50 cm. For the CT to be satisfied there should be an energy deposit in the barrel electromagnetic calorimeter (HPC), > 5 GeV, or an energy deposit in the forward electromagnetic calorimeter, FEMC > 4 GeV. The VTT is similar to the TT but has a tighter cut of $R_{\text{imp}} < 6$ cm and $Z_{\text{imp}} < 10$ cm. Figure 3.1 shows the event classification under the general DELANA tags.

[2]Note that, these are not on-line triggers.

Team tags : DELPHI consists of many different physics analysis groups (teams) working on topics in leptonic and hadronic physics. The team tags are the selection criteria provided by the various teams as a means of identifying leptonic and hadronic candidates. Again the emphasis is on tagging via a loose selection. This is because DELPHI data is reprocessed many times and in view of the different alignment at different times of data taking, events which have been accepted with the loose selection criteria might become good lepton pair candidates (when they are not previously).

As an example, Team 2 in DELPHI is the physics analysis team working on muon pair physics. It uses tagging criteria which involve simple tags on charge multiplicities and more sophisticated tags for $\mu^+\mu^-$ pair detection within the TPC sector boundaries and in the forward region where the track reconstruction efficiency can be low. In detail these criteria are:

- A simple topology tag which requires at least one and not more than 6 charged tracks each with a momentum $p > 5$ GeV/c, an impact parameter of $R_{\text{imp}} < 8$ cm, and $Z_{\text{imp}} < 10$ cm.
- For identification within the TPC sector boundaries, it is required that there are not more than 2 TK's with least one having no TPC information, and that there are signal(s) in the outer detector (OD) in line with two back-to-back TPC sector boundaries.
- For the forward region 'muons' are associated to 'tracks'. The 'tracks' are track candidates with TK's and TE's from the FCA, FCB, and the TPC. The 'muons' are muon candidates determined using calorimeter and muon chamber information.

3.2.2 The Leptonic Micro-DST

To achieve a reduction in the data processing time for the analysis, the DST data was further 'stripped' to make the micro-DST, which contained all the leptonic DST in a compact form. This contained event information for ≤ 8 reconstructed charged tracks and no further cuts were applied when making the micro-DST to make sure no genuine leptonic events were rejected. The contents of the micro-DST can be found in Appendix B.

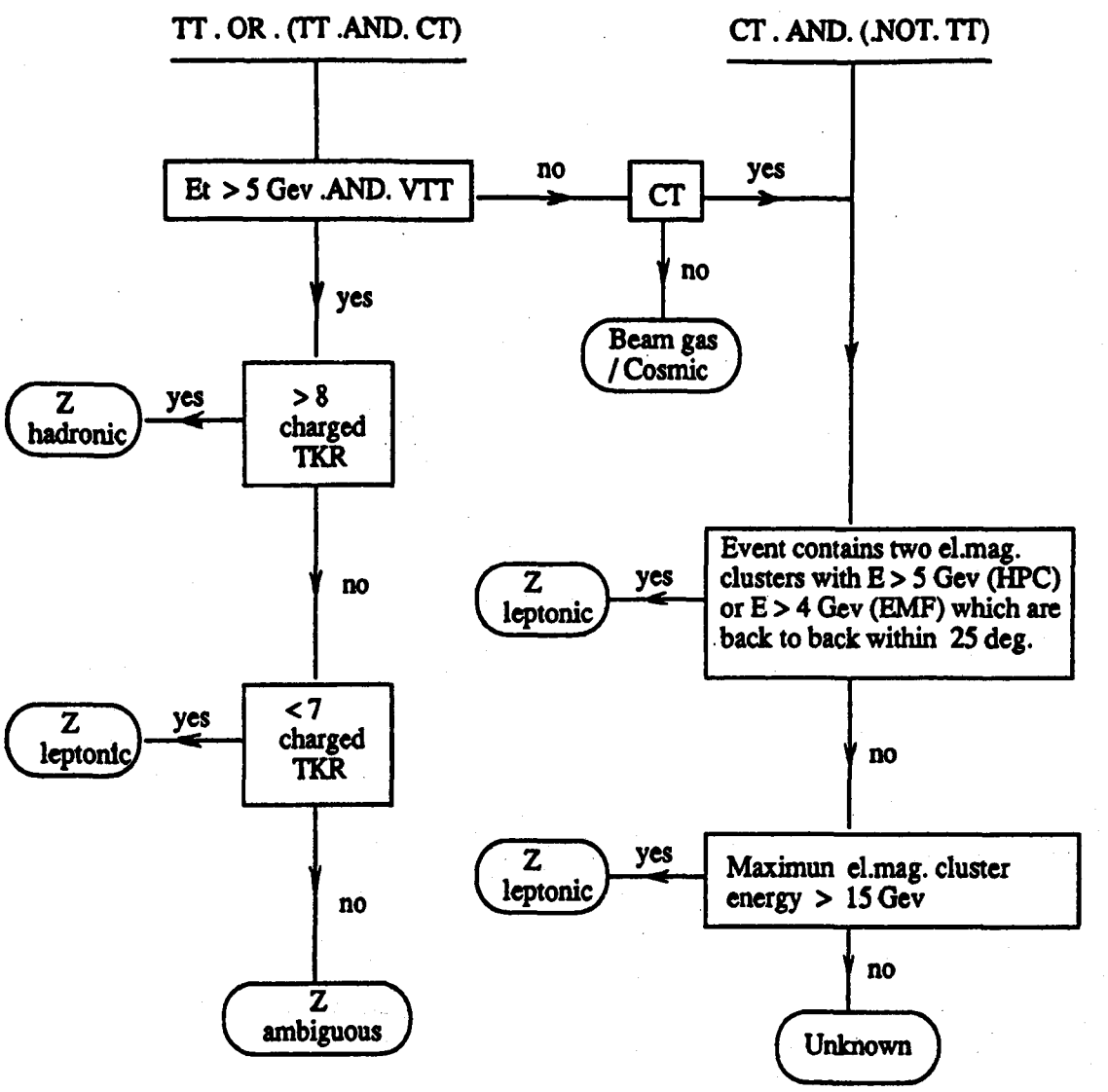

Figure 3.1: A flow chart of showing the classification of the hadronic, leptonic , and ambiguous events under the DELANA tags. From 1993, an event was classified as a leptonic event if it had < 6 charged tracks (TKR) and as a hadronic event if it had > 9 charged tracks (TKR).

3.3 Data Analysis

The previous section described the collection and reduction, to a manageable size, of 'real' data from e^+e^- annihilations. Like other analyses, the analysis described in this thesis uses simulated or Monte Carlo data in conjunction with real data.

3.3.1 Simulated Data

Monte Carlos of $e^+e^-, \mu^+\mu^-, \tau^+\tau^-$, and $e^+e^- \rightarrow e^+e^-X$[3] events were used. The production chain for the real data Micro-DSTs is RAW data $\rightarrow$ TANAGRA data $\rightarrow$ DST data $\rightarrow$ Micro-DST. Similarly for the production of Monte Carlo Micro-DSTs the chain is DELSIM $\rightarrow$ DST data $\rightarrow$ Micro-DST.

[3]This is a so called two-photon process, which is further discussed in detail in Chapter 4.

The DELSIM (DELPHI SIMulation) [35] package produces simulated data with comprehensive tracking of the generated particles through the various sub-detector modules. It includes:

- **Physics simulation.** Different physics routines are used to generate the various possible physics interactions at LEP. For the leptons; BABAMC is used for e^+e^- generation, DYMU3 [36] for $\mu^+\mu^-$, KORALZ [37] for $\tau^+\tau^-$, and [38] for e^+e^-X (two-photon) generation.

- **Detector description.** These are various sets of physics routines which track the particles through the detector and produce secondary interactions and electromagnetic interactions as the particles traverse the material.

- **Detector simulation.** This simulates the behaviour, in detail, of different detector components and produces space points and electronics signals. Those people responsible for the different sub-detectors provide the necessary sub-detector simulation software.

- **Output routines.** The output from the various detector dependent software is written out in the TANAGRA format.

3.3.2 LEP Data Taking Strategy

The data, processed and written on to micro-DSTs, from the LEP runs in the years 1991, 1992, and 1993 forms the basis of the analysis described in this thesis. For the years 1991 and 1993 LEP performed a 'line-scan' (cross-section as a function of energy) with operations at various centre-of-mass energies compared to 1992 when LEP ran at a single centre-of-mass energy point.

In 1991 there were 8 centre-of-mass energy points around the Z^0 peak. Out of these 8 points 7 were scan points, and for the first half of 1991 there was only 1 point close to the Z^0 pole. A similar scheme was adopted in 1993 but this time there were only 4 points, 1 pre-scan point and 3 scan points all close to the Z^0 pole. Table 3.1 shows the different centre-of-mass energies for the different years at LEP.

In 1992, the primary reason for running on-peak only was the fact that the method of resonant depolarization, to accurately determine the LEP energy, proved

Energy (GeV)		
1991	1992	1993
88.464		
89.457		89.433
90.211		
91.208	91.280	91.192
91.239		91.297
91.953		
92.952		93.016
93.702		

Table 3.1: The various energies LEP operated at in the years 1991, 1992, and 1993. The energies, around 91.2 GeV, are referred to as the peak (or on-peak) energy (P) and the others as P-1, P-2, and so on.

to be difficult with the beam optics used. Hence, it was thought the gain from a scan would not be significant.

Carrying out a 3 point scan (1993), compared to a 7 point scan (1991) was to obtain the best possible accuracy on the determination of the mass (M_Z) and width (Γ_Z) of the Z^0. The 3 points were chosen over a 5 or 7 point strategy to give the most efficient use of running time, that is the smallest error on Γ_Z versus the loss of overall statistics for other physics. The optimum energies for the accurate determination of M_Z are essentially P $\pm$ 1 GeV and P $\pm$ 2 GeV for Γ_Z, where P is the peak Z^0 resonance energy. The drawback for 3 points is that there are no degrees of freedom in the fit, at least for hadrons (i.e 3 points and 3 parameters). Thus, the choice of the 7 point scan was to check the predicted shape of the Z^0 resonance. However, it was felt in 1993 that the constraints on the shape would be too loose to check any new physics and the loss on the precision of Γ_Z would be significant.

3.4 The Inclusive Lepton Analysis

In the inclusive lepton analysis, sometimes referred to as the flavour-independent analysis, the leptonic decays $Z^0 \rightarrow l^+l^-$ (where $l = e, \mu, \tau$) are selected without an attempt being made to separate the three flavours. This assumption of universality leads to many advantages.

- The selection efficiency of leptonic events is high compared to other leptonic analysis as no tight cuts are required to separate the three flavours.

- The clean signature of leptonic events, low-multiplicity, back-to-back topology, and high visible momentum, allows easy separation from their potential backgrounds (hadronic events, two-photon events, cosmic events, etc.) and thus low levels of contamination are expected. Note, that the leptonic channels are the main backgrounds to one another.

- As the analysis is independent of flavour it can be based primarily on reconstructed charged particle tracks[4].

- As the event selection criteria for this analysis and the other leptonic analyses are relatively independent, entailing different systematic errors, they provide a good consistency check to each other.

Thus, the main motivation for the inclusive lepton analysis is that it provides a tight cross-check to the flavour separated (or lepton-identified) analyses.
But there are some disadvantages:

- There is an inherent assumption of lepton universality. This is defined as the equality of the gauge couplings of the three lepton doublets.

- The analysis can never truly be flavour independent as the fractions of e^+e^-, $\mu^+\mu^-$, and $\tau^+\tau^-$ have to be computed in order to determine the e^+e^- t-channel contribution. As the tracking detectors are used to select the leptons, the electromagnetic and hadron calorimeters can be used to select a very pure sample of e^+e^- and $\mu^+\mu^-$ events. The situation for $\tau^+\tau^-$ events is different (see Chapter 4).

3.5 Selection Criteria

Various cuts were imposed, on the raw data set to select leptonic events in a manner which is independent to the lepton flavour.

[4]Hereafter reconstructed charged particle tracks will be referred to as tracks.

3.5.1 Quality of Data from Detectors ($R1$, $R2$, $R3$)

It is impossible for the sub-detectors within DELPHI to be 100% functional due to problems such as high voltage failures, gas failures, etc. Hence it is necessary to have information on the various sub-detectors in terms of their data taking or data acquisition abilities. Such information is stored in files called 'Run Quality' files which flag the status of individual sub-detectors in terms of their operational efficiencies. Table 3.2 shows the various flags, 0-9, and their meanings.

Flag	Status Percentage of detector being nominal
0	unusable data
1	< 65 %
2	50 - 65 %
3	65 - 80 %
4	80 - 90 %
5	90 - 95 %
6	95 - 99 %
7	> 99 %
8	detector efficiency varies during run
9	status in unknown

Table 3.2: The flags for the various sub-detector operating efficiencies in DELPHI

For the cross-section[5] analysis it was required that both the SAT and the TPC were fully functional and that there were a certain number of low angle Bhabha events corresponding to a luminosity of at least 0.1 $(\text{nb})^{-1}$ per run. These cuts are called the run-selection criteria and are shown in table 3.3.

Detector	TPC	SAT	Luminosity
Flag	6 - 7	7	0.1 $(\text{nb})^{-1}$

Table 3.3: The requirements on the SAT flag, TPC flag, and the minimum luminosity which constitute to define a good run for the inclusive lepton analysis.

In order to obtain a high purity sample of leptonic events a set of cuts has been used to reduce all backgrounds to a low level. The cuts essentially require a low

[5]As the calculation of the forward-backward asymmetries do not require a knowledge of the luminosity, these run selection criteria are relaxed when determining the asymmetries.

multiplicity, back-to-back topology and some cuts especially designed to reduce the backgrounds due to two-photon, hadron, and cosmic ray events.

3.5.2 Track Multiplicity and Momentum Cut ($C1$, $C2$)

An event was selected if it had between 2 and 6 'good' charged tracks reconstructed in the TPC. To be considered as a good track, a track has to

- Have a reconstructed momentum greater than 0.2 GeV/c.
- Originate near the interaction region, i.e with impact parameters of Z_{imp} less than 4.5 cm, and R_{imp} less than 3.0 cm.

The charged-multiplicity cut itself is enough to suppress most of the hadronic background, as illustrated in figure 3.2, where the charged-multiplicity distribution is shown for the data sample used for the hadronic analysis using similar selection criteria [39].

To suppress the low-energy background events arising from beam-gas, beam-wall, and two-photon interactions, it was demanded that at least one track in the event have a reconstructed momentum greater than 3.0 GeV/c (see figure 3.3 [40]). To ensure a constant lepton selection efficiency, both on-peak (around the Z^0 resonance energy) and off-peak, this cut was changed in 1993 to scale with the different centre-of-mass energies:

$$P_1(\mathrm{GeV/c}) = 3 \times \frac{E_{\mathrm{cm}}}{91.187}, \tag{3.1}$$

where 91.187 represents the Z^0 resonance energy and E_{cm} is the centre-of-mass energy.

3.5.3 Two-Jet Topology Cut ($C3$, $C4$, $C5$)

The emphasis was on identifying an isolated track nearly back-to-back with a well collimated jet.

- The event was divided into two hemispheres by a plane perpendicular to the thrust axis[6]. It was required that one of the hemispheres have a single track and the other between 1 and 5 tracks. The 1 to 5 tracks are hereafter referred to as the jet although no jet-finding algorithm was used.

[6]See Appendix C for a definition of the thrust axis.

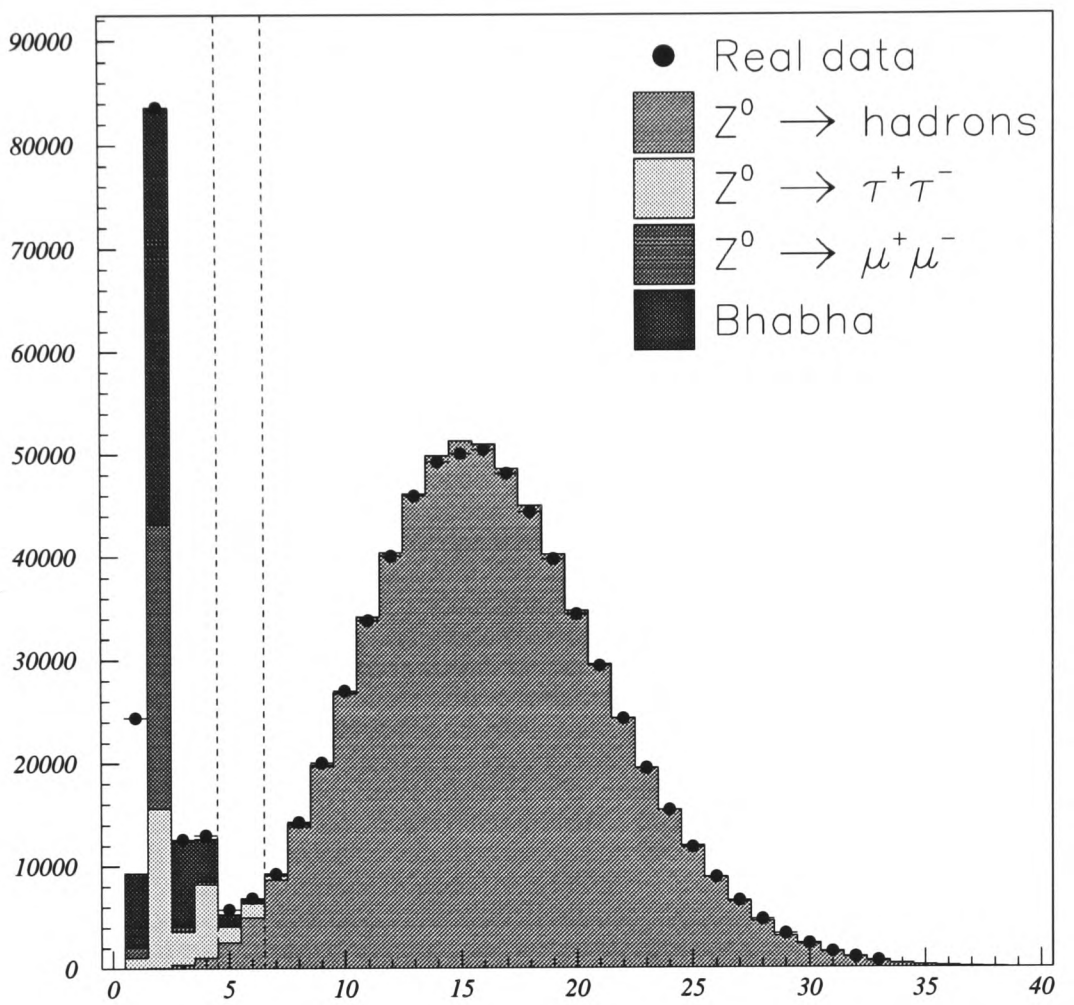

Figure 3.2: The charged multiplicity distribution in a Z^0 decay for Monte Carlo and real data. The choice of the multiplicity cut is so that the best possible separation between hadronic and leptonic decays is achieved. The E_{ch} is a minimum energy requirement of the physics team working on the process $e^+e^- \rightarrow q\overline{q}$ in DELPHI.

- The resultant momentum of the jet was calculated and it was demanded that there be a less than 20^0 deviation between the resultant momentum vector and the backwards projection of the isolated track (i.e an acollinearity of less than 20^0 was demanded for any topology). For two particles with momentum vectors $\boldsymbol{p^\mu}$ and $\boldsymbol{q^\mu}$, the acollinearity η_{acol} is defined as

$$\eta_{\text{acol}} = 180.0 - \arccos\left(\frac{\boldsymbol{p^\mu . q^\mu}}{|\boldsymbol{p}|\,|\boldsymbol{q}|}\right), \tag{3.2}$$

- It was required that the opening angle, the angle between any track in the jet and the resultant momentum of the jet, be less than 30^0. This corresponds to an isolation angle of 150^0 between the isolated track and the jet.

The topology cut results in the rejection of tau 3-3 prong decays. This loss is negligible compared to the increase in the hadronic background events, had this cut

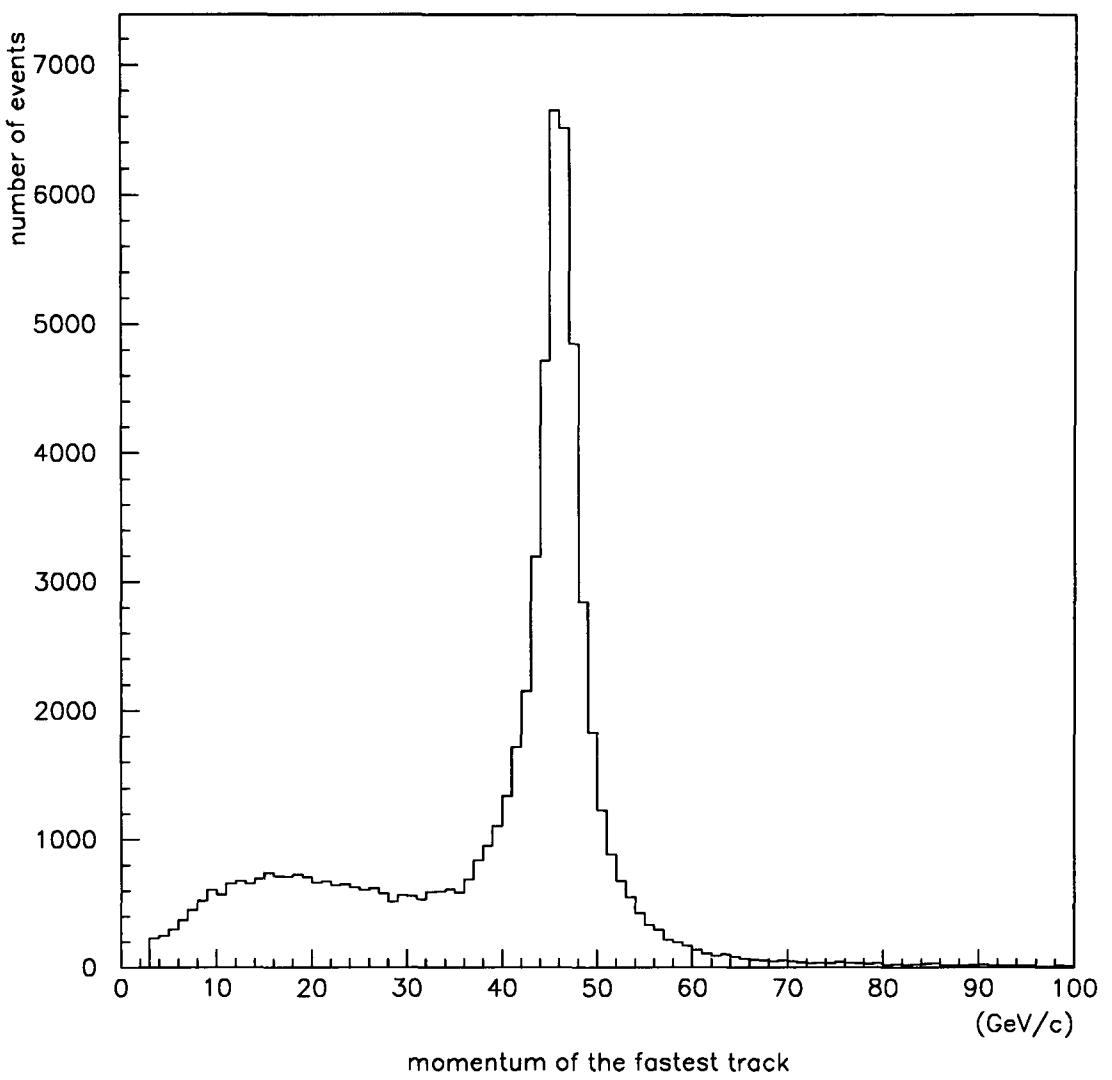

Figure 3.3: Momentum distribution for the highest momentum charged particle in low multiplicity events selected in the inclusive lepton analysis. All cuts of table 3.5 are applied. The peak around 45 GeV/c is due to the high momentum electrons and muons, whereas the low momentum region is occupied mainly by τ decays.

not been applied.

3.5.4 The Missing Momentum (P_t^{miss}) Cut ($C6$)

The two-photon background is further reduced with the use of a cut on the missing transverse momentum ($\boldsymbol{P_t^{miss}}$) in an event, which is defined as the **vector** sum of the transverse momenta and shown below:

$$\boldsymbol{P_t^{miss}} = \sum_{i=1}^{n} \boldsymbol{P_t^i}, \tag{3.3}$$

where $\boldsymbol{P_t^i}$ is the transverse momentum of the i'th track, and n is the total number of tracks in the event.

When a low invariant mass lepton or quark pair is produced in a two-photon process, the total transverse momentum with respect to the beam axis is generally

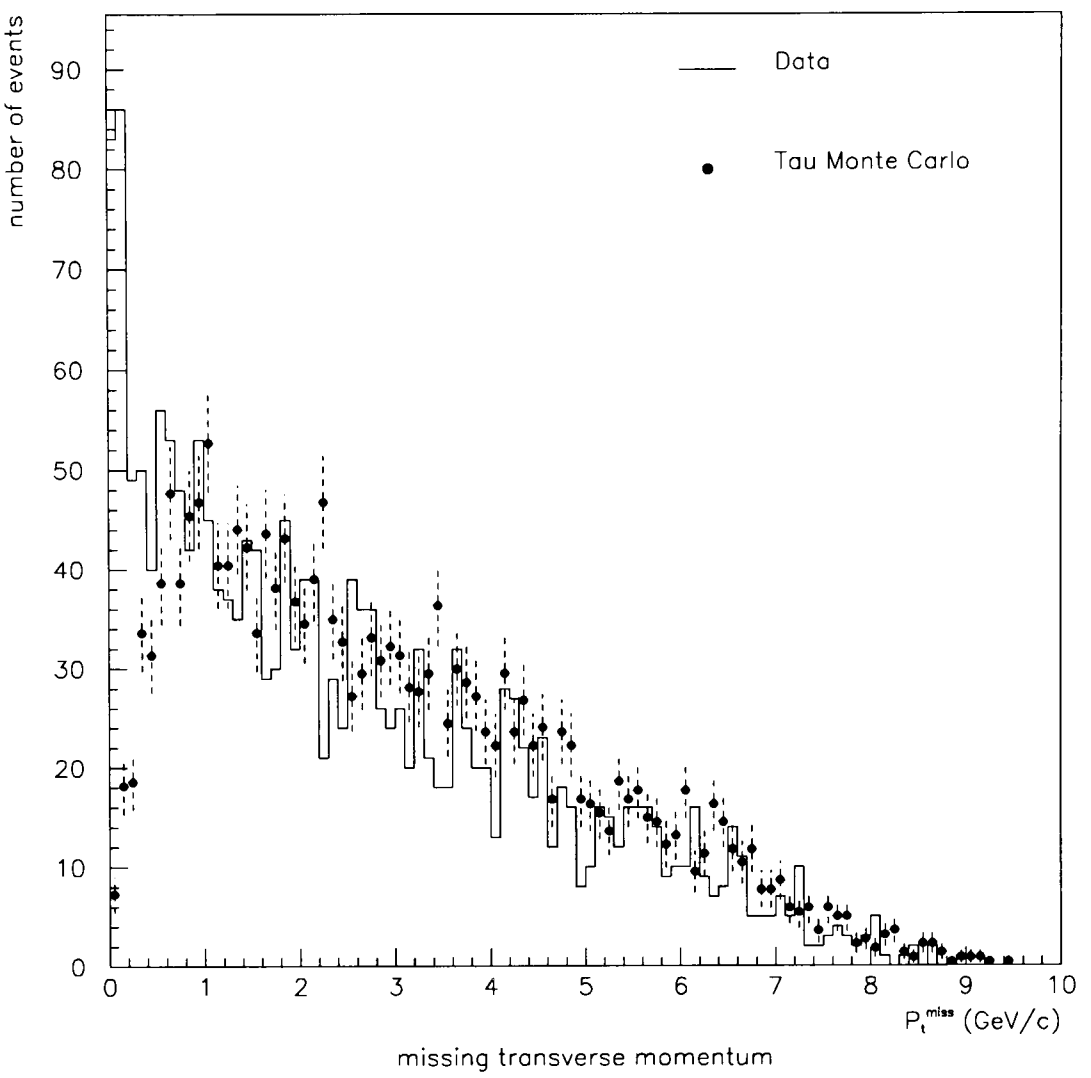

Figure 3.4: The distribution of the missing transverse momentum, all cuts except C6 of table 3.5 are applied. This plot shows only two track events where both tracks have a momentum less than 10 GeV/c. The solid line is the data and the dots represent the tau Monte Carlo. The Monte Carlo has been normalized to the data.

small, implying that the two-photon events are highly back-to-back in the $r\phi$ plane. But e^+e^- and $\mu^+\mu^-$ from Z^0 decays are also back-to-back in the $r\phi$ plane, hence a cut has to be applied which ensures effective removal of the two-photon events and no loss of genuine leptons pairs. Thus a $\boldsymbol{P_t^{miss}}$ cut greater than 0.4 GeV/c is only applied when both tracks in the event have a momentum of less than 10 GeV/c. In the case of tau pairs, from Z^0 decays, the total transverse momentum is large and not compensated, due to the emission of neutrinos. To ensure that this cut does not reject genuine tau pairs, it was tested on a tau Monte Carlo and the loss was found to be approximately 0.1 % (see figure 3.4).

Year	%age of tracks with VD hits
1991	94
1992	91
1993	96

Table 3.4: The percentages for both tracks in 1-1 topology registering vertex detector hits for various years.

3.5.5 Cosmic Vertex Cut ($C7$)

A clean rejection of cosmic ray muons from the data sample is achieved via the requirement (tight), that in an event with two tracks in a 1-1 topology[7], both the particles should originate from close to the beamspot (i.e a tighter vertex requirement is imposed).

Beamspot Position

The beamspot is defined as the position of the interaction of the two beams. Electron-positron collisions within the DELPHI beam pipe occur in a small region which can be described by a two-dimensional Gaussian in the x-y plane. The widths of these two Gaussians are determined by the size and shape of the electron and positron bunches within LEP. These bunches produce an interaction region that is wider in the x (horizontal) plane than in the y (vertical) plane. The size of the interaction region (beamspot) was estimated[8] to be: $\sigma_{x\mathrm{beam}} = 142 \pm 5$ μm and $\sigma_{y\mathrm{beam}} = 7\ ^{+3}_{-7}$ μm. The typical errors on x_{beam} and y_{beam} are 8 μm and 15 μm respectively. For a detailed description of the beamspot determination see [41].

Once the beamspot position has been calculated, it is used to define the R_{imp} (VD) and Z_{imp} (VD) impact parameter cuts. Figures 3.5 (a) and (b) show the R_{imp} (VD) and Z_{imp} (VD) distributions in leptonic events.

- If there were VD hits associated with both the tracks and there was a well reconstructed beamspot, then it was demanded that $|R_{\mathrm{imp}}\,(VD)| < 0.15$ cm and $|Z_{\mathrm{imp}}\,(VD)| < 4.5$ cm.

[7] A 1-1 topology is one in which the two tracks are back-to-back, with one track being in the opposite hemisphere to the other.

[8] This determination was carried out on a run-by-run basis, where a run is defined as a typical data-taking period (approximately 10 runs make up a fill in LEP).

- If either track did not have an associated VD hit or the beamspot was not well reconstructed, then the $|R_{\mathrm{imp}}(\text{no VD})|$ was relaxed to 1.5 cm.

This cut depends heavily on the tracks giving hits in the microvertex detector (VD). The percentages, for different years, of tracks which registered hits in the VD are very high, table 3.4, and it is this information which is used to define the tight vertex cuts for 1-1 events. There is a fall in the 1992 percentage due to the fact that the VD had 4 dead modules which were replaced for the 1993 run.

The leptonic event selection criteria are summarized in table 3.5.

3.5.6 Cross-Section Data Sample

Using the event selection criteria described in the previous section, the number of events selected in 1991 were 23169 events at an integrated luminosity of 10.7 pb^{-1}, 65200 events at an integrated luminosity 24.0 pb^{-1} in 1992, and 67035 events at an integrated luminosity 36.1 pb^{-1} in 1993. The total integrated luminosity for each of the years was calculated from files provided by the SAT and VSAT groups, on a run-by-run basis (i.e the luminosity at one particular energy point is the sum of all the luminosities associated with the different runs at that particular energy point). The luminosities and the associated errors are further discussed in Chapter 5.

3.6 Selection Criteria for the Asymmetry Calculation

Some more consideration has to be given when selecting events for the asymmetry determination. The event selection is the same as in the previous section (table 3.5) but with the following changes:

- As the luminosity is not used in the asymmetry calculation the run-selection cut, table 3.3, is relaxed, i.e there is no requirement for the luminosity to be greater than 0.1 $(\mathrm{nb})^{-1}$ per run.

- To avoid systematic errors associated with the track superposition and 'bad' charge determination in τ decays to more than one charged particle, only 1-1 topology events with oppositely-charged tracks are used.

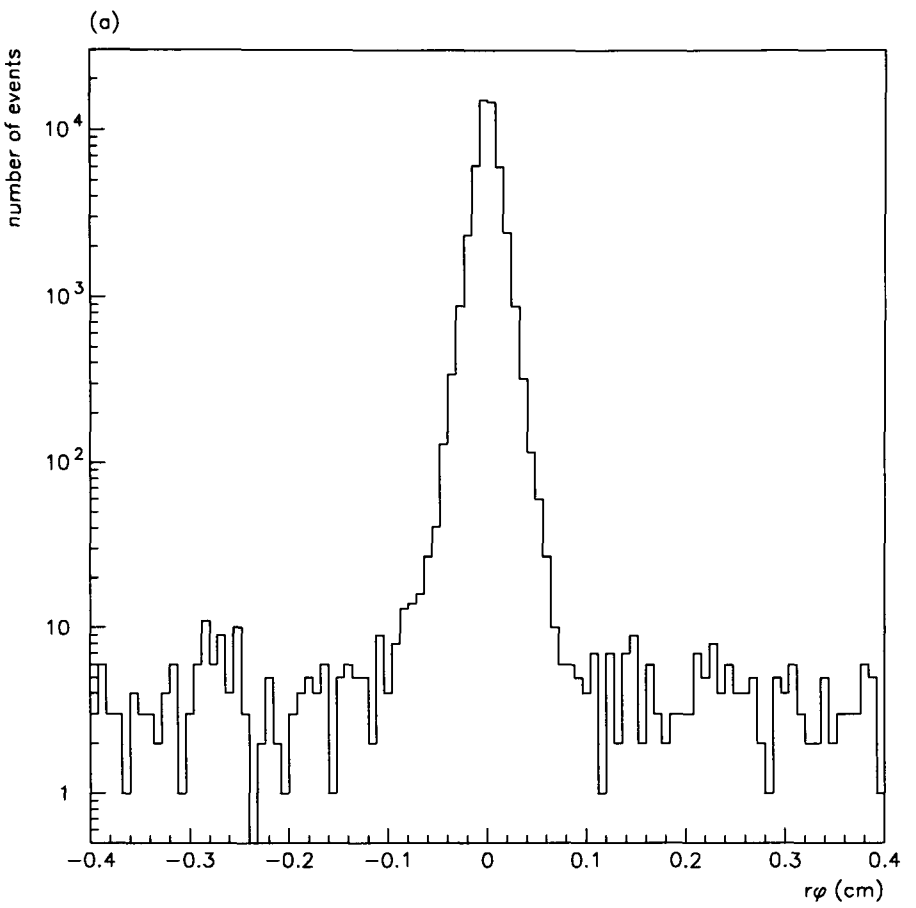

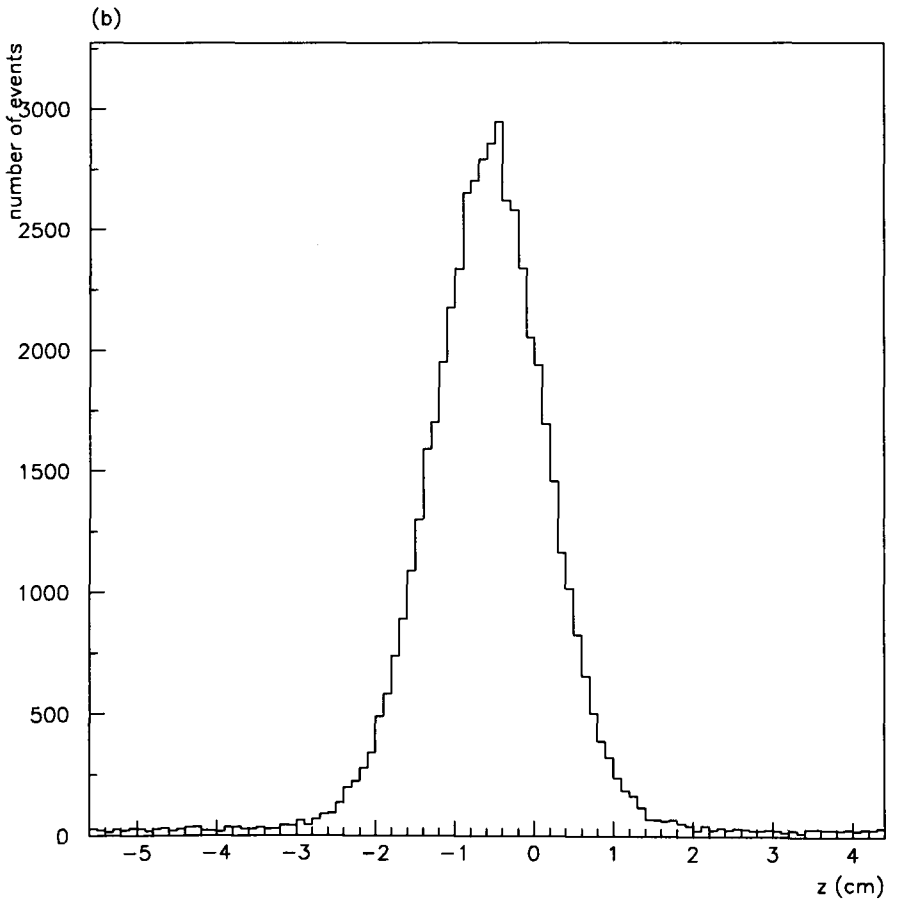

Figure 3.5: The impact parameter distribution for event with two charged tracks. (a) shows the $r\phi$ impact parameter distribution and (b) shows the z coordinate at the point of closest approach to the beam spot in the $r\phi$ plane. All cuts except C1 and C7 of table 3.5.

Cut	Description
R1	Fully functioning SAT
R2	Fully functioning TPC
R3	Luminosity per run > 0.1 (nb)$^{-1}$
C1	≥ 2 charged tracks in the barrel, $43^0 \leq \theta \leq 137^0$ 2-6 'good' charged tracks, good : $\lvert R_{\rm imp}\rvert < 3.0$ cm $\lvert Z_{\rm imp}\rvert < 4.5$ cm P > 0.2 GeV
C2	The momentum of the fastest track, $P_1 > 3.0$ GeV/c.
C3	Event topology : 1 vs jet or jet vs 1 where jet is 1 - 5 charged tracks.
C4	The acollinearity was required to be, $\eta_{\rm acol} \leq 20^0$.
C5	The opening angle $\leq 30^0$ or the isolation angle $\geq 150^0$.
C6	If P_1 and $P_2 \leq 10$ GeV, then, $P_t^{\rm miss} \geq 0.4$ GeV.
C7	If 2 charged tracks, 1-1 topology, then $\lvert R_{\rm imp}\rvert < 0.15$ (VD) or 1.5 (no VD).

Table 3.5: The run and event selection criteria for the inclusive, l^+l^-, analysis.

Year	Number of events (cross-section)	Number of events (asymmetry)	Number of 1-1 events (asymmetry)
1991	23169	23223	18062
1992	65200	65229	51647
1993	67035	67080	53392

Table 3.6: The selected asymmetry events after passing all the cuts in table 3.5 except R1, R2, and R3. A comparison of column 1 and column 2 shows the increase in the number of events after relaxing the R3 cut.

3.6.1 Asymmetry Data Sample

After relaxing the 0.1 $(nb)^{-1}$ per run cut on the luminosity, the asymmetry event sample contains slightly more events than the cross-section sample (see table 3.6). Some 1-1 topology events have a mis-measured charge which results in both tracks in the 1-1 events having the same charge. Events which have tracks reconstructed as having the same charge[9] occur in DELPHI when their momentum is mis-measured. This mis-measurement can occur due to bad track reconstruction in the TPC when the track(s) is either close to one of the TPC sector boundaries or has a very high momentum and thus minimal track curvature[10]. Figure 3.6 shows the distribution of the electric charge multiplied by the inverse momentum of the charged particles of events with two tracks. The entries around 0 $(GeV/c)^{-1}$ represent very high momentum tracks (very high radius of curvature) and hence are very likely to be like-sign events.

To reclaim these like-sign events, a method has been devised which uses the positioning of energy deposits in the HPC (barrel electromagnetic calorimeter).

3.6.2 $\Delta\phi$ Like-Sign Reclaim

In order to understand charge determination with use of energy deposits in the HPC, one has to understand how charged particles are influenced under the DELPHI

[9]These events are called like-sign events.

[10]The radius of curvature, R_T (m), of a track is defined as

$$R_T = \frac{P_T}{0.3BZe} \tag{3.4}$$

where P_T is the momentum (GeV/c) of the track transverse to the magnetic field B (Tesla) and Ze is the charge. Thus, for a 45 GeV/c track in DELPHI (B=1.2 T) the radius of curvature is $\sim$ 125 m.

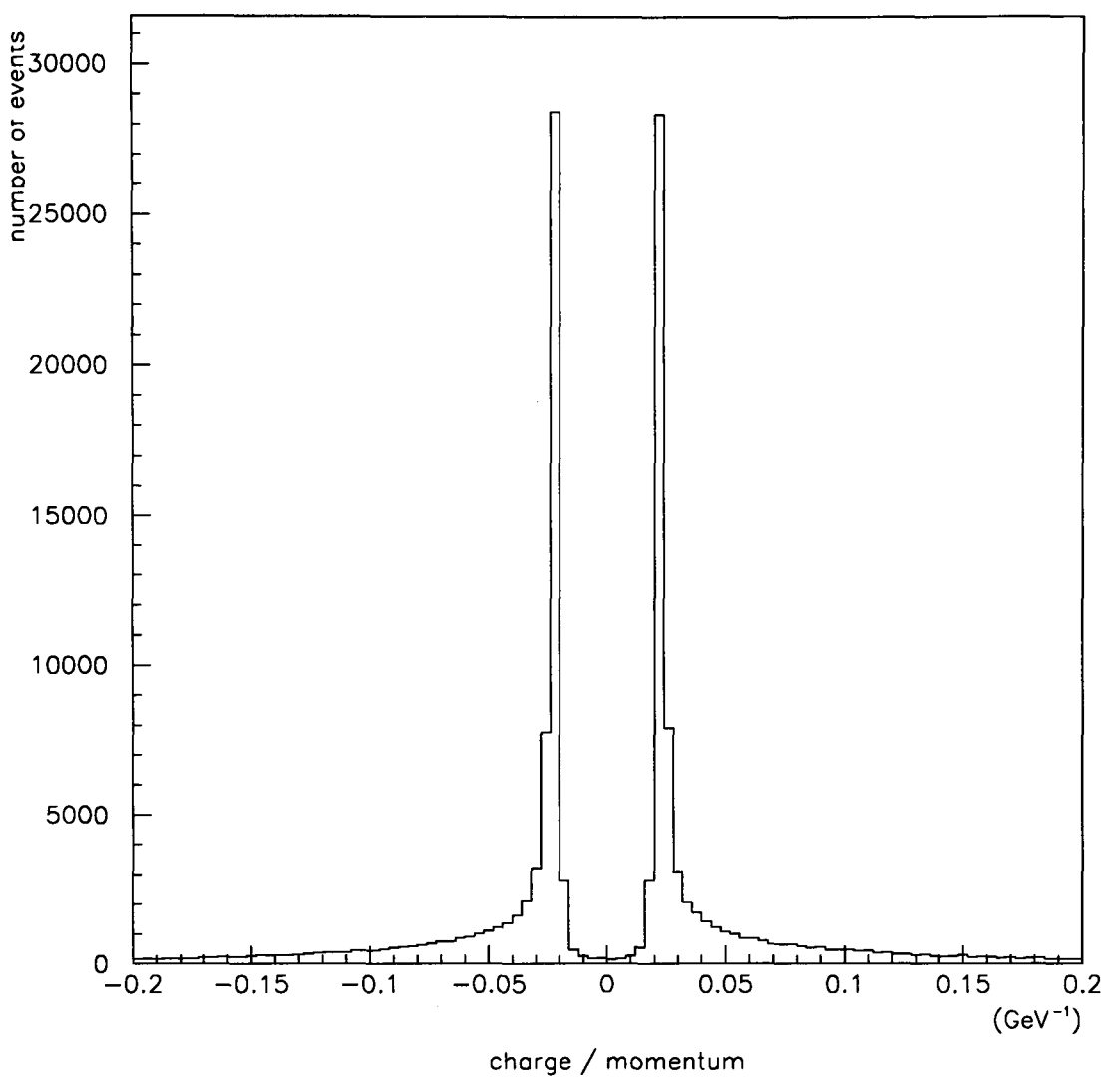

Figure 3.6: Distribution of the electric charge multiplied by the inverse momentum of the charged particles for events with two tracks. All cuts of table 3.5. The overlap around 0 $(\mathrm{GeV/c})^{-1}$ represents very high momentum tracks which can be a possible source of like-sign events.

magnetic field. Figure 3.7 shows that the negatively charged tracks are bent in the direction of increasing ϕ (from x to y) and the positively charged tracks in the direction of decreasing ϕ. The magnetic field is along the direction of the electron beam $(+z)$.

Events were selected if there was an energy deposit, associated with the 1-1 topology tracks, of greater than 1 GeV. The quantity $\Delta\phi$ was defined as the difference in the ϕ[11] angle of the second fastest (ϕ_2) and the fastest (ϕ_1) tracks. That is

$$\Delta\phi = \phi_2 - \phi_1 - 180^0 \tag{3.5}$$

It can be seen from figure 3.7, that under this scheme a negative (positive) $\Delta\phi$ would mean that the fastest track is negative (positive). Once, the fastest track

[11]The azimuth of the energy deposit in the HPC is defined as the angle ϕ.

Year	Like-Signs		Reclaimed		Not-Reclaimed	
	+ +	- -	+ +	- -	+ +	- -
1991	81	89	42	50	39	39
1992	328	360	173	192	155	168
1993	284	281	177	180	107	101

Table 3.7: Table showing the number of like-sign events, both tracks having a negative (positive) charge. Columns 4 and 5 represents the number reclaimed using the $\Delta\phi$ reclaim method and columns 6 and 7 represents the number which fail this method.

was identified as being negative (positive) the other was taken to be positive (negative). Table 3.7 shows the number of like-signs and the number reclaimed under this scheme, for the different years. To check the efficiency of this reclaim method, it was tested on 1-1 topology events that were oppositely charged. Figure 3.8(a) shows the $\Delta\phi$ in the case of the fastest track being positive, and figure 3.8(b) shows the $\Delta\phi$ for a negative fastest track. In figure 3.8(a) the hatched area represents the case when the $\Delta\phi$ reclaim method has failed and identified the fastest positive track as being negative. Similarly, the hatched area in figure 3.8(b) shows the mis-identification of the fastest negative track as being positive. Through the use of such checks it was determined that the $\Delta\phi$ reclaim method failed approximately 24 % of the time. This is further discussed in Chapter 5.

3.7 Chapter Summary

This chapter began with a description of the DELPHI data management system, the aim of which is to reduce the large volume of DELPHI data to a compact size for efficient data analysis. The general output was onto DSTs (Data Summary Tapes) which contain information only relevant to physics analysis. To reduce data processing time, the DSTs were written onto more compact Micro-DSTs. Next, there was a section on the data analysis which mentioned the production of various Monte Carlos and the data taking strategy adopted by LEP in the years 1991, 1992, and 1993. These years being the ones which form the basis of the analysis described in this thesis. The advantages and disadvantages of the inclusive lepton analysis were given along with a comparison with the more conventional leptonic analyses. The last two sections discussed the various cuts used to select a pure

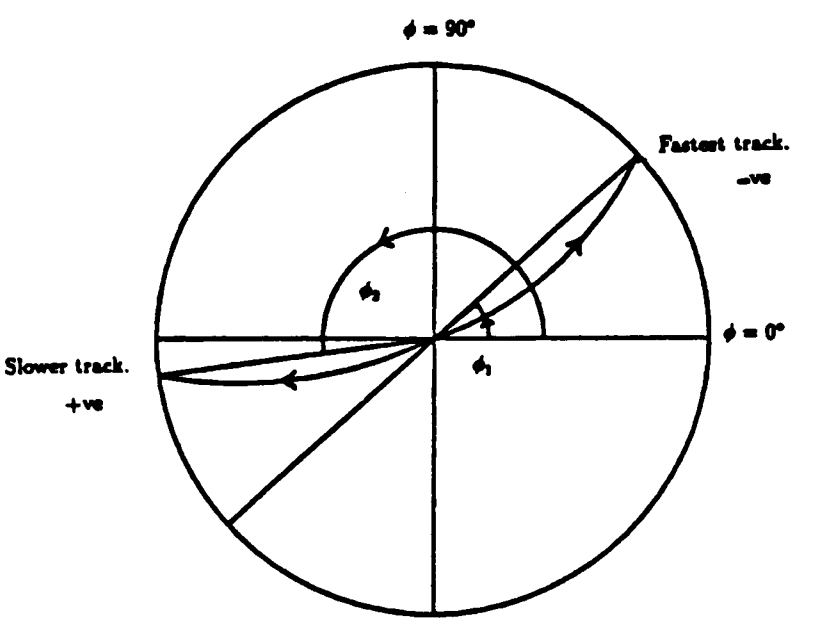

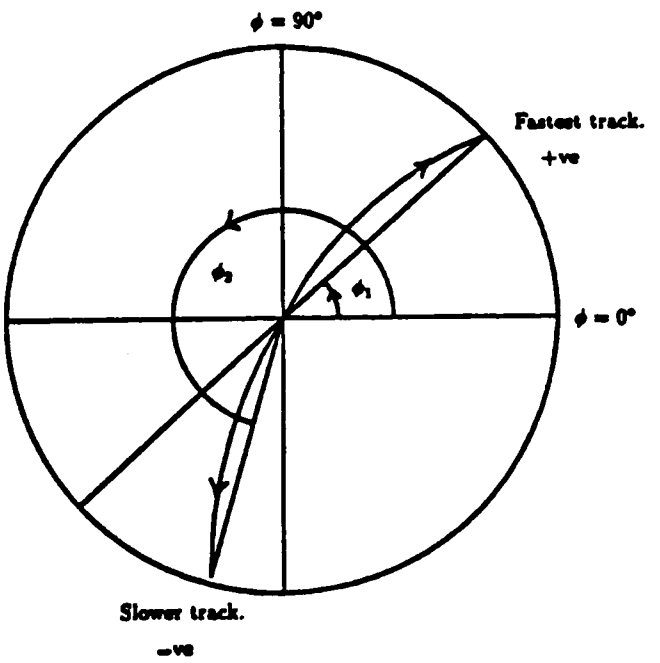

Figure 3.7: The direction positively and negatively charged tracks are bent under the influence of the DELPHI magnetic field. Negative tracks are bent in the direction of increasing ϕ and the positive tracks in the opposite direction.

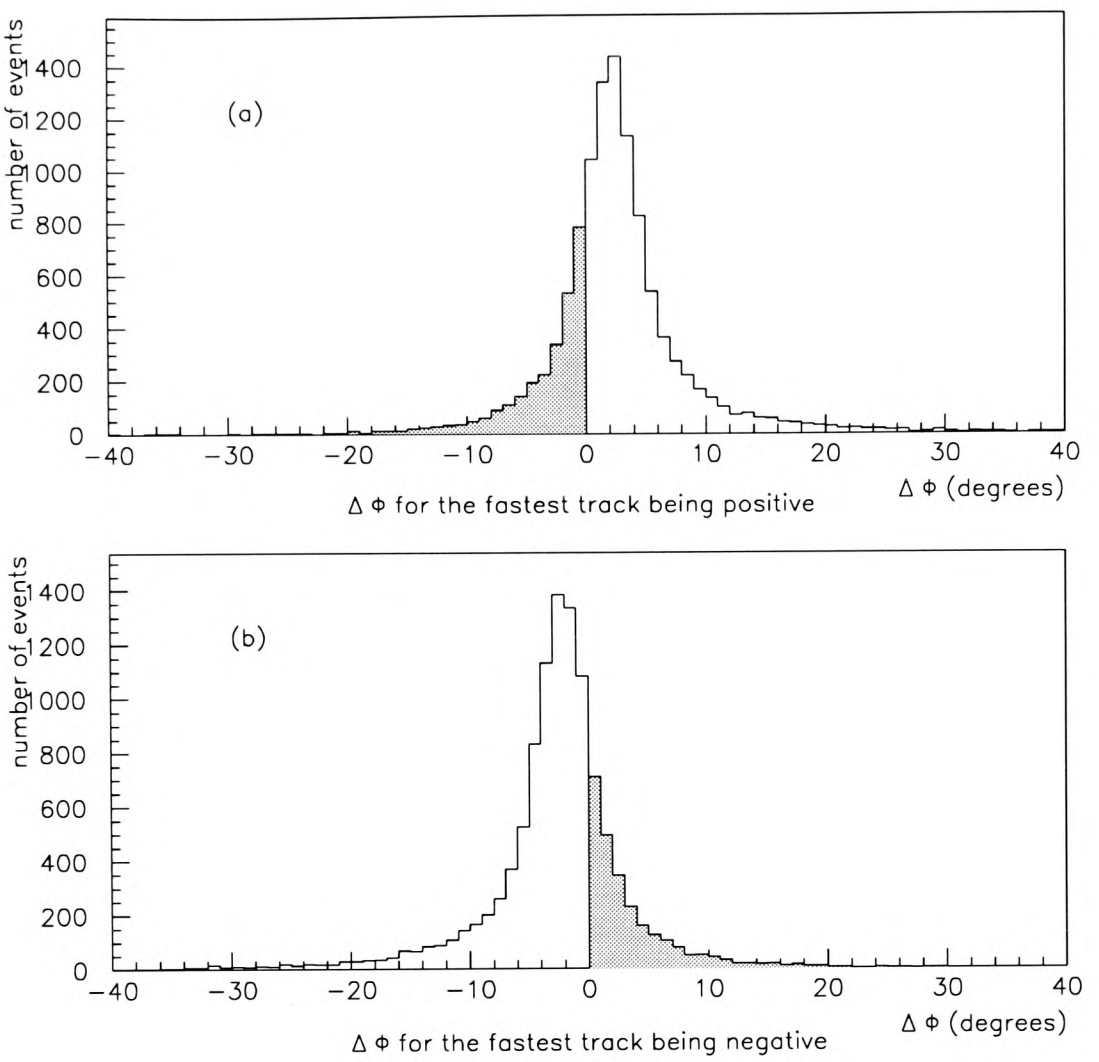

Figure 3.8: The $\Delta\phi$ distribution for two oppositely charged tracks, all cuts of table 3.5 applied. The hatched areas represent the mis-identification of tracks using the $\Delta\phi$ reclaim method.

sample of leptonic events (distinct signatures being the low multiplicity, back-to-back topology, and the high visible momentum) for the determination of the cross-sections and forward-backward asymmetries for the process $e^+e^- \longrightarrow l^+l^-$ (where $l = e, \mu, \tau$). The last section also included the technique through which 1-1 topology events having the same charge (like-sign events) were reclaimed into the data sample for the determination of the forward-backward asymmetries.

Chapter 4

Background and Efficiency Calculations

Chapter Abstract

The backgrounds to the inclusive lepton analysis (two-photon events, hadronic events, and cosmic muon events) are dealt with in detail. The individual lepton selection efficiencies are calculated. As there is heavy reliance on the TPC, the selection efficiencies are divided into the TPC inefficiencies (due to the design of the TPC there are areas in θ and ϕ which are insensitive to the passage of charged tracks) and the TPC live-space efficiencies (these are the reconstruction efficiencies in the regions outside the TPC dead areas). The e^+e^- and $\mu^+\mu^-$ TPC inefficiencies and live-space inefficiencies are calculated from the real data whereas the $\tau^+\tau^-$ contributions are calculated using Monte Carlo simulations. The tau efficiencies were corrected for the discrepancies between the simulated and real data $\tau^+\tau^-$ events. The determination of the trigger efficiency is also discussed.

4.1 Backgrounds

The backgrounds to the inclusive lepton analysis are the ones which can produce low topology events which can contribute to the final-state in the process:

$$e^+e^- \longrightarrow l^+l^-, \tag{4.1}$$

where $l = e, \mu$,or τ and the exchange is via a photon (γ) or a Z^0 boson. These low topology events can contaminate the leptonic final-state in the process above and hence they contribute as backgrounds to the inclusive lepton analysis. Consideration is only given to the main contributors (backgrounds), namely : two-photon ($\gamma\gamma$) events, hadronic events, and cosmic muon events.

4.1.1 The Two-Photon Background

It can be seen from Chapter 3 that the low-energy background due to the beam-gas and beam-wall interactions is reduced via a cut on the fastest track in an event (a momentum of greater than 3 GeV/c). The majority of the two-photon background (which is also a low-energy background) can be reduced using this cut and also the cut on the missing transverse momentum. In this section the residual two-photon background, after the application of all the cuts, is quantified using two different methods. Before going on to describe the methods of the background determination, a brief overview is given of the two-photon process.

A two-photon ($\gamma\gamma$) process is one in which the 'clouds' of virtual photons accompanying the electron and positron beams interact to give a four-fermion final-state (equation 4.2 and figure 4.1):

$$e^+e^- \longrightarrow e^+e^-X, \tag{4.2}$$

where X represents a leptonic ($l\bar{l}$) or hadronic ($q\bar{q}$) final-state. The actual mechanism which describes the production of the four-fermion final-state is complicated and only the essential details are described below.

The cross-section for the two-photon process (for a fixed mass of X) varies as

$$\sigma_{\gamma\gamma} \simeq \left(\frac{\log E}{m_e}\right)^2, \tag{4.3}$$

where E is the beam energy and m_e is the mass of the electron. It increases with the energy, but most of the events from this process have low invariant masses of the produced system due to the typical bremsstrahlung spectrum ($\sim 1/E_\gamma$) of the virtual photons. The lowest order diagrams which contribute to a four-fermion final-state are[1] shown in figure 4.2. The photon propagators in figure 4.2 (a) cause the majority of the photons to be radiated nearly on-mass-shell and hence at small angles relative to the beam. Thus, the e^+e^- in the final-state carries a large fraction of the initial momentum, suffering minimal deflection due to the magnetic field, and hence travel down the beam-pipe. But there exists a finite probability for the particles in the fermionic final-state X to enter the barrel region.

In order to calculate this background a generator was used to simulate the two-photon events corresponding to the data for the years 1991 and 1992. Standard

[1] See for example [42].

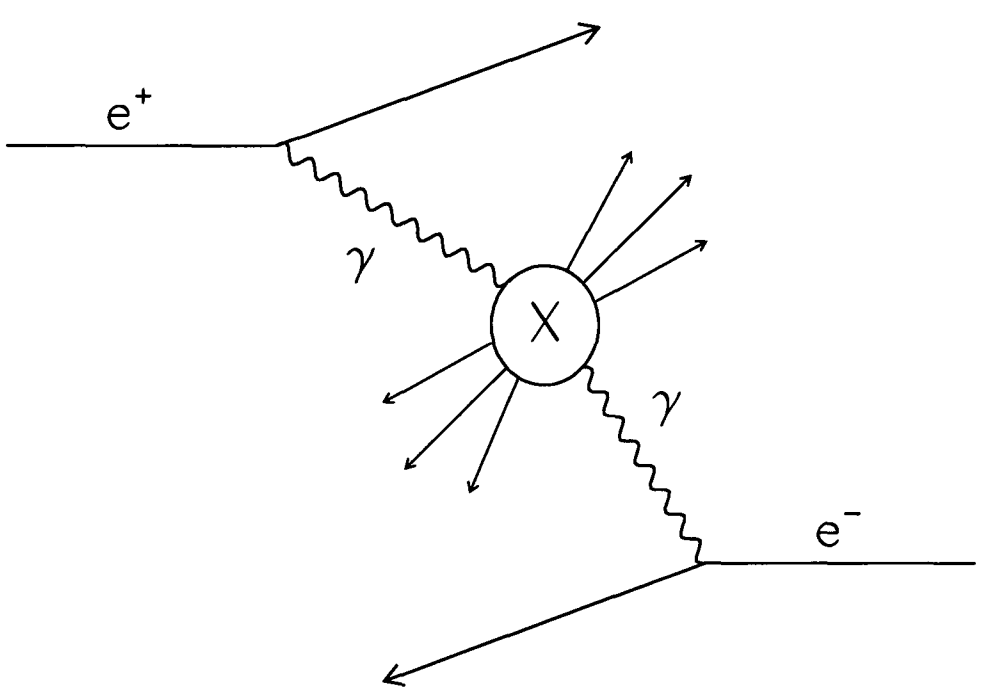

Figure 4.1: The two-photon process in which two virtual photons, each from the e^+ and e^- beams, interact to form a final-state X, where X could be hadrons ($q\bar{q}$) or leptons ($l\bar{l}$).

Monte Carlos were not used in these years due to statistical limitations and also the unavailability of Monte Carlo simulations for electron final-states (ie $e^+e^- \rightarrow e^+e^-e^+e^-$). However a standard Monte Carlo simulation was used for the evaluation of the two-photon background in 1993.

As the two-photon generator [38] was the only source of the calculation for the two-photon background (in 1991 and 1992), a brief description on its usage is given. The different stages in the generator are:

Generation method : The cross-section for the various $\gamma\gamma$ processes can be expressed [43] as the product of the cross-section for the process:

$$\gamma^*\gamma^* \rightarrow \text{final system}, \tag{4.4}$$

and a two-photon luminosity function. This function represents the dimensionless flux of photons which, when multiplied by the collider luminosity gives the

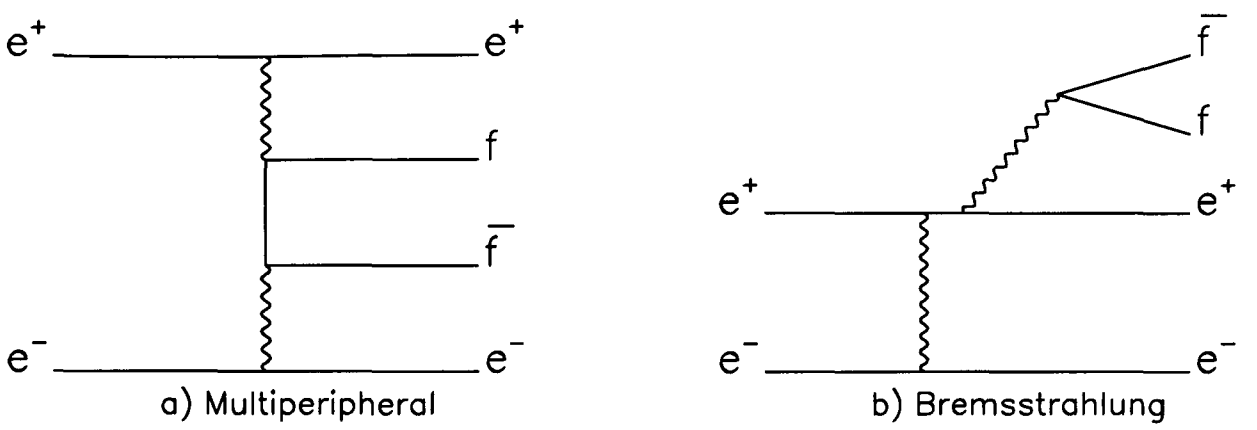

Figure 4.2: Lowest order diagrams contributing to a four-fermion final-state in e^+e^- interactions.

luminosity of the colliding virtual beams. The generation is then a two part process:

- A pair of photons is generated with a probability density approximating the luminosity function.
- Then a pair of fermions, with an invariant mass equal to the invariant mass of the pair of photons, is generated in the centre-of-mass frame and transformed to the lab frame. It is this pair of fermions which in the lab frame forms the leptonic final-state.

Hadronization : In the case of a hadronic final-state there are three models of fragmentation available:

- A Quark Parton Model (QPM) (see figure 4.3 (b)) in which the pair of photons are assumed to have a point-like QED coupling to a quark

pair which subsequently fragments (using the LUND [44] package) into hadrons. This model describes the situation accurately when there is a high momentum transfer involved, as in interactions at small distances.

- The Vector Meson Dominance Model (VDM) (see figure 4.3 (a)) in which the photons transform into virtual vector mesons (ρ, ω, ϕ, ...) which then interact strongly to produce real hadrons. This model takes over from the QPM when the momentum transfer becomes smaller. In this regime the interaction is spread over larger distances and longer times.

- A model which involves the summation of the singly (see figure 4.3 (c)) and doubly resolved (see figure 4.3 (d)) QCD processes. These are processes where one or both of the photons are resolved into their hadronic constituents and can give rise to events with three or four jets. Since the spectator jets coming from the fragments of the resolved photons will tend to go down the beam-pipe, they might escape detection, in which case the QCD processes and the QPM process will give rise to events with similar topologies.

The VDM model is applicable in the regime of low four-momentum transfer (Q^2) of the photons and low transverse momenta (less than 1 GeV/c) of the produced hadrons. In the event selection only events with a momentum greater than 3 GeV/c are selected and hence it is justified not to use the VDM model but the QPM or the QCD model in the case of hadronic final-states.

Usage : There are user-defined inputs for the generator; these are cuts on the different final-states, beam energy, and the square of the invariant mass of the final fermion system. These cuts (set to be loose) are shown in table 4.1.

Different number of events, corresponding to the same integrated luminosities for the different two-photon processes, were generated. After the generation stage, the events were subjected to the event selection criteria of table 3.5 (Chapter 3). Table 4.2 shows the results of the generation of various two-photon final-states (with user defined loose cuts) before and after applying the inclusive lepton analysis cuts. The last column in table 4.2 shows the final cross-sections for different two-photon

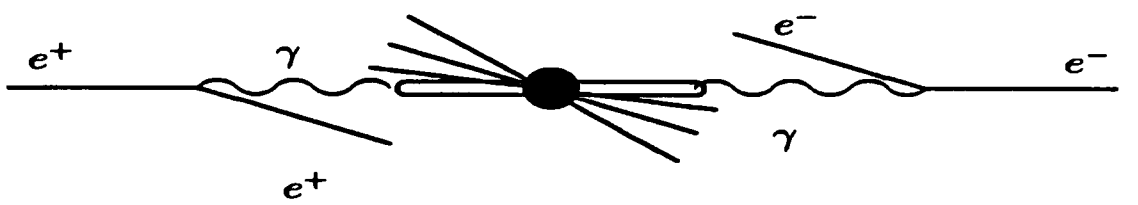

a) Nonperturbative contribution (VDM)

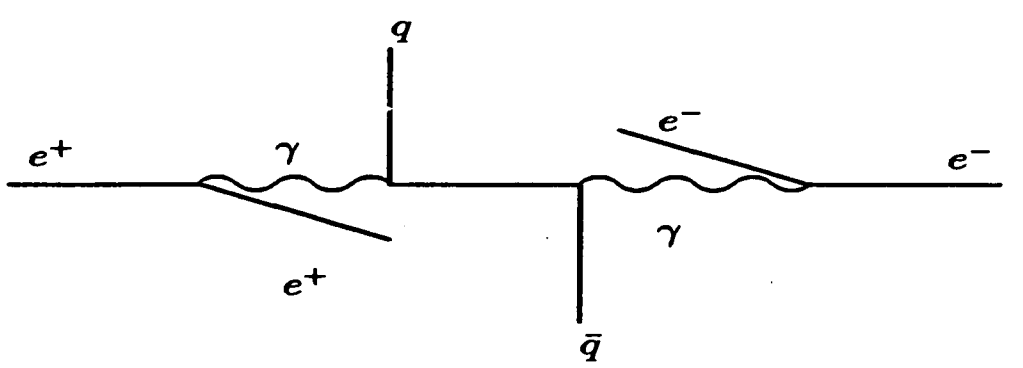

b) Direct photon contribution (QPM)

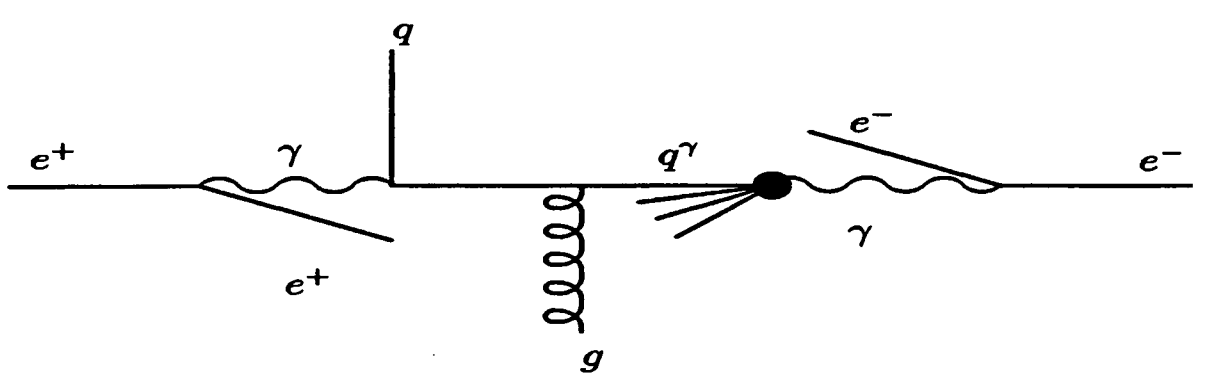

c) QCD singly resolved photon contribution

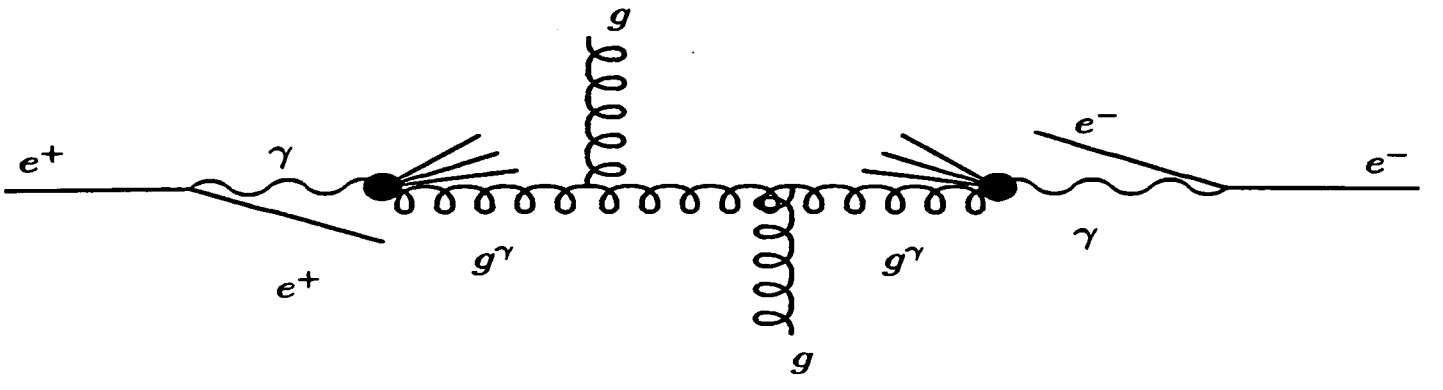

d) QCD doubly resolved photon contribution

Figure 4.3: Processes contributing [45] to the production of hadronic $q\bar{q}$ and leptonic $(l\bar{l})$ states in two-photon collisions.

Input	Cut
Beam energy	46 GeV
Polar angle range of scattered e^+ and e^-	$0^0 \leq \theta \leq 180^0$
Final-state	$e^+e^-, \mu^+\mu^-, \tau^+\tau^-, q\overline{q}$
Invariant mass squared	0.1 GeV^2

Table 4.1: The user defined inputs to the two-photon generator [38].

processes. The error on these cross-sections are of a statistical nature[2] due to the fact that there are finite number of events passing the cuts. Checks were carried

Two-photon final-state	Generated events	Passing cuts	Selected cross-section (pb)
$e^+e^-e^+e^-$	50000	267	2.56 ± 0.16
$e^+e^-\mu^+\mu^-$	100000	497	2.39 ± 0.11
$e^+e^-\tau^+\tau^-$	50000	493	0.67 ± 0.03
$e^+e^-u\overline{u}$	100000	32	0.17 ± 0.03
$e^+e^-d\overline{d}$	50000	-	-

Table 4.2: The results from the two-photon generator, [38]. The number of events generated, selected after applying the inclusive lepton analysis cuts, and the corresponding cross-section for the various final-states are shown. The errors on the cross-sections are statistical.

out to determine the final cross-section dependence on varying the beam energy and on using the QPM or the QCD models for the hadronic final-states. The only significant contribution to the cross-section from the hadronic final-states was from the $u\overline{u}$ quark pair. The cross-section for the process $e^+e- \rightarrow e^+e^-u\overline{u}$ was determined using the QPM and QCD models. The result shown in table 4.2 is an average of the two models, with a variation of approximately 0.1 pb between the models.

The beam energy was also varied to match the range of energies available at LEP. Using the results in table 4.3, it can be estimated that the average change in the cross-sections, as a function of a change in energy, is around 0.2 pb.

Summing up all the cross-sections in table 4.2 (errors added in quadrature) and also adding in quadrature the errors due to the beam energy variations (0.2 pb) and due to the variations in using the QPM or QCD models (0.1 pb), the total two-photon background (as a cross-section) is:

[2]This is not correct strictly speaking, as there are also errors associated with the treatment of the higher-order corrections to the two-photon process.

E_{beam} (GeV)	Cross-section (pb) $e^+e- \rightarrow e^+e^-\mu^+\mu^-$
44.1	2.27 ± 0.10
44.6	2.08 ± 0.09
45.1	2.13 ± 0.10
45.6	2.40 ± 0.11
46.1	2.39 ± 0.11
46.6	2.40 ± 0.11
47.1	2.36 ± 0.11

Table 4.3: The cross-sections at different energies for a $\mu^+\mu^-$ two-photon final-state. The variation of the cross-section with the beam energy can be estimated to be approximately 0.2 pb.

$$(5.9 \pm 0.3) \text{ pb}.$$

Now, to observe how this contributes at the various scan energies, this cross-section was multiplied by the total integrated luminosity (see Chapter 5) at each energy point. Table 4.4 shows the two-photon background at each energy point for the years 1991, 1992, and 1993.

Year	Energy (GeV)	# of two-photon events	# of (1-1) two-photon events	Fraction of total # of events (%)
1991	88.464	4.1	3.5	0.93 ± 0.01
	89.457	3.7	3.1	0.54 ± 0.01
	90.211	3.7	3.2	0.34 ± 0.01
	91.208	14.3	12.2	0.21 ± 0.03
	91.239	24.6	21.0	0.21 ± 0.05
	91.953	3.9	3.3	0.27 ± 0.01
	92.952	3.7	3.1	0.48 ± 0.01
	93.702	4.0	3.4	0.68 ± 0.01
1992	91.280	139.1	118.8	0.21 ± 0.03
1993	89.433	60.6	48.8	0.58 ± 0.03
	91.192	68.8	55.5	0.23 ± 0.04
	91.297	35.4	28.5	0.23 ± 0.02
	93.016	63.2	50.9	0.54 ± 0.03

Table 4.4: The number of two-photon background events for the years 1991 and 1992 calculated using a generator. Whereas the background for 1993 was calculated using Monte Carlo data. The last column shows the two-photon background as a fraction of the total number of detected events (see Chapter 5).

For the year 1993, the calculation of the two-photon background was carried out using different Monte Carlos for the different two-photon final-states. Micro-

DSTs were made of the available Monte Carlo DSTs and the event selection criteria (table 3.5, Chapter 3) applied to them. The two-photon background was calculated as the cross-section:

$$\sigma_{\mathbf{bkg}}^{\gamma\gamma} = \sigma_{\mathbf{gen}}^{\gamma\gamma} \times \frac{N_{\mathbf{sel}}^{\gamma\gamma}}{N_{\mathbf{gen}}^{\gamma\gamma}}, \tag{4.5}$$

where

- $\sigma_{\mathbf{bkg}}^{\gamma\gamma}$ is the two-photon background cross-section.
- $\sigma_{\mathbf{gen}}^{\gamma\gamma}$ represents the visible cross-section of the generated events in the MC.
- $N_{\mathbf{gen}}^{\gamma\gamma}$ is the generated number of two-photon events.
- $N_{\mathbf{sel}}^{\gamma\gamma}$ the number of events passing the cuts.

The error on this cross-section value is again statistical due to the finite number of events selected. Table 4.5 shows the final cross-sections after the event selection, for the various two-photon final-states.

It can be seen, table 4.5, that the visible cross-section for the two-photon electron final-state is larger in comparison with the other channels. This is because the Monte Carlo had been produced (by the people involved in the simulated event production) with weighted events. This meant that each event had to be taken with its proper weight before being used in the analysis.

In order to compute the cross-section for the electron two-photon final-state, the sum of the weights of the events which pass the selection criteria was calculated. Then the cross-section is computed as:

$$\sigma_{\mathbf{bkg}}^{\gamma\gamma}(e^+e^-) = 58.1 \times \frac{\text{sum\_weights}}{500000 \times \frac{\text{nev\_all}}{79336}} \tag{4.6}$$

where

- $\sigma_{\mathbf{bkg}}^{\gamma\gamma}(e^+e^-)$ is the two-photon background for $e^+e^-e^+e^-$.
- sum_weights is the sum of the weights of the events which passed the inclusive lepton selection cuts.
- nev_all is the total number of generated $(e^+e^-e^+e^-)$ events.

Summing up all the cross-sections in table 4.5 (with errors added in quadrature) the total two-photon background using 1993 Monte Carlos is:

$$(6.3 \pm 0.6) \text{ pb.}$$

Within errors this agrees with the cross-section calculated previously (using the generator). To obtain the number of events, as before the two-photon background cross-section was multiplied by the total integrated luminosity at each energy point. Table 4.4 shows the two-photon background number of events for the year 1993 (as well as 1991, and 1992 calculated using a generator).

Type of Monte Carlo	# of events on Monte Carlo	# passing cuts	Visible cross-section (nb)	Cross-section (pb) after cuts
$e^+e^-e^+e^-$	76252	2464	58.1	2.62 ± 0.56
$e^+e^-\mu^+\mu^-$	67264	131	1.28	2.49 ± 0.22
$e^+e^-\tau^+\tau^-$	9142	31	0.2685	0.91 ± 0.16
$e^+e^-q\bar{q}$	15442	7	0.7140	0.32 ± 0.12

Table 4.5: Table showing the two-photon background calculated using different Monte Carlos (1993).

4.1.2 The Hadronic Background

Even though a cut on the charged multiplicity is effective in removing most of the hadronic background, it can be seen from figure 3.2 (Chapter 3) that there is a low-multiplicity tail for the hadronic distribution. This means that a finite number of hadronic events can pass into the final event sample as leptonic events. To calculate this contamination, $q\bar{q}$ Monte Carlos were used. These were produced by generating the $q\bar{q}$ (and gluons), using the Lund Parton Shower (PS) generator [44] and then passing them through DELSIM. As these DSTs contained a large number of events, micro-DSTs were made selecting events with less than 8 charged multiplicity, and no other cuts. Applying the selection criteria, the number of events passing these cuts were recorded for each year (1991, 1992, and 1993). The hadronic background at each energy point was evaluated as:

$$N_{\mathbf{had}}^{\mathbf{bkg}} = \sigma_{\mathbf{had}} \times \mathcal{L} \times \frac{N_{\mathbf{sel}}^{q\bar{q}}}{N_{\mathbf{gen}}^{q\bar{q}}}, \tag{4.7}$$

where

- $\sigma_{\mathbf{had}}$ represents the cross-section for the process $e^+e^- \rightarrow q\bar{q}$ [39].
- $N_{\mathbf{sel}}^{q\bar{q}}$ is the number of hadronic events which passed the cuts.
- $\mathcal{L}$ is the total integrated luminosity determined at each energy point (see Chapter 5).
- $N_{\mathbf{gen}}^{q\bar{q}}$ is the total number of hadronic events on the Monte Carlo.

Table 4.6 shows the number of $q\bar{q}$ generated and written on to Monte Carlo DSTs, the number selected on to the micro-DSTs, and the number passing the event selection (same as the data).

Year	$q\bar{q}$ Monte Carlo DST ($N_{\mathbf{gen}}^{q\bar{q}}$)	$q\bar{q}$ Monte Carlo micro-DST	# passing event selection ($N_{\mathbf{sel}}^{q\bar{q}}$)
1991	151895	1749	16
1992	341751	2664	42
1993	288103	2325	36

Table 4.6: Table showing the micro-DSTs made for the $q\bar{q}$ Monte Carlo (with $<$ 8 charged multiplicity). Column 4 shows the number of hadronic events passing the event selection.

Using the $N_{\mathbf{gen}}^{q\bar{q}}$ and $N_{\mathbf{sel}}^{q\bar{q}}$ in table 4.6, the hadronic cross-section and integrated luminosities, and equation 4.7, the number of hadronic background events can be evaluated (see table 4.7). The total number of hadronic events in each year were:

- In 1991 : 26.8 hadronic events which as a fraction of the total number of detected events (Chapter 5) is (0.12 ± 0.03) %.
- In 1992 : 89.4 hadronic events which is (0.14 ± 0.02) % of the total number of events.
- In 1993 : 88.2 hadronic events which is (0.13 ± 0.01) % of the total number of events.

There is a question as to the behaviour of the $q\bar{q}$ background with energy. With increasing centre-of-mass energy there is more phase-space available, an effect which leads to an increase in the charged track multiplicities. But, due to the low statistics involved in the background calculation, the increase in the $q\bar{q}$ charged multiplicities is considered to make a negligible effect (to the calculation of this background).

Year	Energy (GeV)	# of $q\bar{q}$ events
1991	88.464	0.4
	89.457	0.7
	90.211	1.2
	91.208	7.9
	91.239	13.3
	91.953	1.7
	92.952	0.9
	93.702	0.7
1992	91.280	89.4
1993	89.433	11.5
	91.192	38.8
	91.297	20.9
	93.106	17.0

Table 4.7: The number of background hadronic ($q\bar{q}$) events for the years 1991,1992, and 1993 calculated using simulated events.

4.1.3 The Cosmic Muon Background

Cosmic rays in the DELPHI detector are characterised by tracks traversing the whole of the detector, generally not crossing the interaction region (but some do come into the interaction region). The cosmic muon events are generally 'softer' than the muons from $Z^0 \rightarrow \mu^+\mu^-$, in that they have a large momentum spread peaked towards low momenta (see figure 4.4). Under the influence of the magnetic field, these tracks can be bent and, if crossing the interaction region, fake genuine $\mu^+\mu^-$ events. The cosmic background is proportional to the data taking time and it has been evaluated from real data by counting the cosmic density (number of background events per unit area) in a region close (but different) to the interaction region.

Figure 4.5 shows the impact parameter distributions (Z_{imp} vs. R_{imp}) for two charged track events with all the event selection criteria being met except for the vertex cuts (C1 and C7 of table 3.5 Chapter 3). The interaction region can be identified as being the densely populated area and the remaining entries in the figure are the cosmic muon events which are uniformly (see figure 4.6) distributed in the figure. The first step in the determination of the cosmic background involves defining two boxes. A box around and including the interaction region, and larger

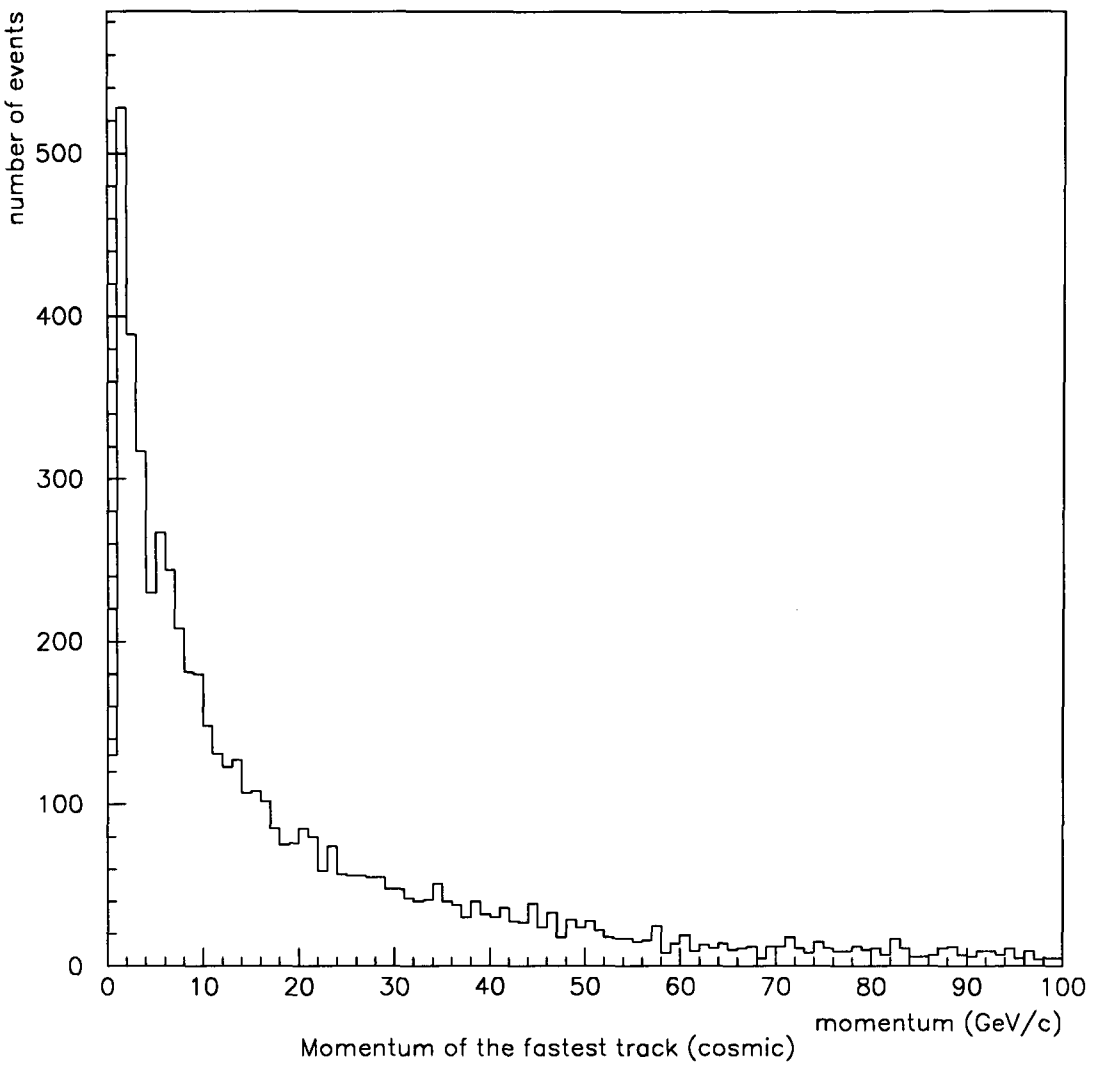

Figure 4.4: The momentum distribution of the fastest track in cosmic events. These were selected by demanding that the events lie well outside the interaction region.

box which includes the smaller box and the interaction region. The reason for using two boxes is that the subtraction of the entries in the two boxes allows the exclusion of the interaction region (that is the exclusion of genuine lepton pair candidates), and hence the determination of the cosmic muon density. This density is given by

$$\frac{\Delta N_{\rm cosm}}{\Delta A} = \frac{N_{\rm cosm}^{\rm box\ 1} - N_{\rm cosm}^{\rm box\ 2}}{A^{\rm box\ 1} - A^{\rm box\ 2}}, \tag{4.8}$$

where

- $A^{\rm box\ 1/2}$ is the area of box 1/2.
- $N_{\rm cosm}^{\rm box\ 1/2}$ is the number of cosmic muon events in box 1/2.

Once these quantities have been determined using the real data, then the cosmic background is just the cosmic muon density ($\frac{\Delta N_{\rm cosm}}{\Delta A}$) multiplied by the area

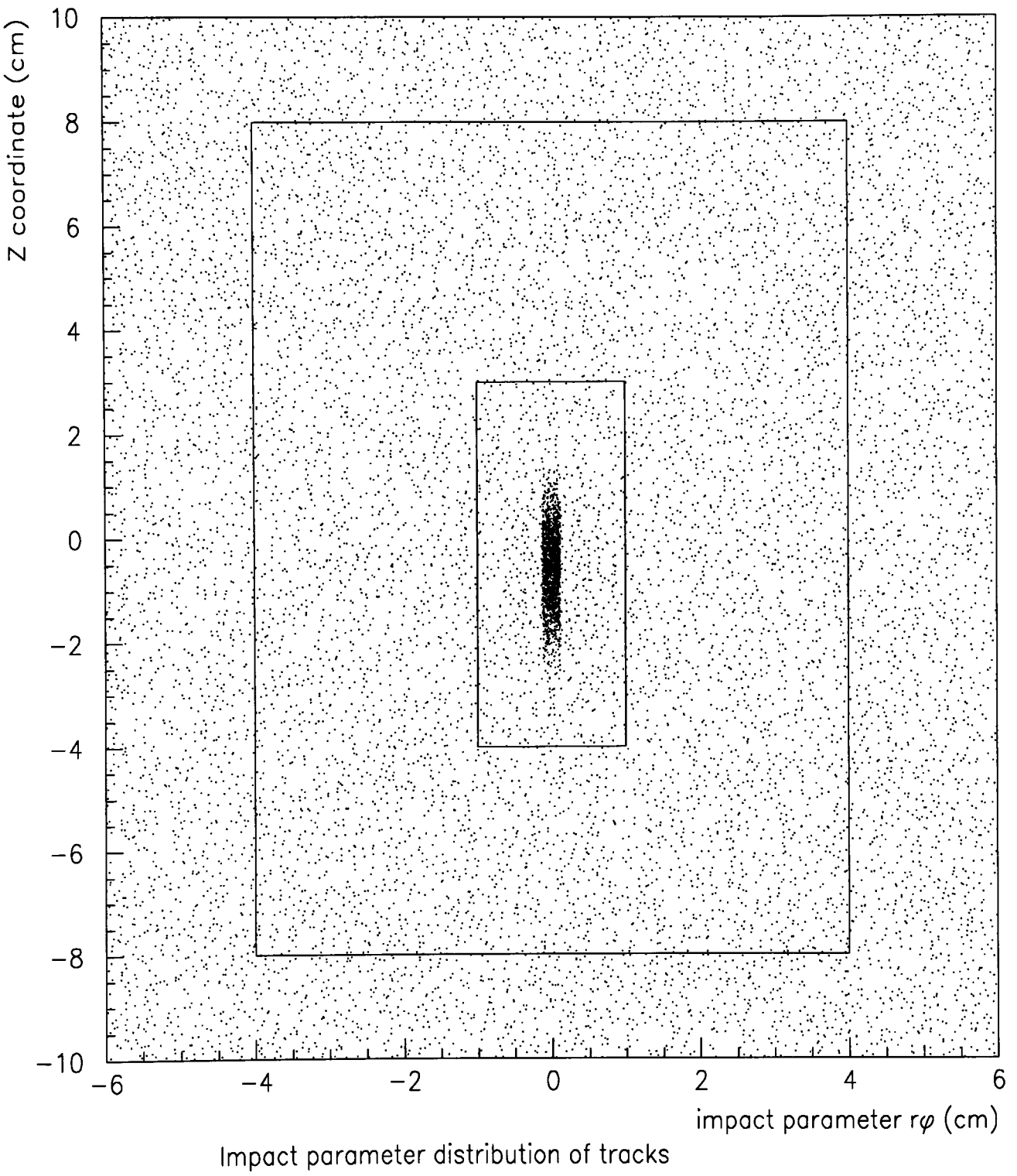

Figure 4.5: The impact parameter distribution. All cuts except the vertex cuts C1 and C7 of table 3.5. The real data can be seen as the densely populated centre of the figure and the cosmic muon background is uniformly distributed inside and outside this region. The cosmic muon density is determined by subtracting the number of entries in the two boxes (hence excluding the interaction region) and dividing by the difference in the areas (of the boxes).

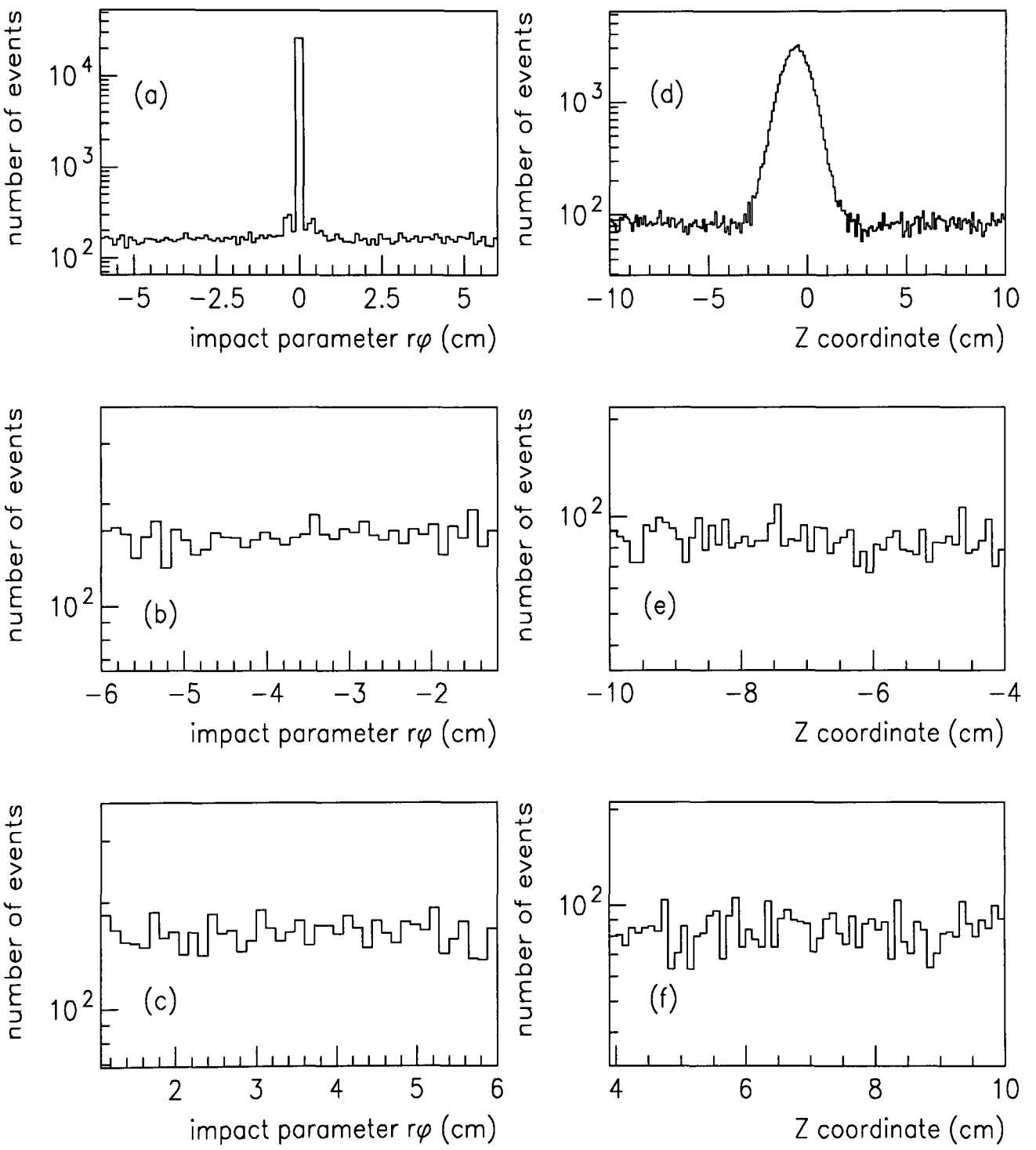

Figure 4.6: The impact parameter distributions of figure 4.5 projected onto the x-axis and the y-axis.(a) shows the projected $r\phi$ impact parameter and (b) and (c) show the same impact parameter excluding the interaction region. (d) shows the projected Z coordinate of the impact parameter and (e) and (f) show the same excluding the interaction region. From these figures it can be seen that the cosmic events are uniformly distributed.

of the acceptance region. The acceptance region is the area defined by the impact parameter cuts on $R_{\rm imp}$ and $Z_{\rm imp}$.

There is subtlety involved in this argument, in that the vertex cuts vary depending on loose cuts if the two tracks in a 1-1 topology have no VD hits and a badly reconstructed beam spot or tight cuts if there are VD hits and a well reconstructed beam spot (meaning different vertex acceptances for different classes of events). There are also two classes of cosmic muon events; 2 track cosmic muons and ≥ 3 track cosmic muons.

Cosmic background (2 tracks) : In Chapter 3 it was established that there would be different vertex acceptances for 1-1 topology events, if there were VD hits (and a well reconstructed beam spot) associated with the tracks. From table 3.4 it can be seen that for 1991, 94% of the events had VD + BS[3], in 1992 this number was 91% and in 1993 it was 96%. The quantity $\frac{\Delta N_{\rm cosm}}{\Delta A}$, the cosmic muon density (equation 4.8), was calculated from the real data for each year. Using this quantity the number of cosmic background events is given by:

$$\begin{aligned} N^{\rm bkg}_{\rm cosm} &= \left[N^{1-1}_{\rm VD} \times 4(Z_{\rm imp}\,({\rm VD}) \times R_{\rm imp}\,({\rm VD})) \times \frac{\Delta N_{\rm cosm}}{\Delta A}\right] \\ &+ \left[N^{1-1}_{\rm no\ VD} \times 4(Z_{\rm imp}({\rm no\ VD}) \times R_{\rm imp}({\rm no\ VD})) \times \frac{\Delta N_{\rm cosm}}{\Delta A}\right], \quad (4.9) \end{aligned}$$

where

- $N^{1-1}_{\rm VD}$ is the fraction of tracks with VD + BS. See above or table 3.4.
- $N^{1-1}_{\rm no\ VD}$ is the fraction of tracks with no VD + BS and is the same as (1 - N^{1-1}_{VD}).
- $\frac{\Delta N_{\rm cosm}}{\Delta A}$ is the cosmic background density.
- $4(Z_{\rm imp}({\rm VD/no\ VD}) \times R_{\rm imp}({\rm VD/no\ VD}))$ is the area defined by the vertex acceptances with/without VD + BS. The values of $Z_{\rm imp}$ and $R_{\rm imp}$ for different classes of events are given in table 3.5.

Using equation 4.9 the number of cosmic background events can be determined for 1-1 topology events (see table 4.8).

[3]where VD + BS means vertex detector hits and a well reconstructed beamspot.

Year	Cosmic bkg. density $\frac{\Delta N_{cosm}}{\Delta A}$ (events/cm^2)	Cosmic bkg. (1-1) topology N_{cosm}^{bkg} (events)	Fraction (%)
1991	22.3 ± 1.4	92.7 ± 5.9	0.40 ± 0.03
1992	52.9 ± 3.3	257.2 ± 13.8	0.39 ± 0.02
1993	69.9 ± 3.5	236.2 ± 13.2	0.35 ± 0.02

Table 4.8: The number of cosmic background events for 1-1 topology events (column 3). The error on the cosmic background density is statistical and translates into a statistical error on the final cosmic background The last column represents the number of 1-1 topology cosmics as a fraction of the total events detected in each year (see Chapter 5).

Cosmic background ($\geq$ 3 tracks) When a high momentum cosmic muon traverses the length of DELPHI there exists a finite probability for it to produce additional tracks through electromagnetic interactions . That is to say, not all cosmic muons appear as 2 track 1-1 topology events, and there can be more than 2 tracks (in an event). Hence, there is a probability for the particles from such secondary interactions to pass through the interaction region. To account for the cosmic background for such a class of events, a similar technique to the one above is employed.

For the two track cosmics, the vertex acceptance could be changed depending on the VD + BS criteria. In the final-states which have more than two tracks it is difficult to apply tight vertex acceptance as the impact parameter distribution for tau pairs has a sizeable spread (see figure 4.7). Thus the cosmic background for $\geq$ 3 tracks events is simply given by:

$$N_{cosm}^{bkg}(3+) = 4(Z_{imp} \times R_{imp}) \times \frac{\Delta N_{cosm}}{\Delta A}(3+), \tag{4.10}$$

where

- $\frac{\Delta N_{cosm}}{\Delta A}(3+)$ is the cosmic background density (defined per event) for $\geq$ 3 tracks events.
- $4(Z_{imp} \times R_{imp})$ is the acceptance region defined by the loose vertex cuts of table 3.5.

The number of cosmic background events for this class of events is shown in table 4.9

Year	Cosmic bkg. density $\frac{\Delta N_{cosm}}{\Delta A}(3+)$ (events/cm^2)	Cosmic bkg. (3+) N_{cosm}^{bkg} (events)	Fraction (%)
1991	2.7 ± 0.3	72.4 ± 8.1	0.31 ± 0.03
1992	3.0 ± 0.3	79.8 ± 9.1	0.12 ± 0.01
1993	3.1 ± 0.4	83.4 ± 9.6	0.12 ± 0.01

Table 4.9: The number of cosmic background events in the case of $\geq$3 charged tracks in the final-state. Column 4 shows the $\geq$ 3 track cosmic background as a fraction of the total number of events detected.

The cosmic background has been evaluated in the two classes; 2 track cosmic events and $\geq$3 track cosmic events. Using the final numbers in table 4.8 and 4.9 the total number of background events due to cosmic muons were calculated as being:

- For 1991 : 165.1 ± 10.0 cosmic events which as a fraction of the total number of events, is $(0.71 \pm 0.04$ %).
- For 1992 : 337.0 ± 17.0 cosmic events or $(0.52 \pm 0.03$ %).
- For 1993 : 320.0 ± 16.0 cosmic events or $(0.48 \pm 0.02$ %).

All that remains to be done is to distribute this background by luminosity (see equation 4.11).

$$N_i^{\mathrm{cosm}} = \frac{\mathcal{L}_i}{\mathcal{L}_{\mathrm{tot}}} \times N^{\mathrm{cosm}}, \tag{4.11}$$

where

- N_i^{cosm} and $\mathcal{L}_i$ are the number of cosmic muon events and luminosity respectively at energy point i.
- N^{cosm} is the total number of cosmic muons events (both 2 track and $\geq$ 3 track classes) for each year.

The total number of cosmic background events for the years 1991, 1992, and 1993 are shown in table 4.10.

4.2 Efficiencies

In order to compute the e^+e^-, $\mu^+\mu^-$, and $\tau^+\tau^-$ selection efficiencies, it is necessary to study the quality of the track reconstruction within DELPHI. As the TPC is

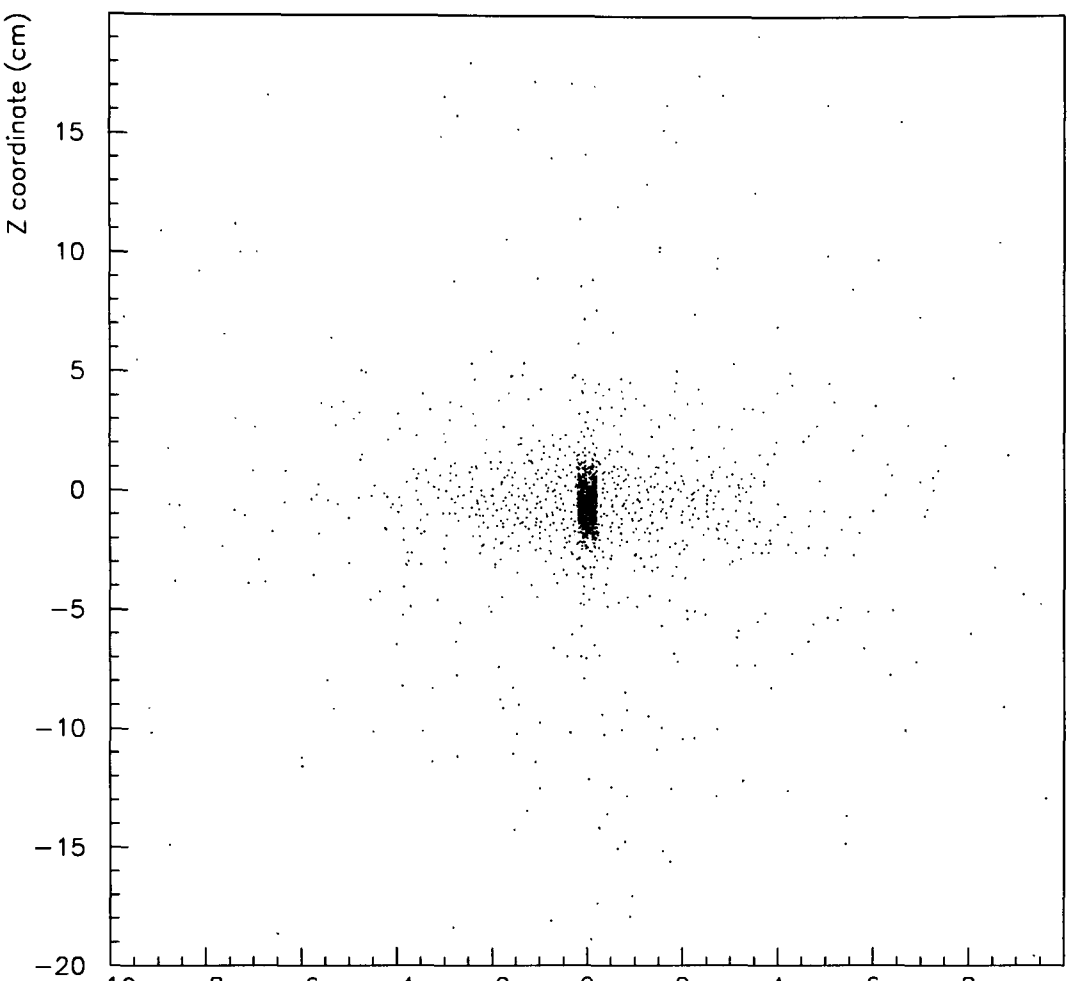

Figure 4.7: The impact parameter distribution for $\tau^+\tau^-$ Monte Carlo events. All cuts except the vertex cuts C1 and C7 of table 3.5. It can be seen that there are sizeable tails in the distribution thus making it difficult to impose tight vertex cuts for high multiplicity ($\geq$ 2 tracks) events.

the only tracking detector which is required to be fully functional (by this analysis) during data taking, it plays a major part in the track reconstruction and hence a detailed study of the TPC is necessary. The selection efficiency calculation depends on two different efficiency calculations:

- The TPC inefficiencies $\varepsilon_{\theta\phi}$. These are due to the dead zones of the TPC in θ and ϕ intervals.

- The live-space efficiencies $\varepsilon_{\text{live}}$ (TPC). This is the efficiency of detecting tracks outside the TPC θ and ϕ cracks.

The initial event selection relied heavily on charged particle tracking and in particular the TPC. Thus, calorimetry can be used to obtain e^+e^- and $\mu^+\mu^-$ pairs

Year	Energy (GeV)	# of cosmic events	# of (1-1) topology cosmic events
1991	88.464	11.1	6.2
	89.457	9.9	5.5
	90.211	9.9	5.5
	91.208	38.2	21.4
	91.239	65.8	36.8
	91.953	10.3	5.8
	92.952	9.9	5.5
	93.702	10.6	5.9
1992	91.280	337	257.2
1993	89.433	85.1	85.1
	91.192	96.6	96.6
	91.297	49.7	49.7
	93.016	88.2	65.2

Table 4.10: The number of cosmic background events as distributed by luminosity for the different years. Column 3 shows the total background whereas column 4 shows the background due to the 2 track 1-1 topology events.

from a sample of leptons. For the case of $\tau^+\tau^-$ pairs a Monte Carlo has to be used. Real data cannot be used to select a sample of taus because the separation of taus from other leptons requires cuts on the charged tracks and the event topologies (i.e the TPC has to be used). The TPC has already been used once and cannot be used again to select taus.

A tau selection based on calorimeters is difficult. Tracking detectors have to be used to remove the two potentially large backgrounds; cosmic muon events (the microvertex detector has to be used), and hadronic events (cuts on the charged multiplicities and isolation angle, both requiring the presence of tracking detectors have to be used). Also, there is a large amount of material present between the TPC and the calorimeters which can influence[4] the passage of charged tracks. Hence for taus, which have a large momentum spread, the purity of a sample selected using the calorimeters will be rather low.

4.3 The TPC Inefficiencies

Due to the design of the TPC there exists a finite probability for tracks to pass through regions which are unable to provide proper track reconstruction. There

[4]For example, only 40 % (approximately) of electrons are seen as single showers in the HPC.

are two such regions in the TPC where events can be lost; the θ 'crack' and the ϕ 'crack'[5].

4.3.1 The θ Inefficiency

The TPC has two equal length halves which are joined at $\theta = 90^0$ that is the z =0 plane. To study the loss of tracks in this region of the TPC the θ distribution of tracks was used. Events were pre-selected (selection before the main event selection of table 3.5) if:

- The fastest track in the event had a momentum $\geq$ 40 GeV/c.
- The second fastest track in the event had a momentum $\geq$ 20 GeV/c.

This pre-selection was sufficient to separate the e^+e^- and $\mu^+\mu^-$ events from the rest of the leptonic sample with reasonable purity. The $\cos\theta$ distribution of the fastest track, folded around $\cos\theta = 0$, was then plotted and a fit to a $(1 + \cos^2\theta)$ distribution was made. The reason for having a folded distribution ($0 \leq \cos\theta \leq 1$), rather than a full distribution ($-1 \leq \cos\theta \leq 1$), was to cancel out the asymmetry implicit in the full distribution. Figure 4.8 shows the folded distribution with the fitted $(1 + \cos^2\theta)$ distribution.

The fit, $(1 + \cos^2\theta)$, was carried out away from the loss region in order not to bias the outcome of the fit. The calculation of the number of expected events in the region outside the crack region ('good' region) was then done using the following method:

$$K \int_{\cos\theta=0.1}^{\cos\theta=0.7} (1 + \cos^2\theta)\, d\theta = N_{\mathbf{good}}, \tag{4.12}$$

where

- K is the constant determined from the $(1 + \cos^2\theta)$ fit.
- $N_{\mathbf{good}}$ is the number of entries in the histogram in the range $0.1 \leq \cos\theta \leq 0.7$.

The variation in the χ^2 from the $(1 + \cos^2\theta)$ fit was also used to define the θ crack region as being $0.0 \leq \cos\theta \leq 0.06$. A similar approach (to the one above) was used

[5]The use of the word 'crack' is just to imply a region where there is little or no track reconstruction in the TPC.

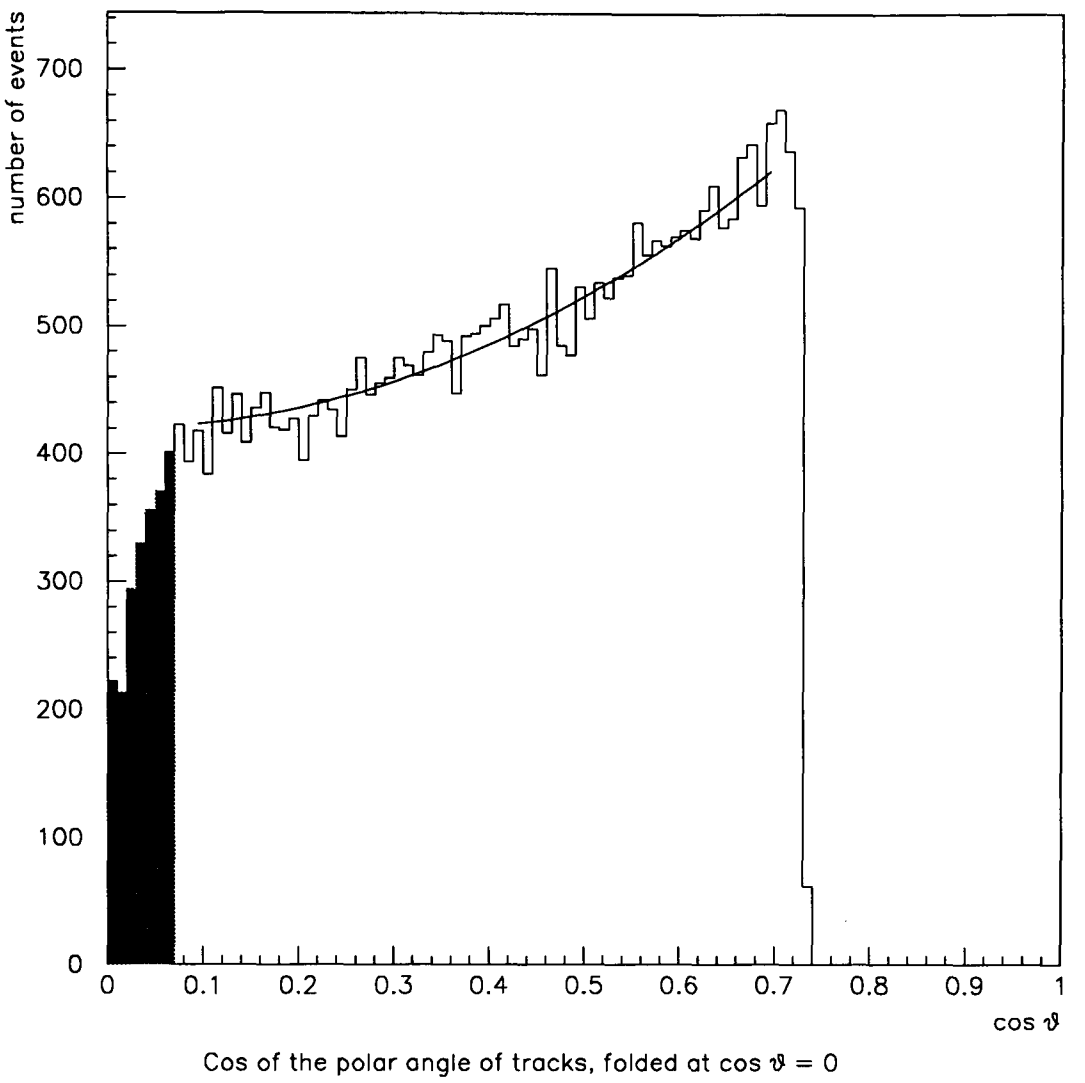

Figure 4.8: The distribution of the cosine of the polar angle θ for tracks in the event samples described in section 4.3.1. The fitted $(1 + \cos^2\theta)$ distribution is also shown. The shaded area represents the extent and the number of entries in the θ crack. This plot is for the LEP data taking period of 1993.

to predict the number of events (N_{pred}) in the crack assuming the distribution to be the same in that region, that is $(1 + \cos^2\theta)$:

$$K \int_{\cos\theta=0}^{\cos\theta=0.06} (1 + \cos^2\theta)\, d(\cos\theta) = N_{\mathrm{pred}}, \tag{4.13}$$

where the $\cos\theta = 0.06$ is the extent of the θ 'crack'. The fractional loss of events in the TPC due to the θ 'crack' is then given by:

$$\varepsilon_\theta^{\mathrm{loss}} = \frac{N_\theta^{\mathrm{pred}} - N_\theta^{\mathrm{obs}}}{(N_\theta^{\mathrm{pred}} - N_\theta^{\mathrm{obs}}) + N^{\mathrm{total}}}, \tag{4.14}$$

where

- N_θ^{pred} is the number of events predicted using a $1 + \cos^2\theta$ distribution.

- N_θ^{obs} is the number of events which are detected even though they have passed down the crack (see section 4.4).

- N^{total} is total number of entries in the histogram, which represents the number of events observed over the barrel region.

Two quantities are determined by looking into the TPC θ inefficiencies.

- $\varepsilon_\theta^{\text{loss}}$ which is the inefficiency in the TPC due to the θ crack (equation 4.14). It represents the fraction of the number of events lost in the TPC central θ region.

- $\varepsilon_{\theta-\text{in}}$ which is the efficiency for the detection of a track once it has passed down the crack. This is calculated using

$$\varepsilon_{\theta-\text{in}} = \frac{N^{\text{obs}}}{N^{\text{pred}}}. \tag{4.15}$$

The results for these quantities are shown in table 4.11.

Year	TPC θ inefficiency $\varepsilon_\theta^{\text{loss}}$	Detection efficiency $\varepsilon_{\theta-\text{in}}$
1991	(1.8 ± 0.1) %	(73.3 ± 1.5) %
1992	(2.0 ± 0.1) %	(70.7 ± 1.7) %
1993	(1.9 ± 0.1) %	(71.6 ± 0.9) %

Table 4.11: The inefficiency caused in the TPC due to the 'crack' at $\theta = 90^0$ (column 2). Column 3 shows the efficiency for the detection of events which have tracks passing down the central θ region.

4.3.2 The ϕ Inefficiency

The TPC end-plates are divided into 6 symmetric sectors in the $r\phi$ plane. These regions between sectors are insensitive to the passage of a charged track as the read-out pads are divided here. As before e^+e^- and $\mu^+\mu^-$ events were pre-selected and the ϕ distribution of the tracks in the event plotted (see figure 4.9(a)). To further emphasize the effect of the ϕ cracks the symmetry of the cracks was used and a distribution folded with a modulo of 60^0 was plotted (figure 4.9(b)). Horizontal lines were fitted to figure 4.9 on either side of the crack region, which is defined as

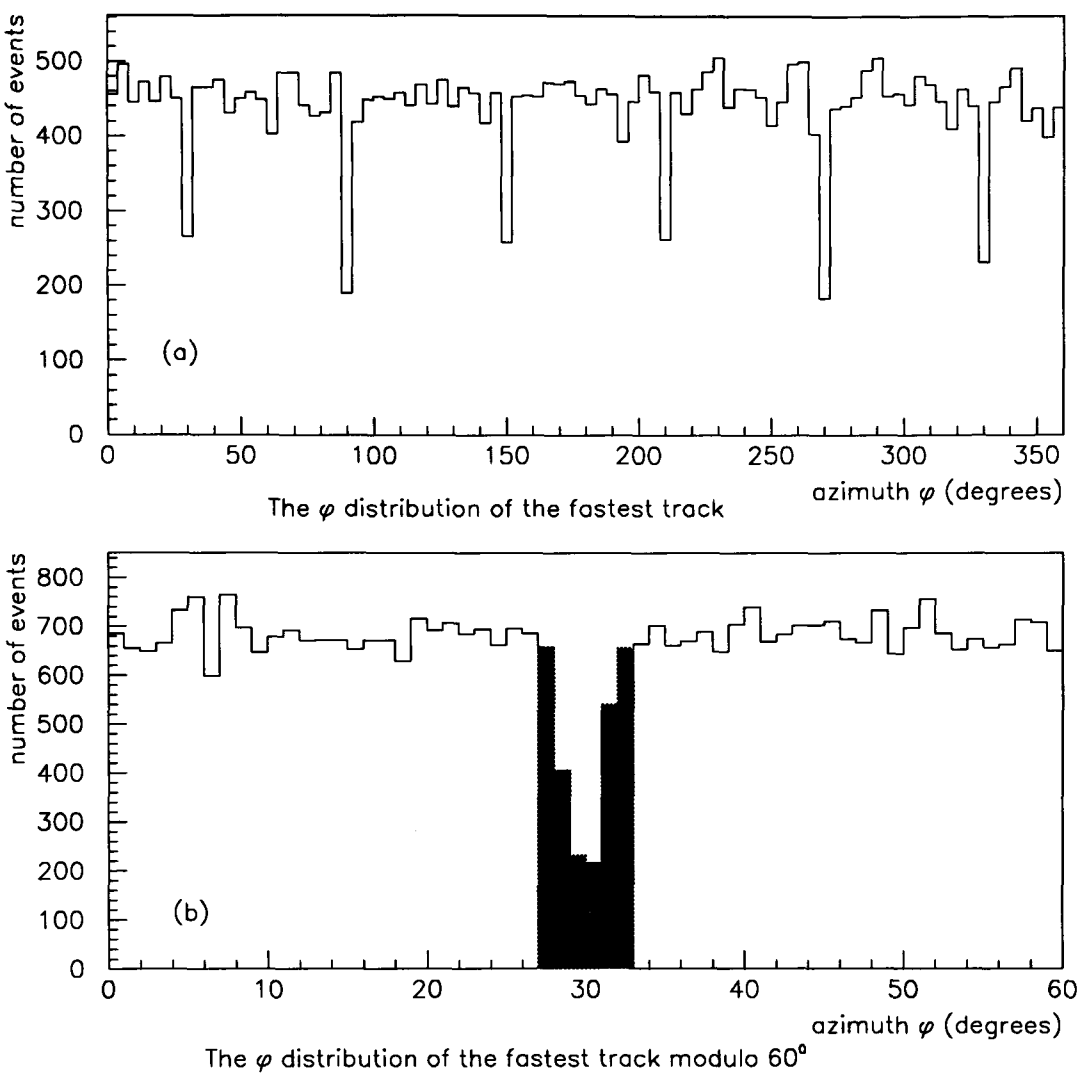

Figure 4.9: The ϕ distribution of tracks in events (a) clearly showing the cracks starting at 30^0 and recurring at intervals of 60^0. (b) shows the same plot with the cracks superimposed on top of each other. These distributions are for a θ cut of $43^0 \leq \theta \leq 137^0$. The shaded area represents the extent and the number of events in the ϕ crack region. These plots correspond to the LEP data taking period of 1993.

(30 ± 3^0), to calculate the number of events per bin. This figure was then used to predict the number of events in the central crack region. The ϕ loss is quantified (equation 4.16) in exactly the same way as equation 4.14. The loss of events due to tracks passing down the ϕ cracks is given in table 4.12:

$$\varepsilon_{\phi}^{\text{loss}} = \frac{N_{\phi}^{\text{pred}} - N_{\phi}^{\text{obs}}}{(N_{\phi}^{\text{pred}} - N_{\phi}^{\text{obs}}) + N^{\text{total}}}, \tag{4.16}$$

where

- N_{ϕ}^{pred} is the predicted number of events.
- N_{ϕ}^{obs} is the actual number of events in the ϕ 'crack'.

Year	TPC ϕ inefficiency $\varepsilon_{\phi}^{\text{loss}}$
1991	(3.23 ± 0.10) %
1992	(3.55 ± 0.10) %
1993	(3.65 ± 0.10) %

Table 4.12: The loss of events in the TPC end-plate sector boundaries (ϕ cracks). These values were calculated using 'fast' e^+e^- and $\mu^+\mu^-$ events.

- N^{total} is total number of events observed over the whole of the azimuth ϕ.

In these last two sections the effects on the loss of tracks and hence events in the TPC cracks (or areas which are insensitive to passage of charged tracks) have been investigated and quantified. It has to be noted that an entry was made to each of the histograms in figures 4.8, 4.9(a), and 4.9(b) once per event and hence the losses in θ and ϕ represent a loss in the total number of events rather than in tracks. The need for the study of correlations between loss of events and loss of tracks is excluded due to the fact that events which have either one or both of the tracks passing through the cracks will be lost (ie these events will not be present in these figures).

The next step involves the combination of the track losses due to the θ and ϕ cracks to obtain a total TPC θ/ϕ inefficiency.

4.4 Combined TPC θ/ϕ Inefficiencies

To combine the effects of the θ and ϕ cracks in the TPC, the following equation is used:

$$\varepsilon_{\theta\phi}(TPC) = \left[P^{\theta-\text{out}} \times \varepsilon^{\theta-\text{out}}(\phi)\right] + \left[P^{\theta-\text{in}} \times \varepsilon^{\theta-\text{in}}\right], \tag{4.17}$$

where

- $\varepsilon_{\theta\phi}$(TPC) is the efficiency which takes into account the loss of events due to the TPC θ and ϕ cracks.
- $P^{\theta-\text{in/out}}$ is the probability of a track lying inside/outside the θ crack.
- $\varepsilon^{\theta-\text{in}}$ is the efficiency of detecting an event which has track(s) inside the central θ region (crack).

- $\varepsilon^{\theta-\text{out}}(\phi)$ is the ϕ efficiency for events outside the θ crack and hence under the influence of the ϕ cracks.

Note that, the way the efficiencies have been combined in equation 4.17, follows from the assumption that the θ and ϕ cracks are independent. That is, once a track has passed down the ϕ cracks it will not be affected by the presence of the θ crack and vice-versa. This is discussed below.

The probability for tracks to lie inside a TPC θ crack is given (assuming a $1+\cos^2\theta$ distribution) by:

$$P^{\theta-\text{in}} = \frac{\int_{\cos\theta=0.0}^{\cos\theta=0.06}(1+\cos^2\theta)d(\cos\theta)}{\int_{\cos\theta=0.0}^{\cos\theta=0.73}(1+\cos^2\theta)d(\cos\theta)}, \tag{4.18}$$

where the numerator represents an integration over the θ crack region and the denominator an integration over the whole of the θ range available. Consequently $P^{\theta-\text{out}}$ is just $(1-P^{\theta-\text{in}})$.

$\varepsilon^{\theta-\text{in}}$, which is the detection efficiency for tracks passing down the central θ region, has been evaluated and the values for the different years are shown in table 4.11. A simple approach cannot be used for $\varepsilon^{\theta-\text{out}}(\phi)$ (which represents the effects due to the ϕ cracks on events which are outside the θ crack) as the loss of tracks in the ϕ cracks is over the entire θ range available. Hence the ϕ loss is defined as:

$$\varepsilon_{\phi}^{\text{total}} = [P^{\theta-\text{out}} \times \varepsilon^{\theta-\text{out}}(\phi)] + [P^{\theta-\text{in}} \times \varepsilon^{\theta-\text{in}}(\phi)], \tag{4.19}$$

where $\varepsilon_{\text{total}}^{\phi}$ is the loss of tracks in the ϕ cracks (see table 4.12) that is the total TPC ϕ inefficiency calculated from the data. Using the equations and quantities calculated (such as ϕ and θ inefficiencies) the TPC efficiency (which takes into account the θ and ϕ inefficiencies) can be determined (see table 4.13).

Year	Total TPC efficiency $\varepsilon_{\theta\phi}$(TPC) (%)
1991	95.62 ± 0.16
1992	95.13 ± 0.14
1993	95.07 ± 0.14

Table 4.13: The final TPC efficiency after the losses due to the cracks in θ and ϕ have been taken into account.

Two tests were carried out to study the degree of correlation between the θ/ϕ inefficiencies.

- Events were selected if they were inside the θ loss region ($88^0 \leq \theta \leq 92^0$). Studying the ϕ modulo 60 distributions it was determined that once a track had passed down the theta crack it was not affected by the inefficiencies due to the ϕ cracks (see figure 4.10(a)).

- Similarly, events were selected inside the ϕ crack ($27^0 \leq |\phi|^{60^0} \leq 33^0$) and the θ distribution for these events was studied. As before, it was found that once a track had passed through a ϕ crack it was not affected by the presence of the inefficiencies due to the θ crack (see figure 4.10(b)).

Hence, these tests have proved that the two sources of losses in the TPC, the θ and ϕ cracks, are anti-correlated. An explanation for these anti-correlated losses is based on the definition of $\varepsilon^{\theta-\mathrm{in}}$ (the efficiency for the detection of events once they passed down the θ crack), see section 4.3.1. The tracking detectors, the ID and the OD, are aligned with the TPC in such a manner that tracks passing down the TPC cracks have a finite probability of reconstruction with the use of these two detectors. As these detectors do not have cracks in line with the TPC θ and ϕ cracks, they are not affected by the TPC inefficiencies. The shaded areas in figures 4.8 and 4.9 represent the number of events which had tracks passing down the θ and ϕ crack regions, but were still reconstructed using the ID and OD.

4.5 The TPC Live-Space Efficiencies

Now that the inefficiencies in the TPC due to the dead or insensitive regions have been dealt with, a comprehensive study has to be made of the live-space efficiencies. These are the efficiencies for TPC track reconstruction within the regions outside (live regions) the θ and ϕ cracks. In the case of e^+e^- and $\mu^+\mu^-$ this was determined by searching for tracks in the hemisphere opposite to the one in which a positive identification had been made. To calculate these efficiencies, events with 1 or 2 charged tracks were selected after the run-selection (table 3.5) and the following cuts were imposed on the tracks:

- Required to be within $43^0 \leq \theta \leq 137^0$, but outside $88^0 \leq \theta \leq 92^0$ (that is excluding the θ crack of $90^0 \pm 2^0$).

- $|\phi|^{60} < 27^0$ or $|\phi|^{60} > 33^0$ (excluding the ϕ cracks).

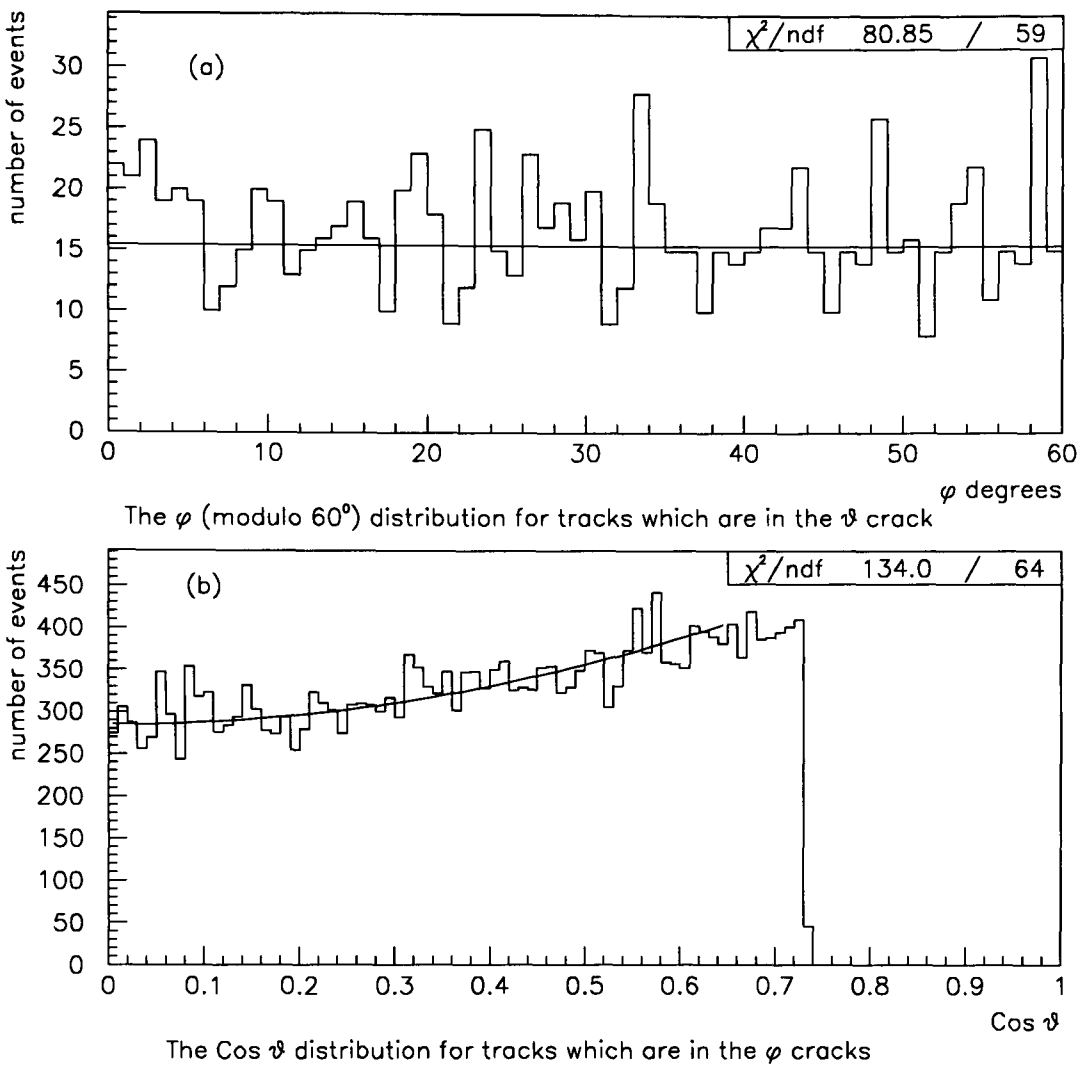

Figure 4.10: (a) : The distribution in ϕ for tracks which are in the θ crack. (b) : The distribution in $\cos\theta$ for tracks which are in the ϕ cracks. These figures validate the assumption that the losses in θ and ϕ are independent. That is to say, that once a track has gone down the θ crack it does not get affected by the presence of the ϕ cracks and vice-versa.

- The impact parameter in $r\phi$ and the Z coordinate ($R_{\mathbf{imp}}$ and $Z_{\mathbf{imp}}$) to be within 1.5 cm and 3.0 cm of the beamspot, respectively.

Now, to positively identify one of the tracks as either being an electron or a muon, tighter cuts were applied. For electrons:

- A deposit of $\geq$ 30 GeV in the barrel electromagnetic calorimeter (HPC).
- No associated muon chamber hits.
- A momentum greater than 25 GeV/c.

For muons:

- Minimal energy deposition in the HPC ($\leq$ 1 GeV).

- One or more muon chamber hits.
- Associated energy of $\leq$ 10 GeV, in the hadron calorimeter (HCAL).
- Momentum greater than 25 Gev/c.

When a track had been positively identified as an electron or a muon, then it was demanded for the other track (this would be the track in the hemisphere opposite to the one in which a positive identification was made) in the event to have a momentum greater than 5 GeV/c and an acollinearity of less than 20^0. But it has to be noted that this is not a true estimate of the efficiency, as there is an inherent loss of tracks due to the effects of the momentum and acollinearity requirements on the second track. Thus, the live-space efficiencies were scaled up by the equivalent efficiencies determined from the electron and muon Monte Carlos, in which this loss (i.e the loss due to these cuts) is negligible. Table 4.14 shows the final live-space efficiencies for e^+e^- and $\mu^+\mu^-$ events. All that remains now is to combine the TPC efficiencies

Year	Lepton pair	Live-Space data efficiency (%)	Live-space MC efficiency (%)	Combined Live-space efficiency $\varepsilon_{\text{live}}$(TPC) (%)
1991	e^+e^-	96.49 $\pm$ 0.26	97.51 $\pm$ 0.22	99.00 $\pm$ 0.39
	$\mu^+\mu^-$	98.89 $\pm$ 0.27	98.85 $\pm$ 0.24	100.00 $-$ 0.36
1992	e^+e^-	95.34 $\pm$ 0.17	96.19 $\pm$ 0.12	99.10 $\pm$ 0.20
	$\mu^+\mu^-$	96.30 $\pm$ 0.15	96.58 $\pm$ 0.15	99.70 $\pm$ 0.20
1993	e^+e^-	96.66 $\pm$ 0.14	97.18 $\pm$ 0.10	99.46 $\pm$ 0.17
	$\mu^+\mu^-$	98.55 $\pm$ 0.11	98.51 $\pm$ 0.06	100.00 $-$ 0.13

Table 4.14: The TPC live-space efficiencies as determined using the data (column 3) and Monte Carlo (column 4). Column 5 shows the combined live-space efficiencies.

(corrected for θ and ϕ cracks) and the TPC live-space efficiencies (corrected for the reconstruction inefficiencies outside the cracks and in the 'good' regions of the TPC). Using table 4.14 and table 4.13 and equation 4.20

$$\varepsilon_{\text{selec}} = \varepsilon_{\theta\phi}(TPC) \times \varepsilon_{\text{live}}(TPC), \tag{4.20}$$

the final selection efficiencies ($\varepsilon_{\text{selec}}$) are calculated and shown in table 4.15.

A check was carried out on the energy dependence of the live-space efficiencies. The TPC live-space efficiencies (determined from the data) were re-calculated in

Year	Lepton pair	Final selection efficiency $\varepsilon_{\text{selec}}$ (%)
1991	e^+e^-	94.60 ± 0.45
	$\mu^+\mu^-$	95.60 ± 0.36
1992	e^+e^-	94.27 ± 0.24
	$\mu^+\mu^-$	94.84 ± 0.24
1993	e^+e^-	94.56 ± 0.22
	$\mu^+\mu^-$	95.07 ± 0.19

Table 4.15: The final electron and muon pair efficiencies taking into account the TPC θ and ϕ cracks and the live-space losses.

the same way as above but at different centre-of-mass energies[6]. The re-calculated live-space efficiencies at the different energies (1993), shown in table 4.16, are in good agreement with the values of table 4.14 ($\varepsilon_{\text{live}}^{e^+e^-} = 96.66 \pm 0.14$ % and $\varepsilon_{\text{live}}^{\mu^+\mu^-} = 98.55 \pm 0.11$ %) justifying the assumption of energy independence (of the live-space efficiencies).

As the Monte Carlos available were for peak energies only, a check similar to the one above was not possible. Hence, the DYMU3 [36] generator was used to perform the check. Events were generated with:

- One track, with a momentum greater than 25 GeV/c, was constrained to be in the barrel region.
- The other track was required to have a momentum greater than 5 GeV/c and a maximum acollinearity of 20^0.

The number of events lost due to the cuts on the second track was observed not to vary with the energy, hence justifying the assumption of energy independence.

4.6 The Tau Efficiency

As mentioned earlier the $\tau^+\tau^-$ efficiency was determined using a Monte Carlo. A micro-DST was made of the DST Monte Carlo and the event selection applied to the real data was applied to the micro-DST. The tau pair efficiency is given by:

$$\varepsilon_{\text{MC}}^{\tau^+\tau^-} = \frac{N_{\text{sel}}^{\tau^+\tau^-}}{N_{\text{gen}}^{\tau^+\tau^-}}, \tag{4.21}$$

[6]This was done for 1993 only where statistics were sufficient to perform such a check.

Energy (GeV)	TPC live-space $\varepsilon_{\text{live}}^{\mu^+\mu^-}$ (%)	TPC live-space $\varepsilon_{\text{live}}^{e^+e^-}$ (%)
89.433	97.94 ± 0.34	96.26 ± 0.34
91.196	98.65 ± 0.15	96.77 ± 0.21
91.297	98.60 ± 0.22	96.64 ± 0.31
93.017	98.67 ± 0.23	96.77 ± 0.35

Table 4.16: The live-space efficiencies for electron and muon pair events (1993) as a function of energy. Comparing these with $\varepsilon_{\text{live}}^{e^+e^-} = 96.66 \pm 0.14$ % and $\varepsilon_{\text{live}}^{\mu^+\mu^-} = 98.55 \pm 0.11$ %, it can be seen that the assumption of energy independence of live-space efficiencies is a valid one.

where $N_{\text{gen}}^{\tau^+\tau^-}$ is the number of simulated tau pairs (on the Monte Carlo) and $N_{\text{sel}}^{\tau^+\tau^-}$ is the number selected (from the simulated events) using the inclusive lepton analysis cuts. The efficiencies evaluated using this method are shown in table 4.17.

Year	Tau efficiency $\varepsilon_{\text{MC}}^{\tau^+\tau^-}$ (%)
1991	56.16 ± 0.44
1992	58.05 ± 0.35
1993	59.17 ± 0.17

Table 4.17: The tau selection efficiencies as determined using a Monte Carlo. Note, that these efficiencies are over the whole of the solid angular range of 4π.

As can be seen from table 4.17 the tau pair efficiencies are much lower than the electron or muon pair efficiencies (see table 4.15). This is due to the fact that the tau pair efficiencies have been calculated over the whole solid angle (4π) whereas the electron and muon pair efficiencies were calculated over the barrel region. It can be seen later on (Chapter 5) that it is not necessary to know the tau pair efficiencies over the barrel region alone, nonetheless for completeness and comparison (to the electron and muon pair efficiencies) the $\tau^+\tau^-$ selection efficiency over the barrel region was evaluated.

A bin-by-bin comparison was made of the $\tau^+\tau^-$ generated in the Monte Carlo before and after the event selection. Two $\cos\theta$ distributions were plotted:

- A $\cos\theta$ distribution of $\tau^+\tau^-$ before (see figure 4.11 (a)) the event selection, that is over 4π.

- A $\cos\theta$ distribution of $\tau^+\tau^-$ after (see figure 4.11 (b)) the event selection, that is over the barrel region.

Dividing these two distributions, the resulting distribution (see figure 4.11 (c)) represents the probability of detecting, over the barrel region, $\tau^+\tau^-$ events which were generated with their initial momentum vectors within $-0.73 \leq \cos\theta \leq 0.73$.

A straight line fit was made to this distribution taking into account the central crack region, and the resulting efficiencies are shown in table 4.18. Note that the acceptance in θ for $\tau^+\tau^-$ events is not a well defined quantity due to the fact that events having initial momentum vectors outside the barrel region can decay into the barrel leading to their acceptance. Thus, the tau barrel selection efficiencies are calculated only to provide a comparison to the e^+e^- and $\mu^+\mu^-$ selection efficiencies.

Year	Tau efficiency over barrel region (%)
1991	83.30 ± 0.77
1992	86.60 ± 0.65
1993	88.37 ± 0.45

Table 4.18: The $\tau^+\tau^-$ selection efficiencies as determined using a Monte Carlo. These were determined using the method of requiring the initial momentum vector of the tau pair to fall inside the barrel region.

4.7 Data and Monte Carlo Comparison for $\tau^+\tau^-$

Any discrepancy between the Monte Carlo simulation of tau pair events and the events in the data, can result in the $\tau^+\tau^-$ efficiency, calculated from the Monte Carlo (see table 4.17), to be an over-estimate or under-estimate of the true efficiency. Two areas of possible disagreement were studied; the modelling of the TPC cracks and topology migration in the $\tau^+\tau^-$ events.

Modelling of TPC cracks. The imperfect modelling (see figure 4.12) of the track reconstruction efficiency in the area around the azimuthal TPC sector boundaries (ϕ cracks) and the θ crack leads to the calculation of a correction factor which has to be applied to the raw efficiencies (table 4.17). The combined

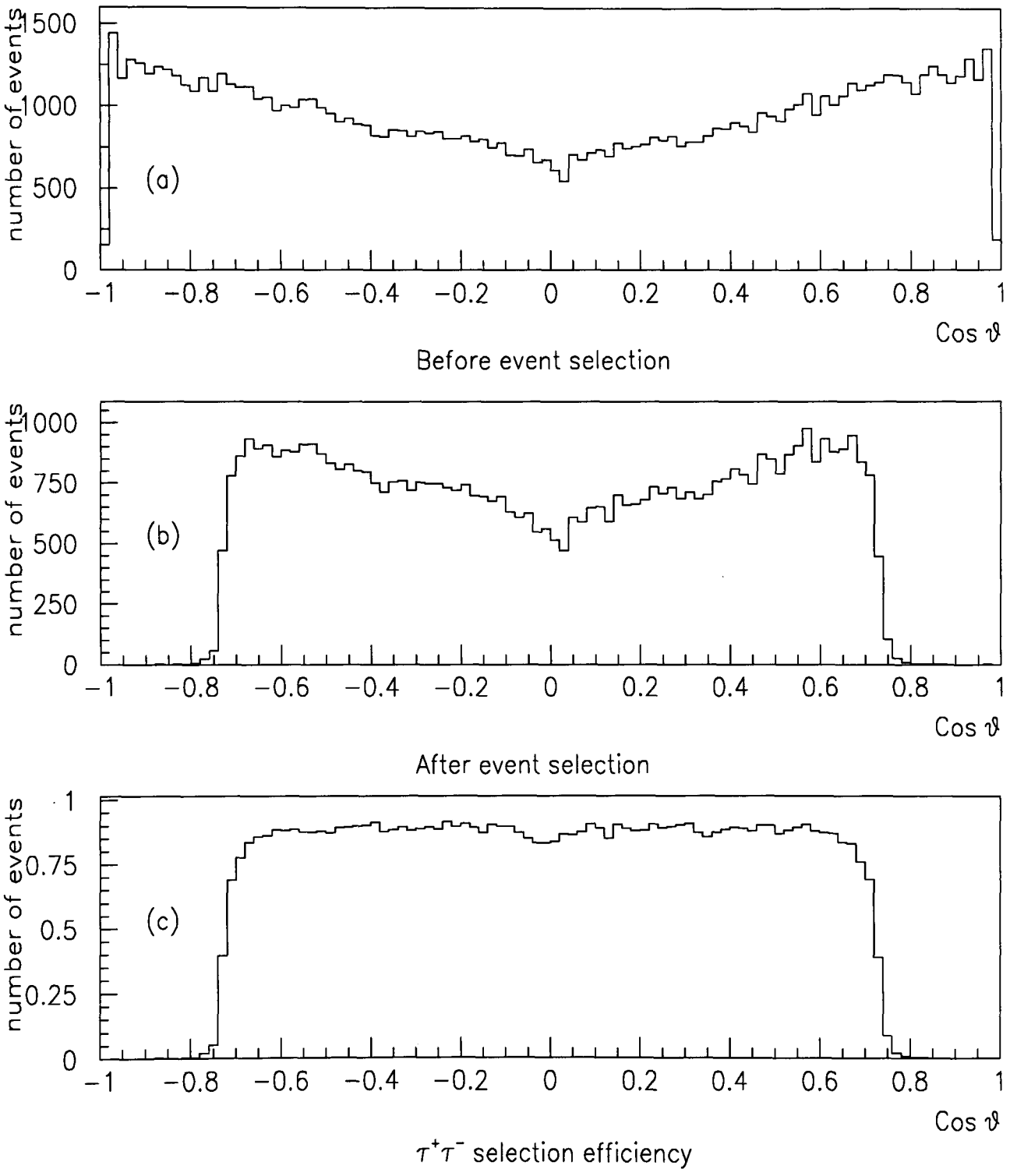

Figure 4.11: The $\tau^+\tau^-$ selection efficiency as a function of theta. (a) shows a distribution of the $\tau^+\tau^-$ over the whole solid angle before any cuts were applied and (b) shows the distribution after the event selection. Dividing (b) by (a) gives (c) which represents the probability of $\tau^+\tau^-$ detection over the barrel region.

TPC efficiency ($\varepsilon_{\rm TPC}$) , which takes into account the θ and ϕ cracks, was calculated in exactly the same manner as in section 4.4 from the data[7] and from the Monte Carlo simulation of tau pair events. The correction factor is the ratio of the $\varepsilon_{\rm TPC}$'s determined from the data and from the Monte Carlo. Table 4.19 gives this correction factor for the different years. The errors on the corrections factors are statistical due to the finite number of events involved. A similar data and Monte Carlo comparison can be found in [46].

Year	TPC correction factor $\varepsilon^{\tau^+\tau^-}_{TPC}$(corr)
1991	0.9930 ± 0.0025
1992	0.9964 ± 0.0021
1993	0.9940 ± 0.0019

Table 4.19: Table showing the correction factors for the discrepancy between data and Monte Carlo (for $\tau^+\tau^-$ events) for the modelling of the TPC θ and ϕ cracks.

Topology migration. This occurs when radiated photons convert in e^+e^- or $\mu^+\mu^-$ events[8] which increase the charged track multiplicity and hence change the topology of an event. A study was carried out to check the level of agreement between the Monte Carlo simulation and the data. Relatively pure samples of electron and muon pair events were selected using the cuts:

- Between 2 and 6 charged tracks in the final-state and
- if there were 2 charged tracks then same cuts as in section 4.5 were applied.

At the initial stage of generation, the Monte Carlo simulation of e^+e^- and $\mu^+\mu^-$ events are 1-1 topology events. The charged multiplicity distributions of the events selected (using the cuts given above) were checked to calculate the number of events not in the 1-1 topology class (and hence representing a topology migration). The same procedure was repeated for the simulated events. The ratio of these numbers (from Monte Carlo and data) gives the

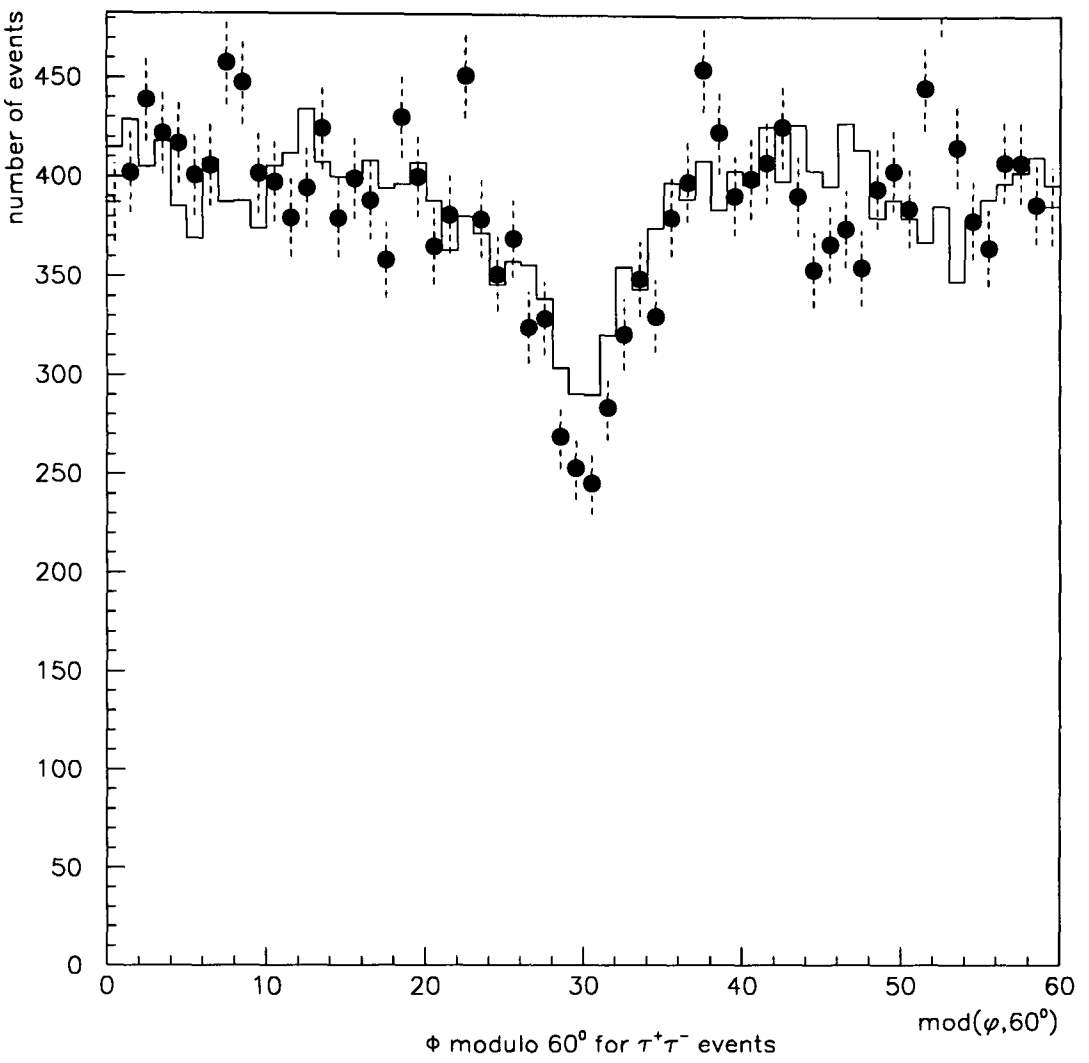

Figure 4.12: The azimuthal angular distribution of tracks in the vicinity of the TPC sector boundaries for real data (black circles) and simulation (solid line) for $e^+e^- \rightarrow \tau^+\tau^-$ events. Due to the momentum spread of the tau events the central crack region is broader than the one for the electrons and muons (see figure 4.9(b)).

level of agreement/disagreement (see table 4.20).

Topology migration, due to photon conversions, can change 1-3 or 1-1[9] topology events into 3-3 topology events, which are rejected in this analysis. This migration is an underestimate in the Monte Carlo (see table 4.20) meaning that more 3-3 events are likely to be lost in the data then in the Monte Carlo[10] (meaning that the raw tau selection efficiency is higher then expected).

[7]Note that, it has been mentioned that a selection of taus independent of the initial event selection is not possible. Hence, for this data and tau Monte Carlo comparison only 1-3 topology events were selected.

[8]The conversion of radiated photons into $\mu^+\mu^-$ events is negligible compared to the conversion into e^+e^- events.

[9]The probability of 1-1 topologies migrating to 3-3 topologies is much smaller then 1-3 migrating to 3-3 topologies.

[10]A possible explanation is a discrepancy, between data and Monte Carlo, in the modelling of the material in DELPHI before the HPC.

Leptonic channel	Migration from 1-1 topology Monte Carlo (%)	Migration from 1-1 topology data (%)	Correction factor
e^+e^-	9.04 ± 0.08	12.66 ± 0.17	1.40 ± 0.02
$\mu^+\mu^-$	2.90 ± 0.05	3.77 ± 0.09	1.30 ± 0.04

Table 4.20: The correction factors for the disagreement between the data and Monte Carlo for e^+e^- and $\mu^+\mu^-$ events. The overall correction factor is the average of the two numbers in column 4, that is 1.35 ± 0.02.

From a tau Monte Carlo sample of 91083 events, 1218 events of the rejected 3-3 topology were actually from converted photons. Thus this number, which is (1.34 ± 0.04) %, was scaled up to (1.81 ± 0.06) % using the ratio in table 4.20. This number represents the expected loss (in data) of events which had migrated from 1-1 or 1-3 topologies to a 3-3 topology. Thus the correction factor which takes into account the topology migration is

$$\begin{aligned} \varepsilon^{\tau^+\tau^-}_{\text{migra}}(\text{corr}) &= \frac{100 - (1.81 \pm 0.06)}{100 - (1.34 \pm 0.04)} \\ &= 0.9952 \pm 0.0007 \end{aligned} \tag{4.22}$$

At the level of precision in this analysis the uncertainty on the tau topological ratios (≈ 1 %) should not affect the tau selection efficiency. This is because, once a selection based on topologies, 1 vs. 1-N (where N=1-5), is made no further attempt is made to separate the different topologies and hence the uncertainty is not propagated through to the selection efficiency calculation.

All that remains now is to correct the raw tau selection efficiencies by the correction factors calculated in this section. The corrected tau efficiency is given by equation 4.23 and shown in table 4.21.

$$\varepsilon^{\tau^+\tau^-}_{\text{MC}}(\text{final}) = \varepsilon^{\tau^+\tau^-}_{\text{MC}} \times \varepsilon^{\tau^+\tau^-}_{\text{TPC}}(\text{corr}) \times \varepsilon^{\tau^+\tau^-}_{\text{migra}}(\text{corr}), \tag{4.23}$$

where

- $\varepsilon^{\tau^+\tau^-}_{\text{TPC}}(\text{corr})$ is the correction factor which takes into account the data and Monte Carlo disagreement for the modelling of the TPC sector boundaries.

- $\varepsilon^{\tau^+\tau^-}_{\text{migra}}(\text{corr})$ is the correction which accounts for the discrepancy in the data and Monte Carlo for the $\tau^+\tau^-$ topology migration effects.

Year	Tau efficiency $\varepsilon_{MC}^{\tau^+\tau^-}$ (final) (%)
1991	55.51 ± 0.51
1992	57.40 ± 0.43
1993	58.52 ± 0.30

Table 4.21: The corrected tau selection efficiency. The effects of the disagreement between data and Monte Carlo for the modelling of the TPC cracks and the topology migration have been taken into account.

4.8 The Trigger Efficiency

The lepton trigger efficiency is defined as the average of the e^+e^-, $\mu^+\mu^-$, and $\tau^+\tau^-$ trigger efficiencies, which are calculated by the groups working on the relevant lepton-identified analyses [47]. The individual trigger efficiencies are calculated by comparing independent sets of trigger components[11]. Table 4.22 shows the trigger efficiencies for the individual channels along with the average which is defined as the lepton trigger efficiency.

Year	Trigger efficiencies (%)			Average trigger efficiency (%) l^+l^-
	e^+e^-	$\mu^+\mu^-$	$\tau^+\tau^-$	
1991	$100.00\ ^{+0.0}_{-0.10}$	99.90 ± 0.10	$100.00\ ^{+0.0}_{-0.10}$	$99.97\ ^{+0.03}_{-0.06}$
1992	> 99.99	99.87 ± 0.08	99.98 ± 0.01	$99.95\ ^{+0.05}_{-0.04}$
1993	> 99.99	99.87 ± 0.08	99.99 ± 0.01	$99.95\ ^{+0.05}_{-0.04}$

Table 4.22: The individual trigger efficiencies for the three leptons families as determined by the groups working on the lepton-identified analyses. Column 5 shows the average lepton trigger efficiency used for the inclusive lepton analysis. Note, the fact that muons being the least ionizing of the three leptons gives them a smaller trigger efficiency in comparison to the other trigger efficiencies.

4.9 Chapter Summary

This chapter started off with a description and calculation of the various backgrounds which contribute to the inclusive lepton analysis. These backgrounds are: the two-photon background, the hadronic background, and the cosmic muon background.

[11] For a complete calculation of these efficiencies using various sub-triggers see [48].

The e^+e^- and $\mu^+\mu^-$ efficiencies were calculated from the data. In order to do so, the TPC inefficiencies (i.e the inefficiencies due to the dead-zones in θ and ϕ and the live-space inefficiencies) were evaluated in detail. In contrast, the $\tau^+\tau^-$ efficiencies were calculated using Monte Carlo simulations as it was difficult to select a sample of taus from the data in a manner independent of the event selection described in Chapter 3. These efficiencies were corrected for the data and Monte Carlo discrepancies in the TPC dead-zones modelling and topology migration. Finally, the trigger efficiencies were calculated as an average of the individual lepton trigger efficiencies.These had bee These had been determined by different groups working on the relevant lepton-identified analyses.

Chapter 5

Cross-Sections and Forward-Backward Asymmetries

Chapter Abstract

This chapter describes the methods used to calculate the leptonic cross-sections and forward-backward asymmetries. A detailed description is given of the various steps taken to obtain the final cross-sections and asymmetries. The associated statistical and systematic errors are also discussed and quantified.

5.1 Cross-Section Computation

In a hermetic detector (with full 4π coverage) the cross-sections can be determined using only the number of events and luminosities at each centre-of-mass energy.[1] In order to take into account the leptonic selection efficiencies, backgrounds and detector inefficiencies, the experimental cross-sections (σ^{exp}) are computed at each energy point ($\sqrt{s}$) using the following expression [50]:

$$\sigma^{\mathrm{exp}}(\mathrm{s}) = \frac{N_{\mathrm{f}} - N_{\mathrm{bkg}} - N_{\mathrm{t-chan}}}{\varepsilon_Z \mathcal{L}}(1 + f_{\delta s}), \tag{5.1}$$

where

- $\mathrm{N_f}$ represents the number of leptons selected from the real data sample.
- $\mathrm{N_{bkg}}$ is the number of background events, which includes two-photon events, hadronic events, and cosmic muon events.

[1] From here onwards the centre-of-mass energy will be referred to as the energy.

- $N_{\mathrm{t-chan}}$ is the estimated contribution from the t-channel Bhabha scattering evaluated using a semi-analytical calculation.
- ε_Z is the overall efficiency. This comprises the trigger efficiency and the leptonic selection efficiencies.
- $\mathcal{L}$ is the integrated luminosity at each energy.
- $f_{\delta s}$ is an unfolding function accounting for the energy spread of the beams.

To evaluate equation 5.1, each of the quantities was determined in a step-by-step manner.

Step 1

This involved the subtraction of the background hadronic and cosmic events according to equation 5.2:

$$N^{\mathrm{observed}} = \frac{N_{\mathrm{f}} - N_{\mathrm{cosmic}} - N_{\mathrm{hadronic}}}{\varepsilon_{\mathrm{trigger}}}, \tag{5.2}$$

where

- N_{cosmic} represents the number of cosmic background events.
- N_{hadronic} is the number of hadronic background events.
- $\varepsilon_{\mathrm{trigger}}$ is the leptonic trigger efficiency.

The cosmic and hadronic backgrounds have already been calculated and are shown in tables 4.10 and 4.7. Correcting for these backgrounds and taking into account the trigger efficiency (section 4.8), the number of leptonic events remaining are shown in table 5.1.

Step 2

The e^+e^- events due to the t-channel have to be subtracted. The decay of the Z^0 into $\mu^+\mu^-$ pairs and $\tau^+\tau^-$ pairs is via a s-channel annihilation process, whereas for the e^+e^-, as well as having the s-channel annihilation there exists the t-channel Bhabha scattering. The assumption of lepton universality in this analysis requires

Year	Energy (GeV)	Luminosity $\mathcal{L}$ $(nb)^{-1}$	Number passing cuts, N_f	Number observed $N^{observed}$
1991	88.464	711.7	440	428.5
	89.457	634.6	683	672.4
	90.211	637.8	1099	1087.9
	91.208	2462.1	6672	6625.9
	91.239	4235.8	11483	11403.9
	91.953	666.1	1440	1428.0
	92.952	634.6	763	752.2
	93.702	681.2	589	577.7
1992	91.280	24010.4	65200	64804.7
1993	89.433	9598.7	10539	10447.4
	91.192	10894.7	29610	29488.8
	91.297	5606.9	15117	15053.6
	93.016	9955.4	11769	11669.4

Table 5.1: Table showing the number of leptonic events passing the event selection (column 4) and the corresponding luminosities (column 3) and energies (column 2). The last column shows the number of leptonic events corrected for the cosmic and hadronic backgrounds and the trigger efficiency.

only s-channel processes and so the t-channel Bhabha scattering is classified as a background and has to be subtracted.

Assuming universality the number of electrons in the lepton sample is:

$$N_{e^+e^-} = \frac{\sigma(\mathrm{s+t})}{\sigma(\mathrm{s})} N_{\mu^+\mu^-/\tau^+\tau^-}, \tag{5.3}$$

which using $\frac{\sigma(\mathrm{s+t})}{\sigma(\mathrm{s})} = \mathcal{K}$ can be written[2] as:

$$N_{e^+e^-} = \mathcal{K} N_{\mu^+\mu^-/\tau^+\tau^-}, \tag{5.4}$$

where

- $N_{e^+e^-}$ represents the total number of electrons (t-channel , s-channel , and s-t channel interference).
- $N_{\mu^+\mu^-/\tau^+\tau^-}$ is the total number of s-channel muons and taus[3].
- $\sigma(\mathrm{s+t})$ and $\sigma(\mathrm{s})$ are the total s+t and s-channel cross-sections for $e^+e^- \to e^+e^-$. The ratio represented by $\mathcal{K}$ takes into account the extra e^+e^- events,

[2] See for example [51].

[3] Due to mass effects, the $Z^0 \to \mu^+\mu^-$ and $Z^0 \to \tau^+\tau^-$ cross-sections are not exactly the same. This is dealt with later on.

due to the t-channel, in the leptonic sample. Note that, these cross-sections are determined in the barrel region only.

The fraction of electrons in the sample can be denoted by equation 5.5:

$$e^+e^-_{\text{frac}} = \frac{N^{\text{observed}}_{e^+e^-}}{N^{\text{observed}}_{e^+e^-} + N^{\text{observed}}_{\mu^+\mu^-} + N^{\text{observed}}_{\tau^+\tau^-}}. \tag{5.5}$$

$N^{\text{observed}}_{\mu^+\mu^-}$ represents the number of muons as seen in DELPHI and hence this depends on the selection efficiency (see section 4.2) of the muons. Similarly $N^{\text{observed}}_{e^+e^-}$ and $N^{\text{observed}}_{\tau^+\tau^-}$ represent the numbers of electrons and taus. Hence equation 5.5 can be written as:

$$e^+e^-_{\text{frac}} = \frac{\mathcal{K}\varepsilon_{e^+e^-}}{\mathcal{K}\varepsilon_{e^+e^-} + \varepsilon_{\mu^+\mu^-} + \varepsilon_{\tau^+\tau^-}}, \tag{5.6}$$

where $\varepsilon_{e^+e^-/\mu^+\mu^-/\tau^+\tau^-}$ represents the $e^+e^-/\mu^+\mu^-/\tau^+\tau^-$ selection efficiency.

To determine this ratio, use was made of two generators; ALIBABA [52], and TOPAZ0 [53]. These programs use a semi-analytical approach to the calculation of the cross-sections and forward-backward asymmetries for e^+e^- annihilations into fermion pairs and Bhabha scattering around the Z^0 pole.

The programs have as inputs two sets of parameters; theoretical parameters and experimental parameters, which the user can modify. The choices for the theoretical parameters are shown in table 5.2 and for the experimental parameters in table 5.3.

Theoretical Parameter	Value
M_Z	91.187 GeV
m_{top}	140 GeV
m_{Higgs}	300 GeV
α(s)	0.120

Table 5.2: The theoretical input parameters for ALIBABA and TOPAZ0.

Both programs give as their output the total cross-section σ(s + t) and the s-channel cross-section σ(s) for the process $e^+e^- \rightarrow e^+e^-$. Using these, the t-channel and the s-t channel interference can be parameterized in the form of the ratio $\frac{\sigma(\text{s+t})}{\sigma(\text{s})}$. Table 5.4 shows the average value of this ratio[4] for 1991, 1992, and 1993. Special

[4]These values are used again for the subtraction of the t-channel electrons from the asymmetry sample, which will be discussed later on.

Experimental Parameter	Value
Maximum acollinearity	20^0
Min. lepton energy	3 GeV
Min. lepton angle	43^0

Table 5.3: The experimental input parameters for ALIBABA and TOPAZ0 chosen to resemble the ones in the event selection described in Chapter 3. The minimum lepton angle refers to the allowed polar angle acceptance. By definition the maximum angle would 180^0 minus this angle.

Year	Energy GeV	$\sigma(s+t)/\sigma(s)$		
		ALIBABA	TOPAZ0	Average
1991	88.464	2.4765	2.4740	2.4752
	89.457	1.8563	1.8549	1.8556
	90.211	1.4914	1.4901	1.4908
	91.208	1.1690	1.1675	1.1682
	91.239	1.1621	1.1606	1.1613
	91.953	1.0510	1.0491	1.0500
	92.952	1.0147	1.0122	1.0134
	93.702	1.0430	1.0400	1.0409
1992	91.280	1.1533	1.1518	1.1522
1993	89.433	1.8660	1.8643	1.8650
	91.192	1.1718	1.1703	1.1710
	91.297	1.1500	1.1484	1.1492
	93.016	1.0156	1.0130	1.0143

Table 5.4: The average values for the ratio $\frac{\sigma(s+t)}{\sigma(s)}$ ($\mathcal{K}$) using ALIBABA and TOPAZ0 for the years 1991, 1992, and 1993. This ratio is used to estimate the t-channel e^+e^- contribution to the leptonic event sample.

attention has to be given to the individual leptons efficiencies of equation 5.6. It can be noted from Chapter 4 that the electron and muon efficiencies as determined from the data were done so over the barrel region. That is to say, it was required that both the lepton and the anti-lepton be in the barrel region of $43^0 \leq \theta \leq 137^0$. But the tau efficiency calculated from the Monte Carlo was over the whole solid angle, 4π. Thus the electron fraction (equation 5.6) should be written as:

$$e^+e^-_{\text{frac}} = \frac{\mathcal{K}\varepsilon^{4\pi}_{e^+e^-}}{\mathcal{K}\varepsilon^{4\pi}_{e^+e^-} + \varepsilon^{4\pi}_{\mu^+\mu^-} + \varepsilon^{4\pi}_{\tau^+\tau^-}}. \tag{5.7}$$

In order to make the efficiencies correspond to the same polar angle range, two methods can be used.

- using a geometrical approach, the electron and muon efficiencies can be scaled to 4π by using the ratio defined in equation 5.8:

$$R^{\text{geom}} = \frac{\int_{\cos 43^0}^{\cos 137^0}(1+\cos^2\theta)\, d(\cos\theta)}{\int_{\cos 0^0}^{\cos 180^0}(1+\cos^2\theta)\, d(\cos\theta)}. \tag{5.8}$$

  That is to say, the electron and muon efficiencies of equation 5.7 can be scaled to 4π according to:

$$\varepsilon^{4\pi}_{e^+e^-/\mu^+\mu^-} = R^{\text{geom}}\varepsilon^{\text{barr}}_{e^+e^-/\mu^+\mu^-}, \tag{5.9}$$

  where $\varepsilon^{\text{barr}}_{e^+e^-/\mu^+\mu^-}$ are the barrel electron/muon selection efficiencies (see section 4.2). As it was required that there be at least two tracks in the barrel region, such a tightly defined acceptance region could be heavily influenced by final state radiative effects. The emission of photons through radiation by one or more of the tracks in an event can cause the event to be rejected, or even if the tracks are outside the barrel region they can fall into the acceptance region (through radiation). There are many permutations in this scenario and as the geometrical approach does not account for these, it was rejected.

- A more realistic approach is one in which the experimental cuts are taken into account. The ratio R^{geom} is redefined to be R^{gen} as in equation 5.10:

$$R^{\text{gen}} = \frac{\sigma(\text{barrel, } 3\text{GeV, } 20^0)}{\sigma(4\pi, \text{ } 3\text{GeV, } 20^0)}, \tag{5.10}$$

  where the numerator and the denominator represent the s-channel cross-sections for $e^+e^- \rightarrow e^+e^-/\mu^+\mu^-$ with cuts on the polar angle acceptance, minimum

Year	Energy GeV	Extrapolation ratio R^{gen}
1991	88.464	0.6420
	89.457	0.6424
	90.211	0.6433
	91.208	0.6434
	91.239	0.6435
	91.953	0.6442
	92.952	0.6413
	93.702	0.6382
1992	91.280	0.6433
1993	89.433	0.6423
	91.192	0.6440
	91.297	0.6440
	93.016	0.6400

Table 5.5: Table showing the ratios used to extrapolate the barrel electron and muon efficiencies to 4π.

lepton energy, and the maximum acollinearity. This ratio was determined using TOPAZ0 and the values are shown in table 5.5.

Now, the electron and muon efficiencies of equation 5.7 can be rewritten as:

$$\varepsilon^{4\pi}_{e^+e^-/\mu^+\mu^-} = R^{\text{gen}}\varepsilon^{\text{barr}}_{e^+e^-/\mu^+\mu^-}, \tag{5.11}$$

and so the electron fraction becomes:

$$e^+e^-_{\text{frac}} = \frac{\mathcal{K}\varepsilon^{\text{barr}}_{e^+e^-}}{\mathcal{K}\varepsilon^{\text{barr}}_{e^+e^-} + \varepsilon^{\text{barr}}_{\mu^+\mu^-} + \frac{\varepsilon^{4\pi}_{\tau^+\tau^-}}{R^{\text{gen}}}}. \tag{5.12}$$

Thus, the expression for the fraction of electrons in the leptonic event sample is now complete including efficiencies which are over the same polar angle range. This can be used, as shown in equation 5.13, to determine the total number of electrons in the sample,

$$N_{e^+e^-} = N^{\text{observed}} \times e^+e^-_{\text{frac}}. \tag{5.13}$$

Hence, the total number of 't-channel and s-t channel' electrons in the sample is:

$$N^{\text{t-chan}}_{e^+e^-} = N^{\text{observed}} \times e^+e^-_{\text{frac}} \times \left[1 - \frac{1}{\mathcal{K}}\right], \tag{5.14}$$

and the number of leptonic events corrected for the (t,s-t) channel (see table 5.6) is:

$$N^{\text{corr}} = N^{\text{observed}}\left[1 - e^+e^-_{\text{frac}}\left(1 - \frac{1}{\mathcal{K}}\right)\right], \tag{5.15}$$

where

- N^{corr} represents the total number of leptonic events corrected for the background events, the trigger efficiency, and the t-channel and the s-t channel interference.
- N^{observed} is the leptonic sample corrected for the hadronic and cosmic backgrounds and the trigger efficiency (see table 5.1).
- $e^+e^-_{\text{frac}}$ is the fraction of electrons in the sample.
- $\mathcal{K}$ is the ratio $\frac{\sigma(\text{s+t})}{\sigma(\text{s})}$.

Year	Energy GeV	Electron Fraction $e^+e^-_{\text{frac}}$	Number of t-channel electrons	Corrected number of leptons N^{corr}
1991	88.464	0.5626	143.6	284.9
	89.457	0.4910	152.2	520.2
	90.211	0.4367	156.4	931.5
	91.208	0.3780	360.7	6265.2
	91.239	0.3766	596.5	10807.4
	91.953	0.3534	24.1	1403.9
	92.952	0.3448	3.4	748.8
	93.702	0.3505	8.0	569.7
1992	91.280	0.3712	3182.2	61622.5
1993	89.433	0.4871	2365.4	8082.0
	91.192	0.3734	1615.5	27873.3
	91.297	0.3688	719.5	14334.1
	93.016	0.3398	56.0	11613.4

Table 5.6: Table showing the number of leptonic events after the correction for the t-channel events.

Step 3

The background due to two-photon events has to be subtracted. As there is an inherent assumption of lepton universality, this background is also assumed to be equally divided into electron, muon, and tau parts, that is to say only a third, $\frac{N_{\gamma\gamma}}{3}$ is subtracted.

The total number of either electrons or muons is:

$$N^{\text{corr}}_{e^+e^-/\mu^+\mu^-} = N^{\text{corr}} \times \frac{\varepsilon^{\text{barr}}_{e^+e^-/\mu^+\mu^-}}{\varepsilon^{\text{barr}}_{e^+e^-} + \varepsilon^{\text{barr}}_{\mu^+\mu^-} + \frac{\varepsilon^{4\pi}_{\tau^+\tau^-}}{R^{\text{gen}}}} - \frac{N_{\gamma\gamma}}{3}, \tag{5.16}$$

where

- $N^{\text{corr}}_{e^+e^-/\mu^+\mu^-}$ represents the number of e^+e^- / $\mu^+\mu^-$ after the correction for the two-photon background.
- N^{corr} is the same as above (see Step 2).
- The efficiency fraction represents the fraction of electrons or muons in the event sample. Note that, this is different to the electron fraction (equation 5.12) in that it does not have $\mathcal{K}$ because the t-channel has already been accounted for.
- $N_{\gamma\gamma}$ is the number of two-photon events (see table 4.4).

Similarly, the total number of $\tau^+\tau^-$ events is:

$$N^{\text{corr}}_{\tau^+\tau^-} = N^{\text{corr}} \times \frac{\varepsilon^{4\pi}_{\tau^+\tau^-}}{R^{\text{gen}}\varepsilon^{\text{barr}}_{e^+e^-} + R^{\text{gen}}\varepsilon^{\text{barr}}_{\mu^+\mu^-} + \varepsilon^{4\pi}_{\tau^+\tau^-}} - \frac{N_{\gamma\gamma}}{3}. \tag{5.17}$$

Thus, these represent the electrons, muons, and taus which have been corrected for all the backgrounds, the trigger efficiency, and the electron t-channel. Now, they have to be corrected for the individual selection efficiencies,

$$N^{\prime\text{corr}}_{e^+e^-} = \frac{N^{\text{corr}}_{e^+e^-}}{\varepsilon^{\text{barr}}_{e^+e^-} R^{\text{gen}}}, \tag{5.18}$$

$$N^{\prime\text{corr}}_{\mu^+\mu^-} = \frac{N^{\text{corr}}_{\mu^+\mu^-}}{\varepsilon^{\text{barr}}_{\mu^+\mu^-} R^{\text{gen}}}, \tag{5.19}$$

$$N^{\prime\text{corr}}_{\tau^+\tau^-} = \frac{N^{\text{corr}}_{\tau^+\tau^-}}{\varepsilon^{4\pi}_{\tau^+\tau^-}}. \tag{5.20}$$

And assuming universality, the number of leptons for one generation is:

$$N^{\prime\text{corr}}_{l^+l^-} = \frac{N^{\prime\text{corr}}_{e^+e^-} + N^{\prime\text{corr}}_{\mu^+\mu^-} + N^{\prime\text{corr}}_{\tau^+\tau^-}}{3}. \tag{5.21}$$

Step 4

The emission of synchrotron radiation leads to a spread in the energy of the beams and this has to be corrected for. The spread at each energy can be approximated by a gaussian of width 51.5 $\pm$ 5 MeV [19], and is taken into account by the factor $(1 + f_{\delta s})$ in equation 5.1.

The measured cross-section can be written as:

$$\sigma\ (\text{meas}) = \int [\sigma(E)G(E - E_0)]\, dE, \tag{5.22}$$

where E is the beam energy, G(E) is the gaussian distribution with a mean E_0. Using a Taylor expansion for equation 5.22, the value of $f_{\delta s}$ can be approximated to be:

$$f_{\delta s} \sim \sigma_E^2 \frac{d^2\sigma}{dE^2}, \tag{5.23}$$

where σ_E is the beam energy spread and σ is the Breit-Wigner lineshape. The values of $(1 + f_{\delta s})$ are calculated using ZFITTER, and are shown in table 5.7. This factor changes the number of leptonic events as:

$$N_{l^+l^-}^{l'\text{corr}} \times (1 + f_{\delta s}). \tag{5.24}$$

Year	Energy (Gev)	Beam energy spread $(1 + f_{\delta s})$
1991	88.464	0.9994
	89.457	0.9991
	90.211	0.9994
	91.208	1.0015
	91.239	1.0015
	91.953	1.0001
	92.952	0.9994
	93.702	0.9996
1992	91.280	1.0012
1993	89.433	0.9994
	91.192	1.0012
	91.297	1.0012
	93.016	0.9995

Table 5.7: The correction factor applied to the cross-sections, to account for the gaussian spread in the beam energy.

Step 5

There is an inherent loss of leptonic events through the application of the 3 Gev/c momentum cut on the fastest track and the 20^0 acollinearity cut. The final number of events can be corrected for this loss. Firstly, ZFITTER was used to calculate:

$$\sigma_{\text{theo}}^{\text{ZFIT}}(\text{no cuts}) = \frac{\sigma_{e^+e^-}^{\text{ZFIT}} + \sigma_{\mu^+\mu^-}^{\text{ZFIT}} + \sigma_{\tau^+\tau^-}^{\text{ZFIT}}}{3}, \tag{5.25}$$

where $\sigma_{\text{theo}}^{\text{ZFIT}}(\text{no cuts})$ represents the theoretical cross-section as calculated by ZFITTER, for leptons ($e^+e^- \rightarrow l^+l^-$) without any cuts imposed and an assumption of lepton universality. $\sigma_{e^+e^-/\mu^+\mu^-/\tau^+\tau^-}^{\text{ZFIT}}$ is the ZFITTER cross-section for the process $e^+e^- \rightarrow e^+e^-/\mu^+\mu^-/\tau^+\tau^-$. Now, to take into account the acollinearity and momentum cuts imposed in the analysis, equation 5.26 is calculated:

$$\sigma_{\text{theo}}^{\text{ZFIT}}(\text{cuts}) = \frac{\sigma_{e^+e^-}^{\text{ZFIT}}(\text{cuts}) + \sigma_{\mu^+\mu^-}^{\text{ZFIT}}(\text{cuts}) + \sigma_{\tau^+\tau^-}^{\text{ZFIT}}(\text{cuts})}{3}, \tag{5.26}$$

where $\sigma_{\text{theo}}^{\text{ZFIT}}(\text{cuts})$ is the ZFITTER theoretical cross-section for leptons with momentum (3 GeV/c) and acollinearity (20^0) cuts. Thus, the correction factor accounting for these cuts is:

$$R_{\text{cuts}}^{\text{corr}} = \frac{\sigma_{\text{theo}}^{\text{ZFIT}}(\text{no cuts})}{\sigma_{\text{theo}}^{\text{ZFIT}}(\text{cuts})}. \tag{5.27}$$

Note, that the cross-sections have already been corrected up to the full solid angle, 4π. Hence, the number of leptonic events corrected for the momentum and acollinearity cuts is:

$$N_{l^+l^-}^{\prime\text{corr}} \times (1 + f_{\delta s}) \times R_{\text{cuts}}^{\text{corr}}. \tag{5.28}$$

The values of $\sigma_{\text{theo}}^{\text{ZFIT}}(\text{no cuts})$ and $\sigma_{\text{theo}}^{\text{ZFIT}}(\text{cuts})$ and $R_{\text{cuts}}^{\text{corr}}$ are given in table 5.8. The theoretical input parameters supplied to ZFITTER for the cross-section calculation are the same as the ones supplied to ALIBABA and TOPAZ0 (see table 5.2).

Step 6

One final correction factor has to be applied. When using ZFITTER to correct for the acollinearity and momentum cuts, one also has to account for the fact that ZFITTER only constrains the anti-lepton, whereas the analysis constrains both the lepton and the anti-lepton to be in the barrel region. TOPAZ0 was used to generate cross-sections for s-channel e^+e^-, $\mu^+\mu^-$, and $\tau^+\tau^-$ events and the following ratio was determined:

$$\mathcal{B}_{\text{constr}}^{\text{track}} = \frac{\sigma\ (1 \text{ track in barrel})}{\sigma\ (2 \text{ tracks in barrel})}, \tag{5.29}$$

where

- σ (1 track in barrel) represents the cross-section for generated events which had one track in the barrel region of $43^0 \leq \theta \leq 137^0$, and

Year	Energy GeV	ZFITTER cross-sections no cuts $\sigma^{\rm ZFIT}_{\rm theo}$ (no cuts)	ZFITTER cross-sections with cuts $\sigma^{\rm ZFIT}_{\rm theo}$(cuts)	Correction factor $R^{\rm corr}_{\rm cuts}$
1991	88.464	0.2703	0.2558	1.0567
	89.457	0.5043	0.4876	1.0345
	90.211	0.8923	0.8718	1.0235
	91.208	1.4858	1.4596	1.0180
	91.239	1.4886	1.4624	1.0179
	91.953	1.2250	1.2016	1.0195
	92.952	0.7128	0.6948	1.0260
	93.702	0.5003	0.4845	1.0326
1992	91.280	1.4900	1.4638	1.0179
1993	89.433	0.4958	0.4792	1.0346
	91.192	1.4837	1.4576	1.0179
	91.297	1.4897	1.4635	1.0179
	93.016	0.6897	0.6719	1.0265

Table 5.8: The correction factors (column 5) used to scale up the number of leptonic events so that the momentum and acollinearity cuts have been accounted for. Column 3 shows the ZFITTER cross-section predictions with no cuts applied and an assumption of universality. Column 4 shows the cross-sections with cuts on the momentum (3 GeV/c) and acollinearity (20^0).

- σ (2 tracks in barrel) represents the cross-section for generated events which had two tracks in the barrel region.

The leptonic sample is corrected by scaling up the number of events using this correction factor (see table 5.9). The final numbers of leptons in the sample, after the correction for the two-photon background (Step 3), the LEP beam energy spread (Step 4), the momentum and acollinearity cuts (Step 5), and the one/two track constraint, are shown in table 5.10.

$$N'^{\rm corr}_{l^+l^-} \times (1 + f_{\delta s}) \times R^{\rm corr}_{\rm cuts} \times \mathcal{B}^{\rm track}_{\rm constr.} \tag{5.30}$$

In summary the various steps used to calculate final lepton cross-sections are:

- The backgrounds due to the cosmic and hadronic events have been subtracted and the resulting number of leptons corrected for the trigger efficiencies;
- the t-channel has been quantified, using the programs ALIBABA and TOPAZ0, and subtracted;

Year	Energy (GeV)	Constraining one or two tracks in the barrel, $B_{\text{constr}}^{\text{track}}$
1991	88.464	1.0102
	89.457	1.0060
	90.211	1.0037
	91.208	1.0028
	91.239	1.0028
	91.953	1.0041
	92.952	1.0082
	93.702	1.0122
1992	91.280	1.0028
1993	89.433	1.0061
	91.192	1.0029
	91.297	1.0030
	93.016	1.0085

Table 5.9: The correction factor applied to the cross-sections, to account for the effect of constraining two tracks or one track in the barrel region.

Year	Energy GeV	Final number of leptons $N_{l^+l^-}^{\text{corr}}$
1991	88.464	169.5
	89.457	304.0
	90.211	539.0
	91.208	3612.4
	91.239	6228.7
	91.953	809.3
	92.952	436.3
	93.702	335.2
1992	91.280	35883.8
1993	89.433	4763.5
	91.192	16116.5
	91.297	8269.6
	93.016	6848.3

Table 5.10: Table showing the final number of fully corrected leptons. These are to be divided by the corresponding luminosities at each energy point to give final inclusive lepton cross-sections.

- the e^+e^- and $\mu^+\mu^-$ efficiencies have been scaled to 4π (note that the $\tau^+\tau^-$ efficiencies were determined over 4π).
- the background due to the two-photon events has been subtracted;
- the effect of the beam energy-spread has been calculated and applied;
- ZFITTER has been used to correct for the 3 GeV/c momentum and 20^0 acollinearity cuts;
- and a final correction has been applied to account for the fact that ZFITTER constrains only one track and not two as required in the analysis.

The final cross-sections, shown in table 5.11, have been calculated by dividing the final number of leptonic events (table 5.10) at each energy point by the corresponding integrated luminosities (table 5.1). Figure 5.1 shows these cross-sections plotted against the center-of-mass energies for the various years.

To complete the cross-section calculation, it has to be mentioned that these cross-sections assume the leptons to be massless (not a valid approximation for the taus). When fitting these measured cross-sections with the theoretical expectation, ZFITTER takes into account the small but finite correction to the cross-sections due to the mass of the tau. This factor in the cross-section to account for the masses of the fermions is:

$$\sqrt{1-4\left(\frac{m_f^2}{s}\right)}, \tag{5.31}$$

where m_f is the mass of the fermion and s is the centre-of-mass energy squared. Using the mass of the tau [12], this factor is approximately 0.9992. That is to say, that the $\tau^+\tau^-$ cross-sections are scaled down by this amount to take into account the large tau mass.

5.2 Uncertainties on the Cross-Sections

5.2.1 Statistical Errors

The cross-sections at each energy point have an associated statistical error depending on the number of selected events at that point:

$$\delta\sigma^{\mathrm{corr}}(\mathrm{s}) = \sigma^{\mathrm{corr}}(\mathrm{s}) \times \frac{\sqrt{N_{\mathrm{f}}}(\mathrm{s})}{N_{\mathrm{f}}(\mathrm{s})}, \tag{5.32}$$

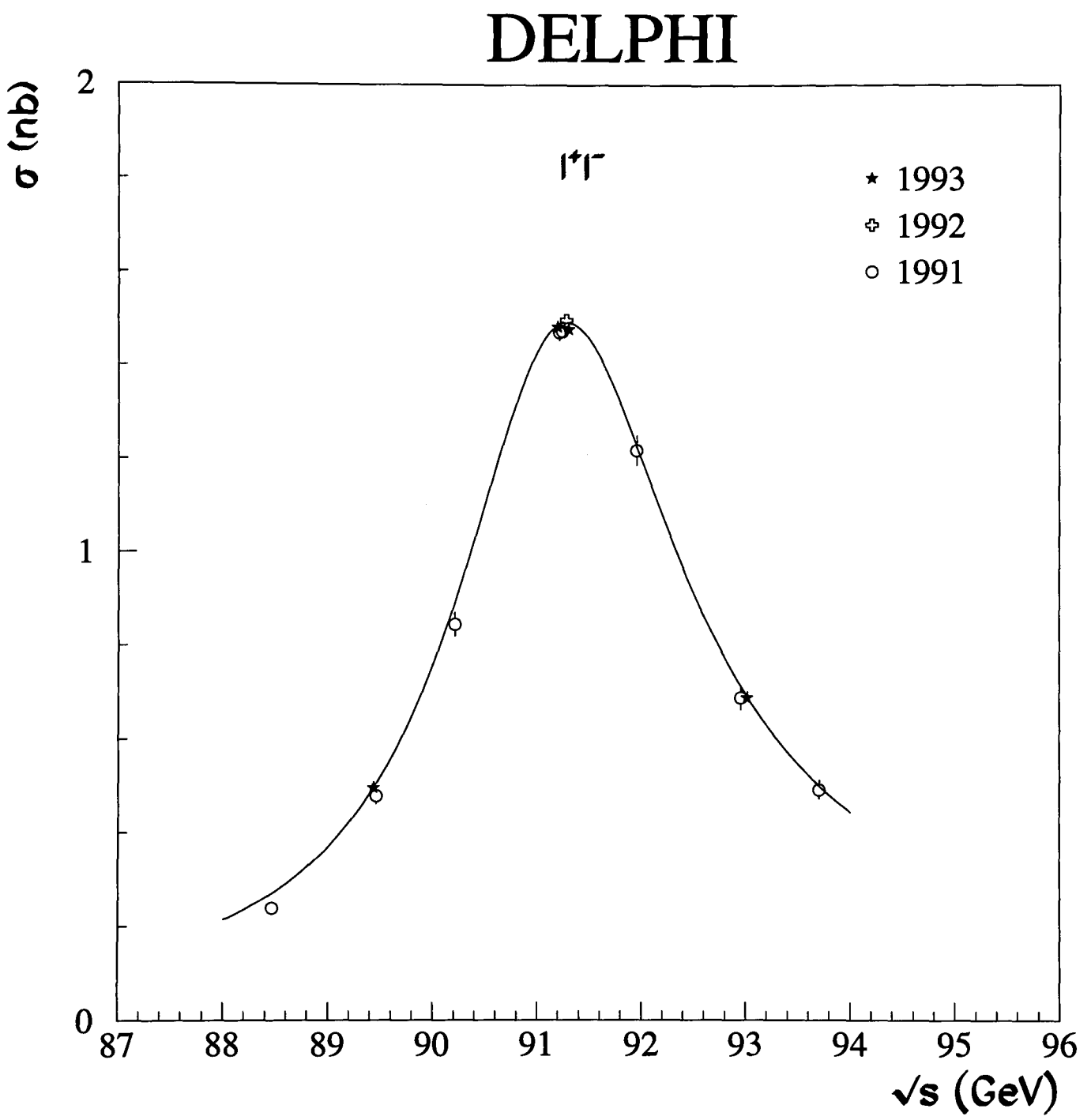

Figure 5.1: The s-channel cross-sections for leptons. These have been corrected to the full solid angle and for the cuts on the momentum and acollinearity. The curve represents the Standard Model prediction as determined using ZFITTER with $m_{\mathrm{top}} = 170$ GeV, $m_{\mathrm{Higgs}} = 300$ GeV and $M_Z = 91.187$ GeV.

Year	Energy (GeV)	Cross-section (nb)	Statistical error (nb)
1991	88.464	0.2381	0.0114
	89.457	0.4791	0.0183
	90.211	0.8451	0.0255
	91.208	1.4672	0.0180
	91.239	1.4705	0.0137
	91.953	1.2150	0.0320
	92.952	0.6875	0.0249
	93.702	0.4920	0.0203
1992	91.280	1.4945	0.0060
1993	89.433	0.4963	0.0050
	91.192	1.4793	0.0088
	91.297	1.4749	0.0122
	93.016	0.6879	0.0065

Table 5.11: The final inclusive lepton cross-sections measured in the years 1991, 1992, and 1993. The results are for one generation and are corrected to the full solid angle and for the cuts on the momentum and acollinearity.

which is

$$\delta\sigma^{\mathrm{corr}}(\mathrm{s}) = \sigma^{\mathrm{corr}}(\mathrm{s}) \times \frac{1}{\sqrt{N_{\mathrm{f}}(\mathrm{s})}}, \tag{5.33}$$

where $\sigma^{\mathrm{corr}}(\mathrm{s})$ represents the final cross-section (table 5.11) at energy point s and $N_{\mathrm{f}}(\mathrm{s})$ the number of selected leptons as in equation 5.1.

5.2.2 Systematic Errors

The possible sources of systematic errors include:

- uncertainties arising from the selection and trigger efficiencies;
- errors on the various backgrounds, that is cosmic, hadronic, and two-photon;
- various errors associated with subtraction of the t-channel events;
- an error on the absolute value of the polar angle θ;
- and errors on the total integrated luminosity.

Efficiency systematics

The trigger efficiencies shown in table 4.22 enter as an average, that is:

$$\varepsilon^{\text{trig}}_{\text{aver}} = \frac{\varepsilon^{\text{trig}}_{e^+e^-} + \varepsilon^{\text{trig}}_{\mu^+\mu^-} + \varepsilon^{\text{trig}}_{\tau^+\tau^-}}{3}, \tag{5.34}$$

and in the cross-section this value enters as:

$$F = \frac{1}{\varepsilon^{\text{trig}}_{\text{aver}}}. \tag{5.35}$$

Hence, the fractional error on F can be expressed as:

$$\frac{\delta \text{F}}{\text{F}} = \frac{1}{\left(\varepsilon^{\text{trig}}_{e^+e^-} + \varepsilon^{\text{trig}}_{\mu^+\mu^-} + \varepsilon^{\text{trig}}_{\tau^+\tau^-}\right)} \times \left[(\delta\varepsilon^{\text{trig}}_{e^+e^-})^2 + (\delta\varepsilon^{\text{trig}}_{\mu^+\mu^-})^2 + (\delta\varepsilon^{\text{trig}}_{\tau^+\tau^-})^2\right]^{\frac{1}{2}}. \tag{5.36}$$

Using equation 5.36 and the trigger efficiencies of table 4.22 , the systematic errors propagating to the final cross-sections (due to the errors on the trigger efficiencies) were estimated and are shown in table 5.12.

Year	Trigger efficiency systematic (%)
1991	0.06
1992	0.03
1993	0.03

Table 5.12: The systematic errors on the cross-sections due to the errors on the trigger efficiencies.

The electron, muon, and tau efficiencies were used to scale the cross-sections to the full solid angle. The way these enter the cross-section calculation is shown at the end of Step 3 (see equations 5.18 - 5.21). The final number of leptons for one generation (assuming universality) can be written as:

$$N'^{\text{corr}}_{l^+l^-} = \frac{N^{\text{corr}}_{l^+l^-}}{3}\left[\frac{1}{R\varepsilon_{e^+e^-}} + \frac{1}{R\varepsilon_{\mu^+\mu^-}} + \frac{1}{\varepsilon_{\tau^+\tau^-}}\right], \tag{5.37}$$

where R represents the barrel to 4π extrapolation ratio (see table 5.5) and the ε's represent the selection efficiencies (see tables 4.15 and 4.21). The fractional error on the cross-section due to the fractional error on $N'^{\text{corr}}_{l^+l^-}$ is:

$$\frac{\delta(N'^{\text{corr}}_{l^+l^-})}{N'^{\text{corr}}_{l^+l^-}} = \frac{\left[\frac{\delta^2\varepsilon_{e^+e^-}}{(R\varepsilon^2_{e^+e^-})^2} + \frac{\delta^2\varepsilon_{\mu^+\mu^-}}{(R\varepsilon^2_{\mu^+\mu^-})^2} + \frac{\delta^2\varepsilon_{\tau^+\tau^-}}{(\varepsilon^2_{\tau^+\tau^-})^2}\right]^{\frac{1}{2}}}{\frac{1}{R\varepsilon_{e^+e^-}} + \frac{1}{R\varepsilon_{\mu^+\mu^-}} + \frac{1}{\varepsilon_{\tau^+\tau^-}}}, \tag{5.38}$$

where the $\delta\varepsilon$'s represents the errors on the selection efficiencies. This equation was used to evaluate the systematic error on the cross-sections due to the errors on the selection efficiencies. The results are shown in table 5.13.

Year	Selection efficiency systematic (%)
1991	0.38
1992	0.28
1993	0.20

Table 5.13: The systematic errors on the cross-sections due to the errors on the selection efficiencies.

Background systematics

The cosmic, hadronic, and two-photon backgrounds are statistics limited and this translates into each one having a systematic uncertainty. Consider the following:

$$N_{\mathrm{bkg}} \pm \delta(N_{\mathrm{bkg}}), \tag{5.39}$$

where N_{bkg} is either of three backgrounds and $\delta(N_{\mathrm{bkg}})$ is the statistical error on the background. Now the corresponding systematic error due to the $\delta(N_{\mathrm{bkg}})$ is:

$$\frac{\delta(N_{\mathrm{bkg}})}{N_{\mathrm{f}}}, \tag{5.40}$$

where N_{f} represents the number of detected leptonic events, that is the number passing the event selection criteria.

- The two-photon background for 1991 and 1992 was determined using a generator and the error on this background was found to be, see section 4.1.1, $\pm$ 0.3 pb. Now, using the total integrated luminosities this corresponds to an uncertainty of 3 events for 1991 and 7 events for 1992. The total number of detected leptonic events for 1991 is 23169 and 65200 for 1992, and so, using equation 5.40 these translate into systematics of 0.013 % and 0.011 %.

  For 1993 a two-photon Monte Carlo was used and the error on the background was found to be $\pm$ 0.63 pb. This value being higher then the value for 1991 and 1992 because the Monte Carlo was statistics limited. The total number of events for 1993 was 67035 and $\pm$ 0.63 pb translates, using the total integrated luminosity, to be 23 events and hence the systematic error is 0.034 %.

- The hadronic background was calculated, as mentioned in section 4.1.2, by applying the leptonic event selection criteria to a sample of simulated $q\bar{q}$ events.

The error on this background arises from the low $q\bar{q}$ statistics at low charged multiplicities.

For 1991, there were a total of 151895 $q\bar{q}$ events of which 16 passed the selection criteria giving an error of $\pm$ 4 events or 25 %. The total number of hadronic events in the sample was determined to be 26.8 which gives an error of $\pm$ 6.7 events, and so using equation 5.40 the final error is $\frac{6.7}{23169}$, which is 0.029 %.

In 1992, due to the availability of a large number of generated events this error was lowered. Out of 341751 generated events, 42 passed the selection criteria meaning that the error is $\frac{1}{\sqrt{42}}$, that is 15.4 %. Therefore, for the total of 89.4 hadronic background events in 1992 the error is 13.8 events and hence the systematic uncertainty is $\frac{13.8}{65200}$, which is 0.021 %.

In 1993, at the time of writing of this thesis only 288103 $q\bar{q}$ had been processed to make a micro-DST of 2325 events, of which 36 events passed the event selection. Thus, on 88.9 background events the error is 16.67 % or 14.8 events. Hence the systematic error is $\frac{14.8}{67035}$, which is 0.022 %.

Note that, at some level there will be an additional systematic error due to the modelling of the low charged multiplicities by the $q\bar{q}$ generator (LUND Parton Shower), but this is assumed to be much smaller than the systematic errors (due to the low statistics) on the $q\bar{q}$ Monte Carlo.

- The cosmic background has been calculated in section 4.1.3. In 1991 it was found to be (165.6 $\pm$ 10.0) events which were distributed by luminosity at each energy point. The total error of $\pm$ 10 events translates into a systematic error of $\frac{10}{23169}$, which is 0.043 %. For the peak points distributing the $\pm$ 10 events gives $\pm$ 2.3 (scan peak point) and $\pm$ 4.0 (pre-scan peak point), which results in a systematic error on the peak points of 0.035 %.

  In 1992 the cosmic background was determined to be (337.0 $\pm$ 17.0) events. Using equation 5.40 the cosmic background systematic is calculated to be $\frac{17}{65200}$, which is 0.026 %.

  Like 1991, in 1993 in view of the scan, the cosmic background of (320.0 $\pm$ 16.0) events was distributed by luminosity. On peak the systematic uncertainty was found to be 0.016 % and the overall error of $\pm$ 16 events means a systematic error of 0.024 %.

The systematic errors due to the two-photon, hadronic, and cosmic backgrounds are given in table 5.14

Year	Two-photon background (%)	Hadronic background (%)	Cosmic background (%)
1991	0.013	0.029	0.035
1992	0.011	0.021	0.026
1993	0.034	0.022	0.017

Table 5.14: The systematic errors on the background events for the different years. Note that the cosmic background errors refer to the peak points.

Errors related to the t-channel subtraction

The ratio $\frac{\sigma(s+t)}{\sigma(s)}$ was determined using two different generators, and it enters the cross-section calculation (see equation 5.15) as:

$$N^{\text{corr}} = N^{\text{observed}} \left[1 - e^+e^-_{\text{frac}} \left(1 - \frac{1}{\mathcal{K}}\right)\right], \tag{5.41}$$

where N^{corr} represents the number of leptonic events corrected for the background events, N^{observed} represents the number of leptonic events passing the event selection and $e^+e^-_{\text{frac}}$ is the electron fraction. Now, the systematic error on the cross-sections due to an error on $\mathcal{K}$ is the fractional error on N^{corr}:

$$\frac{\delta N^{\text{corr}}}{N^{\text{corr}}} = \frac{e^+e^-_{\text{frac}}}{\mathcal{K}^2\left[1 - e^+e^-_{\text{frac}}\left(1 - \frac{1}{\mathcal{K}}\right)\right]}\delta\mathcal{K}. \tag{5.42}$$

There are two sources of error on $\mathcal{K}$; an error due to the intrinsic accuracy of the generators (that is the theoretical errors on the cross-sections predicted by the generators), and an error due to the difference in the cross-sections determined using the generators.

The two different generators gave different values of $\mathcal{K}$ due to the different theoretical approaches adopted (by the generators) for the calculation of the cross-sections for the process $e^+e^- \rightarrow e^+e^-$. Evaluating the error on the difference (between the two generators), $\delta\mathcal{K}$, and substituting it into equation 5.42 gives an estimate of the systematic error. The systematic error evaluated in this way was found to be 0.03 % on the peak energy points, with a maximum value of approximately 0.07 % off-peak points.

The incomplete treatment of the higher order effects for the process $e^+e^- \rightarrow e^+e^-$ lead to theoretical errors on the cross-sections determined using ALIBABA and TOPAZ0. In order to take these into account, the error on the ratio $\frac{\sigma(s+t)}{\sigma(s)}$ has to be computed. The fractional error on this ratio can be written [54] as:

$$\frac{\delta\mathcal{K}}{\mathcal{K}} = \left[\left(\frac{\delta\sigma(s+t)}{\sigma(s+t)}\right)^2 + \left(\frac{\delta\sigma(s)}{\sigma(s)}\right)^2 - 2\rho\left(\frac{\delta\sigma(s+t)}{\sigma(s+t)}\right)\left(\frac{\delta\sigma(s)}{\sigma(s)}\right)\right]^{\frac{1}{2}}, \qquad (5.43)$$

where

- $\frac{\delta\mathcal{K}}{\mathcal{K}}$ represents the fractional error on $\mathcal{K}$.
- $\frac{\delta\sigma(s+t)}{\sigma(s+t)}$ represents the fractional error on the s+t channel cross-sections as quoted by the authors of ALIBABA and TOPAZ0.
- $\frac{\delta\sigma(s)}{\sigma(s)}$ represents the error on the s-channel cross-sections.
- The last term represents the correlation between the errors on the cross-sections $\sigma(s+t)$ and $\sigma(s)$ and ρ is the correlation coefficient.

Theoretical error : TOPAZ0. The theoretical errors on the cross-sections of TOPAZ0 [55] are shown in table 5.15.

Channel σ	Peak Points %	Off-peak Points %
s-channel	0.2	0.3
s+t channel	0.3	0.5

Table 5.15: The theoretical errors assigned to the on-peak and off-peak cross-sections calculated using TOPAZ0.

The correlation coefficient, ρ, can have values of -1 (errors are anti-correlated), 0 (errors are uncorrelated) and 1 (errors are fully correlated). Assuming that the correlation is positive, i.e $0 \leq \rho \leq 1$, the most conservative assumption (i.e the one which gives the largest errors) for ρ would be $\rho = 0$. Using this value of ρ and the values in table 5.15 and substituting them into equation 5.42, the error propagated to the final cross-section due to the theoretical errors (on the TOPAZ0 cross-sections) can be calculated. These values were estimated to be:

- for the peak points: 0.12 %.

Source of of error	On-peak error (%)	Off-peak error (%)
ALIBABA and TOPAZ0 difference in cross-sections	0.03	0.07
Theoretical error on TOPAZ0	0.12	0.22
Theoretical error on ALIBABA	0.19	-

Table 5.16: The systematic errors on the final cross-sections due to the theoretical errors on the cross-sections calculated using ALIBABA and TOPAZ0. Note that, the authors of ALIBABA do not quote theoretical errors associated with the off-peak cross-sections.

- for the off-peak points: a maximum value of 0.22 %.

Theoretical error : ALIBABA. The theoretical error on the cross-sections predicted by ALIBABA [56] are given below:

$$\frac{\delta\sigma(\mathrm{s}+\mathrm{t})}{\sigma(\mathrm{s}+\mathrm{t})} = 0.5\%, \tag{5.44}$$

and

$$\frac{\delta\sigma(\mathrm{s})}{\sigma(\mathrm{s})} = 0.4\%, \tag{5.45}$$

where both these errors are for the cross-sections predicted by ALIBABA on-peak[5]. Using a similar approach as above and $\rho = 0.2$, the error propagated to the final cross-sections due to the theoretical errors (on the cross-sections determined using ALIBABA) was estimated to be 0.19 %.

The errors related to the t-channel subtraction are shown in table 5.16.

It has to be noted that all these errors are correlated to some degree as they originate from the same source, this source being the incomplete treatment of higher order effects in the cross-sections computation in ALIBABA and TOPAZ0. Adopting a conservative approach, it was decided to assign a systematic error of 0.19 % to the final cross-section.

Uncertainties due to variations in m_{top} and m_{Higgs}

Various corrections were made using ALIBABA, TOPAZ0 and ZFITTER. A study was made of the dependence of the cross-sections predicted by these programs (and hence the corrections made to the inclusive lepton analysis cross-sections) on the

[5]The authors only quote theoretical errors, with the associated correlations, for the cross-sections on the peak energy points.

theoretical input parameters of table 5.2. The masses of the top quark and the Higgs boson were varied as shown below:

- The values used for m_{Higgs} were: 60 GeV/c^2 and 1000 GeV/c^2.
- The values used for m_{top} were: 140 GeV/c^2 and 270 GeV/c^2.

Negligible deviations were observed, hence no systematic error was assigned the final cross-sections.

Uncertainties on the polar angle

The polar angle θ is determined using a full vertex fit to each track. If there is an uncertainty in the determination of θ then it will appear as an error in the extrapolation of the cross-sections from the barrel region to the full solid angle.

Using a geometrical approach the cross-section with an angular cut at θ_1 is given by:

$$S_{\text{cut}} = \int_{\cos\theta_{-1}}^{\cos\theta_1} (1 + \cos^2\theta) d(\cos\theta), \tag{5.46}$$

and the cross-section with no angular cuts is given by:

$$S_{\text{total}} = \int_{-1}^{1} (1 + \cos^2\theta) d(\cos\theta), \tag{5.47}$$

Now, these two cross-sections enter the analysis as the ratio:

$$Y = \frac{S_{\text{cut}}}{S_{\text{total}}}, \tag{5.48}$$

for the barrel to 4π extrapolation. Now, if θ_1 varies then the change in the ratio Y due to a change in θ_1 is:

$$\delta(Y) = \frac{3}{4}(1 + \cos\theta_1^2) d(\cos\theta_1). \tag{5.49}$$

Now, for a polar angle cut of 43^0 (0.75 rad) and a shift in θ of < 0.3 mrad [57], gives a geometrical uncertainty on the ratio Y of 0.020 %.

In an experimental approach, the cut on the polar angle was changed by $\pm$ 0.3 mrad and the change in the number of selected events was observed to be approximately 0.022 %

Error on the integrated luminosity

The total integrated luminosities for the years 1991, 1992, and 1993 were determined using a combination of the SAT and VSAT detectors. The errors on the luminosity measurements using these detectors arise from:

- the limited number of small angle Bhabha events leading to finite statistical errors;
- and various systematic errors (see table 5.17). The theoretical error comes from the generators used[6] to simulate small angle Bhabha events. The experimental error has various sources [39] but the largest errors come from the uncertainty on the definition of the acceptance regions of the SAT and VSAT and the cut on the energy of the detected Bhabha events.

Year	Theoretical error on luminosity (%)	Experimental error on luminosity (%)	Combined error (%)
1991	0.30	0.50	0.60
1992	0.25	0.39	0.46
1993	0.25	0.28	0.38

Table 5.17: The errors associated with the luminosity measurements in the various years.

The systematic errors on the final cross-sections are shown in table 5.18.

5.3 Asymmetry Computation

To select a sample of leptonic events for a forward-backward asymmetry analysis, the same event selection criteria, shown in table 3.5, are used. The only difference is that for an asymmetry analysis no knowledge of the integrated luminosities is required and hence the cut on the luminosity (cut R3) is relaxed.

The asymmetry can be determined using two methods:

Counting method In this method, counting the number of events gives the asymmetry in a restricted angular range

$$A_{\mathrm{FB}} = \frac{\sigma_{\mathrm{F}}^{\mathrm{corr}} - \sigma_{\mathrm{B}}^{\mathrm{corr}}}{\sigma_{\mathrm{F}}^{\mathrm{corr}} + \sigma_{\mathrm{B}}^{\mathrm{corr}}}, \tag{5.50}$$

[6] In 1991 two generators were used; BHLUMI [26] and BABAMC [25]. For 1992 and 1993 BHLUMI was used.

Source of systematic error	Year		
	1991 (%)	1992 (%)	1993 (%)
Selection efficiencies	0.38	0.28	0.20
Trigger efficiencies	0.06	0.03	0.03
Two-photon background	0.013	0.011	0.034
Hadronic background	0.029	0.021	0.022
Cosmic background	0.035	0.026	0.017
t-channel subtraction	0.20	0.20	0.20
Variations in $m_{\rm top}$ and $m_{\rm Higgs}$	-	-	-
Uncertainty on the polar angle	0.02	0.02	0.02
Final total	0.44	0.35	0.29

Table 5.18: The systematic errors on the final inclusive lepton cross-sections.

where $\sigma_{\rm F}(\sigma_{\rm B})$ represents the cross-section corrected for inefficiencies and backgrounds with $\cos\theta > 0 (< 0)$. And so in terms of the number of events

$$A_{\rm FB} = \frac{N_{\rm F}^{\rm corr} - N_{\rm B}^{\rm corr}}{N_{\rm F}^{\rm corr} + N_{\rm B}^{\rm corr}}. \tag{5.51}$$

Maximum likelihood fit It can be noted from Chapter 1 that the differential cross-section for the process $e^+e^- \rightarrow l^+l^-$ is given by:

$$\frac{d\sigma}{d\Omega} = F(\mathrm{s})(1 + \cos^2\theta) + G(\mathrm{s})\cos\theta, \tag{5.52}$$

where the $\cos\theta$ term represents the asymmetry in the production of leptons between the forward and backward hemispheres. In this method, at each energy point, a fit is made to the theoretical angular distributions of the leptons, equation 5.52, and compared against the observed distribution. Thus the probability of an event having a particular value of $\cos\theta$ is represented by p_i:

$$p_i(r) = \mathrm{N}(1 + \cos^2\theta_i + r(\mathrm{s})\cos\theta_i), \tag{5.53}$$

where i is the i'th event, s is the centre-of-mass energy, N is a normalization constant and r is the ratio

$$r(\mathrm{s}) = \frac{G(\mathrm{s})}{F(\mathrm{s})}. \tag{5.54}$$

The likelihood $\mathcal{L}$ can be defined as the product of p_i for all the events

$$\mathcal{L}(r) = \prod_{i=1}^{n} p_i, \tag{5.55}$$

where for any specific value of r, $\mathcal{L}$ is the probability density for obtaining the particular set of $\cos\theta$ that are observed experimentally. In the final step, $\mathcal{L}$ is maximized as a function of r in order to find the best value of r:

$$\mathcal{LL} = \log \mathcal{L} = \sum_{i=1}^{n} \log p_i \tag{5.56}$$

Even though this method is more accurate than the counting method, the counting method was preferred. This is because, with the use of the likelihood method there will be complications when the t-channel asymmetry has to be subtracted.

Similar to the cross-section calculation a step-by-step method was adopted for the asymmetry determination.

Step 1

Following the asymmetry event selection[7] the θ at each energy for both positive (see figure 5.2(a)) and negative tracks (see figure 5.2(b))was plotted. Taking into account the fact that there is a 'crack' at $\theta = 90^0$, the number of events in the forward hemisphere and the backward hemisphere were calculated leading to 'raw' values of asymmetries. An average was taken of the uncorrected asymmetries from positive tracks and negative tracks and this was repeated at each energy point.

The raw negative track asymmetry is given by:

$$A^{-}_{\mathrm{FB}}(\mathrm{uncorr}) = \frac{N^{-}_{\mathrm{F}} - N^{-}_{\mathrm{B}}}{N^{-}_{\mathrm{F}} + N^{-}_{\mathrm{B}}}, \tag{5.57}$$

and the raw positive track asymmetry is:

$$-A^{+}_{\mathrm{FB}}(\mathrm{uncorr}) = \frac{N^{+}_{\mathrm{F}} - N^{+}_{\mathrm{B}}}{N^{+}_{\mathrm{F}} + N^{+}_{\mathrm{B}}}, \tag{5.58}$$

The number of events in the forward(backward) hemispheres, $N_{\mathrm{F}}(N_{\mathrm{B}})$, the uncorrected positive and negative asymmetries, and the average uncorrected asymmetries are shown in table 5.19

[7]This is exactly the same as the cross-section event selection (table 3.5) except that there is no requirement for a minimum luminosity and only events with two charged tracks are selected.

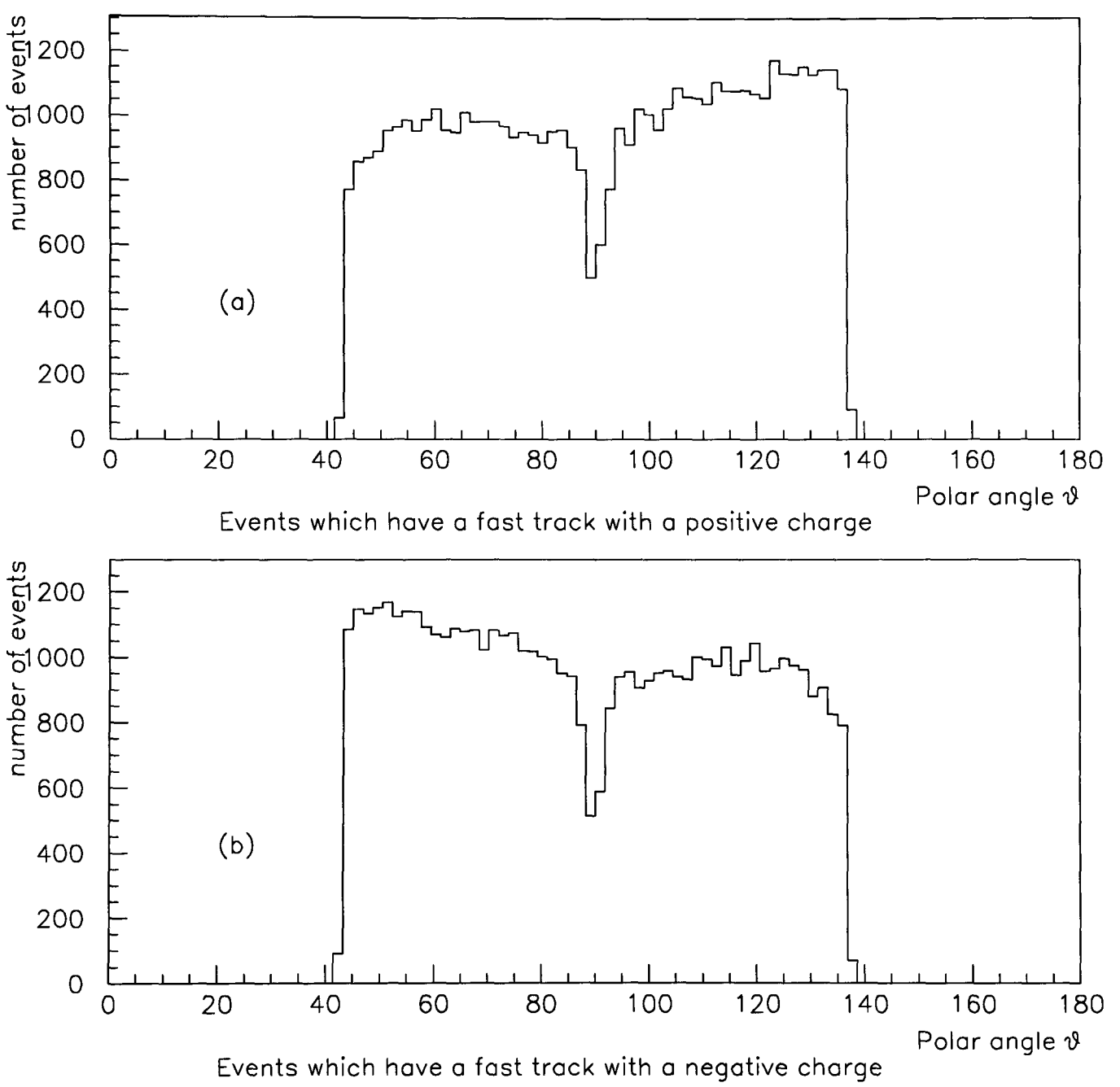

Figure 5.2: The polar angle distributions for the fastest positive and fastest negative tracks in the leptonic sample selected for the asymmetry analysis. Both figures are for 1-1 topology events and correspond to the on-peak data of 1992.

Year	Energy GeV	Lepton N_F^-	Lepton N_B^-	Anti-Lepton N_F^+	Anti-Lepton N_B^+	A_{FB}^- uncorr.	A_{FB}^+ uncorr.	A_{FB}^{ave} uncorr.
1991	88.464	185	138	138	185	0.1455	0.1455	0.1455
	89.457	273	233	231	279	0.0791	0.0941	0.0866
	90.211	448	397	394	453	0.0604	0.0697	0.0650
	91.208	2711	2394	2394	2711	0.0621	0.0621	0.0621
	91.239	4649	4059	4054	4654	0.0678	0.0689	0.0683
	91.953	590	497	497	592	0.0856	0.0872	0.0864
	92.952	334	254	253	333	0.1361	0.1365	0.1363
	93.702	238	203	207	240	0.0794	0.0738	0.0766
1992	91.280	26681	23703	23656	26671	0.0591	0.0599	0.0595
1993	89.433	4563	3732	3732	4572	0.1002	0.1012	0.1007
	91.192	12041	10828	10832	12055	0.0530	0.0534	0.0532
	91.297	6073	5608	5612	6078	0.0398	0.0399	0.0398
	93.016	4877	4058	4057	4892	0.0917	0.0933	0.0925

Table 5.19: Columns 3-6 show the number of tracks in the forward and backward hemisphere for leptons and anti-leptons, columns 7-8 the corresponding asymmetries and column 9 the average asymmetry, no corrections have been applied.

Step 2

A correction for the backgrounds has to be made. The hadronic background is negligible as it is of high (> 2) charged multiplicities, but the two-photon and cosmic background have to be subtracted. It has to be noted that both the cosmic and two-photon backgrounds have no asymmetries and this has an effect of lowering the asymmetry. To account for the decrease in the asymmetry values due to these backgrounds, the asymmetries were scaled up using the scale factor:

$$A_{\text{scale}} = \frac{N_{\text{asy}} - N_{\gamma\gamma} - N_{\text{cosmic}}}{N_{\text{asy}}}, \tag{5.59}$$

where $N_{\gamma\gamma}$ and N_{cosmic} are the two-photon and cosmic backgrounds and N_{asy} represents the number of asymmetry events. Thus the asymmetry corrected for these backgrounds is:

$$A_{\text{FB}}^{\text{ave}}(\text{corr}) = \frac{A_{\text{FB}}^{\text{ave}}(\text{uncorr})}{A_{\text{scale}}}. \tag{5.60}$$

Step 3

The t-channel events have to be subtracted. This is a similar procedure to that of the t-channel subtraction in the cross-section computation but a new electron

fraction has to be calculated as only 1 vs. 1 events make up the final event sample. The fraction of the final events sample which was 1 vs. 1 events was calculated using simulated e^+e^-, $\mu^+\mu^-$ and $\tau^+\tau^-$ events (see table 5.20). The electron fraction in

Year	Lepton pair	Fraction of 1 vs 1 events
1991	e^+e^-	0.8877
	$\mu^+\mu^-$	0.9659
	$\tau^+\tau^-$	0.5545
1992	e^+e^-	0.8984
	$\mu^+\mu^-$	0.9723
	$\tau^+\tau^-$	0.5722
1993	e^+e^-	0.8983
	$\mu^+\mu^-$	0.9696
	$\tau^+\tau^-$	0.5777

Table 5.20: The fraction of 1 vs 1 events in the final event sample for the leptonic channels.

this case is defined as:

$$e^+e^-_{\rm frac}({\rm asym}) = \frac{\mathcal{K}\varepsilon_{e^+e^-}F^{1-1}_{e^+e^-}}{\mathcal{K}\varepsilon_{e^+e^-}F^{1-1}_{e^+e^-} + \varepsilon_{\mu^+\mu^-}F^{1-1}_{\mu^+\mu^-} + \frac{\varepsilon_{\tau^+\tau^-}F^{1-1}_{\tau^+\tau^-}}{R^{\rm gen}}}, \tag{5.61}$$

where

- $\varepsilon_{e^+e^-/\mu^+\mu^-/\tau^+\tau^-}$ represent the electron/muon/tau efficiencies.
- $\mathcal{K}$ is the ratio $\frac{\sigma({\rm s+t})}{\sigma({\rm s})}$, $R^{\rm gen}$ is the barrel to 4π extrapolation ratio.
- $\mathrm{F}^{1-1}_{e^+e^-/\mu^+\mu^-/\tau^+\tau^-}$ represent the fractions shown in table 5.20.

Now, the barrel asymmetry is given by:

$$A^{\rm barr}_{\rm FB} = A^{\rm ave}_{\rm FB}({\rm corr}) - \left(e^+e^-_{\rm frac}({\rm asym}) \times A^{\rm t-chan}_{\rm FB}\right), \tag{5.62}$$

where $A^{\rm ave}_{\rm FB}({\rm corr})$ is the asymmetry as in equation 5.60 and $A^{\rm t-chan}_{\rm FB}$ is the asymmetry due to the t-channel effects.

ALIBABA and TOPAZ0 were used to calculate the t-channel asymmetry. This is defined as:

$$A^{\rm t-chan}_{\rm FB} = A_{\rm FB}({\rm s+t}) - A_{\rm FB}({\rm s}) \tag{5.63}$$

where

- $A_{FB}(s + t)$ and $A_{FB}(s)$ are the asymmetries for the s+t channel and the s-channel.

- A_{FB}^{t-chan} is the asymmetry due to the t and the s-t channel interference for the process $e^+e^- \rightarrow e^+e^-$.

To take into account the $\theta = 90^0$ crack, the forward and backward regions chosen are shown in table 5.21. Due to constraints on the lepton polar angle in

Region	Polar angle coverage
Forward	$43^0 \leq \theta \leq 88^0$
Backward	$92^0 \leq \theta \leq 137^0$

Table 5.21: The forward and backward regions for the asymmetry analysis taking into account the $\pm 2^0$ crack at $\theta = 90^0$.

these programs a direct calculation of equation 5.63 was not possible and a method was devised [58] to calculate the t-channel asymmetry in the polar angle ranges given in table 5.21.

Both programs can be used to calculate the cross-sections, σ, and the asymmetries, A_{FB}. Then using the fact that:

$$\sigma = \sigma_F + \sigma_B, \tag{5.64}$$

and

$$A_{FB} = \frac{(\sigma_F - \sigma_B)}{\sigma}, \tag{5.65}$$

where:

$$\sigma_F = \frac{1}{2}\sigma(1 + A_{FB}), \tag{5.66}$$

$$\sigma_B = \frac{1}{2}\sigma(1 - A_{FB}). \tag{5.67}$$

Now, the forward and backward cross-sections, equation 5.66 and equation 5.67, can be calculated using the two programs in the polar ranges 43^0 - 90^0 and 90^0 - 137^0. These can then be subtracted by their analogous quantities in the ranges 88^0 - 90^0 and 90^0 - 92^0 to give the asymmetries in the required ranges 43^0 - 88^0 and 92^0 - 137^0 as shown in equation 5.68:

$$A_{FB}(s+t) = \frac{\left(\sigma_F^{43-90}(s+t) - \sigma_F^{88-90}(s+t)\right) - \left(\sigma_B^{90-137}(s+t) - \sigma_B^{90-92}(s+t)\right)}{\left(\sigma_F^{43-90}(s+t) - \sigma_F^{88-90}(s+t)\right) + \left(\sigma_B^{90-137}(s+t) - \sigma_B^{90-92}(s+t)\right)}. \tag{5.68}$$

A similar approach (equation 5.68) is used to determine the s-channel asymmetry. Table 5.22 shows the measured asymmetries corrected for the backgrounds (Step 2) and the t-channel asymmetry (Step 3).

Year	Energy GeV	A_{FB} corr.	Electron fraction	A_{FB}^{t-chan}	A_{FB}^{s-chan}
1991	88.464	0.1499	0.5954	0.6357	-0.2296
	89.457	0.0880	0.5249	0.4546	-0.1512
	90.211	0.0657	0.4706	0.3042	-0.0778
	91.208	0.0625	0.4117	0.1224	0.0121
	91.239	0.0688	0.4103	0.1177	0.0205
	91.953	0.0871	0.3862	0.0391	0.0720
	92.952	0.1382	0.3766	0.0123	0.1336
	93.702	0.0782	0.3817	0.0323	0.0658
1992	91.280	0.0600	0.4052	0.1113	0.0149
1993	89.433	0.1020	0.5226	0.4599	-0.1385
	91.192	0.0535	0.4074	0.1253	0.0025
	91.297	0.0401	0.4029	0.1098	-0.0042
	93.016	0.0937	0.3729	0.0139	0.0885

Table 5.22: Column 3 shows the asymmetry corrected for the backgrounds, column 4 shows the electron fraction, column 5 the t-channel asymmetry, and column 6 shows the barrel s-channel asymmetry.

Step 4

The fact that ZFITTER constrains only one track has to be taken into account. The s-channel asymmetries calculated in Step 4 have been done so for the case where both the lepton and anti-lepton are in the barrel region. In order to correct for the case when one lepton is constrained to be in the barrel region, TOPAZ0 was used to calculate

$$A_{FB}^{1\ trk} - A_{FB}^{2\ trks}, \tag{5.69}$$

and so

$$A_{FB}^{s-chan}(1\ \mathrm{trk}) = A_{FB}^{s-chan} + A_{FB}^{1\ trk} - A_{FB}^{2\ trks}, \tag{5.70}$$

where

- $A_{FB}^{1\ trk}$ represents the asymmetries as calculated using TOPAZ0 with one of the two tracks constrained to be in the barrel. Cuts of 3 GeV/c on the momentum and 20^0 on the acollinearity were also applied.

- $A_{FB}^{2\ trks}$ is the same as A_{FB}^{1trk} except that it represents the asymmetries for events with two tracks constrained to be in the barrel region.
- A_{FB}^{s-chan} represents the measured s-channel asymmetries of table 5.22.
- A_{FB}^{s-chan}(1 trk) are the s-channel asymmetries corresponding to events which have one track in the barrel region.

Table 5.23 shows the corrected s-channel asymmetries.

Year	Energy GeV	$A_{FB}^{1\ trk}$	$A_{FB}^{2\ trk}$	A_{FB}^{s-chan}(1 trk)
1991	88.464	-0.2176	-0.2171	-0.2301
	89.457	-0.1377	-0.1372	-0.1517
	90.211	-0.0765	-0.0760	-0.0783
	91.208	-0.0006	-0.0003	0.0118
	91.239	0.0016	0.0021	0.0171
	91.953	0.0456	0.0465	0.0715
	92.952	0.0914	0.0935	0.1327
	93.702	0.1165	0.1199	0.0637
1992	91.280	0.0044	0.0046	0.0147
1993	89.433	-0.1395	-0.1390	-0.1613
	91.192	-0.0016	-0.0017	0.0031
	91.297	0.0055	0.0059	-0.0053
	93.016	0.0939	0.0958	0.1045

Table 5.23: The s-channel asymmetries (column 5) corrected for the effect of constraining one track or two tracks in the barrel region. Columns 3 and 4 show the one and two track asymmetries as calculated using TOPAZ0.

Step 6

The asymmetries shown in table 5.23 are fully corrected s-channel asymmetries over the barrel region. It is worthwhile noting the fact that the asymmetry analysis is over the barrel region only and not over 4π, again due to the t-channel for the electrons which diverges in the forward region. In this final step the s-channel asymmetries are corrected to the full solid angle.

Using the differential cross-section, equation 5.52, the asymmetry can be defined as:

$$A_{FB} = \frac{\int_a^b [F(1+x^2)+Gx]\,dx - \int_c^d [F(1+x^2)+Gx]\,dx}{\int_a^b [F(1+x^2)+Gx]\,dx + \int_c^d [F(1+x^2)+Gx]\,dx}, \tag{5.71}$$

where F and G are energy dependent factors, x is $\cos\theta$, $a = \cos 43^0$ and $b = \cos 88^0$, and $c = \cos 92^0$ and $d = \cos 137^0$ (the polar angle ranges in which the asymmetries are determined). Using the conditions that $d = -a$ and $c = -b$, equation 5.71 can be solved to be:

$$A_{\rm FB} = \frac{(a^2 - b^2)}{2\left[\left(a + \frac{a^3}{3}\right) - \left(b + \frac{b^3}{3}\right)\right]} \frac{G}{\rm F}. \tag{5.72}$$

Now, the asymmetry for 4π can be obtained from equation 5.72 imposing the conditions that $b = 0$ and $a = \cos 2\pi$:

$$A_{\rm FB}^{4\pi} = \frac{3}{8} \frac{G}{\rm F}. \tag{5.73}$$

Using equation 5.72 and equation 5.73, the expression for the 4π asymmetry in terms of the barrel asymmetry is:

$$A_{\rm FB}^{4\pi} = A_{\rm FB}^{\rm s-chan}(1\ {\rm trk}) \times \frac{3(a-b) + (a^3 - b^3)}{4(a^2 - b^2)}. \tag{5.74}$$

Substituting the values of a and b into equation 5.74 the barrel to 4π extrapolation factor for the asymmetries was determined to be 1.162.

A better approach would be to determine the barrel to 4π extrapolation ratio at the different energy points. ZFITTER was used to calculate this ratio and then extrapolate the barrel s-channel asymmetries:

$$A_{\rm FB}^{4\pi}({\rm meas}) = A_{\rm FB}^{\rm s-chan}(1\ {\rm trk}) \times \frac{A_{\rm FB}^{4\pi}({\rm ZFIT})}{A_{\rm FB}^{\rm barr}({\rm ZFIT})}, \tag{5.75}$$

where

- $A_{\rm FB}^{4\pi}$(meas) represents the final asymmetry corrected to the full solid angle but not for the cuts on the momentum and acollinearity.
- $A_{\rm FB}^{\rm s-chan}(1\ {\rm trk})$ are the barrel s-channel asymmetries (see table 5.23).
- $A_{\rm FB}^{4\pi}$(ZFIT) are the asymmetries calculated over the full solid angle (using ZFITTER) with a 3 GeV/c cut on the momentum and 20^0 on the acollinearity.
- $A_{\rm FB}^{\rm barr}$(ZFIT) is the same as $A_{\rm FB}^{4\pi}$(ZFIT) except that it represents asymmetries with one of the two tracks constrained to be in the barrel region.

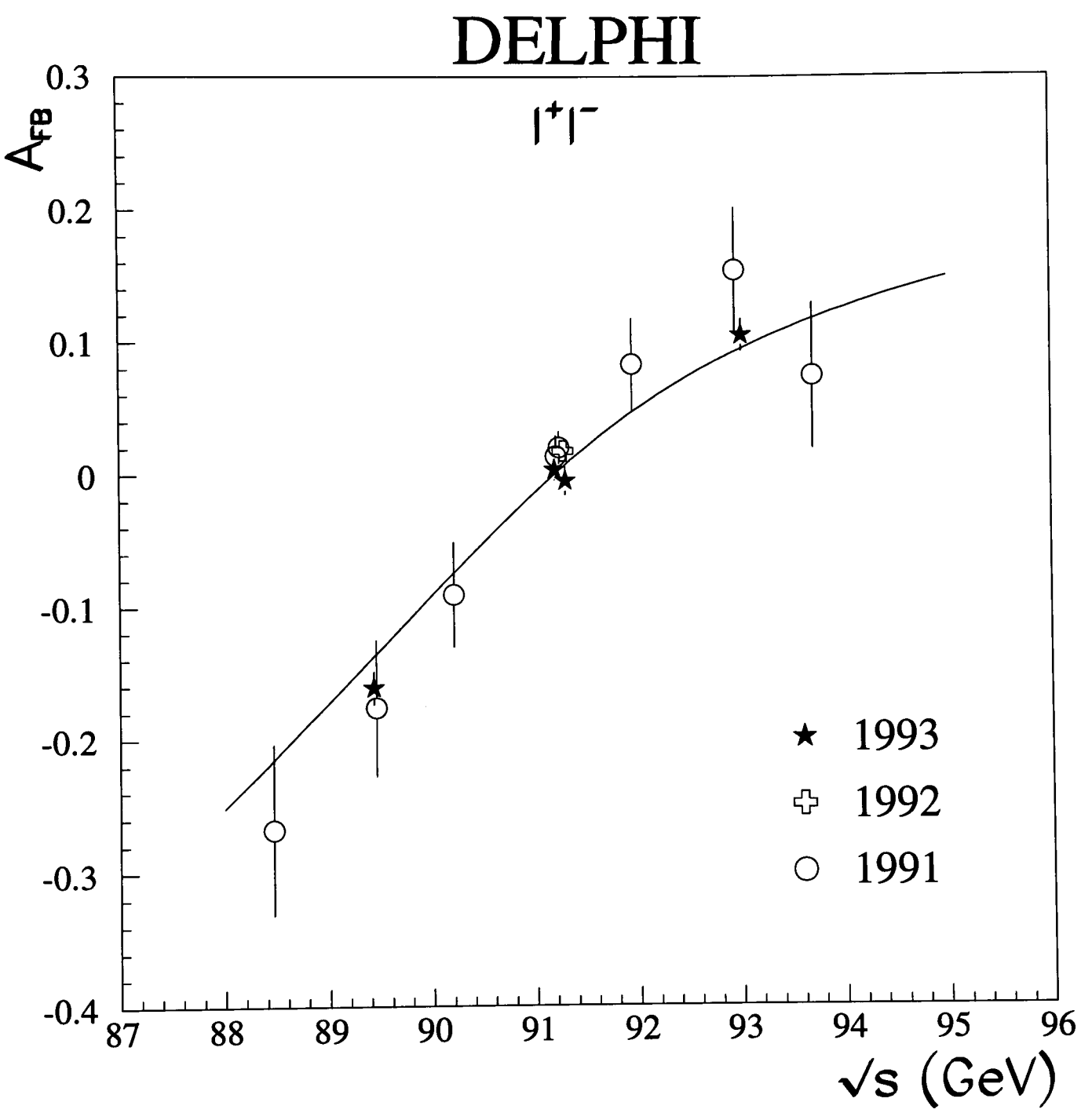

Figure 5.3: The s-channel forward-backward asymmetries for leptons. These have been corrected to the full solid angle but not for the cuts on the momentum and acollinearity. The curve represents the Standard Model prediction as determined using ZFITTER with $m_{\text{top}} = 170$ GeV, $m_{\text{Higgs}} = 300$ GeV and $M_Z = 91.187$ GeV.

Year	Energy GeV	Extrapolation factor	$A_{FB}^{4\pi}$ s-channel	Statistical error
1991	88.464	1.162	-0.2674	0.0640
	89.457	1.162	-0.1763	0.0515
	90.211	1.160	-0.0908	0.0398
	91.208	1.120	0.0132	0.0156
	91.239	1.155	0.0197	0.0124
	91.953	1.158	0.0826	0.0349
	92.952	1.157	0.1536	0.0473
	93.702	1.156	0.0737	0.0549
1992	91.280	1.162	0.0170	0.0052
1993	89.433	1.161	-0.1613	0.0127
	91.192	1.188	0.0031	0.0078
	91.297	1.154	-0.0053	0.0107
	93.016	1.156	0.1045	0.0122

Table 5.24: Table showing the final fully corrected asymmetries over the whole solid angle. Note, no correction due to the 20^0 acollinearity cut and 3 GeV/c momentum cut has been made. Column 3 shows the barrel to 4π extrapolation factor calculated using ZFITTER.

Table 5.24 shows the barrel to 4π extrapolation along with the final s-channel forward-backward asymmetries over the full solid angle. Figure 5.3 shows the final asymmetries plotted against the centre-of-mass energies for the various years.

In summary, the steps used to calculate the asymmetries are:

- Obtaining an average asymmetry using the counting method, where the average is of the asymmetries due to the positive and negative tracks separately;
- applying a correction for the cosmic and two-photon backgrounds;
- accounting for the t-channel asymmetry and the selection inefficiencies;
- correcting the asymmetries to take into account the fact that ZFITTER constrains only one track;
- and finally, extrapolating the s-channel asymmetries to the full solid angle.

5.4 Uncertainties on the Asymmetries

5.4.1 Statistical Errors

The asymmetry has been determined using the counting method according to which

$$A_{\mathrm{FB}}^{4\pi} = \frac{N_{\mathrm{F}} - N_{\mathrm{B}}}{N_{\mathrm{F}} + N_{\mathrm{B}}}. \tag{5.76}$$

If $n = N_{\mathrm{F}}$ and $N = N_{\mathrm{F}} + N_{\mathrm{B}}$ one obtains

$$A_{\mathrm{FB}}^{4\pi} = \frac{2n - N}{N}. \tag{5.77}$$

Thus the error on $A_{\mathrm{FB}}^{4\pi}$ translates as an error on n and this is taken to be the standard deviation of the binomial distribution, which in this case gives:

$$\delta(n) = \sqrt{n\left(1 - \frac{n}{N}\right)}. \tag{5.78}$$

Hence the statistical error on the asymmetry is:

$$\delta(A_{\mathrm{FB}}^{4\pi}) = \frac{2}{N} \times \delta(n). \tag{5.79}$$

These statistical errors on the asymmetries are shown in table 5.24.

5.4.2 Systematic Errors

The possible sources of systematic errors on the forward-backward asymmetries determination are:

- errors associated with the background subtraction;
- errors due the failure of the $\Delta\phi$ like-sign reclaim;
- an error due to both tracks in an event having wrongly assigned charges;
- errors due to the difference in the t-channel asymmetry calculated using ALIBABA and TOPAZ0;
- errors on the electron fraction;
- errors on the t-channel asymmetries (as calculated using ALIBABA and TOPAZ0) due to variations in the masses of the top quark and the Higgs boson;
- an error due to the difference in the asymmetries determined using positive tracks and negative tracks;
- and an error due to the uncertainty on the polar angle θ.

Uncertainties on the background subtraction

The cosmic muon and two-photon backgrounds were used to scale up the asymmetries (Step 2). The errors associated with these backgrounds were determined to make a negligible effect to the asymmetries.

Uncertainty on the like-sign reclaim

It was determined in section 3.6.2 that the HPC $\Delta\phi$ reclaim method failed approximately 24 % of the time. It failed in the sense that even when 2 tracks were found to be of opposite charges, it classified them as like-signs and changed their signs[8]. Thus there will be a certain number of events (which were reclaimed using this method) which will have tracks whose signs have been swapped. The number of swapped-sign events in the reclaimed sample is given by:

$$N_{\mathbf{swapped}} = 0.24 \times N_{\mathbf{reclaimed}}. \tag{5.80}$$

- In 1991, $N_{\mathbf{reclaimed}}$ was 92 events and $N_{\mathbf{swapped}}$ was determined to be 22 events. These were distributed by luminosity and the effect of changing N_{F} and N_{B} according to:

$$A_{\mathrm{FB}}(\mathrm{swapped}) = \frac{(N_{\mathrm{F}} \pm N_{\mathbf{swapped}}) - (N_{\mathrm{B}} \mp N_{\mathbf{swapped}})}{(N_{\mathrm{F}} \pm N_{\mathbf{swapped}}) + (N_{\mathrm{B}} \mp N_{\mathbf{swapped}})}, \tag{5.81}$$

  was studied. This 'swapping' of charges produced an error on the asymmetry of 0.0020 (absolute value).

- Similarly in 1992, $N_{\mathbf{reclaimed}}$ was 365 events and $N_{\mathbf{swapped}}$ was determined to be 91 events. This gave an error of 0.0036 on the asymmetry.

- In 1993, $N_{\mathbf{reclaimed}}$ was 357 events and $N_{\mathbf{swapped}}$ was determined to be 86 events. The observed error on the asymmetry was 0.0021.

Uncertainty on the like-sign events

There is also a probability that both tracks in an event have a wrong charge assignment. The like-sign events discussed so far have been ones in which only one of

[8] As an example, if a 'good' event had a fastest track which was positive and the other track was negative, the $\Delta\phi$ method changed the positive track to have a negative sign and vice-versa.

the tracks in a 2 track event has had a wrong charge assigned to it. If both tracks have a wrongly assigned charge and assuming that the correlation (of wrong charge assignment) between the two tracks is negligible, then the probability that an event has 2 tracks with wrong signs is:

$$P^{2\text{ track}}_{\text{swapped}} = \left(\frac{N_{\text{like-sign}}}{N_{\text{total}}}\right)^2, \tag{5.82}$$

where $N_{\text{like-sign}}$ is the number of like-sign events and N_{total} is the total number of events in the sample. This quantity was found to be negligible.

Difference in the t-channel asymmetry

The t-channel asymmetry is determined by averaging the values calculated using ALIBABA and TOPAZ0. The difference between the values obtained from ALIBABA and TOPAZ0 translates as an error at each energy point. The absolute error due to the difference at each energy point is calculated and scaled up by the electron fraction at that point to give the systematic error.

Table 5.25 shows the systematic error at each energy point due to the difference in the t-channel asymmetry as obtained from ALIBABA and TOPAZ0.

Year	Energy (GeV)	t-channel (ALIBABA)	t-channel (TOPAZ0)	Systematic error (10^{-3})
1991	88.464	0.6376	0.6337	1.65
	89.457	0.4558	0.4532	0.97
	90.211	0.3050	0.3032	0.60
	91.208	0.1232	0.1215	0.49
	91.239	0.0401	0.0380	0.61
	91.953	0.0135	0.0110	0.68
	92.952	0.0337	0.0307	0.80
	93.702	0.1183	0.1169	0.38
1992	91.280	0.1115	0.1111	0.11
1993	89.433	0.4602	0.4594	0.30
	91.192	0.1257	0.1248	0.26
	91.297	0.1101	0.1093	0.23
	93.016	0.0144	0.0133	0.29

Table 5.25: Table showing the systematic error due to the difference in the t-channel asymmetry as determined using ALIBABA and TOPAZ0.

Variations in m_{top} and m_{Higgs}

The t-channel asymmetries were calculated using ALIBABA and TOPAZ0. By varying the masses of the top quark and the Higgs boson it was found there was a negligible effect on the final t-channel asymmetry. Note, that the same variation in m_{top} and m_{Higgs} were made as in the section on the cross-section systematics.

Uncertainty on the electron fraction

The asymmetry electron fraction (equation 5.61) has errors associated with the e^+e^-, $\mu^+\mu^-$, and $\tau^+\tau^-$ efficiencies and the ratio $\mathcal{K}$. The error on the electron fraction can be written as:

$$\delta(e^+e^-_{\mathrm{frac}}) = \frac{-1}{(1+x)^2}\delta x, \tag{5.83}$$

where

$$x = \frac{\varepsilon_{\mu^+\mu^-} + \varepsilon_{\tau^+\tau^-}}{\mathcal{K}\varepsilon^+_e e^-}. \tag{5.84}$$

This equation can be re-written as:

$$\delta(e^+e^-_{\mathrm{frac}}) = (e^+e^-_{\mathrm{frac}})^2 \times \delta x, \tag{5.85}$$

where δx represents the error on equation 5.84. Now, this error on the electron fraction enters the asymmetry analysis scaled by the actual value of the t-channel asymmetry and so the error can be written as :

$$\delta(e^+e^-_{\mathrm{frac}}) = A_{\mathrm{FB}}^{\mathrm{t-chan}} \times (e^+e^-_{\mathrm{frac}})^2 \times \delta x, \tag{5.86}$$

where $A_{\mathrm{FB}}^{\mathrm{t-chan}}$ is the t-channel asymmetry (see table 5.22). Taking into account all the fractional errors on the efficiencies and on $\mathcal{K}$ (which are all uncorrelated) and using the above equation the error on the electron fraction was calculated and is shown in table 5.26.

Difference in the positive and negative track asymmetries

The asymmetries determined using positive tracks and the asymmetries determined using negative tracks should in principle be the same. The reason that they are different is the fact that the forward and backward hemispheres of the TPC do not measure exactly the same θ. Hence, in the asymmetries determination an average

Year	Energy GeV	δx (%)	$\delta(e^+e^-_{\text{frac}})$
1991	91.208	0.0112	0.0002
	91.239	0.0109	0.0002
1992	91.280	0.0080	0.0001
1993	91.192	0.0062	0.0001
	91.297	0.0064	0.0001

Table 5.26: The errors on the asymmetries (column 4) due to the errors on the electron fraction. Column 3 represents the error on x (see equation 5.84).

was taken of the two asymmetries and now a systematic error due to the difference (in the asymmetries) has to be assigned to the final asymmetries. The error due to this difference is given by:

$$\delta(A_{\text{FB}}^{\text{diff}}) = \frac{A_{\text{FB}}^{+} - A_{\text{FB}}^{-}}{A_{\text{scale}}\sqrt{2}} \tag{5.87}$$

where

- A_{scale} is the factor by which the asymmetries are scaled to take into account the backgrounds.
- $A_{\text{FB}}^{+/-}$ are the positive/negative track asymmetries.

Using the asymmetry values from table 5.19 and substituting them into equation 5.87 the resulting error on the final asymmetries are shown in table 5.27.

Uncertainties on the polar angle

It was shown previously that there was a shift of < 0.3 mrad in the polar angle θ. The polar angle cuts were changed by $\pm$ 0.3 mrad and the effects on the absolute values of the asymmetries were observed. It was found that this change made a negligible effect (a change of 8.5×10^{-5} on the peak asymmetry value for 1993) on the measured forward-backward asymmetries.

The systematic errors on the final forward-backward asymmetries are given in table 5.28.

Year	Energy	$\delta(A_{FB}^{diff})$
1991	88.464	-
	89.457	0.0108
	90.211	0.0066
	91.208	-
	91.239	0.0008
	91.953	0.0011
	92.952	0.0003
	93.702	0.0039
1992	91.280	0.0006
1993	89.433	0.0007
	91.192	0.0003
	91.297	0.0001
	93.016	0.0011

Table 5.27: The error on the final asymmetries due to the error on the difference between the positive and negative track asymmetries.

Source of systematic error	Year		
	1991	1992	1993
Two-photon background	-	-	-
Cosmic background	-	-	-
Error on $\Delta\phi$ like-sign reclaim method	0.0020	0.0036	0.0021
Events in which both tracks have wrongly assigned charges	-	-	-
ALIBABA and TOPAZ0 difference in asymmetry	0.0005	0.0001	0.0003
Error on the electron fraction	0.0002	0.0001	0.0001
Difference in the positive and negative track asymmetries	0.0008	0.0006	0.0003
Variations in m_{mtop} and m_{Higgs}	-	-	-
Uncertainties on the polar angle	-	-	-
Final total	0.0022	0.0037	0.0021

Table 5.28: The systematic errors on the final inclusive lepton forward-backward asymmetries.

5.5 Chapter Summary

This chapter described the various steps involved in the determination of the inclusive lepton cross-sections and forward-backwards asymmetries. The cross-sections were corrected for the backgrounds, the trigger and selection efficiencies, the t-channel e^+e^- events (using ALIBABA and TOPAZ0) and extrapolated to the full solid angle using TOPAZ0. Further corrections were made for the LEP beam energy spread, the momentum and acollinearity cuts, and the final cross-sections correspond to events in which one track was constrained to be in the barrel region (this correction was made in light of the fact that ZFITTER constrains only one track). A similar approach was adopted for the forward-backward asymmetries. The same corrections were applied except the corrections for the momentum and acollinearity cuts and the LEP beam energy spread.

Chapter 6

Fits and Discussion of Results

Chapter Abstract

This chapter is divided into two sections. In the first section, the inclusive lepton analysis cross-sections and forward-backward asymmetries are compared with the corresponding results from the lepton-identified analyses. In the second section, the results of the fits (using ZFITTER) to the experimental data, are presented. Various quantities are derived (from the results of the fits) and discussed within the framework of the Standard Model.

6.1 Comparison with Lepton-Identified Analyses

All is now in place to compare the cross-sections and forward-backward asymmetries measured using the inclusive lepton analysis and the lepton-identified channels. The results used for the lepton-identified channels are the ones presented by the DELPHI collaboration at the International Conference on High Energy Physics (ICHEP) in Glasgow (1994). Note that, the results given for 1993 are of a preliminary nature and hence subject to possible change. For comparison purposes, the combined LEP results (average of the four LEP experiments) are also shown.

6.1.1 Comparison of Cross-sections

In order to do a comparison of the inclusive lepton cross-sections with the standard leptonic analyses, ZFITTER was used. This involved:

- correcting (where appropriate) the lepton-identified cross-sections to 4π acceptance and for the cuts on the momenta and acollinearity;
- determining the weighted mean of these at the different energy points;

- and calculating the ratio of the weighted mean (cross-sections) to those measured for the inclusive lepton analysis.

Figure 6.1 shows the cross-sections for the different lepton-identified channels. Note that, the electron and muon cross-sections have not been corrected for cuts on the polar angle acceptance, momenta, and acollinearity. The cuts used by the physics teams working on the different lepton-identified analyses are shown in table 6.1.

Channel	Cross-section		
	Polar angle (degrees)	Acollinearity (degrees)	Minimum energy GeV
e^+e^-	44-136	10	-
$\mu^+\mu^-$	20-160	20,10 [1991]	15
	Asymmetry		
e^+e^-	44-136	10	-
$\mu^+\mu^-$	-	20,10 [1991]	15

Table 6.1: The cuts used by the physics teams working on the lepton-identified cross-sections and asymmetries. The same cuts were used for the years 1991, 1992, and 1993. The tau cross-sections and asymmetries are fully corrected to the full solid angle and for cuts on the momentum and acollinearity. Note that, in the muon channel the cut on the acollinearity was 20^0 in 1992 and 1993 and 10^0 in 1991.

ZFITTER was used to determine, at each energy point, the following quantities:

$$\sigma^{4\pi}_{e^+e^-}(\text{corr}) = \sigma_{e^+e^-}(\text{meas}) \times \frac{\sigma^{4\pi}_{l^+l^-}(\text{ZFIT})}{\sigma_{e^+e^-}(\text{ZFIT})}, \tag{6.1}$$

and similarly

$$\sigma^{4\pi}_{\mu^+\mu^-}(\text{corr}) = \sigma_{\mu^+\mu^-}(\text{meas}) \times \frac{\sigma^{4\pi}_{l^+l^-}(\text{ZFIT})}{\sigma_{\mu^+\mu^-}(\text{ZFIT})}, \tag{6.2}$$

where

- $\sigma^{4\pi}_{e^+e^-/\mu^+\mu^-}$ (corr) are the electron/muon cross-sections corrected to the full solid angle and for the cuts on the momenta and acollinearity.

- $\sigma_{e^+e^-/\mu^+\mu^-}$(meas) represent the measured electron/muon cross-sections as shown in figure 6.1.

- $\sigma_{e^+e^-/\mu^+\mu^-}$(ZFIT) are the electron/muon cross-sections determined with the cuts in table 6.1 using ZFITTER.

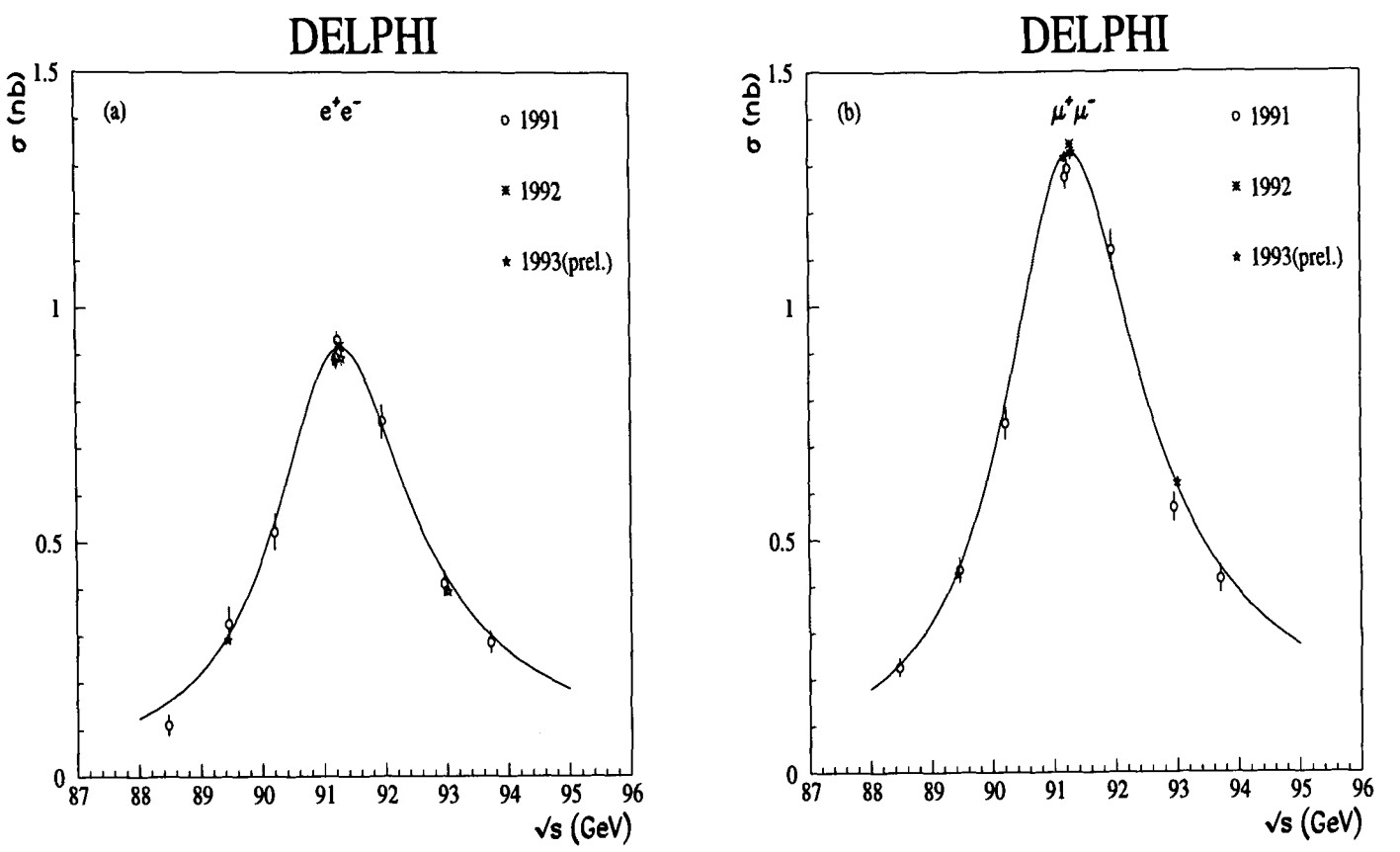

Figure 6.1: Cross-sections in the (a) e^+e^-, (b) $\mu^+\mu^-$ and (c) $\tau^+\tau^-$ channels. Note, the different scales. The electron and muon cross-sections have not been corrected for cuts on the polar angle acceptance, momenta, and acollinearity. The curves represent the Standard Model predictions as calculated using ZFITTER with $M_Z = 91.187$ GeV, $m_{\rm top} = 170$ GeV, $m_{\rm Higgs} = 300$ GeV.

- $\sigma^{4\pi}_{l^+l^-}$(ZFIT) are the lepton cross-sections calculated using ZFITTER with no cuts imposed. These are the averages of the electron, muon, and tau cross-sections (that is cross-sections calculated assuming lepton universality).

The errors on the cross-sections are also scaled up using the fractions in equations 6.1 and 6.2. The fully corrected cross-sections are shown in figure 6.2.

The next step involved the determination of the weighted mean for the lepton-identified cross-sections. The expression used to calculate the weighted mean is:

$$\sigma_{\mathrm{wm}} = \frac{\frac{\sigma_1}{\delta^2(\sigma_1)} + \frac{\sigma_2}{\delta^2(\sigma_2)} + \frac{\sigma_3}{\delta^2(\sigma_3)}}{\frac{1}{\delta^2(\sigma_1)} + \frac{1}{\delta^2(\sigma_2)} + \frac{1}{\delta^2(\sigma_3)}}, \tag{6.3}$$

and the error on σ_{wm} is

$$\delta(\sigma_{\mathrm{wm}}) = \left[\frac{1}{\frac{1}{\delta^2(\sigma_1)} + \frac{1}{\delta^2(\sigma_2)} + \frac{1}{\delta^2(\sigma_3)}}\right]^{\frac{1}{2}}, \tag{6.4}$$

where $\sigma_{1/2/3}$ represent the electron/muon/tau cross-sections and the $\delta(\sigma_{1/2/3})$ the corresponding errors.

In order to compare the weighted mean cross-sections and the inclusive lepton cross-sections, both the statistical and systematic errors have to be used. By comparing event lists it was determined that there was a non-complete overlap (approximately 73 % of the events were common) between the inclusive lepton event sample and the lepton-identified samples. This was due, in part (there are also differences in the event selection criteria and the run selection criteria), to the fact that the polar angle acceptances in the analyses were different. Using the systematic errors on the separate channels (see table 6.2) and the non-complete statistical overlap, the weighted mean cross-sections were re-evaluated and the following ratio determined:

$$R_{\mathrm{comp}} = \frac{\sigma_{\mathrm{identified}}}{\sigma_{\mathrm{inclusive}}} \pm \delta(R_{\mathrm{comp}}), \tag{6.5}$$

where

- $\sigma_{\mathrm{identified}}$ represents the weighted mean of the lepton-identified cross-sections. These were calculated using equation 6.3.
- $\sigma_{\mathrm{inclusive}}$ represents the inclusive lepton cross-sections (see table 5.11).
- R_{comp} is the ratio of the two sets of cross-sections, which should be unity.

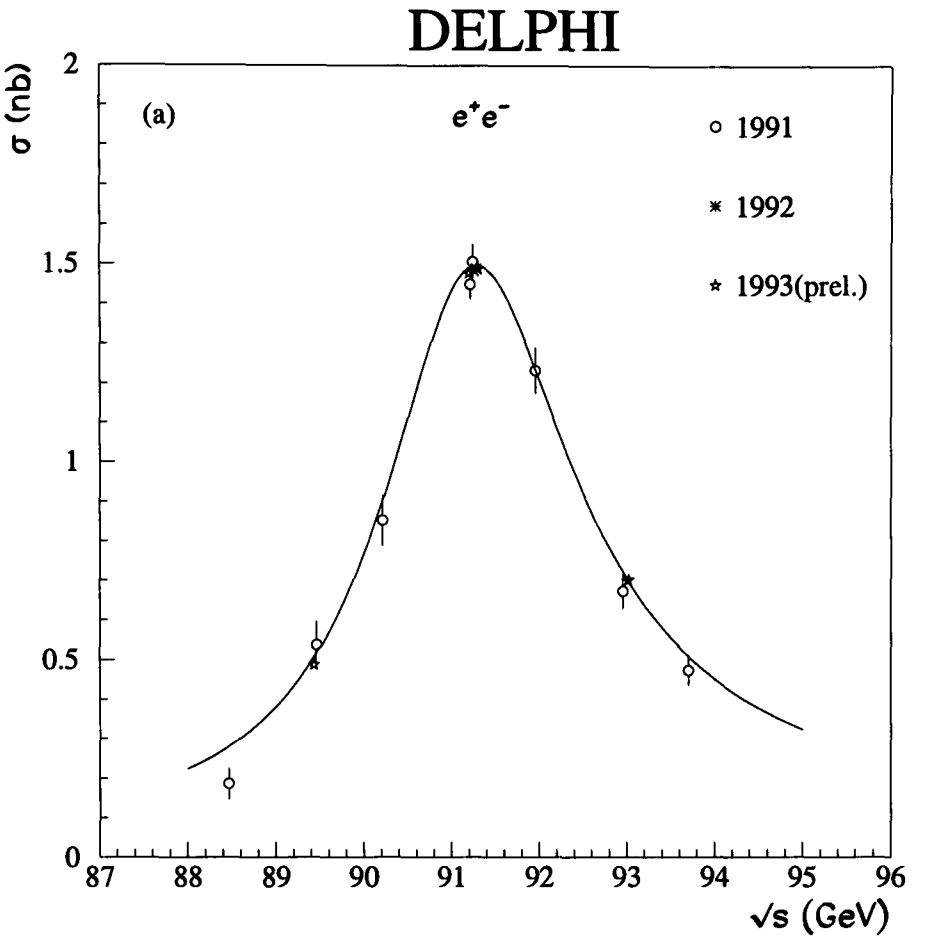

Figure 6.2: Cross-sections in the (a) e^+e^-, (b) $\mu^+\mu^-$ channels. The cross-section have been extrapolated to the full solid angle and corrected for cuts on the momenta and acollinearity. Only statistical errors are shown. The curves represent the Standard Model predictions as calculated using ZFITTER with $M_Z = 91.187$ GeV, $m_{\text{top}} = 170$ GeV, $m_{\text{Higgs}} = 300$ GeV.

Channel	Systematic error (cross-section)		
	1991 (%)	1992 (%)	1993 (%)
e^+e^-	0.50	0.59	1.00
$\mu^+\mu^-$	0.50	0.40	0.50
$\tau^+\tau^-$	0.75	0.60	0.80
	Systematic error (asymmetry)		
	1991	1992	1993
e^+e^-	0.0020	0.0030	0.0032
$\mu^+\mu^-$	0.0030	0.0010	0.0020
$\tau^+\tau^-$	0.0030	0.0017	0.0023

Table 6.2: The systematic errors given for the lepton-identified cross-sections and asymmetries for the various years. Note, the errors associated with the electron channel are for the s-channel only. The errors for 1993 are given as preliminary values and are subject to change.

- $\delta(R_{\mathrm{comp}})$ is the error on the ratio. This was calculated by adding the systematic errors and the uncorrelated statistical errors in quadrature.

The ratios of the cross-sections (equation 6.5) were computed for each energy point and the results are shown in figure 6.3. The level of agreement (disagreement) between the weighted mean of the lepton-identified cross-sections and the inclusive lepton cross-sections is:

- In 1991, taking a weighted mean (over the different energy points), R_{comp} was calculated to be 0.9991 ± 0.0048. The uncertainty on the ratio takes into account the systematic errors and the uncorrelated statistical errors.
- In 1992, R_{comp} was calculated to be 1.0032 ± 0.0050.
- In 1993, R_{comp} was determined to be 0.9946 ± 0.0034.

6.1.2 Comparison of Forward-Backward Asymmetries

To compare the asymmetries, an approach similar to the one above was used. ZFITTER was used to correct (where appropriate) the lepton-identified asymmetries and the inclusive lepton asymmetries to the full solid angle and for the cuts on the momenta and acollinearity. A weighted mean was calculated for the lepton-identified asymmetries. The difference between these mean values and the corrected inclusive lepton asymmetries at various energy points represents a test of the level of agreement (disagreement) between the analyses.

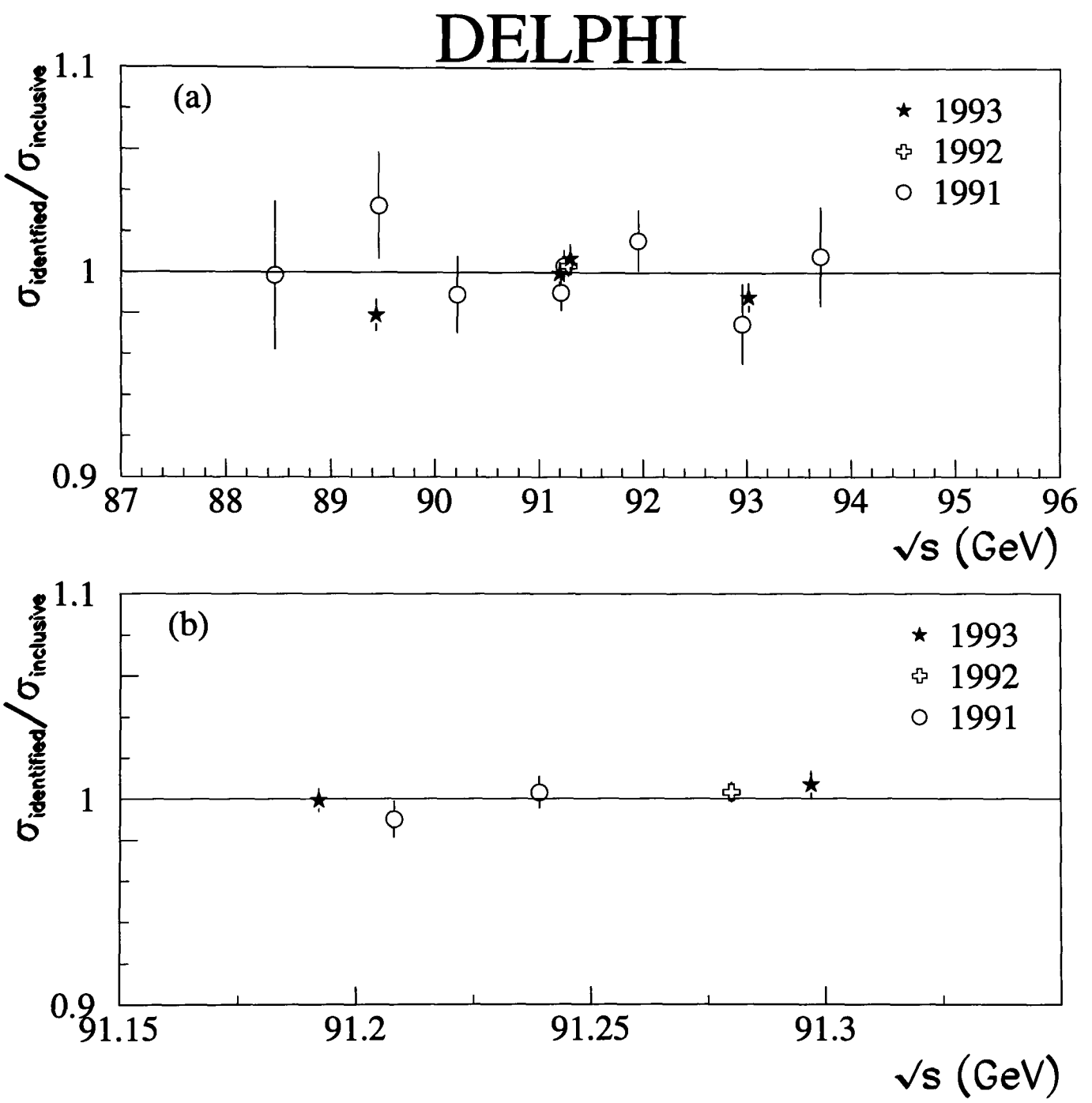

Figure 6.3: The ratio of the cross-sections from the lepton-identified channels and the inclusive lepton channel. For clarity, the peak cross-sections in (a) are shown in (b). The uncertainty on the ratio takes into account the systematic errors and the uncorrelated statistical errors.

Figure 6.4 shows the forward-backward asymmetries for the different lepton-identified channels. Note that, the asymmetries in the electron and muon channels have not been corrected for the polar angle acceptance and for the cuts on the momenta and acollinearity.

The forward-backward asymmetries in the e^+e^- and $\mu^+\mu^-$ lepton-identified channels and the inclusive lepton channel have to be corrected. In order to do this correction, ZFITTER was used to calculate at each energy point:

$$\Delta_{FB}^{\mathrm{ZFIT}} = A_{FB}(\text{no cuts}) - A_{FB}(\text{cuts}), \tag{6.6}$$

and hence the corrected asymmetries are

$$A_{FB}(4\pi) = A_{FB}(\text{measured}) + \Delta_{FB}^{\mathrm{ZFIT}}, \tag{6.7}$$

where

- A_{FB}(no cuts) represents the asymmetries calculated using ZFITTER (in the e^+e^-, $\mu^+\mu^-$, or the inclusive lepton channel) with no cuts imposed. In the case of the inclusive lepton asymmetries, assuming universality, an average was taken of the e^+e^-, $\mu^+\mu^-$, and $\tau^+\tau^-$ asymmetries.

- A_{FB}(cuts) represents the asymmetries which are the same as A_{FB}(no cuts) except that they were determined taking into account the cuts used by the various analyses.

- $A_{FB}(4\pi)$ represents the asymmetries for the lepton-identified channels (e^+e^- or $\mu^+\mu^-$) or the inclusive lepton channel. These have been corrected to the full solid angle and for the cuts on the momenta and acollinearity.

- A_{FB}(measured) represents the asymmetries measured by the various analyses.

The asymmetries corrected using this method are shown in figure 6.5.

Once corrected, a weighted mean was determined for the lepton-identified asymmetries and the difference between these and the inclusive lepton asymmetries was calculated at each energy point. A comparison of the asymmetry event lists showed that there was approximately 64 % correlation[1] between the inclusive lepton sample

[1]This is lower than correlation in the cross-section event samples due to the fact that the muon asymmetries are determined over a larger θ range.

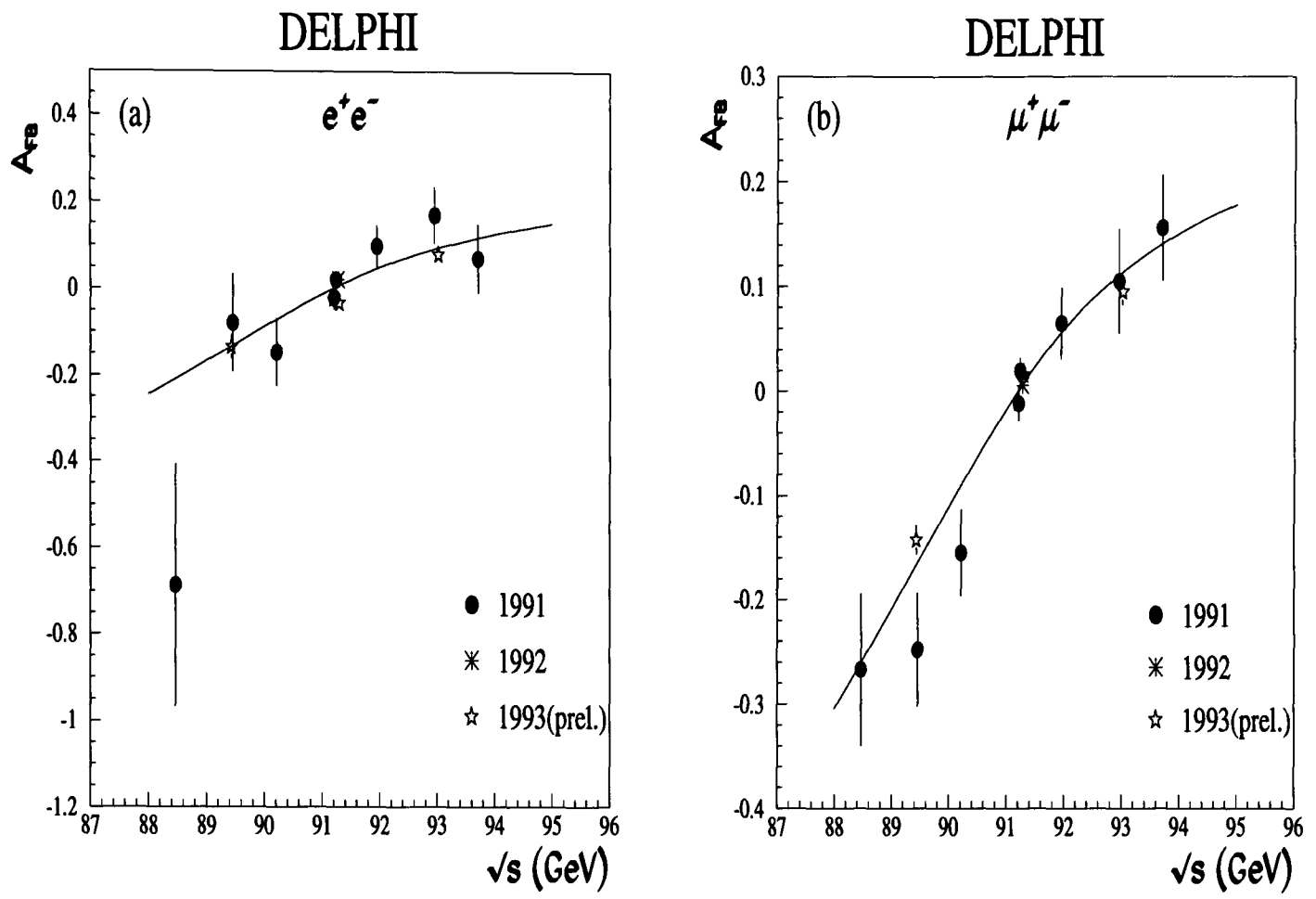

Figure 6.4: Forward–backward asymmetries in the (a) e^+e^-, (b) $\mu^+\mu^-$ and (c) $\tau^+\tau^-$ channels. The asymmetries in the electron and muon channels have not been corrected for the polar angle acceptance and for the cuts on the momenta and acollinearity. The curves represent the Standard Model predictions as calculated using ZFITTER with $M_Z = 91.187$ GeV, $m_{\text{top}} = 170$ GeV, $m_{\text{Higgs}} = 300$ GeV.

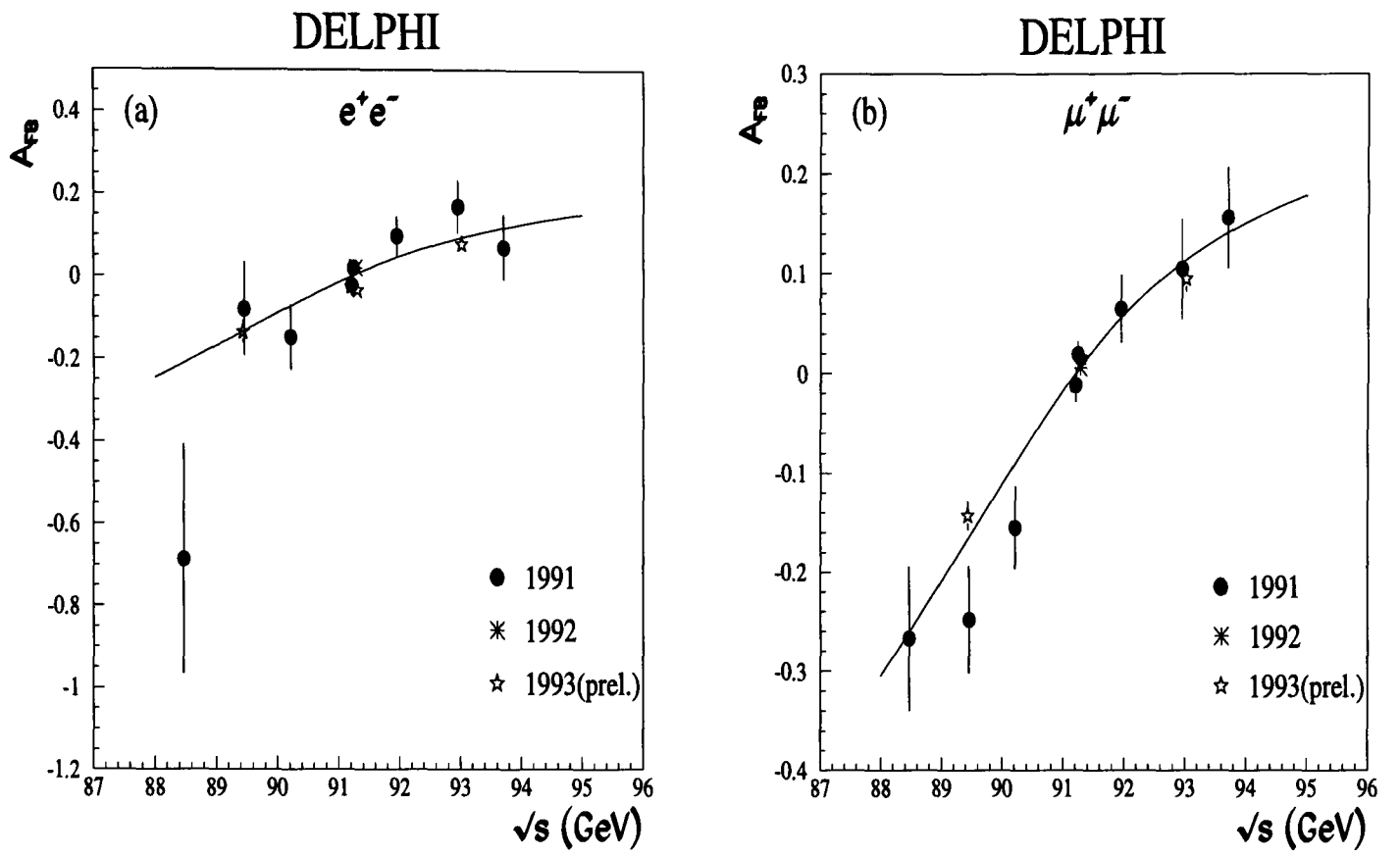

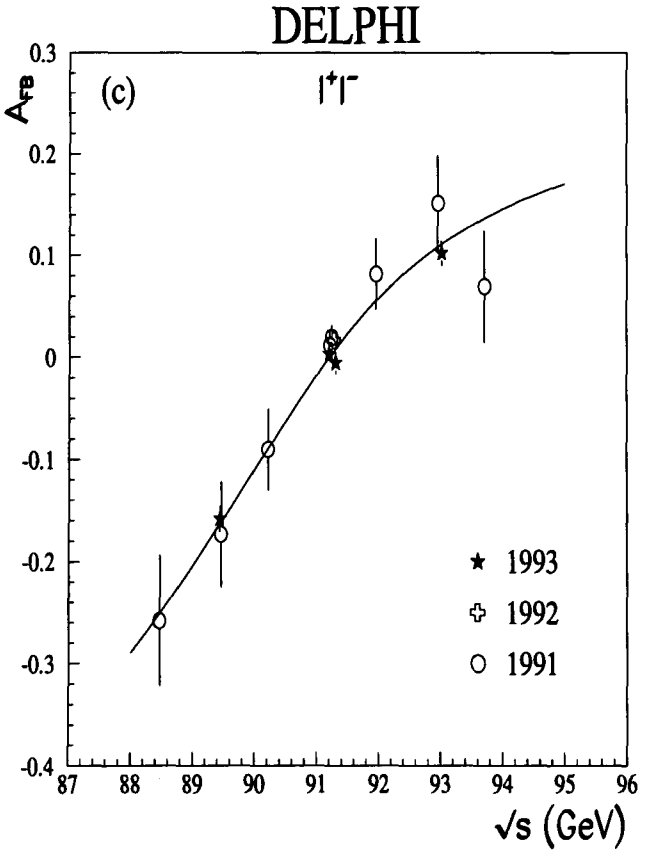

Figure 6.5: Forward–backward asymmetries in the (a) e^+e^-, (b) $\mu^+\mu^-$ and (c) inclusive lepton (l^+l^-) channels. The asymmetries have been extrapolated to the full solid angle and corrected for the cuts on the momenta and acollinearity. The curves represent the Standard Model predictions as calculated using ZFITTER with $M_Z = 91.187$ GeV, $m_{\text{top}} = 170$ GeV, $m_{\text{Higgs}} = 300$ GeV.

and the lepton-identified samples. The uncertainty on the difference between the weighted mean asymmetries and the inclusive lepton asymmetries took into account the systematic errors and the uncorrelated statistical errors.

The difference in the asymmetries mentioned above is given by:

$$\Delta A_{FB}(\text{comp}) = A_{FB}^{\text{identified}} - A_{FB}^{\text{inclusive}} \pm \delta(A_{FB}(\text{comp})), \tag{6.8}$$

where $A_{FB}^{\text{identified}}$ represents the weighted mean of the lepton-identified asymmetries, $A_{FB}^{\text{inclusive}}$ represents the inclusive lepton asymmetries, and $\delta(A_{FB}(\text{comp}))$ represents the uncertainty on the difference which takes into account the uncorrelated statistical errors and the systematic errors. The values of $\Delta A_{FB}(\text{comp})$ (which should be 0) represent the degree of compatibility between the lepton-identified asymmetries and the inclusive lepton asymmetries. Figure 6.6 shows $\Delta A_{FB}(\text{comp})$ for the years 1991, 1992 and 1993. The level of agreement (disagreement) between the lepton-identified asymmetries and the inclusive lepton asymmetries is:

- In 1991, taking a weighted mean (over the different energy points), $\Delta A_{FB}(\text{comp})$ was calculated to be -0.0066 $\pm$ 0.0096. The uncertainty on the difference takes into account the systematic errors and the uncorrelated statistical errors.
- In 1992, $\Delta A_{FB}(\text{comp})$ was calculated to be -0.0071 $\pm$ 0.0069.
- In 1993, $\Delta A_{FB}(\text{comp})$ was determined to be 0.0019 $\pm$ 0.0059.

In summary, comparing the lepton-identified cross-sections and forward-backward asymmetries with the ones measured using the inclusive lepton analysis, it was found that there was good agreement between the two sets of data.

6.2 Fits to Cross-Sections and Asymmetries

This section describes how the Z^0 resonance parameters and the couplings of the Z^0 to charged leptons were extracted from the data by fitting the experimental line-shapes and leptonic asymmetries. The fit to the inclusive lepton cross-sections and asymmetries in conjunction with the hadronic cross-sections[2] were carried out using

[2]The fact that Z^0 decays into hadrons 70 % of the time compared to 10 % for the leptons, allows a fit using hadronic data to give M_Z and Γ_Z with a much better statistical accuracy.

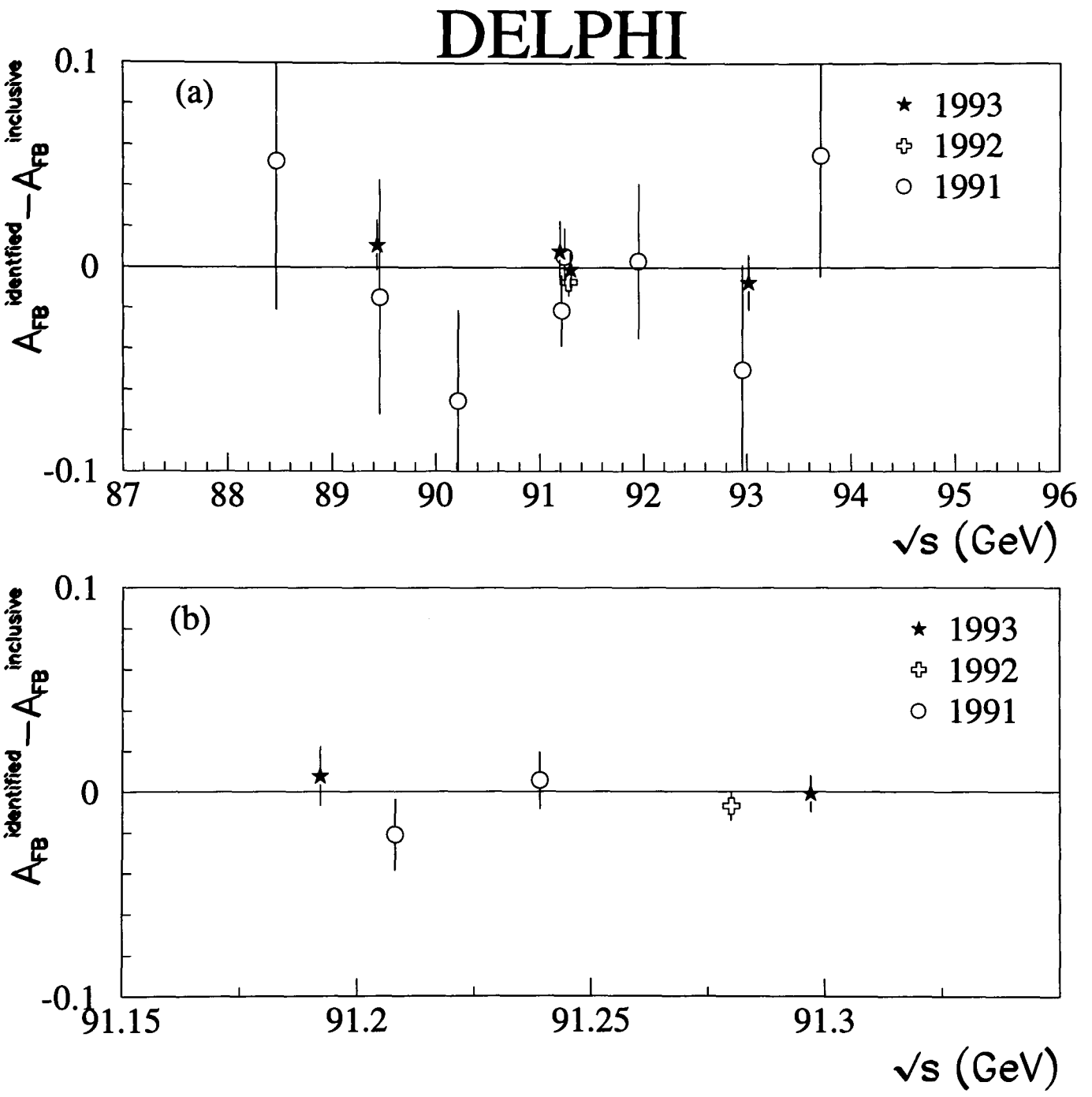

Figure 6.6: The difference between the weighted mean of the lepton-identified asymmetries and the inclusive lepton asymmetries. For clarity, the peak asymmetries in (a) are shown in (b). The uncertainty on the difference takes into account the systematic errors and the uncorrelated statistical errors.

ZFITTER (version 4.6). The theoretical formalism of the ZFITTER calculations allows an almost model independent interpretation of the observed quantities, involving an up-to-date treatment of initial and final-state QED effects, electroweak and QCD corrections. A χ^2 minimization procedure (See section 1.7) was used to fit the theoretical expressions to the measured lineshapes and asymmetries, including a full covariance matrix treatment of the errors. The errors on the LEP energies and their point-to-point correlations were also taken into account.

The correlation (if any) between the systematic errors on the cross-sections and asymmetries for the years 1991, 1992, and 1993 have to be accounted for as well. The approach used involved taking the lowest of the three values of the systematic errors[3] as the common error between the years.

A standard 5 parameter fit was carried out to the inclusive lepton cross-sections and forward-backward asymmetries and the hadronic cross-sections. These parameters are convenient for fitting and averaging as they have minimal correlations between them:

- The mass and total width of the Z^0, M_Z and Γ_Z, where these quantities are defined on the basis of the denominator of the Breit Wigner Z^0 propagator:

$$\frac{1}{(s - M_Z^2 + i\frac{s}{M_Z}\Gamma_Z)}. \tag{6.9}$$

- The hadronic pole/peak cross-section:

$$\sigma_h^0 = \frac{12\pi}{M_Z^2}\frac{\Gamma_e\Gamma_{\mathrm{had}}}{\Gamma_Z^2}, \tag{6.10}$$

  where Γ_e and Γ_{had} are the partial widths of the Z^0 for decays into electrons and hadrons.

- The ratio:

$$R_{\mathrm{l}} = \frac{\Gamma_{\mathrm{had}}}{\Gamma_{\mathrm{l}}}, \tag{6.11}$$

  where Γ_{l} is the partial width of the Z^0 for the decays $Z^0 \to l^+l^-$. Under the assumption of universality the expected [59] difference between the values for Γ_e and Γ_μ and the value for Γ_τ is approximately 0.2 % due to the mass

[3]See table 5.18 and table 5.28 for the systematic errors on the inclusive lepton cross-sections and forward-backward asymmetries.

correction term in Γ_τ. The leptonic partial[4] can be written in terms of the effective vector and axial-vector couplings, $\hat{g}_a^l$ and $\hat{g}_v^l$, as:

$$\Gamma_l = \frac{G_F M_Z^3}{6\pi\sqrt{2}} \left[(\hat{g}_a^l)^2 + (\hat{g}_v^l)^2\right] \left(1 + \frac{3\alpha}{4\pi}\right), \tag{6.12}$$

where G_F is the Fermi coupling constant, α is the QED fine structure constant, and the last factor takes into account the final-state radiation.

- The pole/peak leptonic asymmetry, $(A_{FB}^0)^l$. In terms of the effective vector and axial-vector neutral current couplings, $\hat{g}_v^l$ and $\hat{g}_a^l$, this asymmetry can be written as:

$$(A_{\rm FB}^0)^l = \frac{3}{4}\hat{A}_e\hat{A}_l, \tag{6.13}$$

where

$$\hat{A}_l = \frac{2\hat{g}_v^l\hat{g}_a^l}{(\hat{g}_v^l)^2 + (\hat{g}_a^l)^2}. \tag{6.14}$$

Note that, in this choice of parameters there is an inherent assumption of lepton universality. The results of the 5 parameter fit are shown in table 6.3 and the correlations between the parameters are shown in table 6.4. Also shown in table 6.3 are the DELPHI results and the LEP average results.

Parameter	Inclusive lepton	DELPHI	LEP average
M_Z	91.1876 ± 0.0052 GeV	91.1869 ± 0.0052 GeV	91.1889 ± 0.0044 GeV
Γ_Z	2.4971 ± 0.0061 GeV	2.4951 ± 0.0059 GeV	2.4974 ± 0.0038 GeV
σ_h^0	41.23 ± 0.17 nb	41.26 ± 0.17 nb	41.49 ± 0.12 nb
R_l	20.73 ± 0.09	20.69 ± 0.09	20.795 ± 0.040
$(A_{FB}^0)^l$	0.0195 ± 0.0042	0.0160 ± 0.0029	0.0170 ± 0.0016
χ^2/DF	34/35	160/136	18.4/15

Table 6.3: The results of the 5 parameter fits to the inclusive lepton data (column 2) and the hadronic data. For comparison the corresponding DELPHI results, column 3 (5 parameter fit to the lepton-identified and hadronic data), and the LEP results (same as column 2 and 3 but averages over the LEP experiments) are shown. The method of LEP averaging is discussed below.

LEP Average

The electroweak parameters derived by the LEP experiments were combined [60] taking a weighted mean of the fit variables. For the calculation of the derived quantities an average correlation matrix, or the matrix of any one of the experiments,

[4]For massless leptons.

Parameter	M_Z	Γ_Z	σ_h^0	R_l	$(A_{FB}^0)^l$
M_Z	1.000	0.064	0.003	0.006	0.031
Γ_Z	0.064	1.000	-0.174	-0.001	-0.008
σ_h^0	0.003	-0.174	1.000	0.122	-0.008
R_l	0.006	0.001	0.122	1.000	0.005
$(A_{FB}^0)^l$	0.031	-0.008	-0.008	0.005	1.000

Table 6.4: The correlation coefficients between the Z^0 resonance parameters used in the 5 parameter fit.

can be used. Common errors (common amongst the experiments) arise from the absolute LEP energy scale, the relative energies of the different scan points and the theoretical uncertainty in the Bhabha cross-section used in the luminosity calculations.

Each of the experiments provided[5] a correlation matrix for their parameters, and also a matrix including only the uncertainties introduced by the LEP energy calibrations. The theoretical uncertainty for the calculation of the small angle Bhabha cross-section, which is assumed to be fully correlated amongst the experiments, was taken into account. Using all this information a full covariance matrix of the input parameters was constructed and a χ^2 minimization procedure was used to obtain a combined parameter set (this is the set shown in table 6.3).

6.3 Interpretation of Results

Using the results of table 6.3 and the relations in equations 6.10 - 6.13, the parameters shown in table 6.5 were derived. Various other parameters can be determined from all the results obtained so far.

The values of $\hat{\rho}$ and $\sin^2\theta_{\rm eff}^{\rm lept}$

It was established in Chapter 1, that:

- a measurement of the cross-section leads to the determination of the effective rho ($\hat{\rho}$) parameter,

[5]The responsibility of averaging the results from the four LEP experiments lies with the LEP Electroweak Working Group.

Parameter	Inclusive lepton	DELPHI	LEP average
Γ_{l}	83.82 ± 0.29 MeV	83.86 ± 0.28 MeV	83.96 ± 0.18 MeV
$(\hat{g}_v^{\mathrm{l}})^2$	$(1.65 \pm 0.36)\times10^{-3}$	$(1.35 \pm 0.25)\times10^{-3}$	$(1.44 \pm 0.14)\times10^{-3}$
$(\hat{g}_a^{\mathrm{l}})^2$	0.2505 ± 0.0009	0.2510 ± 0.0009	0.2512 ± 0.0006
Γ_{had}	1.7375 ± 0.0066 GeV	1.7351 ± 0.0064 GeV	1.7459 ± 0.0040 GeV
Γ_{inv}	508.4 ± 5.8 MeV	508.7 ± 5.7 MeV	499.8 ± 3.5 MeV
$\Gamma_{\mathrm{inv}}/\Gamma_{\mathrm{l}}$	6.065 ± 0.069	6.066 ± 0.069	5.953 ± 0.046

Table 6.5: The quantities derived from the results (table 6.3) of the ZFITTER fit to the inclusive lepton data and the hadronic data. Note, that Γ_{inv} is the partial width for Z^0 decays into invisible final states.

- and a measurement of the forward-backward asymmetry leads to the determination of the effective weak mixing angle, $\sin^2\theta^{\mathrm{eff}}_{\mathrm{lept}}$.

Using the relations for the vector and axial-vector couplings:

$$\hat{g}_a = t_3\sqrt{\hat{\rho}}, \tag{6.15}$$

and

$$\sin^2\theta^{\mathrm{eff}}_{\mathrm{lept}} = \frac{1}{4}\left(1 - \frac{\hat{g}_v^{\mathrm{l}}}{\hat{g}_a^{\mathrm{l}}}\right), \tag{6.16}$$

the values of the effective rho parameter and the effective weak mixing angle were determined and are shown in table 6.6.

	Inclusive lepton	DELPHI	LEP average
$\hat{\rho}$	1.0020 ± 0.0036	1.0040 ± 0.0036	1.0047 ± 0.0022
$\sin^2\theta^{\mathrm{eff}}_{lept}$	0.2297 ± 0.0024	0.2317 ± 0.0017	0.2311 ± 0.0009

Table 6.6: The values of the effective rho parameter and the effective weak mixing angle as determined using the inclusive lepton data and the DELPHI lepton-identified data. The combined LEP values are also shown.

The number of light neutrino families

From the measurements of the total width and the partial decay widths into hadrons and leptons, the width of the Z^0 decaying into invisible particles can be derived:

$$\Gamma_{\mathrm{inv}} = \Gamma_Z - \Gamma_{\mathrm{had}} - 3\Gamma_{\mathrm{l}}, \tag{6.17}$$

which can be written as:

$$\Gamma_{\rm inv} = \Gamma_{\rm l}\left(\sqrt{\frac{12\pi R_{\rm l}}{M_Z^2\sigma_{\rm h}^0}} - R_{\rm l} - 3\right). \tag{6.18}$$

The result for $\Gamma_{\rm inv}$ can be converted into a number of light neutrino families

$$\begin{aligned} N_\nu &= \frac{\Gamma_{\rm inv}}{\Gamma_\nu} \\ &= \frac{\Gamma_{\rm inv}}{\Gamma_{\rm l}} \times \left(\frac{\Gamma_{\rm l}}{\Gamma_\nu}\right)^{\rm SM}, \end{aligned} \tag{6.19}$$

where $\left(\frac{\Gamma_{\rm l}}{\Gamma_\nu}\right)^{\rm SM}$ is the Standard Model [39] value of:

$$\left(\frac{\Gamma_{\rm l}}{\Gamma_{\rm inv}}\right)^{SM} = 1.992 \pm 0.002, \tag{6.20}$$

and using the value of $\Gamma_{\rm inv}/\Gamma_{\rm l}$ (table 6.5) the number of neutrino families was determined and is shown in table 6.7.

	Inclusive lepton	DELPHI	LEP average
N_ν	3.045 ± 0.035	3.045 ± 0.035	2.988 ± 0.023

Table 6.7: The number of neutrino families determined using the inclusive lepton data.

The values of α_s and m_{top}

Using the cross-sections and asymmetries and the results derived from the 5 parameter fit, the values of the strong coupling constant $\alpha_{\rm s}$ and the mass of the top quark can be obtained.

α_s

The QED coupling constant, α, represents the strength of the interaction between charged particles and photons. In direct analogy to this, the strong coupling constant, $\alpha_{\rm s}$, represents the coupling of the strong charges (colour) of the quarks, via an appropriate mediating boson (gluon).

To obtain a value for $\alpha_{\rm s}$ the quantity $R_{\rm l}$ (among other quantities) may be used. In fits to the Standard Model this quantity is practically independent of the top and Higgs masses, because in the ratio (which $R_{\rm l}$ represents) of the two partial widths

the main contributions to the weak radiative corrections cancel. Through QCD corrections in the hadronic final states R_l depends on α_s as:

$$R_l = R_l^{\alpha_s=0}(1 + \delta_{\rm QCD}), \tag{6.21}$$

where $R_l^{\alpha_s=0}$ is the value of R_l in the absence of QCD corrections, and the QCD corrections (δ_{QCD}) can be written [61] (approximately) as:

$$\delta_{\rm QCD} = 1.060\left(\frac{\alpha_s}{\pi}\right) + 0.9\left(\frac{\alpha_s}{\pi}\right)^2 - 15\left(\frac{\alpha_s}{\pi}\right)^3. \tag{6.22}$$

For the extraction of α_s a Standard Model fit to all the data (which includes the R_l result) was carried out in which the number of neutrino families was constrained to be 3. The resulting value of the strong coupling constant is given in table 6.8.

	Inclusive lepton	DELPHI	LEP average
α_s	0.123 ± 0.010	0.119 ± 0.010	0.126 ± 0.005

Table 6.8: The value of the strong coupling constant determined by fixing the number of neutrino families to be 3.

m_{top}

It was mentioned in Chapter 1 that the effective rho parameter, $\hat{\rho}$, depended quadratically on the mass of the top and logarithmically on the mass of the Higgs. This dependence [62] is shown below:

$$\hat{\rho} = 1 + \frac{3G_\mu m_{\rm top}^2}{8\pi^2\sqrt{2}} - \frac{11G_\mu M_Z^2 \sin^2\theta_{\rm W}}{12\pi^2\sqrt{2}}\left[\ln\left(\frac{M_{\rm H}}{M_{\rm W}}\right) - \frac{5}{12}\right] + ... \tag{6.23}$$

where G_μ is the Fermi coupling constant, M_W is the mass of the W boson, and θ_W is the weak mixing angle.

A Standard Model fit to the inclusive lepton data (and the hadronic data) was carried out, constraining the value of α_s to be[6] :

$$\alpha_s = 0.123 \pm 0.005, \tag{6.24}$$

yielding the following value for the mass of the top quark:

$$m_{\rm top} = 178\ ^{+22}_{-25}({\rm expt})\ ^{+18}_{-16}({\rm Higgs}), \tag{6.25}$$

[6]This value was determined by the DELPHI collaboration (see [63]).

where (Higgs) represents the variation due to the Higgs boson masses in the range 60 GeV to 1000 GeV, with a central value of 300 GeV. The values given by the DELPHI collaboration and the combined LEP average are:

$$m_{\rm top}\,({\rm DELPHI}) = 170\ ^{+21}_{-24}({\rm expt})\ ^{+18}_{-18}({\rm Higgs}), \tag{6.26}$$

and

$$m_{\rm top}\,({\rm LEP}) = 173\ ^{+12}_{-13}({\rm expt})\ ^{+18}_{-20}({\rm Higgs}). \tag{6.27}$$

One final comparison was done. Recall that, the two quantities directly determined by this analysis are the peak asymmetry, $(A^0_{\rm FB})^{\rm l}$, and the leptonic width, $\Gamma_{\rm l}$ (which is implicit in the definition of $R_{\rm l}$). Figure 6.7 shows these values in comparison to the corresponding values predicted by the Standard Model. It shows the probability contour of fixed χ^2, corresponding to 68 % confidence level, in the $R_{\rm l}$-$(A^0_{\rm FB})^{\rm l}$ plane.

6.4 Summary and Conclusions

This thesis described an inclusive analysis of the lepton pairs produced by the e^+e^- annihilations at LEP. The cross-sections and forward-backward asymmetries for the process $e^+e^- \to l^+l^-$ for the years 1991, 1992 and 1993 were experimentally determined at centre-of-mass energies in the range $|\sqrt{\rm s} - M_Z| < 3$ GeV. The results are shown in tables 5.11 and 5.24.

These cross-section and asymmetry results were compared with the weighted averages (assuming lepton universality) of the lepton-identified results. The lepton-identified results were in the channels $Z^0 \to e^+e^-$, $Z^0 \to \mu^+\mu^-$, and $Z^0 \to \tau^+\tau^-$. Table 6.9 shows the results of the comparison. The primary aim of this analysis was to provide a cross-check to the lepton-identified analyses. This has been done, and it can be seen (table 6.9) that there is a high degree of compatibility between the two sets of analyses.

The cross-sections and asymmetries were also fit together with the hadronic cross-sections measured by DELPHI for the same data samples. A 5 parameter fit was carried out. The parameters used were the mass, M_Z, and total width, Γ_Z, of the Z^0, the ratio of the hadronic partial width, $\Gamma_{\rm had}$, to the leptonic partial width,

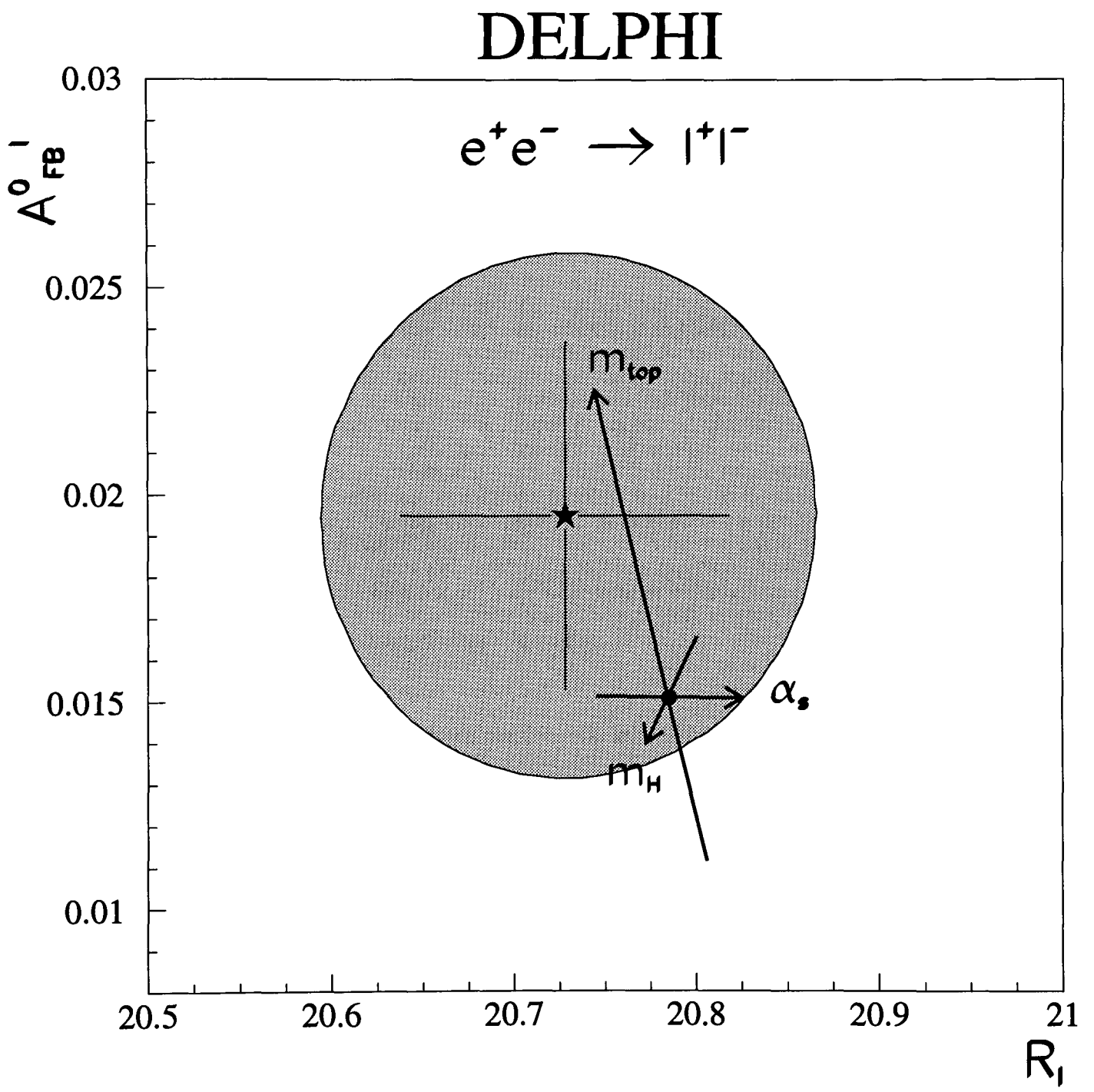

Figure 6.7: The shaded area is enclosed by a contour of constant χ^2 (68 % confidence level) for the peak leptonic asymmetry versus the ratio of the hadronic to leptonic partial widths. The arrowed lines correspond to the variation of the Standard Model prediction when $m_{\rm top}$, $m_{\rm H}$ or $\alpha_{\rm s}$ are varied in the intervals $70 < m_{\rm top}({\rm GeV}) < 270$, $60 < m_{\rm H}({\rm GeV}) < 1000$, $\alpha_{M_Z^2} = 0.123 \pm 0.006$, respectively. The point of intersection of the arrowed lines is the Standard Model prediction for $M_Z = 91.1876$ GeV, $m_{\rm top} = 170$ GeV, $m_{\rm H} = 300$ GeV, and $\alpha_{\rm s} = 0.123$. The arrows point in the direction of increasing values of $m_{\rm top}$, $m_{\rm H}$ and $\alpha_{\rm s}$. The star represents the value determined from the 5 parameter fit to the inclusive lepton data and the hadronic data (see table 6.3).

Year	Ratio of cross-sections R_{comp}	Difference of asymmetries $\Delta A_{FB}(\text{comp})$
1991	0.9991 ± 0.0048	-0.0066 ± 0.0096
1992	1.0032 ± 0.0050	-0.0071 ± 0.0069
1993	0.9946 ± 0.0034	0.0019 ± 0.0059

Table 6.9: Comparison of the results from the inclusive lepton analysis and the lepton-identified analyses. The expected values of R_{comp} and $\Delta A_{FB}(\text{comp})$ are 1 and 0 respectively.

Γ_{l}, and the leptonic peak asymmetry, $(A^0_{FB})^{\text{l}}$. The results of the fit were:

$$\begin{aligned} M_Z &= 91.1876 \pm 0.0052 \text{ GeV} \\ \Gamma_Z &= 2.4971 \pm 0.0061 \text{ GeV} \\ \sigma^0_h &= 41.23 \pm 0.17 \text{ nb} \\ R_{\text{l}} &= 20.73 \pm 0.09 \\ (A^0_{FB})^{\text{l}} &= 0.0195 \pm 0.0042 \\ \chi^2/\text{DF} &= 34/35 \end{aligned}$$

Using the results of the 5 parameter fit and the correlations between the fitted parameters, the values of various parameters can be derived, table 6.10. For comparison purposes, also shown are the Standard Model predictions. The values of M_Z, α_s, and m_{top}, which were obtained by fitting to the inclusive lepton data (and the hadronic data), were used as input to ZFITTER (which was used to calculate the Standard Model predictions).

In the previous sections it has been shown that the experimental results obtained are in agreement with the corresponding current values from the DELPHI collaboration and the combined LEP results. Now, using table 6.10, the conclusion can be drawn that the results from the inclusive lepton analysis are consistent with the corresponding Standard Model predictions which were determined using a value of 178 GeV for the mass of the top quark and assuming a value of 300 GeV for the Higgs boson mass.

Quantity	Derived value	Standard Model prediction
$\Gamma_{\rm l}$ (MeV)	83.82 ± 0.29	83.90
$(\hat{g}_v^{\rm l})^2$	$(1.65 \pm 0.36) \times 10^{-3}$	1.32×10^{-3}
$(\hat{g}_a^{\rm l})^2$	0.2505 ± 0.0009	0.2513
$\Gamma_{\rm had}$ (GeV)	1.7375 ± 0.0066	1.7437
$\Gamma_{\rm inv}$ (MeV)	508.4 ± 5.8	501.6
$\Gamma_{\rm inv}/\Gamma_{\rm l}$	6.065 ± 0.069	5.978
$\hat{\rho}$	1.0020 ± 0.0036	1.0052
$\sin^2\theta^{\rm eff}_{\rm lept}$	0.2297 ± 0.0024	0.2319
N_ν	3.045 ± 0.035	3.000
$\alpha_{\rm s}$	0.123 ± 0.010	Input
$m_{\rm top}$ (GeV)	$178\ ^{+22}_{-25}$(expt) $^{+18}_{-16}$(Higgs)	Input

Table 6.10: Various parameters derived from the 5 parameter fit results. Also shown are the corresponding Standard Model predictions which were calculated using ZFITTER. 'Input' represents the fact these parameters were used as input to ZFITTER when calculating the Standard Model predictions. In additions to these inputs a value of 300 GeV was used for the Higgs boson mass.

References

[1] CDF Collaboration, F.Abe et al., "Evidence for Top Quark Production in $\bar{p}p$ Collisions at $\sqrt{s} = 1.8$ TeV", Preprint FERMILAB-PUB-94/097-E.

[2] P.W. Higgs, Phys. Rev. **145**, 1156 (1966).

[3] S.L. Glashow, Nuc. Phys. **B22** (1961) 579;
S. Weinberg, Phys. Rev. Lett. **19** (1967) 1264;
A. Salam, in: "Elementary Particle Theory", ed. N.Svartholm, Stockholm (1968), p 367.

[4] P.B. Renton, "Electroweak Interactions", Cambridge University Press 1990.

[5] Z Physics at LEP 1, Volume 1, edited by G.Altarelli, R.Kleiss and C.-Verzegnassi, CERN 89-08 (1989).

[6] G.'t Hooft, Nuc. Phys. **B35** (1971) 167.

[7] D.A. Ross, J.C.Taylor, Nucl. Phys. **B51** (1973) 25.

[8] I.J.R. Aitchision and A.J.G.Hey, "Gauge Theories in Particle Physics" (2nd edition), Adam Hilger 1989.

[9] D. Schaile, "Tests of the Electroweak Theory at LEP", Preprint CERN PPE 93-213 (1993), submitted to Fortschr. Phys.

[10] P. Renton , "How Effective is the Weak Mixing Angle", Preprint CERN PPE 93-88 (19993), Z. Phys. **C60** (1993) 643-658.

[11] P. Ratoff, "Electroweak Couplings and Asymmetries at LEP", Talk given at "Electroweak Interactions and Unified Theories", Ed. Frontières, Gif-sur-Yvette, (1991) M69, and CERN Preprint PPE 91-087.

[12] Particle Data Group, "Review of Particle Properties", Phys. Rev. **D45**, Part 2 (1992).

[13] H. Burkhardt et al., Z. Phys. **C43** (1989) 497.

[14] D. Bardin et al., Z. Phys. **C44** (1989) 493; Comput. Phys. Commun. 59 (1990) 303; Nucl. Phys. **B351** (1991) 1.

[15] D. Bardin et al., "ZFITTER : An Analytical Program for Fermion Pair Production in e^+e^- Annihilation", CERN-TH 6443/92 (1992), Phys. Lett. **B229** (1989) 405.

[16] F. James "MINUIT - Function Minimization and Error Analysis", CERN Program Library entry **D506**, Edition - March 1994.

[17] ALEPH : D. Decamp et al., Nucl. Inst. Meth. **A294** (1990) 121;
L3 : B. Adeva et al., Nucl. Inst. Meth. **A289** (1990) 35;
OPAL : K. Ahmet et al., Nucl. Inst. Meth. **A305** (1991) 275.

[18] F. Dydak, "LEP Report", Talk given at the "International Symposium on Lepton-Photon Interactions at High Energies", World Scientific, Singapore (1990).

[19] G. Myatt, "Physics at LEP", Talk given at the "Perkins Conference", World Scientific, Singapore (1994);
L. Arnaudon et al. (The Working Group on LEP Energy), "Measurement of the Mass of the Z Boson and the Energy Calibration of LEP", Phys. Lett. **B307** (1993) 187-193.

[20] The LEP Polarization Collaboration, "Measurement of the LEP Beam Energy by Resonant Spin Depolarization", Preprint CERN PPE 92-49, Phys. Lett. **B284** (1992) 431.

[21] R.C. Fernow, "An Introduction to Experimental Particle Physics", Cambridge University Press 1986.

[22] P. Aarnio et al., "The DELPHI detector at LEP", CERN Preprint PPE 90-128, Nucl. Instr. &Meth. **A303**(1991) 233-276.
DELPHI Collaboration, "DELPHI Technical Proposal", DELPHI 83-66 (1983).

[23] C. Brand et al., "The DELPHI Time Projection Chamber", Nucl. Instr. &Meth. **A283** (1989) 567.

[24] N. Bingefors et al., "The DELPHI Microvertex Detector", Nucl. Instr. & Meth. **A328** (1993) 447.

[25] F.A. Berends et al., "Radiative Corrections to Bhabha Scattering at High Energies", Nucl. Phys. **B304** (1988) 712.

[26] S. Jadach et al., Comput. Phys. Commun. **70** (1992) 305.

[27] M.J. Jonker et al., "Architecture and Performance of the DELPHI Data Acquisition and Control System", DELPHI 91-93 DAS 113 (1991).

[28] J. Fuster et al., "The 1'st and 2'nd Level Trigger User Manual; Summary of the 1992 Trigger Performance", DELPHI 93-42 DAS 144 (1993);
J. Fuster et al., "The Online Software for the First and Second Level Trigger of DELPHI", DELPHI 91-112 DAS 115 (1991).

[29] R. Brun et al., "ZEBRA - Data Structure Management System", CERN Program Library, Q100 (1987).

[30] J.N. Albert et al., "DELFARM 91 Part 1 : Hardware and Software Overview", DELPHI 91-125 PROG 163 (1991).

[31] DELPHI Collaboration, "DELPHI Data Analysis Program (DELANA) User's Guide", DELPHI 89-44 PROG 137 (1989).

[32] "TANAGRA Track Analysis and Graphics Package — User's Guide", DELPHI 87-95 PROG 98 (1987).

[33] J. Wickens, "DELANA Tags for 1991 Data", DELPHI 91-20 PROG 160 (1991).

[34] J. Wickens, "Physics Team Tagging in PXTAG", DELPHI 92-44 PROG 184 (1992).

[35] DELPHI Collaboration, "DELSIM: DELPHI Event Generation and Detector Simulation — User's Guide", DELPHI 89-67 PROG 142 (1989).

[36] J.E. Campagne and R. Zitoun, Z. Phys. **C43** (1989) 469; and Proc. of the Brighton Workshop on Radiative Corrections, Sussex, July 1989.

[37] S. Jadach et al., "The Monte Carlo program KORALZ, version 4.0, for the lepton or quark pair production at LEP/SLC energies" CERN TH 7075-93 (1993). Submitted to Comput. Phys. Commun.

[38] S. Nova et al., "MONTE-CARLO : Event Generator for Two-Photon Physics", DELPHI 90-35 PROG 152 (1990).

[39] DELPHI Collaboration, "Measurements of the Lineshape of the Z^0 and Determination of Electroweak Parameters from its Hadronic and Leptonic Decays", CERN Preprint PPE 94-08 (1994), Submitted to Nucl. Phys. B;
DELPHI Collaboration, "Improved Measurements of Cross-Sections and Asymmetries at the Z^0 Resonance", CERN Preprint PPE 94-31 (1994), Submitted to Nucl. Phys. B;
DELPHI Collaboration, "Precision Determination of the Z^0 Resonance Parameters", Paper presented at the ICHEP Conference, Glasgow (1994).

[40] T. Todorov, private communication.

[41] DELPHI Collaboration, D. Johnson, D. Reid and W. Trischuk, "A beamspot Database for Lifetime Measurements", DELPHI 92-36 PHYS 168 (1992).

[42] A. Buijs et al., "TWOGEN, a Simple Monte Carlo Generator for Two-Photon Reactions", CERN preprint PPE 93-199 (1993), and submitted to Comp. Phys. Comm.

[43] H. Kolanoski, "Two-Photon Physics at e^+e^- Storage Rings", Springer-Verlag 1984.

[44] T. Sjostrand, Comput. Phys. Commun. **28** (1983) 227;
T. Sjostrand, Comput. Phys. Commun. **39** (1986) 347.

[45] DELPHI Collaboration, "Study of Hard Scattering Processes in Multihadron Production from $\gamma\gamma$ collisions ate LEP", CERN preprint 94-04 (1994), and submitted to Zeit. f. Physik C.

[46] P. Ratoff, "A Preliminary Measurement of the Total Cross Section and the Forward-Backward Asymmetry for the $e^+e^- \rightarrow \tau^+\tau^-$ Reaction with 1993 Data", DELPHI 94-113 PHYS 430 (1994), paper submitted to the "ICHEP Conference" Glasgow;
W. Bonivento and P. Ratoff, "An Improved Measurement of the Total Cross-Section and the Forward-Backward Asymmetry for the $e^+e^- \rightarrow \tau^+\tau^-$ Reaction with 1992 Data", DELPHI 94-68 PHYS 388 (1994);
F. Matorras, "A Selection for τ Lepton Studies", DELPHI 92-124 PHYS 225 (1992).

[47] P. Checchia, private communication for the e^+e^- trigger efficiencies;
R. Lindner, private communication for the $\mu^+\mu^-$ trigger efficiencies;
P. Ratoff, private communication for the $\tau^+\tau^-$ trigger efficiencies.

[48] C.J. Beeston, "A Study of the Reaction $e^+e^- \rightarrow \mu^+\mu^-$ Around the Z^0 Pole", D.Phil thesis, University of Oxford (1992) and RALT-141;
B. Nijjhar and D.W. Reid, "Trigger Efficiency Calculation for $e^+e^- \rightarrow \mu^+\mu^-$ in the Region $45^0 \leq \theta \leq 135^0$", DELPHI 91-21 PHYS 92 (1991);
P.M. Kluit, "Evaluation of the Trigger Efficiency for $e^+e^- \rightarrow \mu^+\mu^-$ in 1991", DELPHI 92-34 PHYS 167 (1992).

[49] P.N.Ratoff and D.W.Reid, private communication.

[50] M. Winter, "Determination of the Parameters of the Z Line-Shapes at LEP", DELPHI 92-151 PHYS 242 (1992).

[51] S.D. Hodgson, "A Flavour-Independent Analysis of the Leptonic Decay Modes of the Z^0", D.Phil thesis, University of Oxford, and RALT-151.

[52] W.J.P. Beenakker et al., Nucl. Phys. **B349** (1991) 323.

[53] G. Montagna et al., Nucl. Phys. **B401** (1993) 3, and Comput. Phys. Commun. **76** (1993) 328.

[54] L. Lyons, "Statistics for Nuclear and Particle Physicists", Cambridge University Press 1986.

[55] O. Nicrosini (co-author of TOPAZ0 program), private communication.

[56] W.J.P. Beenakker (co-author of ALIBABA program), private communication.

[57] P. Checchia, private communication.

[58] G. Zumerle, private communication.

[59] LEP Collaborations, "Combined Preliminary Data on Z^0 Parameters from the LEP Experiments and Constraints on the Standard Model", CERN Preprint being prepared from contributions of the LEP experiments to the 27th International Conference on High Energy Physics, Glasgow, Scotland, 20-27 July 1994.

[60] LEP Collaborations, "Updated Parameters of the Z^0 Resonance from Combined Preliminary Data of the LEP Experiments", CERN Preprint 93-157 (1993).

[61] T. Hebbeker et a., "The Ratio R of Hadronic and Electronic Z widths and the Strong Coupling Constant α_s", CERN preprint PPE 94-44 (1944), and Phys. Lett. **B331** (1994) 165.

[62] J.E. Augustin, "LEP Physics", CERN preprint PPE 93-83 (1993).

[63] DELPHI Collaboration, Z. Phys. **C59** (1993) 21.

Appendix A

DELPHI Members

P.Abreu[20], W.Adam[7], T.Adye[37], E.Agasi[30], I.Ajinenko[43], R.Aleksan[39], G.D.Alekseev[14], A.Algeri[13], S.Almehed[23], S.J.Alvsvaag[4], U.Amaldi[7], A.Andreazza[27], P.Antilogus[24], W-D.Apel[15], R.J.Apsimon[37], Y.Arnoud[39], B.Åsman[45], J-E.Augustin[18], A.Augustinus[30], P.Baillon[7], P.Bambade[18], F.Barao[20], R.Barate[12], G.Barbiellini[47], D.Y.Bardin[14], G.J.Barker[34], A.Baroncelli[41], O.Barring[7], J.A.Barrio[25], W.Bartl[50], M.J.Bates[37], M.Battaglia[13], M.Baubillier[22], K-H.Becks[52], M.Begalli[36], P.Beilliere[6], Yu.Belokopytov[43], P.Beltran[9], D.Benedic[8], A.C.Benvenuti[5], M.Berggren[18], D.Bertrand[2], F.Bianchi[46], M.Bigi[46], M.S.Bilenky[14], P.Billoir[22], J.Bjarne[23], D.Bloch[8], J.Blocki[51], S.Blyth[34], V.Bocci[38], P.N.Bogolubov[14], T.Bolognese[39], M.Bonesini[27], W.Bonivento[27], P.S.L.Booth[21], G.Borisov[43], H.Borner[7], C.Bosio[41], B.Bostjancic[44], S.Bosworth[34], O.Botner[48], B.Bouquet[18], C.Bourdarios[18], T.J.V.Bowcock[21], M.Bozzo[11], S.Braibant[2], P.Branchini[41], K.D.Brand[35], R.A.Brenner[7], H.Briand[22], C.Bricman[2], L.Brillault[22], R.C.A.Brown[7], J-M.Brunet[6], L.Bugge[32], T.Buran[32], H.Burmeister[7], A.Buys[7], J.A.M.A.Buytaert[7], M.Caccia[7], M.Calvi[27], A.J.Camacho Rozas[42], R.Campion[21], T.Camporesi[7], V.Canale[38], K.Cankocak[45], F.Cao[2], F.Carena[7], L.Carroll[21], C.Caso[11], M.V.Castillo Gimenez[49], A.Cattai[7], F.R.Cavallo[5], L.Cerrito[38], V.Chabaud[7], A.Chan[1], M.Chapkin[43], Ph.Charpentier[7], J.Chauveau[22], P.Checchia[35], G.A.Chelkov[14], L.Chevalier[39], P.Chliapnikov[43], V.Chorowicz[22], J.T.M.Chrin[49], V.Cindro[44], P.Collins[34], J.L.Contreras[18], R.Contri[11], E.Cortina[49], G.Cosme[18], F.Couchot[18], H.B.Crawley[1], D.Crennell[37], G.Crosetti[11], J.Cuevas Maestro[33], S.Czellar[13], E.Dahl-Jensen[28], J.Dahm[52], B.Dalmagne[18], M.Dam[32], G.Damgaard[28], E.Daubie[2], A.Daum[15], P.D.Dauncey[34], M.Davenport[7], J.Davies[21], W.Da Silva[22], C.Defoix[6], P.Delpierre[26], N.Demaria[46], A.De Angelis[7], H.De Boeck[2], W.De Boer[15], S.De Brabandere[2], C.De Clercq[2], M.D.M.De Fez Laso[49], C.De La Vaissiere[22], B.De Lotto[47], A.De Min[27], H.Dijkstra[7], L.Di Ciaccio[38], J.Dolbeau[6], M.Donszelmann[7], K.Doroba[51], M.Dracos[7], J.Drees[52], M.Dris[31], Y.Dufour[7], F.Dupont[12], D.Edsall[1], L-O.Eek[48], P.A.-M.Eerola[7], R.Ehret[15], T.Ekelof[48], G.Ekspong[45], A.Elliot Peisert[35], M.Elsing[52], J-P.Engel[8], N.Ershaidat[22], M.Espirito Santo[20], D.Fassouliotis[31], M.Feindt[7], A.Fenyuk[43], A.Ferrer[49], T.A.Filippas[31], A.Firestone[1], H.Foeth[7], E.Fokitis[31], F.Fontanelli[11], K.A.J.Forbes[21], J-L.Fousset[26], S.Francon[24], B.Franek[37], P.Frenkiel[6], D.C.Fries[15], A.G.Frodesen[4], R.Fruhwirth[50], F.Fulda-Quenzer[18], H.Furstenau[15], J.Fuster[7], D.Gamba[46], M.Gandelman[17], C.Garcia[49], J.Garcia[42], C.Gaspar[7], U.Gasparini[35], Ph.Gavillet[7], E.N.Gazis[31], J-P.Gerber[8], P.Giacomelli[7], D.Gillespie[7], R.Gokieli[51], B.Golob[44], V.M.Golovatyuk[14], J.J.Gomez Y Cadenas[7], G.Gopal[37], L.Gorn[1], M.Gorski[51], V.Gracco[11], A.Grant[7], F.Grard[2], E.Graziani[41], G.Grosdidier[18], E.Gross[7], B.Grossetete[22], P.Gunnarsson[45], J.Guy[37], U.Haedinger[15], F.Hahn[52], M.Hahn[45], S.Hahn[52], S.Haider[30], Z.Hajduk[16], A.Hakansson[23], A.Hallgren[48], K.Hamacher[52], G.Hamel De Monchenault[39], W.Hao[30], F.J.Harris[34], V.Hedberg[23], T.Henkes[7], R.Henriques[20], J.J.Hernandez[49], J.A.Hernando[49], P.Herquet[2], H.Herr[7], T.L.Hessing[21], I.Hietanen[13], C.O.Higgins[21], E.Higon[49], H.J.Hilke[7], T.S.Hill[1], S.D.Hodgson[34], T.Hofmokl[51], S-O.Holmgren[45], P.J.Holt[34], D.Holthuizen[30], P.F.Honore[6], M.Houlden[21], J.Hrubec[50], K.Huet[2], K.Hultqvist[45], P.Ioannou[3],

P-S.Iversen[4], J.N.Jackson[21], R.Jacobsson[45], P.Jalocha[16], G.Jarlskog[23], P.Jarry[39], B.Jean-Marie[18], E.K.Johansson[45], M.Jonker[7], L.Jonsson[23], P.Juillot[8], G.Kalkanis[3], G.Kalmus[37], F.Kapusta[22], M.Karlsson[45], E.Karvelas[9], S.Katsanevas[3], E.C.Katsoufis[31], R.Keranen[7], B.A.Khomenko[14], N.N.Khovanski[14], B.King[21], N.J.Kjaer[7], H.Klein[7], A.Klovning[4], P.Kluit[30], A.Koch-Mehrin[52], J.H.Koehne[15], B.Koene[30], P.Kokkinias[9], M.Koratzinos[32], K.Korcyl[16], A.V.Korytov[14], V.Kostioukhine[43], C.Kourkoumelis[3], O.Kouznetsov[14], P.H.Kramer[52], M.Krammer[50], C.Kreuter[15], J.Krolikowski[51], I.Kronkvist[23], W.Krupinski[16], K.Kulka[48], K.Kurvinen[13], C.Lacasta[49], C.Lambropoulos[9], J.W.Lamsa[1], L.Lanceri[47], P.Langefeld[52], V.Lapin[43], I.Last[21], J-P.Laugier[39], R.Lauhakangas[13], G.Leder[50], F.Ledroit[12], R.Leitner[29], Y.Lemoigne[39], J.Lemonne[2], G.Lenzen[52], V.Lepeltier[18], T.Lesiak[16], J.M.Levy[8], E.Lieb[52], D.Liko[50], J.Lindgren[13], R.Lindner[52], A.Lipniacka[18], I.Lippi[35], B.Loerstad[23], M.Lokajicek[10], J.G.Loken[34], A.Lopez-Fernandez[7], M.A.Lopez Aguera[42], M.Los[30], D.Loukas[9], J.J.Lozano[49], P.Lutz[6], L.Lyons[34], G.Maehlum[32], J.Maillard[6], A.Maio[20], A.Maltezos[9], F.Mandl[50], J.Marco[42], M.Margoni[35], J-C.Marin[7], C.Mariotti[41], A.Markou[9], T.Maron[52], S.Marti[49], C.Martinez-Rivero[42], F.Martinez-Vidal[49], F.Matorras[42], C.Matteuzzi[27], G.Matthiae[38], M.Mazzucato[35], M.Mc Cubbin[21], R.Mc Kay[1], R.Mc Nulty[21], J.Medbo[48], C.Meroni[27], W.T.Meyer[1], M.Michelotto[35], I.Mikulec[50], L.Mirabito[24], W.A.Mitaroff[50], G.V.Mitselmakher[14], U.Mjoernmark[23], T.Moa[45], R.Moeller[28], K.Moenig[7], M.R.Monge[11], P.Morettini[11], H.Mueller[15], W.J.Murray[37], B.Muryn[16], G.Myatt[34], F.Naraghi[12], F.L.Navarria[5], P.Negri[27], S.Nemecek[10], W.Neumann[52], R.Nicolaidou[3], B.S.Nielsen[28], B.Nijjhar[21], V.Nikolaenko[43], P.E.S.Nilsen[4], P.Niss[45], A.Nomerotski[35], V.Obraztsov[43], A.G.Olshevski[14], R.Orava[13], A.Ostankov[43], K.Osterberg[13], A.Ouraou[39], P.Paganini[18], M.Paganoni[27], R.Pain[22], H.Palka[16], Th.D.Papadopoulou[31], L.Pape[7], F.Parodi[11], A.Passeri[41], M.Pegoraro[35], J.Pennanen[13], L.Peralta[20], H.Pernegger[50], M.Pernicka[50], A.Perrotta[5], C.Petridou[47], A.Petrolini[11], G.Piana[11], F.Pierre[39], M.Pimenta[20], S.Plaszczynski[18], O.Podobrin[15], M.E.Pol[17], G.Polok[16], P.Poropat[47], V.Pozdniakov[14], P.Privitera[38], A.Pullia[27], D.Radojicic[34], S.Ragazzi[27], H.Rahmani[31], J.Rames[10], P.N.Ratoff[19], A.L.Read[32], M.Reale[52], P.Rebecchi[18], N.G.Redaelli[27], M.Regler[50], D.Reid[7], P.B.Renton[34], L.K.Resvanis[3], F.Richard[18], J.Richardson[21], J.Ridky[10], G.Rinaudo[46], A.Romero[46], I.Roncagliolo[11], P.Ronchese[35], C.Ronnqvist[13], E.I.Rosenberg[1], E.Rosso[7], P.Roudeau[18], T.Rovelli[5], W.Ruckstuhl[30], V.Ruhlmann-Kleider[39], A.Ruiz[42], K.Rybicki[16], H.Saarikko[13], Y.Sacquin[39], G.Sajot[12], J.Salt[49], J.Sanchez[25], M.Sannino[11,40], S.Schael[7], H.Schneider[15], M.A.E.Schyns[52], G.Sciolla[46], F.Scuri[47], A.M.Segar[34], A.Seitz[15], R.Sekulin[37], M.Sessa[47], R.Seufert[15], R.C.Shellard[36], I.Siccama[30], P.Siegrist[39], S.Simonetti[11], F.Simonetto[35], A.N.Sisakian[14], G.Skjevling[32], G.Smadja[39,24], N.Smirnov[43], O.Smirnova[14], G.R.Smith[37], R.Sosnowski[51], D.Souza-Santos[36], T.Spassov[20], E.Spiriti[41], S.Squarcia[11], H.Staeck[52], C.Stanescu[41], S.Stapnes[32], G.Stavropoulos[9], F.Stichelbaut[2], A.Stocchi[18], J.Strauss[50], J.Straver[7], R.Strub[8], B.Stugu[4], M.Szczekowski[7], M.Szeptycka[51], P.Szymanski[51], T.Tabarelli[27], O.Tchikilev[43], G.E.Theodosiou[9], A.Tilquin[26], J.Timmermans[30], V.G.Timofeev[14], L.G.Tkatchev[14], T.Todorov[8], D.Z.Toet[30], O.Toker[13], A.Tomaradze[2], B.Tome[20], E.Torassa[46], L.Tortora[41], D.Treille[7], W.Trischuk[7], G.Tristram[6], C.Troncon[27], A.Tsirou[7], E.N.Tsyganov[14], M.Turala[16], M-L.Turluer[39], T.Tuuva[13], I.A.Tyapkin[22], M.Tyndel[37], S.Tzamarias[21], B.Ueberschaer[52], S.Ueberschaer[52], O.Ullaland[7], V.Uvarov[43], G.Valenti[5], E.Vallazza[7], J.A.Valls Ferrer[49], C.Vander Velde[2], G.W.Van Apeldoorn[30], P.Van Dam[30], M.Van Der Heijden[30], W.K.Van Doninck[2], J.Van Eldik[30], P.Vaz[7], G.Vegni[27], L.Ventura[35], W.Venus[37], F.Verbeure[2], M.Verlato[35], L.S.Vertogradov[14], D.Vilanova[39], P.Vincent[24], L.Vitale[47], E.Vlasov[43], A.S.Vodopyanov[14], M.Vollmer[52], M.Voutilainen[13], V.Vrba[41], H.Wahlen[52], C.Walck[45], F.Waldner[47], A.Wehr[52], M.Weierstall[52], P.Weilhammer[7], A.M.Wetherell[7], J.H.Wickens[2], M.Wielers[15], G.R.Wilkinson[34], W.S.C.Williams[34], M.Winter[8], M.Witek[16], G.Wormser[18], K.Woschnagg[48], A.Zaitsev[43], A.Zalewska[16], D.Zavrtanik[44], E.Zevgolatakos[9], N.I.Zimin[14],

M.Zito[39], D.Zontar[44], R.Zuberi[34], G.Zumerle[35], J.Zuniga[49]

[1]Ames Lab. and Dept. of Physics, Iowa State University, Ames IA 50011, USA
[2]Physics Dept., Univ. Instelling Antwerpen, Universiteitsplein 1, B-2610 Wilrijk, Belgium and IIHE, ULB-VUB, Pleinlaan 2, B-1050 Brussels, Belgium
[3]Physics Laboratory, University of Athens, Solonos Str. 104, GR-10680 Athens, Greece
[4]Department of Physics, University of Bergen, Allégaten 55, N-5007 Bergen, Norway
[5]Dipartimento di Fisica, Università di Bologna and INFN, Via Irnerio 46, Bologna, Italy
[6]Collège de France, Lab. de Physique Corpusculaire, F-75231 Paris Cedex 05, France
[7]CERN, CH-1211 Geneva 23, Switzerland
[8]Centre de Recherche Nucléaire, F-67037 Strasbourg Cedex, France
[9]Institute of Nuclear Physics, N.C.S.R. Demokritos, GR-15310 Athens, Greece
[10]FZU, Inst. of Physics of the C.A.S. High Energy Physics Division, Czechoslovakia
[11]Dipartimento di Fisica, Università di Genova and INFN, Genova, Italy
[12]Institut des Sciences Nucléaires, Université de Grenoble 1, Grenoble, France
[13]Research Institute for High Energy Physics, SEFT, University of Helsinki, Finland
[14]Joint Institute for Nuclear Research, Dubna, Moscow, Russian Federation
[15]Institut für Experimentelle Kernphysik, Universität Karlsruhe, Karlsruhe, Germany
[16]High Energy Physics Lab., Institute of Nuclear Physics, Krakow, Poland
[17]Centro Brasileiro de Pesquisas Físicas, rua Xavier Sigaud 150, Rio de Janeiro, Brazil
[18]Université de Paris-Sud, Lab. de l'Accélérateur Linéaire, F-91405 Orsay, France
[19]School of Physics and Materials, University of Lancaster, GB-Lancaster LA1 4YB, UK
[20]LIP, IST, FCUL - Av. Elias Garcia, 14-1°, P-1000 Lisboa Codex, Portugal
[21]Dept. of Physics, University of Liverpool, P.O. Box 147, GB-Liverpool L69 3BX, UK
[22]LPNHE, Universités Paris VI et VII, 4 place Jussieu, Paris, France
[23]Department of Physics, University of Lund, Sölvegatan 14, S-22363 Lund, Sweden
[24]Université Claude Bernard de Lyon, IPNL, F-69622 Villeurbanne Cedex, France
[25]Universidad Complutense, Avda. Complutense s/n, E-28040 Madrid, Spain
[26]Univ. d'Aix - Marseille II - CPP, F-13288 Marseille Cedex 09, France
[27]Dipartimento di Fisica, Università di Milano and INFN, Via Celoria 16, Milan, Italy
[28]Niels Bohr Institute, Blegdamsvej 17, DK-2100 Copenhagen 0, Denmark
[29]NC, Nuclear Centre of MFF, Charles University, Areal MFF, Praha 8, Czechoslovakia
[30]NIKHEF-H, Postbus 41882, NL-1009 DB Amsterdam, The Netherlands
[31]National Technical University, Physics Department, GR-15773 Athens, Greece
[32]Physics Department, University of Oslo, Blindern, N-1000 Oslo 3, Norway
[33]Dpto. Fisica, Univ. Oviedo, C/P.Jimenez Casas, S/N-33006 Oviedo, Spain
[34]Department of Physics, University of Oxford, Keble Road, Oxford OX1 3RH, UK
[35]Dipartimento di Fisica, Università di Padova and INFN, Via Marzolo 8, Padua, Italy
[36]Depto. de Fisica, Pontificia Univ. Católica, C.P. 38071 RJ-22453 Rio de Janeiro, Brazil
[37]Rutherford Appleton Laboratory, Chilton, GB - Didcot OX11 OQX, UK
[38]Dipartimento di Fisica, Università di Roma II and INFN, Tor Vergata, Rome, Italy
[39]Centre d'Etude de Saclay, DSM/DAPNIA, F-91191 Gif-sur-Yvette Cedex, France
[40]Dipartimento di Fisica-Università di Salerno, I-84100 Salerno, Italy
[41]Istituto Superiore di Sanità, INFN, Viale Regina Elena 299, I-00161 Rome, Italy
[42]C.E.A.F.M., C.S.I.C. - Univ. Cantabria, Avda. los Castros, S/N-39006 Santander, Spain
[43]Inst. for High Energy Physics, Serpukov P.O. Box 35, Protvino, Russian Federation
[44]J. Stefan Institute and Dept. of Physics, University of Ljubljana, Ljubljana, Slovenia
[45]Fysikum, Stockholm University, Box 6730, S-113 85 Stockholm, Sweden
[46]Dipartimento di Fisica Sperimentale, Università di Torino and INFN, Turin, Italy
[47]Dipartimento di Fisica, Università di Trieste and INFN, Trieste, Italy
[48]Department of Radiation Sciences, University of Uppsala, P.O. Box 535, Uppsala, Sweden
[49]IFIC, Valencia-CSIC, and D.F.A.M.N., U. de Valencia, Burjassot (Valencia), Spain
[50]Institut für Hochenergiephysik, Österr. Akad. d. Wissensch., A-1050 Vienna, Austria
[51]Inst. Nuclear Studies and University of Warsaw, Ul. Hoza 69, PL-00681 Warsaw, Poland
[52]Fachbereich Physik, University of Wuppertal, Wuppertal, Germany

Appendix B

The Contents of a Leptonic Micro-DST

In the micro-DST, all angles are given in degrees, distances are given in cm, energies are given in GeV, and momenta are given in GeV/c. For each event, the following information is stored.

General event information.

1) Run Number
2) Event number
3) LEP fill number
4) File sequence number
5) Centre of mass energy
6) Magnetic field
7) Number of charged tracks
8) Number of neutral tracks
9) Number of unassociated muon chamber TERs
10) Acollinearity (of two tracks with highest momentum)
11) Word containing B1 trigger bits
12) Word with Pythia trigger bits
13) Spare word
14) Spare word
15) Spare word
16) Number of data blocklets following (= number of charged tracks + number of neutral pas + 1 for extra muon hits

then 1 word per blocklet:

17 - 17+blocklets-1) blocklet identifier and word-count, packed in 1 word

For the two tracks with greatest momentum:

1) Blocklet identifier - 50 for charged tracks
2) Quality flag - bits flagging useful points of information about the track

bit 1: ID used in track fit
bit 2: TPC used in track fit
bit 3: OD used in track fit
bit 4: FCA used in track fit
bit 5: FCB used in track fit

3) Momentum
4) Theta of the track at the perigee
5) Phi of the track at the perigee
6) Charge

7) $\delta(p)/p$
8) $\delta(\theta)$
9) $\delta(\phi)$
10) track length
11) χ^2 of the fitted track
12) Isolation angle
13) DELANA mass code assigned to the track
14) Impact parameter (signed) - closest approach in $r\phi$
15) Z at closest approach in $r\phi$
16) Time of flight from TOF
17) Error on time of flight
18) Word for outer detector timing information - not yet available
19) Total energy associated with the track by the Combined Calorimetry code
20) Total energy in the electromagnetic calorimeters associated with the track
21) Total energy in the hadron calorimeters associated with the track
22) Number of muon chamber hits associated with the track
23) TOF information (TDC+256*ADC) external
24) TOF extra blocklet word 8 (TDC+256*ADC) internal

Calorimeter information:
1) Blocklet identifier for Combined Calorimetry (CCA)
2) Total associated energy (E) in CCA
3) $\delta(E)$
4) x coordinate of the start of the shower
5) y coordinate of the start of the shower
6) z coordinate of the start of the shower
7) θ direction of the shower
8) ϕ direction of the shower
9) DELANA mass identifier of the shower
10) dummy words to make
11) cca blocklet
12) standard

13) Blocklet id for electromagnetic calorimetry
14) Total associated energy (E) in FEMC and HPC
15) $\delta(E)$
16) x coordinate of the start of the shower
17) y coordinate of the start of the shower
18) z coordinate of the start of the shower
19) θ direction of the shower
20) ϕ direction of the shower
21) DELANA mass identifier of the shower
22) Layer information: number of layers hit
23) Layer pattern - if layer n is hit then bit $n-1$ is set
24) Detector identifier, so that FEMC can be distinguished from HPC

25) Blocklet id for hadron calorimetry
26) Total associated energy (E) in HCAL
27) $\delta(E)$
28) x coordinate of the start of the shower
29) y coordinate of the start of the shower
30) z coordinate of the start of the shower
31) θ direction of the shower

32) ϕ direction of the shower
33) DELANA mass identifier of the shower
34) Layer information: number of layers hit
35) Layer pattern - if layer n is hit then bit $n-1$ is set
36) Detector identifier

Muon chamber information
1) Blocklet identifier = 52
2) Number of layers in muon chambers associated with the track by EMMASS
3) Global chi**2
4) Expected number of missed layers
5) Hit information - information for each TER associated (up to 7)
1) Detector id*10 + submodule id*1000 + and doublet/triplet flag*10000 + whether TER is active(1)/deactive(0) after EMMASS
2) layer chi**2

Other tracks (up to 6)
1) Blocklet identifier = 50
2) Quality word (as for first two tracks)
3) Momentum
4) θ
5) ϕ
6) Charge
7) $\delta(p)/p$ 8) $\delta(\theta)$
9) $\delta(phi)$
10) Track length
11) χ^2 of the fitted track
12) Isolation angle
13) DELANA mass code
14) Impact param (signed) - closest approach in rphi.
15) Z at closest approach in $r\phi$
16) Time of flight from TOF, 9999 if there is no information
17) Error on TOF
18) Word for outer detector timing information (not yet available)
19) Total energy associated with the track by the Combined Calorimetry code
20) Total energy in the electromagnetic calorimeters associated with the track
21) Total energy in the hadron calorimeters associated with the track
22) Number of muon chamber hits associated with the track

Neutral tracks - up to 10
1) Blocklet identifier = 51
2) Detector identifier (bitted word - bit 1 CCA, bit 2 HPC/FEMC, bit 3 HCAL)
3) Shower energy in CCA)
4) shower energy in HPC/FEMC)if there is cca data then the emcal/hcal data
5) shower energy in HCAL)will have been used to produce it
6) x)
7) y)these values are for the first shower found on the DST -
8) z)MAKE_DST looks first at CCA, then at HPC/FEMC, then at HCAL
9) θ)
10) ϕ)
11) DELANA mass id

Unassociated muon chamber hits
1) Blocklet identifier = 52
2) Number of TERs for which information is recorded below
3) Total number of TERs that were present

Per TER
a) Submodule identifier
b) R
c) $r\phi$
d) z
e) x
f) y
g) θ
h) ϕ
i) Doublet/triplet flag

Simulation information (if any)
1) Blocklet identifier = 53
2) Number of charged particles for which information is recorded below (max 10)
3) Total number of charged particles that were present
4) Number of neutral particles for which information is recorded below (max 10)
5) Total number of neutral particles that were present

For each simulated particle - charged particles first then neutrals
1) Momentum
2) Energy
3) θ at production
4) ϕ at production
5) Charge
6) Mass identifier
7) Number of generations
8) Number of generations recorded (max 10, if word 7 > 10 then the 10 earliest generations will be recorded)
9)....18) Mass ids of particles. The first one is the initial state particle, the last one will usually be the final state particle.

Information on the $l\bar{l}$ system - zero if not available
1) PX
2) PY
3) PZ
4) E
5) P
6) $\cos\theta$
7) PHI
8) Mass code 1
9) Mass code 2

Information on the VD refit
1) Blocklet identifier = 54
2) Number of charged tracks for which refit has been attempted (NCHVD)
3) Beamspot quality - 0 is good

For each track:
4 - 4+NCHVD-1) Number of vertex detector hits associated with the track

For each track, the track perigee parameters before and after the refit, with respect to the beamspot.
a) Signed impact parameter before refit
b) z before refit
c) θ before refit
d) ϕ before refit
e) $1/p$ (signed) before refit

a) Signed impact parameter after refit
b) z after refit
c) θ after refit
d) ϕ after refit
e) $1/p$ (signed) after refit

Appendix C

The Thrust Axis

Event shape variables are useful in describing the geometries found in e^+e^- annihilations. In this appendix the **thrust** is described. It is an interesting quantity as it provides an approximation to the initial direction of motion of the lepton pair, in particular for $\tau^+\tau^-$.

By definition the thrust is :

$$T = \frac{\sum_{i=1}^{N} |\boldsymbol{p_i} \cdot \boldsymbol{n}|}{\sum_{i=1}^{N} |\boldsymbol{p_i}|} \tag{C.1}$$

where the sum is taken over all particles i of the event and where the axis **n** for which the maximum is obtained is called the thrust axis. For ideal two-jet events one obtains $T = 1$ while perfectly spherical events lead to $T = 1/2$. The thrust major axis ($T_{\mathbf{major}}$), which is defined in analogy to T, is orthogonal to the thrust axis and the thrust minor axis ($T_{\mathbf{minor}}$) is orthogonal to both the T and the ($T_{\mathbf{major}}$) axes.

Appendix D

Glossary

BARREL - The barrel region, in the analysis presented in this thesis, is the polar angle acceptance of $43^0 \leq \theta \leq 137^0$

BCO - Beam Cross Over

Blocklet - a piece of DELPHI data, beginning and ending with a word count, and having two words set aside for identifiers and error flags

BRICH - Barrel Ring Imaging CHerenkov detector

Cosmics - Muons from cosmic rays that traverse DELPHI

DAS - Data Acquisition System

DELANA - the DELPHI software for event reconstruction

DELFARM - the cluster of workstations where the DELPHI data is processed

DELPHI - the DEtector with Lepton, Photon and Hadron Identification

DELSIM - DELPHI SIMulation program

DST - Data Summary Tape

Energy - Throughout refers to the centre-of-mass energy

EPA - The Electron Positron Accumulator

FASTBUS - A crate based electronics system used in DELPHI read-out

FCA - Forward Chamber A

FCB - Forward Chamber B

FEMC - Forward Electromagnetic Calorimeter

FIP - Fastbus Intersegment Processor

FRICH - Forward Ring Imaging CHerenkov detector

FSR - Final-State Radiation

HCAL - Hadron Calorimeter

HOF - Forward Hodoscope (scintillators)

HPC - High density Projection Chamber - the barrel electromagnetic calorimeter

IBA - Improved Born Approximation

ID - Inner Detector

ISR - Initial-State Radiation

LEP - the Large Electron Positron collider

Lineshape - The cross-section for the process $e^+e^- \rightarrow f^+f^-$ (f = fermion) as a function of the centre-of-mass energy

m.i.p - Minimum Ionizing Particle

MSM - Minimal Standard Model

MUB - Barrel Muon Chambers

MUF - Forward Muon Chambers

MWPC - MultiWire Proportional Chamber

Octant - The DELPHI barrel region is divided into eight octants for triggering purposes

On-Peak - Refers to the peak energy point of 91.2 GeV

Off-peak - Refers to the energy points within $\pm$ 3 Gev of the peak energy point

OD - Outer Detector

PS - Proton Synchrotron

PXDST - software which strips TANAGRA data down to DST data

Quadrant - The DELPHI barrel region is divided into four quadrants for triggering purposes

RF - Radio Frequency

RICH - Ring Imaging CHerenkov detector

SAT - Small Angle Tagger - the DELPHI luminometer

SPS - Super Proton Synchrotron

TANAGRA - data structure for DELPHI data, containing information from all levels of the event reconstruction (TD to TV)

TB - Track Bundle

TD - Track Data

TE - Track Element

TK - TracK

TV - Track Vertex

TOF - Time Of Flight scintillators

TPC - Time Projection Chamber

T1-4 - the first, second, third and fourth level triggers

VD - microVertex Detector

VSAT - the second DELPHI luminometer positioned close to the beam pipe.